ILMATIETEEN LAITOS
METEOROLOGISKA INSTITUTET
FINNISH METEOROLOGICAL INSTITUTE

159
CONTRIBUTIONS

WAVES IN ARCHIPELAGOS

JAN-VICTOR BJÖRKQVIST

FINNISH METEOROLOGICAL INSTITUTE
CONTRIBUTIONS
No. 159

WAVES IN ARCHIPELAGOS

Jan-Victor Björkqvist

Institute for Atmospheric and Earth System Research
Faculty of Science
University of Helsinki
Helsinki, Finland

ACADEMIC DISSERTATION IN GEOPHYSICS

To be presented with the permission of the Faculty of Science of the University of Helsinki for public examination and criticism in auditorium E204 of the Physicum building (Gustaf Hällströmin katu 2, Helsinki) on the 10th of January, 2020, at 12 o'clock noon.

Finnish Meteorological Institute
Helsinki, 2020

Supervisor Dr Heidi Pettersson
Marine Research
Finnish Meteorological Institute
Helsinki
Finland

Pre-examiners Prof. Jaak Monbaliu
Department of Civil Engineering
Katholieke Universiteit Leuven
Leuven
Belgium

Prof. Alexander Babanin
Department of Infrastructure Engineering
University of Melbourne
Melbourne
Victoria
Australia

Opponent Dr Luigi Cavaleri
Institute of Marine Sciences (ISMAR) - National Research Council (CNR)
Venice
Italy

Custos Prof. Petteri Uotila
Institute for Atmospheric and Earth System Research
Faculty of Science
University of Helsinki
Helsinki
Finland

ISBN 978-952-336-092-1 (paperback)
ISSN 0782-6117
Edita Prima Oy
Helsinki 2020

ISBN 978-952-336-093-8 (pdf)
Helsinki 2020

ILMATIETEEN LAITOS
METEOROLOGISKA INSTITUTET
FINNISH METEOROLOGICAL INSTITUTE

Published by
Finnish Meteorological Institute
(Erik Palménin aukio 1), P.O. Box 503
FIN-00101 Helsinki, Finland

Series title, number and report code of publication
Finnish Meteorological Institute
Contributions 159, FMI-CONT-159

Date
January 2020

Author
Jan-Victor Björkqvist

Title
Waves in Archipelagos

Abstract

Waves are important for both the leisure and safety of the human population. Open-sea waves have been studied since the 1940's and their central properties are known. The wave field is described by the so called wave spectrum, which is a decomposition of the wave energy with respect to the wave frequency. In practice, the wave field is still often reduced to a few parameters, most importantly the dominant frequency (so called peak frequency) and the significant wave height. These parameters, however, does not sufficiently describe an archipelago wave field, but waves in archipelagos have still received relatively little attention from the scientific community. This thesis focuses on waves in archipelagos, and the study was carried out by using both numerical models and instrumental observations from the Helsinki archipelago and the Archipelago Sea in the Baltic Sea.

Waves in archipelagos are heavily affected by the numerous small islands; they attenuate long waves arriving from the open sea, while also defining new fetches for local waves. As a result, the wave spectrum has a wide frequency range where the energy is practically constant. The existence of this energy carrying range is in contrast to open sea measurements where the energy is concentrated around one dominant frequency. This study proposed a characteristic frequency that quantified the centre of the energy carrying range. For a traditional open sea spectrum the characteristic frequency closely resembled the dominant frequency, thus making it suitable for a wide range of wave conditions. The height of single waves in the archipelago were lower relative to the significant wave height. As a consequence, there was a large (10-15%) discrepancy between two definitions of the significant wave height; in the open sea this discrepancy is typically only 7-8%.

The three numerical models of this study simulated the archipelago wave field well. The largest discrepancy with the observations was found in an area just outside the archipelago that was sheltered by a peninsula. Inside the archipelago the models disagreed slightly on the energy distribution within the energy carrying range. These small differences strongly affected the dominant frequency in a way that was not representative of the good model performance. The differences were inconsequential for the significant wave height. During certain conditions the energy of the shortest waves were underestimated when using more advanced methods to calculate the energy transfer from the wind to the waves, most probably because a too small friction velocity. A simple older method to determine the friction velocity reproduced the shorter waves well. Coarse operational wind products were sufficient to force the high-resolution coastal wave models. Providing wind data only every third hour reduced the variability in the modelled wave field in the time scales between 2 and 10 hours. An hourly wind product captured all variations well, except for the statistical sampling variability in the measurements.

Spatial properties of the wave field were inferred from high-frequency wave staff measurements taken by R/V *Aranda*. These measurements were used to form a new wave spectrum where the waves are decomposed according to their inverse phase-speed. The new spectrum agreed well with the spatial wavenumber spectrum for the shortest waves, while the frequency spectrum did not. The good agreement between the inverse phase-speed spectrum and the wavenumber spectrum meant that the effect of the Doppler shift was small. The reason for the disparate results of the frequency domain were attributed to wave non-linearities. Using direct measurements to determining the waves as a function of their phase speed can be useful when studying the interaction between the wind and the waves, since no additional current measurements are needed to quantify the real wave speed relative to the wind.

Publishing unit
Finnish Meteorological Institute, Marine Research Unit

Classification (UDC)
551.46

Keywords
sea surface waves, archipelagos, wave modelling, wave measurements, Baltic Sea

ISSN and series title
0782-6117 Finnish Meteorological Institute Contributions

ISBN	Language	Pages
978-952-336-092-1 (paperback) 978-952-336-093-8 (pdf)	English	137

ILMATIETEEN LAITOS
METEOROLOGISKA INSTITUTET
FINNISH METEOROLOGICAL INSTITUTE

Utgivare
Meteorologiska institutet
(Erik Palméns plats 1)
PB 503, 00101 Helsingfors

Publikationens serie och nummer
Finnish Meteorological Institute
Contributions 159, FMI-CONT-159

Datum
Januari 2020

Författare
Jan-Victor Björkqvist

Rubrik
Skärgårdens vågor

Sammandrag

Havsvågor är viktiga för människor både ur ett rekreations- och säkerhetsperspektiv. Det öppna havets vågor har studerats sedan 1940-talet och deras centrala egenskaper är kända. Vågfältet beskrivs av det så kallade vågspektrumet, i vilket vågornas energi bryts med avseende på deras frekvens. I praktiken reduceras vågfältet ofta till några beskrivande parametrar, varav de viktigaste är den dominanta vågfrekvensen och den signifikanta våghöjden. Dessa parametrar beskriver inte vågorna i skärgården tillräckligt bra, men skärgårdens vågor har ändå fått tämligen lite vetenskaplig uppmärksamhet. Denna avhandling undersökte skärgårdens vågor både med numeriska modeller och observationer från Helsingfors skärgård och Skärgårdshavet.

Skärgårdens vågor påverkas i betydande grad av skärgårdens otaliga små öar; de dämpar längre vågor som anländer från det öppna havet, medan de samtidigt skapar nya svepsträckor för lokala vågor. Därför har vågspektrumet ett brett frekvensband där vågenergin är praktiskt taget konstant. Existensen av ett sådant här energibärande frekvensband står i kontrast till observationer från det öppna havet där energin är starkt koncentrerad kring en dominant frekvens. I detta arbete definierades en ny karakteristisk frekvens vilken beskriver medelpunkten av det energibärande frekvensbandet för skärgårdsvågor. För de typiska vågorna i öppna havet var denna nya karakteristiska frekvens nära den traditionella dominanta frekvensen, vilket gjorde denna nya parameter lämplig för att beskriva vågfält under vitt skilda omständigheter. I skärgården var höjden på de enskilda vågorna (i förhållande till den signifikanta våghöjden) lägre än på det öppna havet. Som en följd skilde sig de två traditionella definitionerna på den signifikanta våghöjden starkt (10-15%); på öppna havet är denna skillnad oftast bara 7-8%.

De tre numeriska vågmodellerna simulerade vågfältet i skärgården väl. De största felen fanns i ett område utanför skärgården som var delvis skyddat av Porkala udden. Inom skärgården betonade modellerna energidistributionen i det energibärande frekvensbandet på olika vis. För den traditionella dominanta frekvensen införde de små skillnaderna en stark avvikelse gentemot observationerna, även om denna avvikelse inte stod i proportion till de egentliga skillnaderna mellan modellerna och observationerna. För beräknandet av den signifikanta våghöjden var skillnaderna obetydliga. Under vissa omständigheter underbetonades energin för de korta vågorna ifall energiflödet från vinden till vågorna beräknades enligt en mera avancerad metod. Detta var troligen ett resultat av en för låg friktionshastighet. En äldre metod för att beräkna energiflödet till vågorna uppvisade inte en liknande avvikelse. De grova operativa vindprodukterna var tillräckliga för att driva vågmodellerna vid kusten, men modellerna kunde inte simulera vågfältets variationer med en tidsskala på 2–10 timmar ifall vindinformationen uppdaterades bara var tredje timme. Med vinddata som gavs varje timme kunde modellen fånga alla variationer, förutom den statistiska variabiliteten i vågobservationerna.

Genom att använda R/V *Arandas* högfrekventa vågobservationer tagna med kapacitiva trådar kunde även spatiell information deduceras. Dessa observationer användes för att definiera ett nytt vågspektrum i vilket vågorna beskrivs genom deras (inverterade) fashastighet istället för deras frekvens eller vågnummer (inversen av våglängden). Detta nya vågspektrum stämde överens med det rent spatiella vågnummerspektrumet för de kortaste vågorna, medan frekvensspektrumet gav olika resultat. Dopplereffekten bedömdes vara liten, eftersom den skulle ha påverkat fashastighetsspektrumet. Orsaken till skillnaderna var vågornas icke-linjära egenskaper, vilka påverkade den högfrekventa delen av frekvensspektrumet. Att beskriva vågorna med hjälp av den direkt observerade fashastigheten kan vara användbar då man undersöker interaktionen mellan vinden och vågorna, eftersom man då inte behöver skilda vattenströmningsmätningar för att bestämma vågornas verkliga hastighet i förhållande till vindhastigheten.

Publikationsenhet
Meteorologiska institutet, enheten för havsforskning

Klassificering (UDK)
551.46

Nyckelord
ytvågor, skärgård, vågmodellering, vågobservationer, Östersjön

ISSN ja och serietitel
0782-6117 Finnish Meteorological Institute Contributions

ISBN
978-952-336-092-1 (paperback) 978-952-336-093-8 (pdf)

Språk
engelska

Sidantal
137

Preface

I never much liked physics. Don't get me wrong, it was OK, but more in the sense that it proved the usefulness of the mathematics I was learning. Especially wave motion felt foreign: $\cos(kx-\omega t)$. I mean, these guys can't even get time running in the right direction. Luckily you didn't have to choose the subjects for the matriculate exam in advance back then; I pretended to prepare for the physics questions, but then still wrote mostly history and philosophy. In the University I majored in mathematics and—while the courses in particle physics never really felt right—got swept away by algebraic topology.

With a looming graduation I realised that I was not flushed with job options. I secured a grant from the University covering a part of my salary for certain intern positions. Armed with this discount tag I thought I'd have a shot at the summer positions at FMI. I wasn't thrilled. My one-course-dabble with atmospheric physics a few years back had not ended well. I was, nonetheless, called in for an interview to the Marine research unit. During that interview Prof. Jari Haapala (now head of the unit) said that they were "*more of the $F = m\vec{a}$ kind of guys*", which felt mildly reassuring.

Now, I won't keep you in suspense. I got the job. The work was intriguing, but my interest was really peaked when I realised that several mathematicians worked in the field. In one of our many discussions Prof. Kimmo Kahma (also a proud mathematician) told me that, by the time he got into waves, he had read even less physics than I had. "*You will be fine*", he told me, "*as long as you have a strong background in Fourier analysis"*. Well, I didn't. To be more exact: I had never done a single Fourier transform in my life. I wasted no time and enrolled in the first possible course at the University. It turned out, however, that I didn't really have the prerequisites, since they assumed that everyone knew a lot of functional analysis. So that was fun. I still managed, and followed up with an applied course, taught by Prof. Kahma himself. Shortly after that I enrolled as Dr. Heidi Pettersson's PhD student and everything, more or less, fell into place.

I have been lucky that several people have overseen my work, thus providing a wealth of opinions. I want to thank my supervisor Dr. Heidi Pettersson for her patience and guidance over the years, and Dr. Laura Tuomi for introducing me to the art of numerical wave modelling. I was also privileged to work under the guidance of Prof. Kimmo Kahma before he retired, thus giving me a chance to absorb some scraps of his decades of knowledge.

Thanks to Dr. Lauri Laakso for encouraging me to visit Miami, and to Prof. William Drennan for inviting me to RSMAS; I learned a great deal during my visits, especially from my talks with Dr. Nathan Laxague and Dr. Milan Curic. The hospitality of Dr. Victor Alari from the Tallinn University of Technology is also very appreciated. I also want to express my gratitude to Jaak Monbaliu and Alexander Babanin for taking the time to function as the pre-examiners of my thesis, and to Luigi Cavaleri for agreeing to be my opponent. Lastly, I would like to thank Professors Matti Leppäranta and Petteri Uotila, my co-authors, my family, and all my friends who have supported me during the years.

Jan-Victor Björkqvist
Helsinki, December 2019

Contents

List of publications

I Björkqvist, J.-V., Tuomi, L., Fortelius, C., Pettersson, H., Tikka, K., and Kahma, K. K., 2017. Improved estimates of nearshore wave conditions in the Gulf of Finland, *Journal of Marine Systems*, 171, pp. 43–53, DOI: 10.1016/j.jmarsys.2016.07.005.

II Björkqvist, J.-V., Vähä-Piikkiö, O., Alari. V., Kuznetsova, A., and Tuomi, L., 2019. WAM, SWAN and WAVEWATCH III in the Finnish archipelago – the effect of spectral performance on bulk wave parameters, *Journal of Operational Oceanography*, DOI: 10.1080/1755876X.2019.1633236

III Björkqvist, J.-V., Pettersson, H., and Kahma, K. K., 2019: The wave spectrum in archipelagos, *Ocean Science*, 15, pp. 1469–1487, DOI: 10.5194/os-15-1469-2019.

IV Björkqvist, J.-V., Pettersson, H., Drennan, W. M., and Kahma, K. K.: A New Inverse Phase Speed Spectrum of Nonlinear Gravity Wind Waves, *Journal of Geophysical Research: Oceans*, 124, pp. 6097–6119, DOI: 10.1029/2018JC014904

The authors contributions

The author is fully responsible for the summary. In Paper I the author did the wave model simulations, data analysis and a main part of the writing. In Paper II the author participated in the planning and execution of some of the field measurements, did the WAM model simulations, the data analysis, and the main part of the writing. In Paper III the author participated in the planning and execution of some of the field measurements, and is responsible for the data analysis and the main part of the writing. In Paper IV the author participated in the design and construction of the wave measurement device, and in the data collection during the field expedition with R/V *Aranda*. The author also processed the raw wave data, and did the data analysis and the major part of the writing.

1 Introduction

1.1 Why study waves?

Waves bring us joy and recreation, but they can also be a security concern for seafarers and coastal constructions (SPM, 1984; Kahma et al., 2016b; Leijala et al., 2018). In addition to their direct effects, wind generated sea surface waves play an intriguing part in several processes by interacting with both the air-sea boundary and the sea bottom. They serve as a medium for the wind that generates them to penetrate below the surface; unlike currents that move matter, the waves capture the energy of the wind and propagate it to sub-surface layers, either locally or at a distant, before finally reaching the shore.

The energy and momentum trapped in the wave motion (and lost through breaking) increase the sub-surface turbulence (Terray et al., 1996; Babanin and Haus, 2009), thus enhancing the vertical mixing of the upper layer (Qiao et al., 2004; Huang and Qiao, 2010). At the same time the waves also impact the lowest atmospheric layer, releasing some of their energy as an increased turbulence in the air, or even creating low-level jets (Högström et al., 2009; Semedo et al., 2009). The fluxes of momentum, heat, and greenhouse gases have also been proposed to be partially controlled by waves (Sahlée et al., 2012; Kahma et al., 2016a; Gutiérrez-Loza et al., 2018). Waves also deform and break sea ice, which can possibly result in an enhanced melting (Squire, 2007; Steele, 1992).

While waves don't transport matter directly, their orbital motions cumulatively move the water particles through the so called Stokes drift (Kenyon, 1969). This movement affects the drift of objects and the dispersion of materials at sea (Perrie et al., 2003; Tuomi et al., 2018) and is also a factor in the creation of Langmuir turbulence, which enhances the mixing of the surface layer (Langmuir, 1938; Belcher et al., 2012). When a wave breaks it also loses momentum to its surroundings, thus creating slopes in the water level that are eventually released into currents. This effect is particularly dominant at shallow surf zones where heavy wave breaking can take place (Longuet-Higgins, 1970), possibly leading to dangerous rip currents. Nearshore currents affect sediment transport and the living conditions of benthic animals, especially in combination with the near bottom orbital velocities of longer waves (Nielsen, 1988; Erm et al., 2011; Kaitaranta et al., 2013; Rinne et al., 2014).

Waves are an integral part of evolving weather patterns and ecosystems by linking otherwise disconnected events, not only in place, but also in time through the effects of swell. Conversely, how the waves develop are determined by their environment. Archipelagos—made up of a collection of small islands—have an irregular fetch geometry and complex bathymetrical conditions. Waves formed under such conditions are unique and deserve to be studied.

1.2 Describing the wave field

The wave spectrum contains the information of the sea state and describes how the energy of the wave field is distributed between different frequencies (ω) and directions (θ).

Parameters derived from the spectrum are a robust way to describe the central features of the wave field, with typical examples being the total energy and the dominant wave frequency. These variables, especially their growth with fetch, have been extensively studied (Toba, 1972; Hasselmann et al., 1973; Donelan et al., 1985; Kahma and Calkoen, 1992).

Waves shorter than the dominant wave frequency are typically described by a power law in spectral space. Different theoretical and dimensional arguments for ω^{-5} and ω^{-4} power laws have been presented, and both forms have experimental support (Phillips, 1958; Kitaigorodskii, 1962; Toba, 1973; Kahma, 1981; Kitaigorodskii, 1983; Phillips, 1985; Battjes et al., 1987; Banner, 1990). Consequently, spectral parameterizations and prognostic tails in wave models have assumed either an ω^{-4} or ω^{-5} structure (Hasselmann et al., 1973; Donelan et al., 1985; Komen et al., 1994; Booij et al., 1999). Yet, a body of research suggests that the rear face is made up of an wind-dependent ω^{-4} equilibrium range that transitions to a constant ω^{-5} saturation range for the highest frequencies. Significant efforts have been made to understand the energy levels of these two regions and the transition between them (e.g. Toba, 1973; Forristall, 1981; Kahma, 1981; Donelan et al., 1985; Resio and Perrie, 1989; Resio et al., 2004; Romero et al., 2010; Lenain and Melville, 2017).

1.3 Modelling the wave field

The possibility to describe the evolution of central wave parameters—combined with the existing parameterizations of the spectrum—led to the development of parametric wave prediction models (e.g. Hasselmann et al., 1976). There even existed a hope that the nonlinear wave interactions (Hasselmann, 1962) would force the wave spectra to a universal form. Nonetheless, later studies found that the connection between the peak frequency and the total energy varied with the fetch geometry, which consequently disproved the existence of a universal spectral shape (Holthuijsen, 1983; Kahma and Pettersson, 1994; Pettersson, 2004; Pettersson and Kahma, 2005).

Third-generation numerical wave models solve the action balance equation and predict the evolution of the wave spectrum without imposing any a priori restrictions on its shape. While originally developed for deep water (WAMDIG, 1988), models have also been adapted for coastal areas (Booij et al., 1999; Monbaliu et al., 2000). Examples of three popular models are WAM (WAMDIG, 1988; Komen et al., 1994), SWAN (Booij et al., 1999), and WAVEWATCH III® (WW3, Tolman et al., 2002). They are all based on the same principle, while differing in their numerical implementation and parameterization of the physical processes controlling wave evolution.

Special techniques have been implemented to account for islands smaller than the spatial resolution of the model (Tolman, 2003), and they have been proved to account for the attenuating effect of the islands well (Ponce de León and Guedes Soares, 2005, 2010). Numerical studies in water bodies with small islands have also been made, such as in the Baltic Sea (Tuomi et al., 2014), the Aegean Sea (Soukissian et al., 2004; Mazarakis et al., 2012), and Lake Superior (Anderson et al., 2015). Cavaleri et al. (2018), again, provided a thorough review of the state of modelling waves in coastal and inner seas, while also discussing the limitations of our current modelling approaches.

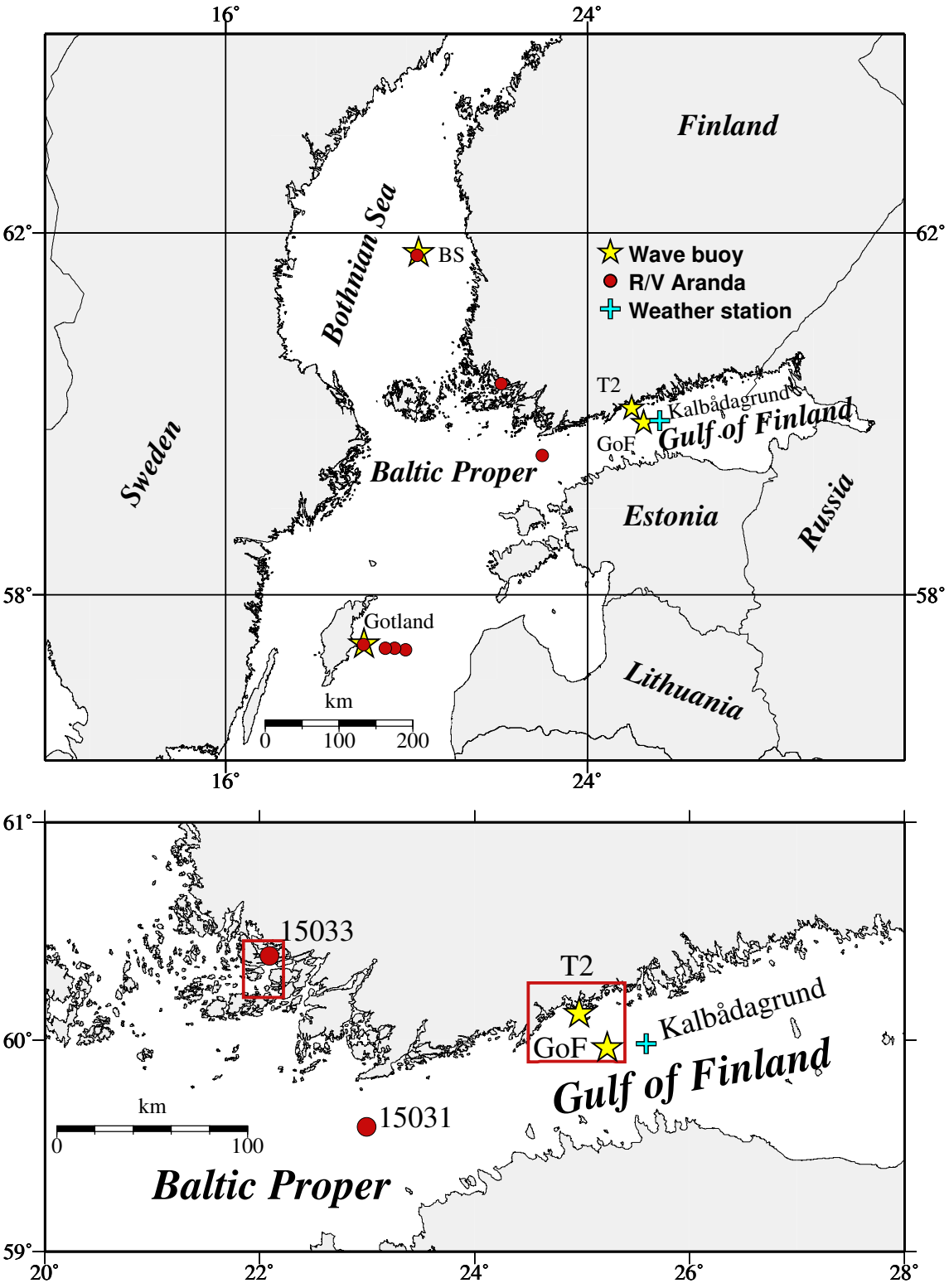

Figure 1.1: A map of the measurement locations in the Baltic Sea. The red boxes in the lower panel show the areas for the maps of the Archipelago Sea (Fig. 1.4) and the Helsinki archipelago (Fig. 1.3). Only permanent wave buoys are shown in this map. For an overview of all the wave measurements in the Helsinki archipelago, see Fig. 1.3. For the 15033 site, see Fig. 1.4.

Figure 1.2: A photograph of the Helsinki archipelago outside of Suomenlinna. (Photo: Jan-Victor Björkqvist)

1.4 Waves in the Baltic Sea

The Baltic Sea is a semi-enclosed basin with a longest fetch of about 700 km and a total area of 377,000 km^2. The wave climate in the Baltic Sea has been thoroughly mapped by both measurements and numerical wave hindcasts (Kahma et al., 2003; Jönsson et al., 2003; Cieślikiewicz and Paplińska-Swerpel, 2008; Räämet and Soomere, 2010; Tuomi et al., 2011; Pettersson et al., 2013; Björkqvist et al., 2018). The highest significant wave height of 8.2 m was measured in the Baltic Proper main basin (Tuomi et al., 2011). Nonetheless, the operational wave buoy in the Bothnian Sea sub-basin recently measured an 8.1 m significant wave height during the storm Aapeli in January 2019. A significant wave height over 9 m has been modelled both in the northern and southern part of the Baltic Proper (Tuomi et al., 2011; Björkqvist et al., 2018).

The Gulf of Finland (GoF) is a 60–120 km wide and 350 km long sub-basin of the Baltic Sea (Fig. 1.1). The narrowness of the gulf restricts wave growth and lines the wave directions along the basin (Kahma and Pettersson, 1994; Pettersson et al., 2010). Even though the dominant wind direction is from the south-west (Soomere and Keevallik, 2003), strong easterly winds are also possible. A 5.2 m significant wave height has been measured by the GoF wave buoy during strong winds from both east (Pettersson et al., 2013) and south-west (Tuomi et al., 2011).

Large parts of the Finnish coastline has a dense coastal archipelago. The main area of interest in this study was the Helsinki archipelago (Fig. 1.2), which is located on the southern Finnish coast in the GoF (Fig. 1.3). Measurements in the Helsinki archipelago have been conducted for coastal planning purposes (Kahma et al., 2016b), but they have seen limited scientific use. The other nearshore area studied in this thesis was the Archipelago Sea, which (together with the Åland Sea) separates the Baltic Proper from the Bothnian Sea (Fig. 1.1). It is only about 8,300 km^2 large, but still has over 40,000 islands. Very little wave measurements are available from the Archipelago Sea, but Tuomi et al. (2014) presented observations from a short campaign showing that the swell from the Baltic Proper was effectively attenuated by the islands and bottom processes. Wave mea-

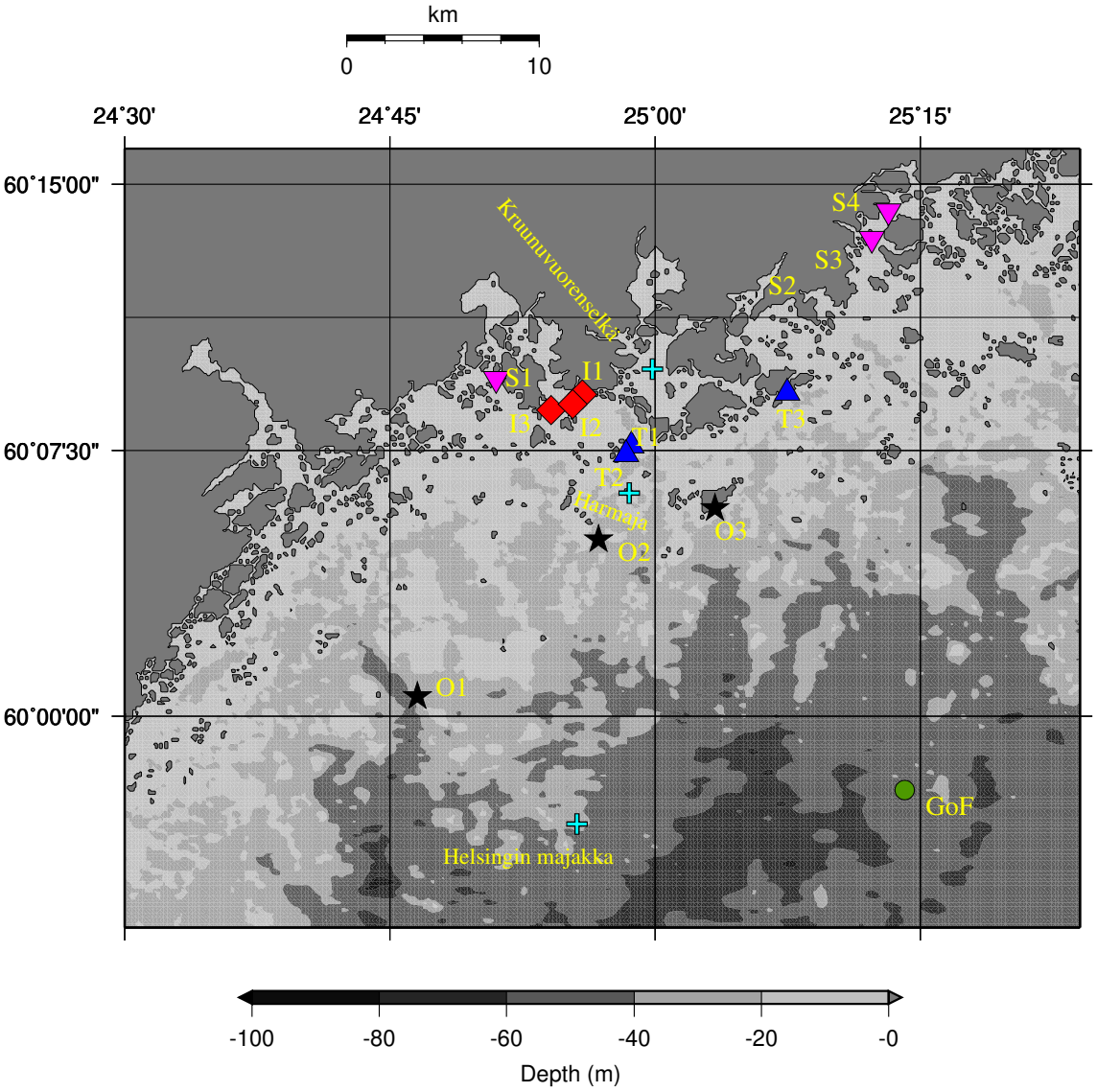

Figure 1.3: Measurement locations in the Helsinki archipelago. A plus (+) denotes wind measurements. The abbreviations are codes used for the wave buoy sites in Paper III, where O=Outer archipelago, T=Transition zone, I=Inner archipelago, and S=Sheltered archipelago. For the corresponding site names, see Table 3.1. The depth information is from the 0.1 nmi bathymetrical grid used in Paper I & II.

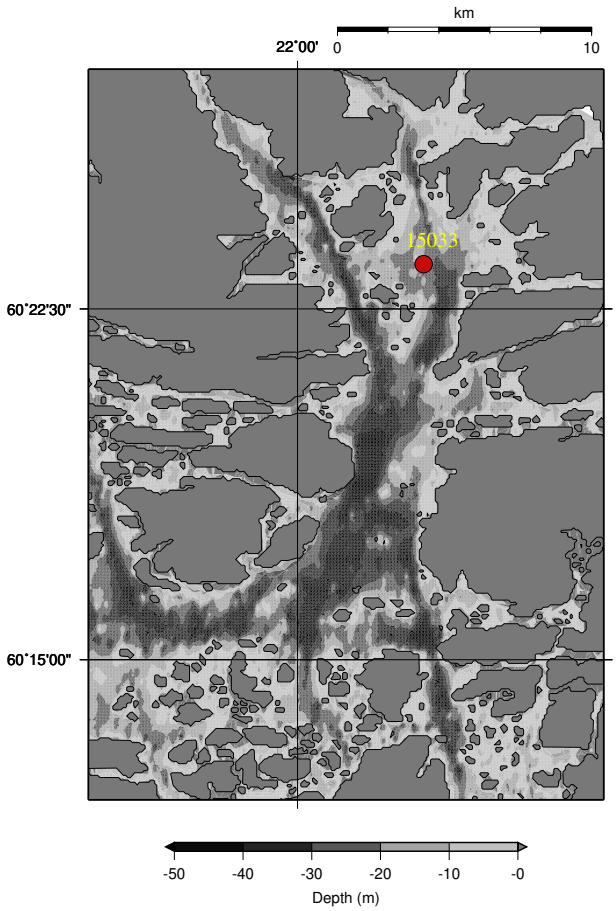

Figure 1.4: The measurement location in the Archipelago Sea where high-frequency measurements were available with several wave staffs. Measurement were taken with R/V *Aranda*.

surements from the Utö station at the southern edge of the Archipelago Sea exist (Tuomi and Björkqvist, 2014; Laakso et al., 2018), but this location is heavily exposed to waves propagating from the Baltic Proper.

1.5 Outline and aims of this study

Already Kahma (1979) presented wave measurements from the Bothnian Sea archipelago. Still, the characteristic features of waves in archipelagos have not yet been extensively studied, partly because of the relatively limited observational data. The main aim of this thesis was to fill this knowledge gap using in situ measurements and numerical models.

The properties of the waves inside the archipelago were compared with open sea measurements and results from previous studies. Special weight was given to the evolution of the wave spectrum through different parts of the archipelago (Paper II & III). In addition to quantifying the change in the spectral shape, the consequences for derived wave parameters, such as the significant wave height and the peak frequency, were also determined. The rear face of the spectrum was studied using high-frequency wave staff measurements (Paper IV). From these measurements, a new inverse phase-speed spectrum was defined,

and its properties were compared to the traditional frequency and wavenumber spectra.

Results from three numerical wave models were validated against extensive wave buoy measurements inside and outside the archipelago (Paper I & II). The abilities of the models to capture different features of the archipelago wave field were determined, as was the role of different forcing factors, such as the atmospheric and the bathymetrical data. The remaining challenges concerning archipelago implementations of the wave models, and the possible connection to the physical parameterization of the source terms, were discussed.

The main aims of this thesis were the following:

1. Identify how the wave spectrum changes when the waves propagate from the open sea towards the coast through the archipelago, and how the wave field in the archipelago compare with open sea wave conditions.

2. Determine how the atypical spectral shapes affect widely used wave parameters, such as the significant wave height and the peak frequency, and find suitable parameters to characterize the wave field in archipelagos.

3. Study how well state-of-the-art numerical wave models can reproduce the wave spectrum in the archipelago, how adequate the available wind forcings and bathymetrical data are for this task, and how the differences and shortcomings of the models are reflected in typical wave parameters and their validation.

4. Compare different numerical solutions and parameterizations of the physics, and identify topics where further study could lead to more accurate archipelago wave simulations.

5. Describe the rear face of the spectrum in different spectral domains, especially by using high-frequency measurements to define and study a new inverse phase-speed spectrum.

6. Study the power-law structures and their transitions are in all spectral domains, and use the inverse phase-speed spectrum to help explain the different results of the frequency spectrum and the wavenumber spectrum.

2 Definitions and mathematical methods

2.1 The wave spectrum

The investigation of sea surface waves starts with describing the water surface displacement at each time and location, denoted $\eta(x, y, t)$ (m). A Fourier transform of the autocorrelation function of $\eta(x, y, t)$ gives a frequency-wavenumber representation of the sea surface, called the wave spectrum. The full three-dimensional wave spectrum describes the variance density of the wave field as a function of the (angular) frequency, ω (rad s^{-1}), the wavenumber, k (rad m^{-1}), and the direction, θ (rad). This spectrum is denoted $\mathbb{F}(\omega, k, \theta)$ and normalized so that the total variance (m^2) of $\eta(x, y, t)$ is the integral

$$\mathrm{D}^2(\eta) = \iiint \mathbb{F}(\omega, k, \theta) k \; \mathrm{d}k\mathrm{d}\omega\mathrm{d}\theta. \tag{2.1}$$

Depending on the application and/or available data the spectrum is often given either as the wavenumber spectrum $\Psi(k, \theta)$ ($\mathrm{m}^4\mathrm{rad}^{-1}$), or as the frequency spectrum $\mathcal{S}(\omega, \theta)$ ($\mathrm{m}^2\mathrm{s\ rad}^{-1}$). These spectra follow by integration of Eq. 2.1 (over ω and k respectively). They can, however, also be determined directly from spatial or temporal data if only one or the other are available. The omnidirectional variants of these spectra are further obtained by integration:

$$F(k) = \int \Psi(k, \theta) k \; \mathrm{d}\theta \tag{2.2}$$

$$S(\omega) = \int \mathcal{S}(\omega, \theta) \; \mathrm{d}\theta. \tag{2.3}$$

If both the frequency and wavenumber of a single wave component is known, it is also possible to determine its phase-speed, since $c = \omega k^{-1}$ ($\mathrm{m\ s}^{-1}$). Previous studies have deduced spectral phase-speed information of e.g. transient eddies (Hayashi, 1982; Randel and Held, 1991). This work, however, also examined a representation of the wave field—formally defined for the first time in Paper IV—where the directional wave spectrum is given as a function of the inverse phase-velocity $\boldsymbol{\nu} = \mathbf{k}\omega^{-1}$ ($\mathrm{s\ m}^{-1}$), or the inverse phase-speed $\nu = |\boldsymbol{\nu}| = c^{-1}$. Also this spectrum was obtained by integration from the full spectrum:

$$\mathcal{Q}(\nu, \theta)\nu \, \mathrm{d}\nu = \int_{k/\omega=\nu} \mathbb{F}(\omega, k, \theta) k \; \mathrm{d}\omega\mathrm{d}k \tag{2.4}$$

$$\mathcal{Q}(\nu, \theta) = \frac{1}{\nu} \int \mathbb{F}(\omega, \omega\nu, \theta) \, \omega\nu \; \mathrm{d}\omega \left|\frac{\mathrm{d}k}{\mathrm{d}\nu}\right| \tag{2.5}$$

$$= \frac{1}{\nu} \int \mathbb{F}(\omega, \omega\nu, \theta) \, \omega^2\nu \; \mathrm{d}\omega \tag{2.6}$$

$$= \frac{1}{\nu} \int \mathbb{F}(k/\nu, k, \theta) \, \frac{k^2}{\nu^2} \; \mathrm{d}k, \tag{2.7}$$

where the last step simply switches the integrating variable from ω to k. This spectrum has the units $\mathrm{m^4 s^{-2} rad^{-1}}$, since the normalisation was chosen to resemble that of the wavenumber spectrum. Thus, the omnidirectional form ($\mathrm{m^3 s^{-1}}$) is given as (cf. Eq. 2.2):

$$Q(\nu) = \int \mathcal{Q}(\nu, \theta)\nu \, \mathrm{d}\theta. \tag{2.8}$$

The Jacobian $|\mathrm{d}k/\mathrm{d}\nu|$ was applied in Eq. 2.5 to give $Q(\nu)$ as variance density—not variance mass—with respect to ν, thus conserving the property of the integral being the variance of the wave field. Nevertheless, the definitions using integration were not applied in practice in this study, since observational data favours an approach where the variance was binned (see Sect. 2.1.2). Equations 2.4–2.7 are given here for completeness.

2.1.1 Fast Fourier Transform (FFT)

The omnidirectional frequency spectrum $S(\omega)$ is typically determined from a water level elevation time series at one point, i.e. $\eta(t)$. Assuming an ergodic process, the wave spectrum can be calculated from a single time series (e.g. Bendat and Piersol, 1986). The proper definition for the wave spectrum—as the power spectrum of $\eta(t)$—is the Fourier transform of the auto-covariance function of $\eta(t)$. Nevertheless, because of practical considerations, the spectrum is almost exclusively calculated using the Fourier transform of the original data, given here with the normalisation:

$$X(\omega_n) = \frac{1}{N} \sum_{j=0}^{N-1} \eta_j e^{-i2\pi nj/N}, \tag{2.9}$$

where $n \in \mathbb{N}$, N is the number of points in the observational time series, and η_j is the j:th data point. Typically, the Fourier transform is computed using the Fast Fourer Transform (FFT). The (singe sided) wave spectrum then follows as

$$S(\omega_n) = \frac{N\Delta t}{\pi} \langle |X(\omega_n)|^2 \rangle, \tag{2.10}$$

where $1 \leq n \leq N/2$ (assuming that N is even), Δt is the sampling time, $|\cdot|$ is the complex modulus, and $\langle \cdot \rangle$ is a general notation for the averaging that is required to achieve statistical stability. This stability is achieved by averaging elementary frequency bins, or by calculating the FFT from several blocks of the time series and averaging the results of these transforms. The latter technique was used by the Datawell wave buoys (Datawell, 2017), while the former was implemented to the wave staff data in Paper IV.

To avoid window leakage the original time series, η_j, were tapered with a window. The Datawell wave buoys used a Tukey window (Datawell, 2017), while a Blackman-Harris window was used for the wave staff data in Paper IV. The loss of variance caused by the window tapering was compensated in Eq. 2.10 to not violate the condition of Eq. 2.1.

2.1.2 Wavelet Directional Method (WDM)

The data from the multiple wave staffs (see Sect. 3.1.2) were analyzed using the Wavelet Directional Method (WDM, Donelan et al., 1996). The WDM gives information about the height $W(t, f)$ (m), as a function of time, t (s), and frequency (actually scale), f (Hz). This complex amplitude can be used to calculate the variance $|W(t, f)|^2$ (m^2). Using the phase lag between the different wave staffs the WDM determines the wavenumber $W_k(t, f)$ (rad m^{-1}) and the direction $W_\theta(t, f)$ (rad) of the waves. An exhaustive methodological description of the WDM is given in Donelan et al. (1996).

A number of different wavelets might be used. Following Donelan et al. (1996) and Tamura et al. (2014) we chose to use the Morlet wavelet (Grossmann and Morlet, 1984), which has a better frequency resolution compared to e.g. the Meyer wavelets (Meyer, 1989). The Morlet wavelets, however, are not orthogonal, thus leading to a loss of information for scales in between wavelets. This is compensated for by using intermediate wavelets (so called voices). Since voices are not independent, a large number of voices can give the illusion of a good frequency resolution, when in reality the neighboring frequencies are mostly dependent.

To convert the wavelet power, $|W(t, f)|^2$, to spectral density (m^2 Hz^{-1}s^{-1}) the proper normalization is given by

$$\mathbb{W}(t, f) = \frac{1}{\Delta t \Delta f} \frac{C_\mathrm{w}}{C_\mathrm{v}} |W(t, f)|^2, \tag{2.11}$$

where Δt and Δf is the time resolution and frequency resolution, C_v is the number of voices (including the base wavelet), and C_w is a factor accounting for the possible non-orthogonalities of the wavelets. For the orthogonal Meyer wavelets $C_\mathrm{w} = 1$ and for the Morlet wavelets used in this study $C_\mathrm{w} = 1.03565$.

Since the wavenumber modulus and the wave direction is known for each pair (f, t), an estimate for the wavenumber spectra, $F(k)$, was obtained by binning the variance $\mathbb{W}(t, f)\Delta t \Delta f$ with respect to the wavenumber modulus $W_k(t, f)$, and normalizing with the chosen bin width Δk. The directional wave spectra, $\mathcal{S}(\omega, \theta)$ and $\Psi(k, \theta)$, were determined by a similar binning technique with respect to both k and/or θ. Finally, the inverse phase-speed spectra, $Q(\nu)$ and $\mathcal{Q}(\nu, \theta)$ were calculated by binning the variance with respect to $\nu = k(2\pi f)^{-1}$ and/or θ. An overview of the chosen bin sizes etc. are found in the methods section of Paper IV.

2.1.3 Dimensionless quantities

Dimensionless quantities are a convenient way to describe physical processes. They allow us to compare experimental data from different conditions and establish possible universal properties. Dimensional analysis was adopted early to help study the wave spectrum, and the dimensionless quantities of the frequency and wavenumber spectra are established (Phillips, 1958; Kitaigorodskii, 1962). They are gathered in Table 2.1, along with the dimensionless quantities of the newly defined inverse phase-speed spectrum, which were determined in Paper IV.

Table 2.1: Dimensionless quantities Π_n of the different spectral representation. Also the forms of the ranges for rear face of the spectrum are given, where α is the saturation constant (Phillips, 1958) and α_u is the equilibrium constant (Kahma, 1981).

	$S(\omega)$ (m^2 s)	$F(k)$ (m^3)	$Q(\nu)$ (m^3 s^{-1})
Π_1	$\frac{S(\omega)\omega^4}{Ug}$	$\frac{F(k)k^{2.5}g^{0.5}}{U}$	$\frac{Q(\nu)\nu^4 g^2}{U}$
Π_2	$\frac{S(\omega)\omega^5}{g^2}$	$F(k)k^3$	$Q(\nu)\nu^5 g^2$
Π_3	$\frac{\omega U}{g}$	$\frac{kU^2}{g}$	$U\nu$
Equilibrium range	$\alpha_u U g \omega^{-4}$	$\frac{\alpha_u}{2} U g^{-0.5} k^{-2.5}$	$\alpha_u U g^{-2} \nu^{-4}$
Saturation range	$\alpha g^2 \omega^{-5}$	$\frac{\alpha}{2} k^{-3}$	$\alpha g^{-2} \nu^{-5}$

The dimensionless forms determine power law properties for certain parts of the wave spectrum. The rear face of the spectrum consists of an equilibrium range, followed by a saturation range. The equilibrium range scales with the wind speed, while the saturation range does not (Table 2.1). A schematic illustration of these ranges can be found in Fig. 2.1. If the water depth, h, is deep ($kh > \pi$), the ranges in the different spectral domains can be connected using linear theory, which is seen by the use of the same constants in all three domains. These dimensionless coefficients, α and α_u, are determined experimentally.

Phillips (1958) determined the constant α for the saturation range in the frequency domain. Following studies have calculated a value for α using both frequency and wavenumber measurement (e.g. Forristall, 1981; Leckler et al., 2015; Lenain and Melville, 2017). The equilibrium range constant was determined by Toba (1973) using laboratory data (and the friction velocity u_* instead of the wind speed U). Also the equilibrium range constant has been widely studied since (e.g. Forristall, 1981; Kahma, 1981; Donelan et al., 1985; Kahma, 1986; Resio et al., 2004). Both constants were determined for the inverse phase-speed spectrum based on the data of this study (Paper IV).

Although the equilibrium constant, α_u, have been considered universal, there is also evidence that it depends on the strength of the wind forcing (Donelan et al., 1985). The strength of the forcing wind is given relative to the phase speed of the spectral peak, U/c_p (also called the inverse wave age). This dependency can be accounted for by multiplying the equilibrium range with the dimensionless quantity $(U/c_p)^{p-1}$, following Donelan et al. (1985).

The exact transition between these two ranges has not yet been determined. Still, if the saturation range is assumed universal, the equilibrium level follows from the transition point (or vice versa). That is (in the frequency domain):

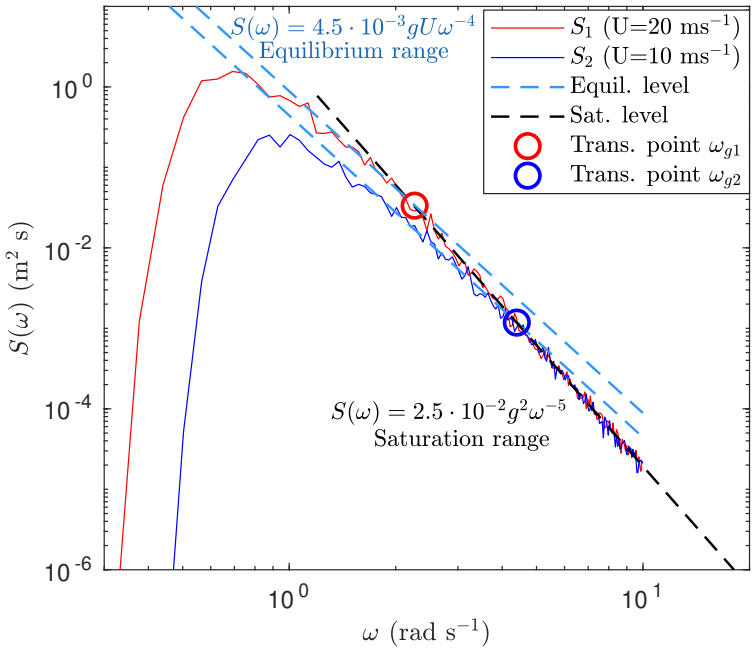

Figure 2.1: Schematic spectra showing the wind-dependent ω^{-4} equilibrium range and the transition to an ω^{-5} saturation range. The transition point $\omega_g U/g$ will be constant if the saturation level is fixed and the equilibrium level depend linearly on the wind speed.

$$\alpha_u \left(U/c_p\right)^{p-1} U g \omega_g^{-4} = \alpha g^2 \omega_g^{-5} \tag{2.12}$$

$$\frac{\omega_g U}{g} = \frac{\alpha}{\alpha_u}\left(\frac{U}{c_p}\right)^{1-p}, \tag{2.13}$$

where ω_g is the transition frequency, and g is the acceleration caused by gravity. Assuming deep-water linear theory, the phase speed is given by $c_p = g/\omega_p$, where ω_p is the peak frequency (Eq 2.19). For $p = 0$ the expression thus becomes $\omega_g/\omega_p = \alpha/\alpha_u =$ constant. In other words, the transition happens at a certain multiple of the peak frequency. This has been proposed by e.g. Banner (1990).

For $p = 1$ the term (U/c_p) vanishes, and the transition is determined by a constant dimensionless frequency: $\omega_g U/g = \alpha/\alpha_u$. This is consistent with Kahma (1981). Therefore, assuming a constant saturation range, the study of the equilibrium levels and transition points are just two sides of the same coin.

If deep water linear wave theory is assumed, the dimensionless transition frequency is the inverse wave age of the wave component with the frequency ω_g, since $\omega U/g = U/c$. Similarly, $kU^2/g = (U/c)^2$ in the wavenumber domain. In the inverse phase-speed domain no theoretical assumptions are needed, since $U\nu \equiv U/c$ by definition; this was the main motivations for defining the inverse phase-speed spectrum, $Q(\nu)$.

2.2 Wave parameters

2.2.1 Wave height

Many wave parameters are calculated using spectral moments, given as

$$m_n = \int \omega^n S(\omega)\,\mathrm{d}\omega. \tag{2.14}$$

The significant wave height, H_s, is calculated as

$$H_s = H_{m_0} = 4\sqrt{m_0}, \tag{2.15}$$

where $m_0 = \mathrm{D}^2(\eta)$ is the variance of the wave field. The notation H_{m_0} is used to distinguish Eq. 2.15 from the older definition, which is the mean height of the highest one-third of the individual waves in the time series. This parameter, $H_{1/3}$, is calculated by determining the individual wave height between two zero down-crossing and, after sorting them in descending order, calculating:

$$H_{1/3} = \frac{1}{N_\mathbf{w}/3} \sum_{i=1}^{N_\mathbf{w}/3} H_i, \tag{2.16}$$

where H_i is the height of a single wave and $N_\mathbf{w}$ is their total number.

The single highest wave of the time series is

$$H_{max} = \max\{H_i \,:\, 1 \leq i \leq N_\mathbf{w}\}, \tag{2.17}$$

while the maximum crest height is determined directly from the vertical displacement time series

$$\eta_{max} = \max\{\eta_j \,:\, 1 \leq j \leq N\}, \tag{2.18}$$

where N is the amount of data points.

2.2.2 Wave frequency

The definition of the peak frequency is the location of the spectral maximum, that is

$$\omega_p = \arg\max_\omega \, S(\omega). \tag{2.19}$$

In practise some smoothing method is often used when dealing with discrete spectra. All the papers in this study used a parabolic fit near the peak, but other methods also exist, such as that of Young (1995):

$$\omega_p^q = \frac{\int \omega S(\omega)^q \,\mathrm{d}\omega}{\int S(\omega)^q \,\mathrm{d}\omega}, \tag{2.20}$$

where q is a free parameter. Young (1995) proposed Eq. 2.20 with $q = 4$ as an alternative definition for the peak frequency. Although not an unbiased estimate for atypical wave conditions, Eq. 2.20 defines the "characteristic" frequency used in this study:

$$\omega_c = \omega_p^{q=4}. \tag{2.21}$$

The mean frequency is defined using the spectral moments as

$$\omega_m = \frac{m_1}{m_0}, \tag{2.22}$$

but is also obtained from 2.20 as $\omega_m = \omega_p^{q=1}$.

The wave periods follows from the wave frequency as

$$T_x = 2\pi \left(\omega_x\right)^{-1}, \tag{2.23}$$

where x refers to any of the frequency parameters ($x = p$ for ω_p etc.).

The spectral narrowness parameter by Battjes and van Vledder (1984) quantifies the narrowness (or peakedness) of the omnidirectional spectrum, and is defined as:

$$\kappa^2 = \frac{1}{{m_0}^2}\left(\left[\int_0^\infty S(\omega)\cos(\frac{\omega}{\omega_{m_{02}}})\,\mathrm{d}\omega\right]^2 + \left[\int_0^\infty S(\omega)\sin(\frac{\omega}{\omega_{m_{02}}})\,\mathrm{d}\omega\right]^2\right), \tag{2.24}$$

where $\omega_{m_{02}} = \sqrt{\frac{m_2}{m_0}}$. For an extremely narrow spectrum κ^2 tends to 1, while a wide spectrum has a κ^2 value close to 0.

3 The experimental set-up

3.1 Observational data

3.1.1 Wave buoy measurement

Most of the wave data in this study originated from Datawell Directional Waveriders. The larger (70–90 cm) buoys are equipped with accelerometers, and measure the accelerations, pitch, roll, and orientation of the device. They are all part of of FMI's operational fleet, but the Suomenlinna wave buoy (T2) is owned by the City of Helsinki. Additional measurements were made with smaller GPS-based DWR-G4 buoys. The majority of the G4-measurements were commissioned by the City of Helsinki (Kahma et al., 2016b), but some were also performed purely for research purposes. An overview of the measurement locations are given in Table 3.1, and a more detailed description of the data sets can be found in Papers I–IV.

3.1.2 Wave staff measurements

Wave staffs are submerged in the water and function as capacitors, with the capacitance changing with the water level. The omnidirectional wave spectrum can be calculated from the vertical water level displacements measured by a single wave staff. The thin wave staffs can measure shorter waves compared to wave buoys; wave staffs are a couple of mm thick, while wave buoys function as natural low-pass filters because of their size.

Directional and wavenumber spectra from the data taken with multiple wave staffs simultaneously were obtained using the WDM (Donelan et al., 1996, see also Sect. 2.1.2). The five wave staffs were installed in a fixed array that was submerged in front of a stationary R/V *Aranda*. The measurements were corrected for the movement of the ship following Drennan et al. (1994), and the motion correction and the calibration were validated against measurements from the Bothnian Sea wave buoy. A more detailed description of the experimental set-up is given in Paper IV.

3.1.3 Wind measurements

Wind data from the GoF were available from three FMI automatic weather stations (Fig. 1.3 Table 3.2). Paper II also used measurements from Kruunuvuorenselkä (Fig. 3.1), which have previously not been presented in any scientific paper.

Wind data was gathered by R/V *Aranda* simultaneously as the set-up measured the waves. Wind eddy covariance measurements were taken from the bow at the heights of 10.1 m and 16.2 m, of which the lower one was used since it was close to the 10 metre reference height.

A more detailed description of the wind measurements are found in the respective original articles.

Table 3.1: An overview of the wave measurement sites. R/V *Aranda* was a moving platform, while all other sites were fixed. The years refer to the years used in the study; data from the operational wave buoys of Gulf of Finland and Bothnian Sea are available for a longer time.

Station name	depth	Years	Device	Paper
Other				
R/V *Aranda* (15031–15044)	25–235 m	2015	Wave staffs	IV
Bothnian Sea (BS)	120 m	2015	DWR Mk-III	IV
Gulf of Finland (GoF)	62 m	2012–2018	DWR Mk-III / DWR4	I–III
Outer archipelago				
Harmaja (O1)	29 m	2012	DWR-G4	I–III
Isosaari (O2)	7 m	2014	DWR-G4	II, III
Berggrund (O3)	27 m	2015	DWR-G4	II, III
Transition Zone				
Länsikari (T1)	10 m	2013	DWR-G4	III
Suomenlinna (T2)	22 m	2016–2018	DWR Mk-III	II, III
Itä-Villinki (T3)	9 m	2013	DWR-G4	II, III
Inner archipelago				
Hernesaari (I1)	13 m	2012	DWR-G4	II, III
Ruumiskari (I2)	12 m	2014	DWR-G4	II, III
Jätkäsaari (I3)	13 m	2012	DWR-G4	II, III
Sheltered archipelago				
Koivusaari (S1)	5 m	2012	DWR-G4	III
Ramsinniemi (S2)	9 m	2013	DWR-G4	III
Vuosaaren satama (S3)	8 m	2013	DWR-G4	III
Talosaari (S4)	7 m	2013	DWR-G4	III

Table 3.2: Wind measurements platforms.

Station name	Height	Years	Eddy covariance	Paper
Kalbådagrund	32 m	2012–2016	No	I–III
Helsingin majakka	32 m	2012–2016	No	II
Harmaja	18 m	2012–2016	No	I–III
Kruunuvuorenselkä	13 m	2016	No	II
R/V *Aranda*	10 m	2015	Yes	IV

Figure 3.1: The wind measurements from inside the archipelago at Kruunuvuorenselkä (Fig. 1.3) (Photo: Jan-Victor Björkqvist).

3.2 Wave modelling

3.2.1 The principle of wave models

Phase averaged third-generation wave models are the state-of-the-art, and impose no a priori restrictions on the shape of the wave spectrum. These models solve the wave action balance equation, which in Cartesian coordinates can be written as:

$$\frac{\partial N}{\partial t} + \frac{\partial c_x N}{\partial x} + \frac{\partial c_y N}{\partial y} + \frac{\partial c_\sigma N}{\partial \sigma} + \frac{\partial c_\theta N}{\partial \theta} = \frac{G_{tot}}{\sigma}, \tag{3.1}$$

where $N(t, x, y; \sigma, \theta) = \mathcal{S}(t, x, y; \sigma, \theta)/\sigma$ is the wave action density, $\sigma = \omega - U_c k$ is the intrinsic frequency, U_c is the current speed, c_X is the propagation velocity of the wave variance with respect to different variables, t is the time, x, y are the Cartesian coordinates, and θ is the propagation direction. The reason for modelling the action density instead of the variance density is that the action density is conserved in the presence of currents, while the variance is not. In deep water without ambient currents the intrinsic frequency, σ, reduces to the frequency, ω. Eq. 3.1 can then be written in terms of the variance density, $\mathcal{S}(t, x, y; \omega, \theta)$.

The left side of Eq. 3.1 describes the propagation of wave variance and is solved numerically using an explicit or implicit solver. The explicit solvers of different order are subject to the CFL-condition. Implicit solvers are unconditionally stable, but require iteration to converge.

The right side term, G_{tot}, is the sum of source terms describing the change in wave variance that is caused by physical processes. In deep water the three processes considered

are the energy input by the wind (G_{in}), the dissipation of energy through whitecapping (G_{ds}), and the weakly non-linear four wave interactions (G_{nl}). The source terms accounting for finite depth effects are e.g.the bottom friction (G_{bot}), depth-induced wave breaking (G_{brk}), and non-linear three wave interactions (G_{nl3}).

3.2.2 WAM, SWAN, and WAVEWATCH III

Three numerical wave models were used in this study. WAM (WAMDIG, 1988; Komen et al., 1994; Monbaliu et al., 2000) was used in Papers I and II, while SWAN (Booij et al., 1999) and WAVEWATCH III® (WW3, Tolman et al., 2002) were used in Paper II. The models differ in their numerical scheme (used to solve the left side of Eq. 3.1) and their parameterization of the physical processes (right side of Eq. 3.1).

WAM is the oldest of the models and is built around a fixed set of source terms, as documented in Komen et al. (1994) and Bidlot et al. (2007). SWAN has a couple of options for the choice of deep water source terms, but the ones based on the work of Komen et al. (1984) and Komen et al. (1994) were chosen for this study. WW3 has the widest setting of source terms, but was implemented using the deep water source terms package of Ardhuin et al. (2010) (ST4). The weakly non-linear four wave interactions were calculated using the Discreet Interaction Approximation (DIA, Hasselmann et al., 1985) in all set-ups.

The depth-induced wave breaking formulation of Battjes and Janssen (1978) was used in all three models. The bottom friction was following Hasselmann et al. (1973) in WAM and SWAN, while the SHOWEX bottom friction (Ardhuin et al., 2003) was used in WW3. The non-linear three-wave interactions were only switched on in SWAN, using the Lumped Triad Approximation (LTA, Eldeberky, 1996).

WAM uses the explicit first order upwind scheme, while SWAN uses the implicit four sweep scheme. WW3 was run with the explicit third-order upwind scheme, since no implicit schemes were available for structured grids in v5.16 (although this possibility has been added in the newest version).

More exact descriptions of all the model settings are given in the first two original articles, but the details of the coastal implementations are also summarized in Table 3.3.

3.2.3 Bathymetric data

The nearshore model set-ups were implemented using a single nested grid covering the Helsinki archipelago (24° 28'–25° 24' E, 59° 52'–60° 16' N). The primary bathymetrical grid had a resolution of 0.1 nmi (185 m) and was mainly based on information from nautical charts (Björkqvist et al., 2014, Paper I). A second 0.1 nmi grid was also used in Paper I. This alternative grid was constructed within the *Velmu* project run by the Finnish Environmental Institute (http:// www.ymparisto.fi/en-US/VELMU/) using data from water quality stations and the Baltic Sea Bathymetric Database (BSBD, 2013).

The high-resolution grids were nested inside a 1 nmi (1.85 km) Baltic Sea grid. This coarser grid was based on ETOPO1 (Amante and Eakins, 2009) and data from IOW (Seifert et al., 2001) in Paper I. In Paper II it was based on Seifert et al. (2001) and

Table 3.3: Settings and physical parameterisations used in the wave models. All models were implemented with a 0.1 nmi structured grid nested inside a 1 nmi Baltic Sea grid.

Used in Paper	I, II	II	II
	WAM	SWAN	WW3
Model version	Cycle 4.5.1 (I), 4.5.4 (II)	41.10AB	v5.16
Advection time step	2 s	10 min, 5 iterations	5 s
Intra-spectral time step	N/A	N/A	2 s
Source term integration time step	2 s (I), 10 min (II)	10 min	10 min
Global time step	N/A	N/A	30 s
Propagation scheme	First order upwind	Fully implicit four sweep	Third order upwind
Wind input	Janssen (1991)	Komen et al. (1984); Wu (1982)	Ardhuin et al. (2010)
Dissipation	Komen et al. (1994): δ =0.5 (I), 0.6 (II)	Komen et al. (1994): $\delta = 1$	Ardhuin et al. (2010)
Bottom friction	Hasselmann et al. (1973)	Hasselmann et al. (1973)	SHOWEX (Ardhuin et al., 2003)
Wave breaking	Battjes and Janssen (1978)	Battjes and Janssen (1978)	Battjes and Janssen (1978)
Non-linear four wave	DIA (Hasselmann et al., 1985)	DIA (Hasselmann et al., 1985)	DIA (Hasselmann et al., 1985)
Non-linear triad	–	LTA (Eldeberky, 1996)	-

Table 3.4: The different numerical weather prediction systems used to force the wave models in this study.

Model name	Version	Resolution	Years	Operational data	Paper
HIRLAM	version 7.4	7.5 km* / 3 h	2012	Yes	I
HIRLAM	version 7.4	7.5 km / 1 h	2012–2015	Yes	II
HIRLAM	version 7.4	7.5 km / 3 h	2016	Yes	II
HARMONIE	cycle 38h1	1 km / 15 min	2012	No	I
HARMONIE	cycle 38h1.2	2.5 km / 1 h	2016	No	II

* Given to the wave model at a 11 km resolution.

the Baltic Sea Bathymetric Database (BSBD, 2013).

3.2.4 Wind forcing

Two different Numerical weather prediction (NWP) systems—HIRLAM and HARMONIE (HIRLAM-B, 2018)—were used to force the wave models runs (Table 3.4). The HIRLAM data originated from FMI's operational weather forecasts, while the HARMONIE hindcasts were made specifically for this study. The HIRLAM data given to the models was coarse compared to the wave model resolution (7.4–11 km vs 0.185 km) and HARMONIE was therefore implemented as an alternative forcing with a resolution of 1–2.5 km. The wind data were available with a time interval between 15 min and 3 hours. An overview of the NWP's are given in Table 3.4 and in the methods sections of Papers I and II.

4 The observed archipelago wave field

4.1 The wave spectrum

A schematic figure of an archipelago-type spectrum is presented in Fig. 4.1. The wide frequency range with constant energy, between roughly 1 and 2 rad s^{-1}, will henceforth be called the energy carrying range. Since the frequency bins in a measured wave spectrum are χ^2 distributed (e.g. Bendat and Piersol, 1986), it was possible to simulate random samples from this underlying, idealised, spectrum. These samples showed that the spectral peak was random within the energy carrying range—something already found in Paper II. The third "measured" sample (red) might also mistakenly be interpreted to signify a multimodal sea state, even though we know that the underlying spectrum showed no such characteristics.

Paper III found a systematic transition of the mean spectral shape in the Helsinki archipelago. In the open sea the mean spectrum was unimodal, while the flat spectrum in the archipelago was dominated by a wide energy carrying range (Fig. 2 in Paper III). The spectral shape was quantified by the κ^2 narrowness parameter (Eq. 2.24), which was smaller where the mean spectrum was visibly wider (Table 2 in Paper III).

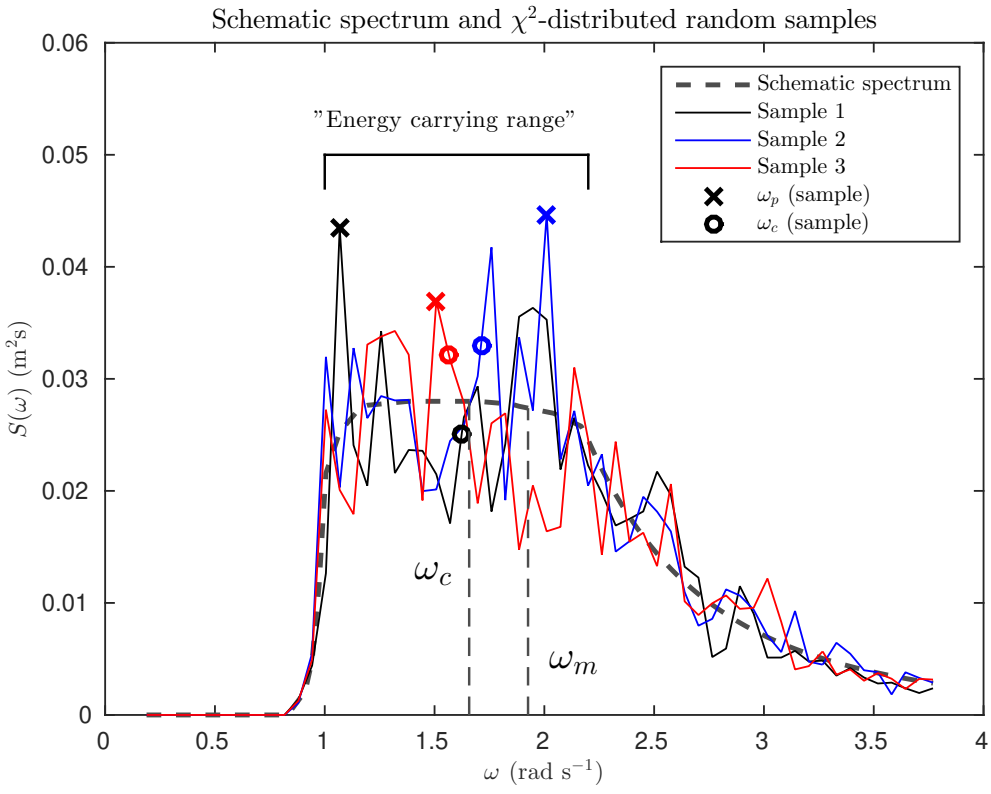

Figure 4.1: A schematic archipelago-type spectrum. The three sample spectra are numerically generated from the schematic spectrum using a χ^2-distribution with 31 degrees of freedom. ω_m is the mean frequency and ω_c is the characteristic frequency (Eq. 2.21).

The dominant wind sectors in the GoF are from south-east/east and from south-west. Fig. 4.2 illustrates wave spectra that were generated by winds from these dominant sectors in four different areas: the Open sea, the Outer archipelago, the Transition zone, and the Inner archipelago. These areas were represented by one measurement site each (GoF, O1, T2, and I3 respectively). Each case contained 7–11 spectra and had a mean wind speed of 11–13 m s^{-1}. The spectra for the Open sea and the Transition zone were coinciding, as were the spectra for the Outer and Inner archipelago.

In Paper III the spectral shape in the Transition zone was found to depend strongly on the wind direction because of the anisotropic fetch and bottom conditions. This variation was also evident when comparing the spectra generated by south-westerly winds (left column) and south-easterly winds (right column) (Fig. 4.2). In the Open sea the easterly winds produced a more peaked spectrum, since the westerly fetch geometry resulted in a stronger disagreement between the fetch restricting the growth of the peak frequency and the fetch restricting the growth of the total wave energy, as found by Kahma and Pettersson (1994). A similar difference was seen in the Outer archipelago, where the waves generated by the south-westerly winds were affected by the Porkkala peninsula, as noted in Paper I. The general trend, however, was the widening of the spectrum when moving into the archipelago towards the shore.

In the Transition zone the strong sheltering by islands in the east (especially Isosaari) resulted in a wide spectrum, while the nearshore Inner archipelago site was sheltered in such a way for both dominant wind directions. The spectral shape in the Transition zone during easterly winds was close the ideal archipelago spectrum in Fig. 4.1, as was the spectra in the Inner archipelago. The low κ^2 narrowness values (0.01–0.03) agreed with this visual assessment. Nonetheless, the energy carrying range in the Transition zone's extended to lower frequencies than in the Inner archipelago because of the higher exposure to open-sea waves.

4.2 The spectral tail

The equilibrium values of the spectra in Fig. 4.2 agreed with $\alpha_u = 3.3 - 4.5 \cdot 10^{-3}$ found by Kahma (1981) and Kahma (1986) (Fig. 4.3). The open sea GoF buoy had larger equilibrium levels compared to the more sheltered locations, with the exception of the easterly wind case in the Transition zone. Since the wave buoys could not measure waves shorter than 3.6 rad s^{-1} (0.6 Hz), they were complemented with high-frequency wave staff measurements from R/V *Aranda* (Paper IV). The wave staff spectra from the open sea (sites 15031 & 15035) had equilibrium values of $\alpha_u \approx 4.5 \cdot 10^{-3}$. These spectra transitioned from ω^{-4} to ω^{-5} around $\omega U/g = 4 - 5$, which is in the frequency range where the wave buoys measurements ended. The wave staff spectra had only a short ω^{-5} range before transitioning back to an ω^{-4} power-law. This second ω^{-4} range had lower equilibrium values and was observed to continue to at least $\omega U/g = 20$ (Paper IV).

The only high-frequency measurements from the archipelago (site 15033 in the Archipelago Sea, Fig. 1.4) were compared to wave buoy data gathered roughly 160 km away in the Helsinki archipelago (site I3, Fig. 1.3). The shortest fetch at 15033 was about 2 km, with a 15 km narrow passage to the south. The shortest fetch at I3 was around 1.5 km, but

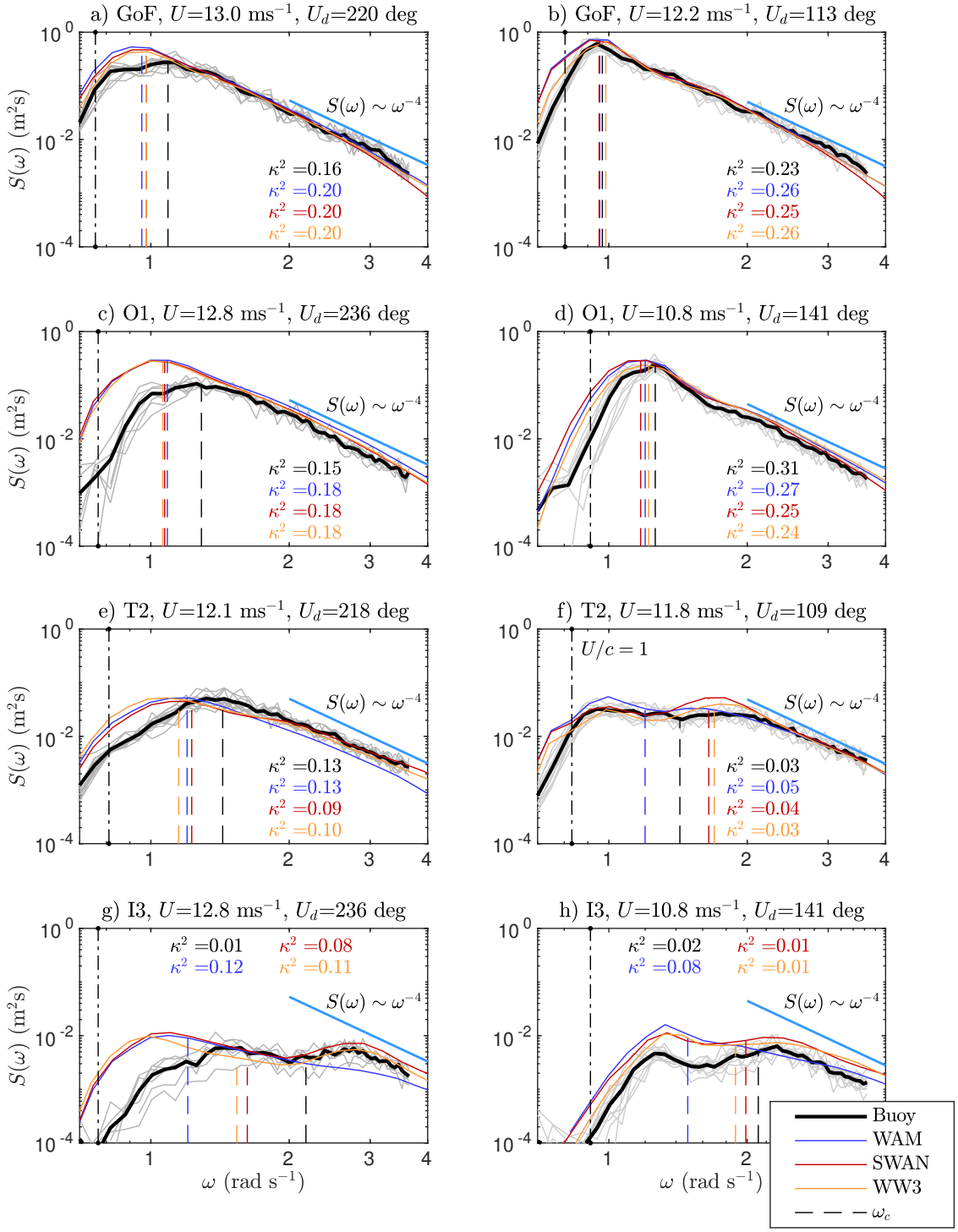

Figure 4.2: Observed and modelled wave spectra at four locations off Helsinki (see Fig. 1.3) for south-westerly (left column) and easterly (right column) winds. The vertical dashed lines shows the characteristic frequency integrated up to 0.58 Hz (see Eq. 2.21).

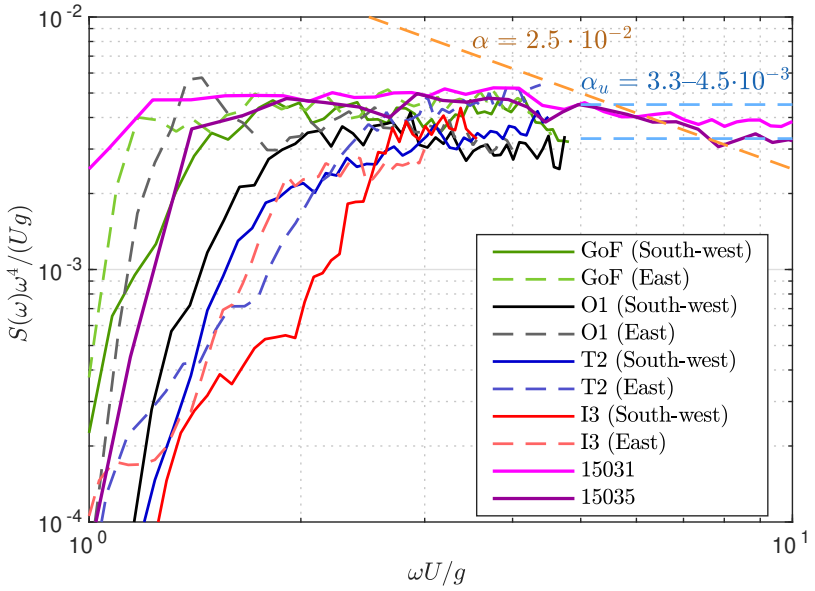

Figure 4.3: The wave buoy spectra from Fig. 4.2 plotted with an equilibrium normalisation along high-frequency spectra obtained at the mouth of the GoF (15031) and the Bothnian Sea (15035) with R/V *Aranda*.

it was exposed to attenuated open sea waves propagating from the Gulf of Finland.

Wave spectra for 2 hours were compared (Fig. 4.4 a). The mean wind speed measured at R/V *Aranda* was between 9.6 and 7.6 m s^{-1} (mean 8.6 m s^{-1}). There exists no wind measurements at location I3, but the wind speed at Harmaja was 9.0–9.9 m s^{-1} (mean 9.5 m s^{-1}). The wind speed at Kruunuvuorenselkä was approximately 8.7 m s^{-1} (a proportionality constant 0.91 determined through linear regression). Kruunuvuorenselkä is slightly more exposed than I3, and 8.7 m s^{-1} was used as an upper estimate. The wind speed at an inland weather station (Kaisaniemi) was only 3.2 m s^{-1} during the I3 measurements. The wind speed interpolated linearly between Harmaja and Kaisaniemi was 5.6 m s^{-1}, which will serve as a lower bound. The best estimate for the wind speed at I3 was therefore 7.1 m s^{-1} ($\pm$ 1.5 m s^{-1})—about 75% of the wind speed at Harmaja.

The wave spectra from the two locations agreed well up to the Nyquist frequency of the wave buoy after being scaled with the wind speed. The energy below $\omega = 2.4$ rad s^{-1} was missing in the wave staff measurements because site 15033 wasn't exposed to open sea waves. In the wave staff measurements only a short ω^{-5} range was visible before a transition to a second ω^{-4} range (Fig. 4.4). The high-frequency spectra were mostly described by an ω^{-4} tail (shown up to 10 rad s^{-1}), which is similar to the open sea spectra in Fig. 4.3.

The data in Paper IV, Fig. 4.3, and Fig. 4.4 suggest that the rear face of the spectrum has a similar structure both in the archipelago and the open sea. Still, more high-frequency measurements from archipelago conditions are required to confirm this conclusion.

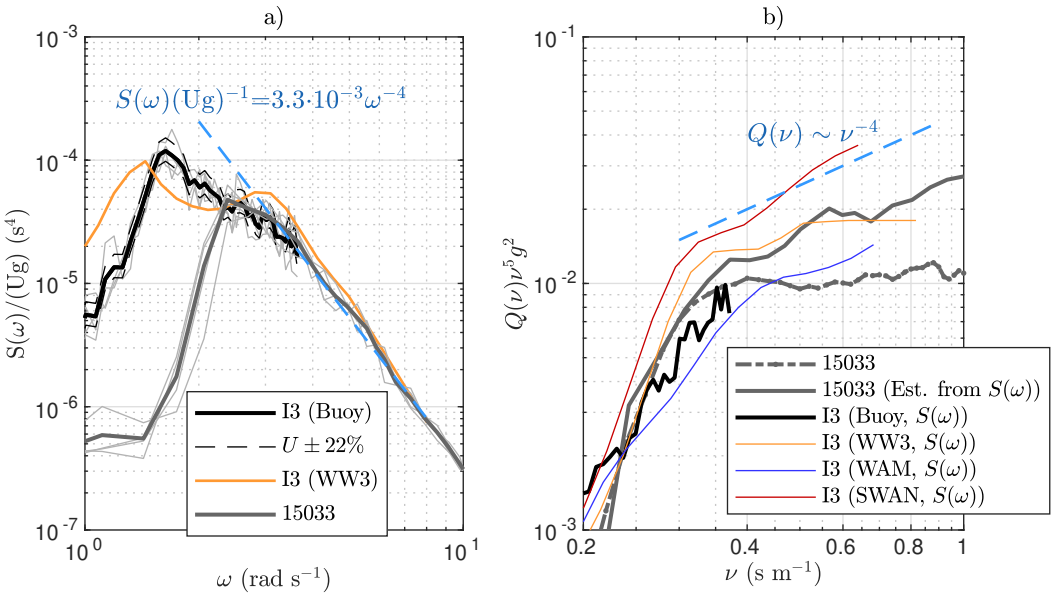

Figure 4.4: Wave spectrum from I3 in the Helsinki archipelago (18 Oct 2012, $U = 7.1 \pm 1.5$ m s^{-1}), and a high-frequency spectrum from 15033 in the Archipelago Sea roughly 160 km away (09 July 2015, $U = 8.6$ m s^{-1}). Panel a) shows the wave spectra normalized by Ug. Panel b) shows the inverse phase-speed saturation spectra (not scaled with U). Solid lines in panel b) are estimates calculated from the frequency spectra.

4.2.1 Wavenumber and inverse-phase speed spectra

The equilibrium-to-saturation transition in the Archipelago Sea wavenumber spectra took place at roughly $kU^2/g = 10$, which is $U/c = \sqrt{10} = 3.2$ if deep water linear theory is assumed. This transition point agreed with $U\nu = U/c = 3$, which was identified in the inverse phase-speed spectra (Fig. 11 in Paper IV). Still, the equilibrium range in the frequency domain typically didn't end before $\omega U/g = U/c = 4 - 5$, even extending up to $\omega U/g = 8 - 9$ for strongly forced spectra.

Unlike the short ω^{-5} range in the frequency domain, both the wavenumber and the inverse phase-speed spectra had a clear k^{-3} (and ν^{-5}) saturation range. The saturation constants determined from the wavenumber and inverse phase-speed domains also agreed well, being $\alpha/2 = F(k)k^3 \approx 6 \cdot 10^{-3}$ and $\alpha = Q(\nu)\nu^5 g^2 \approx 1 \cdot 10^{-2}$ (the latter shown in Fig. 4.4b). The saturation constant determined from the frequency spectra was roughly twice as large, which was consistent with Forristall (1981).

The incompatibility between the wavenumber and frequency domains has been previously identified by Wang and Hwang (2004) and Lenain and Melville (2017). In Paper IV the main reason for the discrepancies was determined to be wave non-linearities. The Doppler shift, as proposed by e.g. Banner (1990), was excluded as a leading explanation, since it would also have affected the inverse phase-speed spectra, thus breaking the agreement between the k^{-3} and ν^{-5} saturation regimes.

4.3 The characteristic wave frequency, ω_c

The peak frequency is practically undefined in an archipelago-type spectrum with a broad energy carrying range (Fig. 4.1). The strong scatter makes the peak frequency less useful in assessing wave model performance (Paper II), but it is also questionable to which degree it actually characterizes the wave field in archipelago conditions (Paper III).

In Paper III a more stable characteristic frequency, ω_c, was defined using the integral in Eq. 2.20 with $q = 4$; this expression has been proposed as a definition for the peak frequency by Young (1995). For more exposed location the characteristic frequency was close to the spectral peak (Fig. 4.2), while being slightly biased for wave growth affected by a narrow fetch geometry (Paper III). The advantage over the mean frequency was that ω_c quantified the centre of the energy carrying range in an archipelago type spectrum (Fig. 4.1, Fig. 4.2f). The characteristic frequency can thus be though of as a generalization of the peak frequency, since it is equivalent to the peak frequency for narrow spectra.

4.4 Implications for wave height parameters

4.4.1 Highest individual waves and $H_{1/3}$

The traditional definition of the significant wave height is the mean of the highest one-third of the individual waves ($H_{1/3}$, Eq. 2.16). By assuming deep water, Gaussian water level displacements, and a narrowbanded spectrum, it follows that the individual wave heights would be Rayleigh distributed with a parameter of $\sqrt{4m_0}$, where m_0 is the variance of the wave field (Longuet-Higgins, 1952). Since the variance is more easily calculated than the height of every single wave, these two definitions for the significant wave height were connected on a theoretical basis as:

$$H_{1/3} = 4\sqrt{m_0} \Leftrightarrow H_{1/3}/H_{m_0} = 1. \tag{4.1}$$

Experimental studies have found that the above equality doesn't hold precisely. Forristall (1978) determined the ratio $H_{1/3}/H_{m_0}$ to be 0.942 using storm wave data. Longuet-Higgins (1980) used a scaled Rayleigh distribution of $\alpha_R\sqrt{4m_0}$ and found $H_{1/3}/H_{m_0} = \alpha_R = 0.925$ for the data of Forristall (1978). Longuet-Higgins (1980) found the coefficient α_R to depend on the spectral width; it is therefore expected that the ratio $H_{1/3}/H_{m_0}$ would be smaller than $\approx 0.93 - 0.94$ in the archipelago where the wave spectra are wide.

The open sea GoF data was in good agreement with previous studies, with $H_{1/3}/H_{m_0} = 0.927$. The ratio determined from the data in the Transition zone (T2) was only $H_{1/3}/H_{m_0} = 0.881$, which indicated a decrease in the highest wave height compared to the standard deviation $\sqrt{m_0}$. The single highest wave at T2 was, on average, $H_{max}/H_{m_0} = 1.58$, which was lower than 1.68 predicted by Forristall (1978). It was also lower than the respective value determined from the GoF open sea data (1.61).

The predictions based on the Rayleigh-type distributions determined in previous studies overestimated the height of the highest single wave in the archipelago (Table 3 in Paper III). Paper III found that the finite water depth didn't explain the differences between the results in the archipelago and the open sea. The results were best explained by the wider

spectral shape, and linear fits to the narrowness parameter κ^2 resulted in the equations:

$$H_{1/3}/H_{m_0} = 0.85 + 0.15\kappa^2 \quad (4.2)$$
$$H_{max}/H_{m_0} = 1.57 + 0.27\kappa^2. \quad (4.3)$$

The deviations from the theoretical results of Longuet-Higgins (1952) were therefore determined to be caused by the violation of the narrowbanded assumption, not the deep water assumption. Indeed, for a narrowbanded spectrum ($\kappa^2 \to 1$) both equations agreed with the theoretical results of Longuet-Higgins (1952) (Table 3 in Paper III). A lot of scatter still exists, with the correlation coefficients being only $r = 0.64$ (Eq. 4.2) and $r = 0.15$ (Eq. 4.3).

4.4.2 Confidence intervals

According to Donelan and Pierson (1983), the degrees of freedom of the total wave field variance, m_0, depend on the spectral shape in the following way:

$$\text{d.o.f.}(\hat{m}_0) = \frac{l\left[\sum_{i=1}^{N}\hat{S}(\omega)\right]^2}{\sum_{i=1}^{N}\left[\hat{S}(\omega)\right]^2}, \quad (4.4)$$

where l is the degrees of freedom of one frequency bin in the wave spectrum, and $\hat{S}(\omega)$ underlines that the spectrum is a sample. Since a single spectral bin is χ^2_l-distributed, also $\hat{m}_0$ will be χ^2-distributed with the degrees of freedom of Eq. 4.4. Thus, for k=d.o.f.($\hat{m}_0$):

$$\hat{H}_{m_0} = H_{m_0}\sqrt{\frac{\chi^2_k}{k}}. \quad (4.5)$$

The confidence limits for the measured significant wave height in the open sea (GoF) were, on average, up to 50% higher than for the wider spectra of the archipelago (Table 2 in Paper III). Following Table 2 in Paper III, the confidence limits in the Transition zone (T2) can be calculated by using $k = 410$. Still, the degrees of freedom varied with the wind direction, being only 250 for the more peaked spectra generated by southerly winds (Fig. 4 a in Paper III).

5 The modelled archipelago wave field

5.1 The wave spectrum

The three wave models mostly reproduced the wave spectra well, which was also reflected in the general agreement between the measured and modelled κ^2 values (Fig. 4.2). The largest discrepancy was the overestimated energy for south-westerly winds in the Outer archipelago (Fig. 3 in Paper I & Fig. 4.2c). This behaviour was identified for WAM at location O1 in the Outer archipelago (Paper I), and the bias persisted at location O3, located 13 km south-west of O1 (Paper II). Paper II also found that SWAN and WW3 behaved like WAM in the Outer archipelago despite having different numerical schemes and parameterizations of the physical processes. The long-wave energy that was overestimated in the models for south-westerly winds propagated through the Transition zone to the Inner archipelago (Fig. 4.2g).

All models captured the wave spectrum more accurately during easterly winds (Fig. 4.2, right column). WAM showed a slight tendency to overestimate the low-frequency energy inside the archipelago, while SWAN and WW3 overestimated the local wave growth (Fig. 4b in Paper II). The same tendencies were found in the Inner archipelago point I3 (Fig. 4.2h). Nonetheless, the discrepancies with the measurements were smaller than for south-westerly winds.

The rear face of the spectrum was also mostly simulated well by the models. The main exception was found in the Transition zone, where WAM and WW3 modelled too little energy in the spectral tail during south-westerly winds even though SWAN reproduced the high-frequency part of the spectrum correctly (Fig. 6a in Paper II & Fig. 4.2e). In the Inner archipelago WAM underestimated the local wind sea, which was captured well by SWAN and WW3 (Fig. 4.2g).

The simulated wave spectra in the inner Helsinki archipelago were also compared with high-frequency wave staff measurements from the Archipelago Sea, as presented in Sect. 4.2 (Fig. 4.4). The observed tail mostly followed an ω^{-4} power law (as assumed in SWAN). The shape of the tail in WW3 were in good accord with the wave staff measurements, although the energy levels were slightly too high. WW3 adds a diagnostic ω^{-5} tail for the highest frequencies, which was consistent with the short transition seen in the wave staff measurements. The inverse phase-speed spectrum showed a ν^{-5} saturation, which is theoretically consistent with a continued ω^{-5} tail if non-linearities are assumed weak.

5.2 Bulk wave parameters

All three models agreed on the significant wave height, which was simulated well inside the archipelago (Paper II). The modelled wave height was slightly too large at the locations closest to the shore, but the most significant bias was in the Outer archipelago at O1 and O3, as discussed in Sect. 5.1. The small intermodel variations in spectral shape did not translate into notable differences in the significant wave height.

The validation of the peak period, T_p, was very challenging because of its instabil-

ity in archipelago conditions (Paper II). The slight differences in how the three models simulated the wave spectrum were visible in the peak period in a mean sense: SWAN and WW3 had a negative bias, since they more consistently determined the peak period to be that of the shorter, locally generated, waves; WAM had a positive bias in the peak period because of the overestimation of the longer waves. Still, if only the peak period is validated, the disparities appear greater than the actual small differences between the model spectra (Fig. 4 in Paper II, and Fig 4.2 f).

The characteristic frequency, ω_c, agreed with the measurements for easterly winds at the GoF and O1 (Fig. 4.2). For south-westerly winds the bias roughly corresponded to the difference in peak frequencies. Inside the archipelago the discrepancy between the measured and modelled characteristic frequency reflected the low- or high-frequency bias' of the model. The combined information from the significant wave height (H_s), the characteristic frequency (ω_c), and the spectral narrowness parameter (κ^2) gave a good grasp on how well the wave spectrum was modelled.

5.3 The wind forcing and the bathymetry

Paper I validated the NWP systems HIRLAM and HARMONIE against the open sea Kalbådagrund station and the Harmaja station (Fig. 1.3). The same models were validated in Paper II also against measurements from Helsingin majakka and Kruunuvuorenselkä. The newly acquired measurements from the Kruunuvuorenselkä research station provided the first opportunity to validate NWP-systems in this area of the Helsinki archipelago.

The operational HIRLAM products were sufficient to force the wave models in the archipe-lago, even though the spatial resolution was an order of magnitude coarser compared to the wave models (7.4 km vs 0.185 km). The higher resolution HARMONIE model outperformed HIRLAM only at Kruunuvuorenselkä in the archipelago. Nevertheless, the results of the coarser HIRLAM were adequate even in this area (Table 4 in Paper II).

Increasing the temporal resolution of the wind forcing from 3 h to 1 h improved the quality of the wave simulation. The impact was determined from the variance density spectrum calculated from the significant wave height time series at T2 (Fig. 5.1). This spectrum of H_s is denoted $\mathcal{H}_s(f)$ (m^{2}h) to distinguish it from the wave spectrum. The frequency, f, had units h^{-1}, and the spectrum above (24 h)$^{-1}$ followed an f^{-3} power law. The WAM-simulation that used the 1 h HARMONIE winds matched the observations up to (3 h)$^{-1}$, but the fastest variations in significant wave height weren't captured when WAM was forced with 3 h HIRLAM winds (Fig. 5.1a).

The tail of $\mathcal{H}_s(f)$ was dominated by the statistical variability of the observed significant wave height. Thus, the discrepancy with WAM-HARMONIE above (3 h)$^{-1}$ was not a shortcoming of the model. Adding a simulated χ^2-variability to the WAM-HARMONIE time series using Eq. 4.5 and 410 d.o.f. (Table 2 in Paper III), the spectrum $\mathcal{H}_s(f)$ calculated from the model time series coincided with the observations (Fig. 5.1b). The WAM-HIRLAM data, again, differed from the observations even with the added simulated variability, meaning that using a 3 h time step in the wind forcing loses some variations in the wave field that would be possible to capture with a numerical wave model.

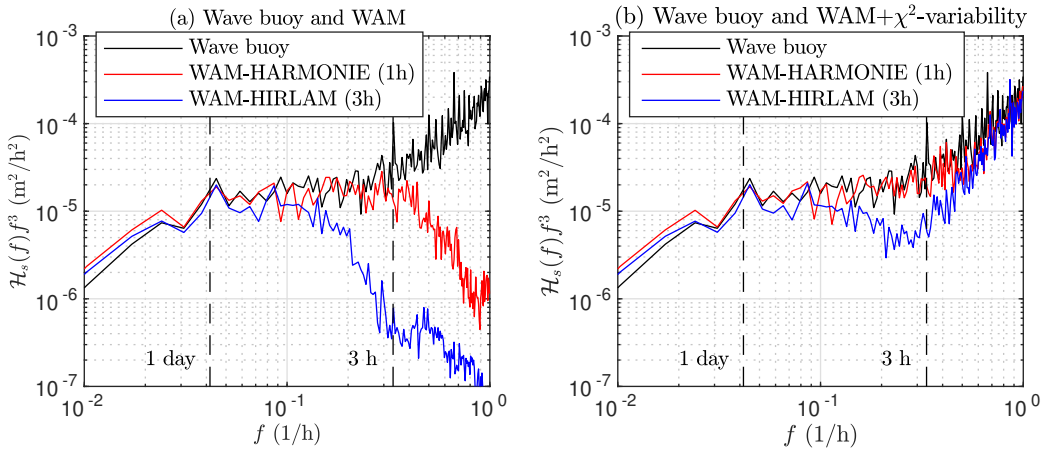

Figure 5.1: The variance density spectra, $\mathcal{H}_s(f)$, of the H_s data in the Transition zone. Panel (a) shows the spectrum (multiplied by f^3) of the wave buoy data, and spectra of the WAM data that were produced with an hourly wind forcing (HARMONIE) and with winds available every third hour (HIRLAM). Panel (b) shows the same data, but with a simulated χ^2-variability added to the model data. The spectra have been calculated from the 2016 significant wave height data at location T2.

Accurate bathymetrical information is important for the model performance, and this aspect was explored in Paper I. The two high-resolution bathymetrical grids used in the WAM simulations produced almost identical results. Also the influence of the bottom related processes were small in the Outer archipelago, suggesting that small variations in the bathymetrical information were not responsible for the observed errors in the Outer archipelago. The accuracy of the available bathymetrical information was deemed sufficient for the purposes of wave modelling in archipelagos.

6 Discussion

6.1 Parameterizing the archipelago spectrum

Traditionally the omnidirectional wave spectrum has been described by its peak frequency and total energy. The energy has been quantified either directly, or e.g. through the value of the constant α in the JONSWAP spectrum. While the fetch geometry has been found to influence the relationship between the energy and the spectral peak, the spectra affected by narrow and slanting fetch have still been well described as less peaked versions of traditional spectra (Pettersson, 2004).

In archipelago conditions two issues exist: i) there is a need to quantify the width of the spectrum, ii) the peak frequency is ill-defined. The archipelago spectra with their wide energy carrying regions can no longer be fitted to traditional spectral parameterisations by modifying the peakedness parameter (Fig. 4.1). The width of this energy carrying range is also not constant, as readily seen when comparing panels f) and h) in Fig. 4.2. It therefore follows that the the low-frequency part of the archipelago spectrum cannot be parameterized as a fixed modification to any existing spectral model. The spectral width was successfully quantified using the κ^2 narrowness parameter (Battjes and van Vledder, 1984); the width parameter ν_{LH} by Longuet-Higgins (1980) had no descriptive value in the data set of this study.

In this study the characteristic frequency, ω_c, was proposed to describe the archipelago spectrum instead of the ill-defined peak frequency. In the archipelago ω_c was roughy representative of the middle of the energy carrying range, which is a defining property of the archipelago type spectrum. It also reverted to an unbiased estimate of the peak frequency for narrow spectra, which is why this definition was originally proposed as an alternative definition for the peak frequency by Young (1995).

The triplet $(m_0, \omega_c, \kappa^2)$ can serve as a starting point for a parameterization of the archipela-go spectrum. Wave spectra inside the archipelago typically show no overshooting, but the γ peakedness parameter would need to be retained if the parameterization should cover also traditional fetch-limited spectra. Nevertheless, it is entirely possible that some other width parameter will turn out to be more useful. A way to reliably define the upper frequency of the energy carrying range might also be needed, since it represents the peak frequency of the shortest fetch, and thus the start of an ω^{-4} rear face. It might even turn out that an additional parameter must be added to account for the possible slope within the energy carrying range. The construction of a parameterization that would cover the entire transition of the spectrum (Fig. 2 in Paper III) is a formidable challenge that wasn't solved in this study.

6.2 Individual wave heights

If we assumed a universal distribution, the number of waves in a time series would determine the expected maximum height of a single wave. The shorter wave periods in the archipelago (compared to the open sea) would mean a larger number of waves, and thus a higher expected maximum wave. Yet, the exact opposite was found. The decrease in the

height of the single waves, with respect to the significant wave height H_{m_0}, for a wider spectrum has been proposed to be caused by the de-correlation of following crests and troughs (Casas-Prat and Holthuijsen, 2010). This explanation was supported by the data in this study, since the maximum wave crests η_{max}/H_{m_0} determined from the open sea data (0.93) and the archipelago data (0.92) were consistent. The crest heights also followed Casas-Prat and Holthuijsen (2010) and the theoretical results of Longuet-Higgins (1952).

The ratio $H_{1/3}/H_{m_0}$ depended on the spectral narrowness κ^2, but with a significant amount of scatter. The dependence on the spectral width were in line with Longuet-Higgins (1980), who scaled the assumed Rayleigh distribution—and thus $H_{1/3}/H_{m_0}$—using the spectral width coefficient, ν_{LH}. Also Vandever et al. (2008) found a similar connection between ν_{LH} and $H_{1/3}/H_{m_0}$.

Vandever et al. (2008) found no dependence of the highest single wave with respect to the significant wave height and the spectral width ν_{LH}, possibly because the authors used $H_{1/3}$ instead of H_{m_0}, thus scaling the single highest waves with the mean of the highest waves. In Paper IV a connection between H_{max}/H_{m_0} and κ^2 was established with a weak correlation ($r = 0.15$). Despite the scatter, Eq. 4.2 and Eq. 4.3 are consistent with the theoretical results of Longuet-Higgins (1952) for a very narrow spectrum ($\kappa^2 \approx 1$). It is still unclear if the poor correlation was caused mainly by the difficulty to define a good metric for the spectral width, and it is therefore possible that the scatter could be reduced by choosing a different width parameter.

The different behaviour of the crest heights and the wave heights are important for practical applications. The maximum crest height is relevant for e.g. wave overtopping, while the safety of vessels are threatened by large wave heights. In archipelago conditions the ratio between the wave height and the crest height varied with the spectral width, which needs to be accounted for if results from observations are generalized to cover larger areas.

6.3 The rear face in different spectral domains

The existence of both a wind-dependent ω^{-4} (or $k^{-2.5}$) equilibrium range and a constant ω^{-5} (or k^{-3}) saturation range has theoretical and experimental support (Phillips, 1958; Kitaigorodskii, 1962; Hasselmann, 1974; Kahma, 1981; Forristall, 1981; Kitaigorodskii, 1983; Romero et al., 2010; Tamura et al., 2014). Nevertheless, the behaviour of the two spectral domains have not been consistent when comparing the frequency and the wavenumber spectrum from spatio-temporal measurements (Wang and Hwang, 2004; Lenain and Melville, 2017). Lenain and Melville (2017) found that the wavenumber spectra transitioned to a saturation regime, while the frequency spectra did not. Results to this affect were also obtained in Paper IV.

Kitaigorodskii et al. (1975) and Banner (1990) attributed the distortion of the hypothetical ω^{-5} power-law to currents and Doppler effects by the orbital velocities of longer waves. Later studies have highlighted the role of higher order harmonics, and determined the Doppler distortion caused by the orbital motion of longer waves to be comparatively small (Wang and Hwang, 2004; Janssen, 2009; Leckler et al., 2015; Guimarães, 2018).

In Paper IV the good agreement between the inverse phase-speed spectra (subject to the Doppler shift) and the wavenumber spectra (not subject to the Doppler shift) offered more experimental support for the importance of wave non-linearitites.

For the fetch-limited data from the Archipelago Sea the equilibrium levels varied less in the inverse phase-speed spectrum compared to the frequency spectrum. This disagreement raises the question if the U/c_p dependence of α_u (found by Donelan et al. (1985)) is a real intrinsic part of the wave field, or if it is mainly an artefact of the stronger higher order harmonics that are caused by the steeper waves.

Leckler et al. (2015) attacked the problem with non-linearitites by removing the higher order components from the frequency spectrum, thus determining the first order spectrum. A fundamental question is: are wave models simulating the frequency spectrum or the first order spectrum? Both source terms and the wave propagation are calculated assuming linear wave theory, or in essence that the frequency spectrum is the same as the first order spectrum. These models are then tuned and validated mostly against frequency measurements, which have been distorted by wave non-linearities.

In the case of parameterizing the energy input from the wind, the determining factor is U/c, which in a (deep water) model is $U\omega/g$. This implicitly assumes that all the energy in the frequency ω travels with the speed of the free harmonic, which is not the case (Hara and Karachintsev, 2003; Wang and Hwang, 2004; Leckler et al., 2015). The wind input at $U\omega/g$ will be different for the first order spectrum and the full frequency spectrum. Since the harmonics make up one physical wave, their common attribute is therefore their phase speed. The discrepancy is solved if the inverse-phase speed spectrum is used, since the spectrum $Q(\nu)$ contains the energy all harmonics that have a phase speed ν^{-1}. Nonetheless, the Q-spectrum have to be based on measurements of the phase speed; estimating it from the frequency spectrum, $S(\omega)$, adds no new information.

The presence of ambient currents will affect the inverse phase-speed measurements. This is not a problem when quantifying the wind input, since the relevant reference frame is relative to the wind. When quantifying dissipation caused by wave breaking, the relevant reference frame is intrinsic, which favours the use of the wavenumber spectrum. If the full wave spectrum is available, all three spectra—$S(\omega)$, $F(k)$, and $Q(\nu)$—can be directly calculated; they are all distinct representations of the wave field in the sense that none of them can be converted to the other (without theoretical simplifications). They all have value in describing different aspects of the wave field, and the question becomes choosing the right tool for the particular application at hand.

6.4 Modelling challenges

All results of the models were representative only of their chosen set-ups. Preliminary comparisons—where the source terms were used ”out of the box” without any additional tuning—showed that the ST4 package (Ardhuin et al., 2010) agreed best with the data in this study. Nonetheless, SWAN, and especially WW3, has many different source terms (e.g. Tolman and Chalikov, 1996; van der Westhuysen et al., 2007; Zieger et al., 2015), and choosing different ones could significantly alter the results. Changing the propagation scheme could also affect the simulations, but probably to a lesser extent (Perrie et al.,

2017).

The common issue found in all three models was the overestimated significant wave height for south-westerly winds in the Outer archipelago points that were partially sheltered by the Porkkala peninsula (Paper I and II). The behaviour persisted when using different wind forcings, bathymetrical data, propagation schemes, and source terms. The wave field was made up by two wave systems with slightly different directions, both travelling slower than the wind. Still, the measured spectrum was not unimodal, while the modelled spectrum was (Fig. 4 in Paper I). One possibility is that DIA could not capture the interaction between these to actively forced wave systems accurately enough, which should to be tested with simulations calculating the interactions exactly (e.g. van Vledder, 2006).

In the archipelago WAM underestimated the energy of the spectral tail for south-westerly winds, and a similar (but weaker) tendency was observed for WW3 (Fig. 4.2 e & g). SWAN was implemented with the oldest physical parameterization of the wind input (Komen et al., 1984; Wu, 1982), but still outperformed the other models in this specific aspect. Both WAM and WW3 were implemented with a wind input where the wave-supported stress was determined from the wave spectrum. As noted by Ardhuin et al. (2010), this type of parameterizations are highly sensitive to the highest frequencies. Higher energy levels in the tail will increase u_*, which will in turn further increase the energy in the spectral tail through the positive feedback.

Paper II found that the friction velocity in WAM and WW3 were lower when the high-frequency energy was underestimated (using u_* by SWAN as a benchmark). The older wind input of SWAN was immune to this aforementioned feedback mechanism, thus providing a certain robustness inside the archipelago. It is possible that the determination of the wave-supported stress was influenced by the excess long wave energy, thus decreasing the friction velocity. The sheltering term in the parameterization of Ardhuin et al. (2010) might have partially compensated for the unwanted feedback, which would explain why WW3 performed slightly better than WAM. Nevertheless, no friction velocity measurements were available in the Helsinki archipelago, which means that there was no way of saying to what degree the friction velocity was under/overestimated by any of the models.

The ST6 source term package in WW3 (Zieger et al., 2015) was recently re-tuned by Liu et al. (2019), and it was found to reproduce an ω^{-4} to ω^{-5} transition well. Validating this updated source term package against the measurements of Paper II—and the continued measurements at T2—would be a useful study into the modelling of the rear face of the spectrum in the archipelago. Ideally, the continued measurements at T2 in the Transition zone would be accompanied with a field campaign collecting friction velocity measurements and high-frequency wave data.

The resolution of the atmospheric forcing has been found to be important for the accuracy of the wave simulations (Cavaleri and Bertotti, 2004; Tisler et al., 2007), but our results indicated that a 7.5 km wind product was adequate to force the wave simulations in the archipelago. Nonetheless, the lack of a proper land mask (Fig. 1 in Paper I) is one aspect that might still restrict the potential of the high-resolution HARMONIE model in the archipelago.

A coarse temporal resolution of the forcing wind data (3 h) restricted how well the

wave model captured fast variations in the wave field, while a 1 h temporal resolution mostly missed only the statistical measurement variability (Fig. 5.1). WAM-HARMONIE (1 h) captured 87 % of all variations of a time scale between 2 h and 10 h. The same number for WAM-HIRLAM (3 h) was only 45 %.

Paper I was based on regular grids since unstructured grids are not available in WAM. Although unstructured grids are possible both in SWAN and WW3, all models were implemented with structured grids for Paper II to allow for a comparison with the results in Paper I. Generally, the 0.1 nmi structured grid implementations performed well. Tuomi et al. (2014) found that the low-frequency energy modelled with a 0.5 nmi structured grid was improved when creating sub-grid obstructions using 0.1 nmi data; the land-sea mask with an 0.1 nmi accuracy was accounted for explicitly in the grid of this study. Nonetheless, it is possible that the results could possibly be improved by using even higher spatial resolutions either directly or as sub-grid obstructions. Building an unstructured grid would also be an attractive goal, but the very complex coastline and small islands makes the generation of unstructured meshed in archipelagos difficult. A compromise might be achieved by using structured grids with adaptive resolutions. Such a feature has been have been added to WW3 (SMC, Li, 2011), and it works like an automatic ”on-demand” nesting of areas where a higher spatial resolution is required.

7 Conclusions

The wave field in the archipelago was studied. The observations consisted of extensive wave buoy measurement from the Helsinki archipelago in the Gulf of Finland, Baltic Sea, and high-frequency wave staff measurements from R/V *Aranda*, part of which were from the Archipelago Sea. Wind data were provided by four automatic weather stations in the GoF and a Sonic anemometer on R/V *Aranda*. The wave field in the Helsinki archipelago was also modelled using three state-of-the-art, high-resolution, numerical wave models. The models were forced by winds from two numerical weather prediction (NWP) systems with different resolutions. The material was used to study the properties of the wave spectrum, namely how it evolves through the archipelago and how well different parts of the spectrum can be reproduced by the numerical models.

The measurements from R/V *Aranda* were used to study the equilibrium and saturation ranges and their transition point in the rear face of the spectrum. The Wavelet Direction Method (WDM) was used to extract wavenumber spectra from the wave staff data. A new, previously undefined, inverse phase-speed spectrum was also defined, formulated, and studied. This spectrum is denoted $Q(\nu)$, where $\nu = |\boldsymbol{\nu}|$ is the modulus of the inverse phase-velocity $\boldsymbol{\nu} = \boldsymbol{k}\omega^{-1}$.

The main conclusions of this study are the following:

1. The wave spectra in the archipelago differed significantly from the unimodal shape observed in the open sea. A unimodal shape was still visible in the outer edge of the archipelago, but inside the archipelago, close to the shore, the spectral shape was flat. The flat shape of the archipelago spectrum was characterized by a broad frequency range where the spectral density was almost constant ("the energy carrying range"). The results of the study were grouped to make them more presentable, but the transition was in reality more continuous; the spectral shape in the middle of the archipelago varied between the above mentioned extremes, depending only on the amount of sheltering present for different wind directions. The tail of the archipelago spectrum mostly followed an ω^{-4} power law in the frequency domain in both the wave buoy observations and the high-frequency wave staff observations—for this part the archipelago spectra agreed with the open sea measurements.

2. The flat shape of the wave spectrum in the archipelago made the peak frequency ill-defined, since the statistical variability in the energy carrying range introduced strong scatter. An integrated mean frequency weighted by $S(\omega)^4$ was proposed as a new "characteristic" frequency, ω_c, to be used over varying wave conditions throughout the archipelago. For an archipelago type spectrum ω_c quantified the centre of the energy carrying range, while it was an unbiased estimate for the peak frequency for waves growing from a straight shoreline. Young (1995) proposed the expression with $q = 4$ as an alternative definition for the peak frequency, but substituting $\omega_p := \omega_c$ cannot be recommended for waves growing in a narrow fetch geometry or in the archipelago. Rather, ω_c can be used as an additional frequency parameters with desirable limiting properties for both narrow and wide spectra.

3. The spectral significant wave height (H_{m_0}) and the traditional mean-of-the-highest-third ($H_{1/3}$) disagreed strongly in the middle of the archipelago. The average value was determined to be $H_{1/3} = 0.881 H_{m_0}$ using a linear fit, while the respective value for the highest individual wave was $H_{max} = 1.58 H_{m_0}$. Both these ratios were lower than results determined using open sea data. The reason for the differences to open sea measurements was determined to be the increase in spectral width, not the finite water effects; the results varied as a function of the spectral peakedness κ^2, although especially the H_{max}/H_{m_0} data had strong scatter.

4. The numerical wave models—WAM, SWAN, and WAVEWATCH III® —all simulated the significant wave height well in the archipelago with the configurations chosen in this study. In the archipelago the dominant peak in the measured wave spectrum varied randomly within the energy carrying range. The numerical models determined the peak period in a more deterministic fashion by favouring some part of the energy carrying range; SWAN typically simulated more energy in the higher frequency part of the energy carrying range, while WAM was biased toward the lowest frequencies. Despite the quite accurately simulated wave spectra, the statistical variations in the energy carrying range caused poor scatter statistics and a strong (positive or negative) bias for the modelled peak period. The largest inaccuracy in the simulated wave field was found in the Outer archipelago, where all models overestimated the wave energy significantly for locations partially sheltered by a peninsula. Inside the archipelago the wave models also underestimated the high-frequency wave energy, in certain conditions, when implemented with wind-input source terms that determined the wave supported stress from the wave spectrum.

5. The operational wind products were adequate for forcing the high-resolution coastal wave models even though the discrepancy between the spatial resolutions were one order of magnitude. The higher resolution atmospheric forcing performed better than the coarser operational product only when compared against newly acquired wind measurements close to the coast inside the archipelago. A coarse temporal resolution (3 h) of the wind forcing limited how well the variations in the time scale of 2–10 hours were modelled, while shorter variations disagreed with the measurements also when using hourly forcing data. Nevertheless, the fastest variations were dominated by the statistical variability of the measurements, which a numerical wave model does not even attempt to reproduce. Thus, it can be concluded that all variations in the significant wave height—that are within the realm of the model to simulate—can be captured by using hourly wind forcing data. Even though the existing operational products are adequate, the further development of high-resolution atmospheric models can reasonably be expected to increase the accuracy of coastal wave simulations, especially if the land-sea mask of the archipelago areas are improved.

6. The high-frequency wave-staff data collected in the Archipelago Sea showed that the spectrum saturated to roughly $F(k)k^3 = 6 \cdot 10^{-3}$ at $kU^2/g = 10$. The new inverse phase-speed spectrum was consistent with the wavenumber domain and

showed a saturation to $Q(\nu)\nu^5 g^2 = 1 \cdot 10^{-2}$ at roughly $U\nu = 3$. The transition to a saturation regime was less clear in the frequency spectrum $S(\omega)$, but a transition to $S(\omega)\omega^5 g^{-2} = 2.5 \cdot 10^{-2}$ could be identified at $\omega U/g = 4 - 5$. Nevertheless, at $U\omega/g = 10$ the frequency spectra transitioned back to an ω^{-4} power-law, which continued to at least $U\omega/g = 20$. The equilibrium constant varied less in the Q-spectrum compared to the frequency spectrum, where α_u showed a strong dependence on the strength of the forcing, U/c_p. The main reason for the discrepancies between the wavenumber and frequency domain was concluded to be wave non-linearities, since a strong Doppler effect would have broken the observed consistency between the saturation ranges in the inverse phase-speed and the wavenumber domains.

7. The transition point between the equilibrium and saturation ranges was best described using the inverse wave age, U/c. The speed of the wave component relative to the forcing wind is also a central parameter when calculating the energy input from the wind to the waves. Since the $Q(\nu)$-spectrum gives the apparent (inverse) phase-speed directly from the measurement, no additional current measurements are needed to determine the true relative speed between a wave component and the wind. This might turn out to be a useful feature in future studies. For processes governed by intrinsic wave properties, such as energy dissipation caused by wave breaking, the wavenumber domain should be favoured.

Future work is needed to determine a parameterisation for the wave spectrum that can cover all the different shapes from a peaked to a flat spectrum. This will require additional parameters quantifying the spectral width (e.g. κ^2), and possibly the slope of the energy carrying range.

The first challenge in modelling the wave field in the archipelago was the consistent overestimation of energy in the semi-sheltered areas just outside the archipelago that persisted when using different source terms and propagation schemes; neither could the error be attributed to the bathymetry or the atmospheric forcing. The second challenge was the underestimation of the high-frequency wave energy and the friction velocity in the wind input source term of Janssen (1991)—and to a lesser extent in that of Ardhuin et al. (2010)—under certain conditions in the archipelago. A tuning of these source terms against friction velocity measurements and high-frequency wave data from the archipelago should be performed, but such data are unfortunately sparse.

List of abbreviations

BS	Bothnian Sea
BSBD	Baltic Sea Bathymetric Database
CFL	Courant–Friedrichs–Lewy (condition)
DIA	Discrete Interaction Approximation of the non-linear four-wave interactions
DWR	Directional Waverider
ETOPO	Global relief model of Earth's surface
FFT	Fast Fourier Transform
FMI	Finnish Meteorological Institute
GoF	Gulf of Finland
GPS	Global Positioning System
HARMONIE	A non-hydrostatic convection-permitting atmospheric model
HIRLAM	High-resolution limited area model
IOW	Leibniz Institute for Baltic Sea Research Warnemuunde (Germany)
JONSWAP	Joint North Sea Wave Observation Project
LTA	Lumped Triad Approximation
NWP	Numerical Weather Prediction
R/V	Research Vessel
SHOWEX	Shoaling Waves Experiment
SWAN	Simulating WAves Nearshore
WAM	WAve Model
WDM	Wavelet Directional Method
WW3	WAVEWATCH III®

References

Amante, C. and Eakins, B.W. (2009). *ETOPO1 1 Arc-Minute Global Relief Model: Procedures, Data Sources and Analysis*. Technical report. NOAA. 25 p.

Anderson, J.D., Wu, C.H., and Schwab, D.J. (2015). Wave climatology in the Apostle Islands, Lake Superior. *Journal of Geophysical Research: Oceans*, 120(7), pp. 4869–4890. doi:10.1002/2014JC010278.

Ardhuin, F., O'Reilly, W.C., Herbers, T.H.C., and Jessen, P.F. (2003). Swell Transformation across the Continental Shelf. Part I: Attenuation and Directional Broadening. *Journal of Physical Oceanography*, 33(9), pp. 1921–1939. doi:10.1175/1520-0485(2003)033¡1921:STATCS¿2.0.CO;2.

Ardhuin, F., Rogers, W.E., Babanin, A.V., Filipot, J.-F., Magne, R., Roland, A., van der Westhuysen, A., Queffeulou, P., Lefèvre, J.-M., Aouf, L., Collard, F., and Westhuysen, A.V.d. (2010). Semiempirical Dissipation Source Functions for Ocean Waves. Part I: Definition, Calibration, and Validation. *Journal of Physical Oceanography*, 40(9), pp. 1917–1941. doi:10.1175/2010JPO4324.1.

Babanin, A.V. and Haus, B.K. (2009). On the Existence of Water Turbulence Induced by Nonbreaking Surface Waves. *Journal of Physical Oceanography*, 39(10), pp. 2675–2679. doi:10.1175/2009jpo4202.1.

Banner, M.L. (1990). Equilibrium Spectra of Wind Waves. *Journal of Physical Oceanography*, 20(7), pp. 966–984. doi:10.1175/1520-0485(1990)020¡0966:ESOWW¿2.0.CO;2.

Battjes, J.A. and Janssen, J.P.F.M. (1978). Energy loss and set-up due to breaking of random waves. In: *Proceedings of 16th International Conference on Coastal Engineering*, August 27–September 3, 1978, Hamburg, Germany, pp. 169–587. doi: 10.1061/9780872621909.034.

Battjes, J.A. and van Vledder, G.Ph. (1984). Verification of Kimura's Theory for Wave Group Statistics. In: *Proceedings of 19th International Conference on Coastal Engineering*, Septemver 3–7, 1984, Houston Texas, pp. 642–648. doi: 10.1061/9780872624382.044.

Battjes, J.A., Zitman, T.J., and Holthuijsen, L.H. (1987). A Reanalysis of the Spectra Observed in JONSWAP. *Journal of Physical Oceanography*, 17(8), pp. 1288–1295. doi:10.1175/1520-0485(1987)017¡1288:AROTSO¿2.0.CO;2.

Belcher, S.E., Grant, A.L.M., Hanley, K.E., Fox-Kemper, B., Van Roeke, L., Sullivan, P.P., Large, W.G., Brown, A., Hines, A., Calvert, D., Rutgersson, A., Pettersson, H., Bidlot, J.-R., Janssen, P.A.E.M, and Polton, J.A. (2012). A global perspective on Langmuir turbulence in the ocean surface boundary layer. *Geophysical Research Letters*, 39(17). doi:10.1029/2012GL052932.

Bendat, J.S. and Piersol, A.G. (1986). *Random Data: Analysis and Measurement Procedures*, Second Edition, John Wiley & Sons, Inc., New York.

Bidlot, J.-R., Janssen, P., and Abdalla, S. (2007). A revised formulation of ocean wavedissipation and its model impact. *ECMFW Technical Report Memorandum*, 509 (January).

Björkqvist, J.-V., Tuomi, L., Pettersson, H., Fortelius, C., Tikka, K., and Kahma, K.K. (2014). The effect of boundary field accuracy on high-resolution coastal wave modelling. In: *Measuring and Modeling of Multi-Scale Interactions in the Marine Environment - IEEE/OES Baltic International Symposium 2014, BALTIC 2014*.

Björkqvist, J.-V., Lukas, I., Alari, V., van Vledder, G.Ph., Hulst, S., Pettersson, H., Behrens, A., and Männik, A. (2018). Comparing a 41-year model hindcast with decades of wave measurements from the Baltic Sea. *Ocean Engineering*, 152, pp. 57–71. doi: 10.1016/J.OCEANENG.2018.01.048.

Booij, N., Ris, R., and Holthuijsen, L.H. (1999). A third-generation wave model for coastal regions 1. Model description and validation. *Journal of Geophysical Research*, 104(C4), pp. 7649–7666. doi:10.1029/98jc02622.

BSBD (2013). Baltic Sea Hydrographic Commission, Baltic sea bathymetry database version 0.9.3. `http://data.bshc.pro/`.

Casas-Prat, M. and Holthuijsen, L.H. (2010). Short-term statistics of waves observed in deep water. *Journal of Geophysical Research: Oceans*, 115(C9). doi: 10.1029/2009JC005742.

Cavaleri, L. and Bertotti, L. (2004). Accuracy of the modelled wind and wave fields in enclosed seas. *Tellus*, 56A, pp. 167–175.

Cavaleri, L., Abdalla, S., Benetazzo, A., Bertotti, L., Bidlot, J.-R., Breivik, Ø., Carniel, S., Jensen, R.E., Portilla-Yandun, J., Rogers, W.E., Roland, A., Sanchez-Arcilla, A., Smith, J.M., Staneva, J., Toledo, Y., van Vledder, G.Ph., and van der Westhuysen, A.J. (2018). Wave modelling in coastal and inner seas. *Progress in Oceanography*, 167, pp. 164–233. doi:10.1016/j.pocean.2018.03.010.

Cieślikiewicz, W. and Paplińska-Swerpel, B. (2008). A 44-year hindcast of wind wave fields over the Baltic Sea. *Coastal Engineering*, 55(11), pp. 894–905. doi: 10.1016/j.coastaleng.2008.02.017.

Datawell, B. (2017). Datawell Waverider Reference Manual, March 2019, *Datawell BV*, `http://www.datawell.nl/Support/Documentation/Manuals.aspx`

Donelan, M.A., Drennan, W.M., and Magnusson, A.K. (1996). Nonstationary Analysis of the Directional Properties of Propagating Waves. *Journal of Physical Oceanography*, 26(9), pp. 1901–1914. doi:10.1175/1520-0485(1996)026¡1901:NAOTDP¿2.0.CO;2.

Donelan, M.A., Hamilton, J., and Hui, W.H. (1985). Directional Spectra of Wind-Generated Waves. *Philosophical Transactions of the Royal Society A: Mathematical, Physical and Engineering Sciences*, 315(1534), pp. 509–562. doi: 10.1098/rsta.1985.0054.

Donelan, M.A. and Pierson, W.J. (1983). The Sampling Variability of Estimates of Spectra of Wind-Generated Gravity Waves. *Journal of Geophysical Research*, 88(C7), pp. 4381–4392. doi:10.1029/JC088iC07p04381.

Drennan, W.M., Donelan, M.A., Madsen, N., Katsaros, K.B., Terray, E.A., and Flagg, C.N. (1994). Directional Wave Spectra from a Swath Ship at Sea. *Journal of Atmospheric and Oceanic Technology*, 11(4), pp. 1109–1116. doi:10.1175/1520-0426(1994)011¡1109:DWSFAS¿2.0.CO;2.

Eldeberky, Y. (1996). Nonlinear transformation of wave spectra in the nearshore. Ph.D. thesis, *Delft University of Technology*.

Erm, A., Alari, V., Lips, I., and Kask, J. (2011). Resuspension of sediment in a semi-sheltered bay due to wind waves and fast ferry wakes. *Boreal Environment Research*, 16(suppl. A), pp. 149–163.

Forristall, G.Z. (1978). On the statistical distribution of wave heights in a storm. *Journal of Geophysical Research*, 83(C5), pp. 2353–2358. doi:10.1029/JC083iC05p02353.

Forristall, G.Z. (1981). Measurements of a saturated range in ocean wave spectra. *Journal of Geophysical Research*, 86(C9), pp. 8075–8084. doi:10.1029/JC086iC09p08075.

Grossmann, A. and Morlet, J. (1984). Decomposition of Hardy functions into square integrable wavelets of constant shape. *SIAM Journal on Mathematical Analysis*, 15(5), pp. 723–736. doi:10.1137/0515056.

Guimarães, P.V. (2018). Sea surface and energy dissipation. Ph.D. thesis, *Loire Bretagne University*.

Gutiérrez-Loza, L., Ocampo-Torres, F.J., and García-Nava, H. (2018). The Effect of Breaking Waves on CO2 Air–Sea Fluxes in the Coastal Zone. *Boundary-Layer Meteorology*, 168(2), pp. 343–360. doi:10.1007/s10546-018-0342-x.

Hara, T. and Karachintsev, A.V. (2003). Observation of Nonlinear Effects in Ocean Surface Wave Frequency Spectra. *Journal of Physical Oceanography*, 33(2), pp. 422–430. doi:10.1175/1520-0485(2003)033¡0422:OONEIO¿2.0.CO;2.

Hasselmann, K. (1962). On the non-linear energy transfer in a gravity-wave spectrum Part 1. General theory. *Journal of Fluid Mechanics*, 12(4), pp. 481–500. doi: 10.1017/S0022112062000373.

Hasselmann, K. (1974). On the spectral dissipation of ocean waves due to white capping. *Boundary-Layer Meteorology*, 6(1-2), pp. 107–127. doi:10.1007/BF00232479.

Hasselmann, K., Barnett, T.P., Bouws, E., Carlson, H., Cartwright, D.E., Enke, K., Ewing, J.A., Gienapp, H., Hasselmann, D.E., Kruseman, P., Meerburg, A., Muller, P., Olbers, D.J., Richter, K., Sell, W., and Walden, H. (1973). Measurements of Wind-Wave Growth and Swell Decay during the Joint North Sea Wave Project (JONSWAP). *Ergnzungsheft zur Deutschen Hydrographischen Zeitschrift*, A(12), pp. 1–95.

Hasselmann, K., Sell, W., Ross, D.B., Müller, P., Hasselmann, K., Sell, W., Ross, D.B., and Müller, P. (1976). A Parametric Wave Prediction Model. *Journal of Physical Oceanography*, 6(2), pp. 200–228. doi:10.1175/1520-0485(1976)006¡0200:APWPM¿2.0.CO;2.

Hasselmann, S., Hasselmann, K., Allender, J.H., Barnett, T.P., Hasselmann, S., Hasselmann, K., Allender, J.H., and Barnett, T.P. (1985). Computations and Parameterizations of the Nonlinear Energy Transfer in a Gravity-Wave Specturm. Part II: Parameterizations of the Nonlinear Energy Transfer for Application in Wave Models. *Journal of Physical Oceanography*, 15(11), pp. 1378–1391. doi:10.1175/1520-0485(1985)015¡1378:CAPOTN¿2.0.CO;2.

Hayashi, Y. (1982). Space-time spectral analysis and its applications to atmospheric waves. *Journal of the Meteorological Society of Japan*. Ser. II 60(1), pp. 156–171.

HIRLAM-B (2018). HIRLAM system documentation. `http://hirlam.org`.

Högström, U., Smedman, A., Sahlée, E., Drennan, W.M., Kahma, K.K., Pettersson, H., and Zhang, F. (2009). The Atmospheric Boundary Layer during Swell: A Field Study and Interpretation of the Turbulent Kinetic Energy Budget for High Wave Ages. *Journal of the Atmospheric Sciences*, 66(9), pp. 2764–2779. doi:10.1175/2009JAS2973.1.

Holthuijsen, L.H. (1983). Observations of the Directional Distribution of Ocean-Wave Energy in Fetch-Limited Conditions. *Journal of Physical Oceanography*, 13(2), pp. 191–207. doi:10.1175/1520-0485(1983)013¡0191:OOTDDO¿2.0.CO;2.

Huang, C.J. and Qiao, F. (2010). Wave-turbulence interaction and its induced mixing in the upper ocean. *Journal of Geophysical Research: Oceans*, 115(C4), pp. 1–12. doi: 10.1029/2009JC005853.

Janssen, P. (1991). Quasi-linear Theory of Wind-Wave Generation Applied to Wave Forecasting. *Journal of Physical Oceanography*, 21(11), pp. 1631–1642. doi:10.1175/1520-0485(1991)021¡1631:QLTOWW¿2.0.CO;2.

Janssen, P. (2009). On some consequences of the canonical transformation in the Hamiltonian theory of water waves. *Journal of Fluid Mechanics*, 637, pp. 1–44. doi: 10.1017/S0022112009008131.

Jönsson, A., Broman, B., and Rahm, L. (2003). Variations in the Baltic Sea wave fields. *Ocean Engineering*, 30(1), pp. 107–126. doi:10.1016/S0029-8018(01)00103-2.

Kahma, K.K. (1979). On a two-peak structure in steady-state fetch-limited wave spectra. Licentiate thesis in Geophysics, *University of Helsinki*.

Kahma, K.K. (1981). A Study of the Growth of the Wave Spectrum with Fetch. *Journal of Physical Oceanography*, 11(11), pp. 1503–1515. doi:10.1175/1520-0485(1981)011¡1503:ASOTGO¿2.0.CO;2.

Kahma, K.K. (1986). On prediction of the fetch-limited wave spectrum in steady wind. *Finnish Marine Research*, (253), pp. 53–78.

Kahma, K.K. and Calkoen, C.J. (1992). Reconciling Discrepancies in the Observed Growth of Wind-generated Waves. *Journal of Physical Oceanography*, 22(12), pp. 1389–1405. doi:10.1175/1520-0485(1992)022¡1389:RDITOG¿2.0.CO;2.

Kahma, K.K., Donelan, M.A., Drennan, W.M., and Terray, E.A. (2016a). Evidence of Energy and Momentum Flux from Swell to Wind. *Journal of Physical Oceanography*, 46(7), pp. 2143–2156. doi:10.1175/JPO-D-15-0213.1.

Kahma, K.K. and Pettersson, H. (1994). Wave growth in a narrow fetch geometry. *The Global Atmosphere and Ocean System*, 2, pp. 253–263.

Kahma, K.K., Pettersson, H., and Tuomi, L. (2003). Scatter Diagram Wave Statistics from the Northern Baltic Sea. *MERI – Report Series of the Finnish Institute of Marine Research*, 49, pp. 15–32.

Kahma, K.K., Björkqvist, J.-V., Johansson, M.M., Jokinen, H., Leijala, U., Särkkä, J., Tikka, K., and Tuomi, L. (2016b). *Turvalliset rakentamiskorkeudet Helsingin rannoilla 2020, 2050 ja 2100*. Technical report. 96, City of Helsinki, Real Estate Department, Geotechnical Division.

Kaitaranta, J., Niemistö, J., Buhvestova, O., and Nurminen, L. (2013). Quantifying sediment resuspension and internal phosphorus loading in shallow near-shore areas in the Gulf of Finland. *Boreal Environment Research*, 18(6), pp. 473–487.

Kenyon, K.E. (1969). Stokes drift for random gravity waves. *Journal of Geophysical Research*, 74(28), pp. 6991–6994. doi:10.1029/JC074i028p06991.

Kitaigorodskii, S.A. (1962). Applications of the theory of similarity to the analysis of wind generated wave motion as stochastic process. *American Geophysical Union of the National Academy of Sciences*, pp. 73–80.

Kitaigorodskii, S.A. (1983). On the Theory of the Equilibrium Range in the Spectrum of Wind-Generated Gravity Waves. *Journal of Physical Oceanography*, 13(5), pp. 816–827. doi:10.1175/1520-0485(1983)013¡0816:OTTOTE¿2.0.CO;2.

Kitaigorodskii, S.A., Krasitskii, V.P., and Zaslavskii, M.M. (1975). On Phillips' Theory of Equilibrium Range in the Spectra of Wind-Generated Gravity Waves. *Journal of Physical Oceanography*, 5(3), pp. 410–420. doi:10.1175/1520-0485(1975)005¡0410:OPTOER¿2.0.CO;2.

Komen, G.J., Hasselmann, K., Hasselmann, K., Komen, G.J., Hasselmann, K., and Hasselmann, K. (1984). On the Existence of a Fully Developed Wind-Sea Spectrum. *Journal of Physical Oceanography*, 14(8), pp. 1271–1285. doi:10.1175/1520-0485(1984)014¡1271:OTEOAF¿2.0.CO;2.

Komen, G.J., Cavaleri, L., Donelan, M.A., K.Hasselmann, Hasselmann, S., and Janssen, P. (1994). *Dynamics and Modelling of Ocean Waves*. Cambridge University Press, Cambridge.

Laakso, L., Mikkonen, S., Drebs, A., Karjalainen, A., Pirinen, P., and Alenius, P. (2018). 100 Years of atmospheric and marine observations at the Finnish Utö Island in the Baltic Sea. *Ocean Science*, 14(4), pp. 617–632. doi:10.5194/os-14-617-2018.

Langmuir, I. (1938). Surface Motion of Water Induce by Wind. *Science*, 87(2250), pp. 119–123. doi:10.1126/science.87.2250.119.

Leckler, F., Ardhuin, F., Peureux, C., Benetazzo, A., Bergamasco, F., and Dulov, V. (2015). Analysis and Interpretation of Frequency–Wavenumber Spectra of Young Wind Waves. *Journal of Physical Oceanography*, 45(10), pp. 2484–2496. doi:10.1175/JPO-D-14-0237.1.

Leijala, U., Björkqvist, J.-V., Johansson, M.M., Pellikka, H., Laakso, L., and Kahma, K.K. (2018). Combining probability distributions of sea level variations and wave run-up to evaluate coastal flooding risks. *Natural Hazards and Earth System Sciences*, 18, pp. 2785–2799. doi:10.5194/nhess-18-2785-2018.

Lenain, L. and Melville, W.K. (2017). Measurements of the directional spectrum across the equilibrium-saturation ranges of wind-generated surface waves. *Journal of Physical Oceanography*, 47(8), pp. 2123–2138. doi:10.1175/JPO-D-17-0017.1.

Ponce de León, S. and Guedes Soares, C. (2005). On the sheltering effect of islands in ocean wave models. *Journal of Geophysical Research: Oceans*, 110(C9). doi: 10.1029/2004JC002682.

Ponce de León, S. and Guedes Soares, C. (2010). The sheltering effect of the Balearic Islands in the hindcast wave field. *Ocean Engineering*, 37(7), pp. 603–610. doi: 10.1016/j.oceaneng.2010.01.011.

Li, J.G. (2011). Global Transport on a Spherical Multiple-Cell Grid. *Monthly Weather Review*, 139(5), pp. 1536–1555. doi:10.1175/2010mwr3196.1.

Liu, Q., Rogers, W.E., Babanin, A.V., Young, I.R., Romero, L., Zieger, S., Qiao, F., and Guan, C. (2019). Observation-Based Source Terms in the Third-Generation Wave Model WAVEWATCH III: Updates and Verification. *Journal of Physical Oceanography*, 49(2), pp. 489–517. doi:10.1175/jpo-d-18-0137.1.

Longuet-Higgins, M.S. (1952). On the Statistical Distribution of the Heights of Sea Waves. *Journal of Marine Research*, 11(3), pp. 245–266.

Longuet-Higgins, M.S. (1970). Longshore currents generated by obliquely incident sea waves, 1. *Journal of Geophysical Research*, 75(33), pp. 6790–6801. doi: 10.1029/jc075i033p06790.

Longuet-Higgins, M.S. (1980). On the distribution of the heights of sea waves: Some effects of nonlinearity and finite band width. *Journal of Geophysical Research*, 85(C3), p. 1519. doi:10.1029/JC085iC03p01519.

Mazarakis, N., Kotroni, V., Lagouvardos, K., and Bertotti, L. (2012). High-resolution wave model validation over the Greek maritime areas. *Natural Hazards and Earth System Sciences*, 12(11), pp. 3433–3440. doi:10.5194/nhess-12-3433-2012.

Meyer, Y. (1989). Orthonormal Wavelets. In: Combes Jean-Michel, , Grossmann, A., Philippe, and Tchamitchian, eds, *Wavelets*, pp. 21–37. Berlin, Heidelberg: Springer Berlin Heidelberg.

Monbaliu, J., Padilla-Hernández, R., Hagreaves, J.C., Albiach, J.C.C., Luo, W., Sclavo, M., and Günter, H. (2000). The spectral wave model, WAM, adapted for applications with high spatial resolution. *Coastal Engineering*, 41, pp. 41–62.

Nielsen, P. (1988). Three simple models of wave sediment transport. *Coastal Engineering*, 12(1), pp. 43–62. doi:10.1016/0378-3839(88)90014-2.

Perrie, W., Tang, C.L., Hu, Y., and DeTracy, B.M. (2003). The Impact of Waves on Surface Currents. *Journal of Physical Oceanography*, 33(10), pp. 2126–2140. doi: 10.1175/1520-0485(2003)033¡2126:TIOWOS¿2.0.CO;2.

Perrie, W., Toulany, B., Roland, A., Dutour-Sikiric, M., Chen, C., Beardsley, R.C., Qi, J., Hu, Y., Casey, M., and Shen, H. (2017). Modeling North Atlantic Nor'easters with Modern Wave Forecast Models. *Journal of Geophysical Research: Oceans*, 123, pp. 533–557. doi:10.1002/2017JC012868.

Pettersson, H. (2004). Wave growth in a narrow bay. Ph.D. thesis, *University of Helsinki*.

Pettersson, H. and Kahma, K.K. (2005). Directional measurements of wave growth in a short and narrow fetch geometry. *Journal of Atmospheric and Ocean Science*, 10(1), pp. 15–29. doi:10.1080/17417530500062853.

Pettersson, H., Kahma, K.K., and Tuomi, L. (2010). Wave Directions in a Narrow Bay. *Journal of Physical Oceanography*, 40(1), pp. 155–169. doi:10.1175/2009JPO4220.1.

Pettersson, H., Lindow, H., and Brüning, T. (2013). *Wave climate in the Baltic Sea 2012*, HELCOM, Baltic Sea Environment Fact Sheet 2018.

Phillips, O.M. (1958). The equilibrium range in the spectrum of wind-generated waves. *Journal of Fluid Mechanics*, 4(4), pp. 426–434. doi:10.1017/S0022112058000550.

Phillips, O.M. (1985). Spectral and statistical properties of the equilibrium range in wind-generated gravity waves. *Journal of Fluid Mechanics*, 156, pp. 505–531. doi: 10.1017/S0022112085002221.

Qiao, F., Yuan, Y., Yang, Y., Zheng, Q., Xia, C., and Ma, J. (2004). Wave-induced mixing in the upper ocean: Distribution and application to a global ocean circulation model. *Geophysical Research Letters*, 31(L11303), pp. 1–4. doi:10.1029/2004GL019824.

Randel, W.J. and Held, I.M. (1991). Phase speed spectra of transient eddy fluxes and critical layer absorption. *Journal of the Atmospheric Sciences*, 48(5), pp. 688–697.

Resio, D., Long, C.E., and Vincent, C.L. (2004). Equilibrium-range constant in wind-generated wave spectra. *Journal of Geophysical Research*, 109(C01018), pp. 1–14. doi: 10.1029/2003JC001788.

Resio, D. and Perrie, W. (1989). Implication of an f^{-4} Equilibrium Range for Wind-Generated Waves. *Journal of Physical Oceanography*, 19(2), pp. 193–204. doi: 10.1175/1520-0485(1989)019¡0193:IOAERF¿2.0.CO;2.

Rinne, H., Kaskela, A., Downie, A.L., Tolvanen, H., von Numers, M., and Mattila, J. (2014). Predicting the occurrence of rocky reefs in a heterogeneous archipelago area with limited data. *Estuarine, Coastal and Shelf Science*, 138, pp. 90–100. doi: 10.1016/j.ecss.2013.12.025.

Romero, L., Melville, W.K., Romero, L., and Melville, W.K. (2010). Airborne Observations of Fetch-Limited Waves in the Gulf of Tehuantepec. *Journal of Physical Oceanography*, 40(3), pp. 441–465. doi:10.1175/2009JPO4127.1.

Räämet, A. and Soomere, T. (2010). The wave climate and its seasonal variability in the northeastern Baltic Sea. *Estonian Journal of Earth Sciences*, 59(1), p. 100. doi: 10.3176/earth.2010.1.08.

Sahlée, E., Drennan, W.M., Potter, H., and Rebozo, M.A. (2012). Waves and air-sea fluxes from a drifting ASIS buoy during the Southern Ocean Gas Exchange experiment. *Journal of Geophysical Research: Oceans*, 117(C08003), pp. 1–12. doi: 10.1029/2012JC008032.

Seifert, F., Tauber, B., and Kayser, B. (2001). A high resolution spherical grid topography of the Baltic Sea – 2nd edition. In: *Baltic Sea Science Congress Stockholm 25-29. November 2001, Poster 147*.

Semedo, A., Saetra, Ø., Rutgersson, A., Kahma, K.K., and Pettersson, H. (2009). Wave-Induced Wind in the Marine Boundary Layer. *Journal of the Atmospheric Sciences*, 66(8), pp. 2256–2271. doi:10.1175/2009jas3018.1.

Soomere, T. and Keevallik, S. (2003). Directional and extreme wind properties in the Gulf of Finland Baltic. *Proceedings of the Estonian Academy of Sciences, Engineering*, 9(2), pp. 73–90.

Soukissian, T.H., Prospathopoulos, A.M., and Diamanti, C. (2004). Wind and Wave Data Analysis for the Aegean Sea - Preliminary Results. *Journal of Atmospheric & Ocean Science*, 8(2-3), pp. 163–189. doi:10.1080/1023673029000003525.

SPM (1984). Shore Protection Manual, Vol. I, *Dept. of the Army, Waterways Experiment Station, Corps of Engineers, Coastal Engineering Research Center,*.

Squire, V.A. (2007). Of ocean waves and sea-ice revisited. *Cold Regions Science and Technology*, 49(2), pp. 110–133. doi:10.1016/j.coldregions.2007.04.007.

Steele, M. (1992). Sea ice melting and floe geometry in a simple ice-ocean model. *Journal of Geophysical Research*, 97(C11), pp. 17729-17738.

Tamura, H., Drennan, W.M., Sahlée, E., and Graber, H.C. (2014). Spectral form and source term balance of short gravity wind waves. *Journal of Geophysical Research: Oceans*, 119(11), pp. 7406–7419. doi:10.1002/2014JC009869.

Terray, E., Donelan, M.A., Agrawal, Y., Drennan, W.M., Kahma, K.K., Williams, A., Hwang, P., and Kitaigorodskii, S.A. (1996). Estimates of Kinetic Energy Dissipation under Breaking Waves. *Journal of Physical Oceanography*, 26(5), pp. 792–807. doi: 10.1175/1520-0485(1996)026¡0792:EOKEDU¿2.0.CO;2.

Tisler, P., Gregow, E., Niemelä, S., and Savijärvi, H. (2007). Wind Field Prediction in Coastal Zone: Operational Mesoscale Model Evaluation and Simulations with Increased Horizontal Resolution. *Journal of Coastal Research*, 23(3), pp. 721–730. doi: 10.2112/05-0450.1.

Toba, Y. (1972). Local Balance in the Air–Sea Boundary Processes I. On the Growth Process of Wind Waves. *Journal of the Oceanographical Society of Japan*, 28, pp. 109–121. doi:10.1007/BF02109772.

Toba, Y. (1973). Local Balance in the Air–Sea Boundary Processes III. On the Spectrum of Wind Waves. *Journal of the Oceanographical Society of Japan*, 29, pp. 209–220. doi:10.1007/BF02109506.

Tolman, H.L. (2003). Treatment of unresolved islands and ice in wind wave models. *Ocean Modelling*, 5(3), pp. 219–231. doi:10.1016/S1463-5003(02)00040-9.

Tolman, H.L. and Chalikov, D.V. (1996). Source Terms in a Third-Generation Wind Wave Model. *Journal of Physical Oceanography*, 26, pp. 2497–2518.

Tolman, H.L., Balasubramaniyan, B., Burroughs, L.D., Chalikov, D.V., Chao, Y.Y., Chen, H.S., and Gerald, V.M. (2002). Development and Implementation of Wind-Generated Ocean Surface Wave Modelsat NCEP. *Weather and Forecasting*, 17(2), pp. 311–333. doi:10.1175/1520-0434(2002)017¡0311:DAIOWG¿2.0.CO;2.

Tuomi, L. and Björkqvist, J.-V. (2014). Wave forecasting in coastal archipelagos. In: *Measuring and Modeling of Multi-Scale Interactions in the Marine Environment - IEEE/OES Baltic International Symposium 2014, BALTIC 2014*.

Tuomi, L., Kahma, K.K., and Pettersson, H. (2011). Wave hindcast statistics in the seasonally ice-covered Baltic Sea. *Boreal Environment Research*, 16(6), pp. 451–472.

Tuomi, L., Pettersson, H., Fortelius, C., Tikka, K., Björkqvist, J.-V., and Kahma, K.K. (2014). Wave modelling in archipelagos. *Coastal Engineering*, 83, pp. 205–220.

Tuomi, L., Vähä-Piikkiö, O., Alenius, P., Björkqvist, J.-V., and Kahma, K.K. (2018). Surface Stokes drift in the Baltic Sea based on modelled wave spectra. *Ocean Dynamics*, 68(1), pp. 17–33. doi:10.1007/s10236-017-1115-7.

Vandever, J.P., Siegel, E.M., Brubaker, J.M., and Friedrichs, C.T. (2008). Influence of Spectral Width on Wave Height Parameter Estimates in Coastal Environments. *Journal of Waterway, Port, Coastal, and Ocean Engineering*, 134(3), pp. 187–194. doi: 10.1061/(ASCE)0733-950X(2008)134:3(187).

van Vledder, G.Ph. (2006). The WRT method for the computation of non-linear four-wave interactions in discrete spectral wave models. *Coastal Engineering*, 53(2-3), pp. 223–242. doi:10.1016/j.coastaleng.2005.10.011.

WAMDIG (1988). The WAM Model—A Third Generation Ocean Wave Prediction Model. *Journal of Physical Oceanography*, 18(12), pp. 1775–1810. doi:10.1175/1520-0485(1988)018¡1775:TWMTGO¿2.0.CO;2.

Wang, D.W. and Hwang, P. (2004). The Dispersion Relation of Short Wind Waves from Space–Time Wave Measurements. *Journal of Atmospheric and Oceanic Technology*, 21(12), pp. 1936–1945. doi:10.1175/JTECH-1669.1.

van der Westhuysen, A.J., Zijlema, M., and Battjes, J.A. (2007). Nonlinear saturation-based whitecapping dissipation in SWAN for deep and shallow water. *Coastal Engineering*, 54(2), pp. 151–170. doi:10.1016/j.coastaleng.2006.08.006.

Wu, J. (1982). Wind-stress coefficients over sea surface from breeze to hurricane. *Journal of Geophysical Research*, 87(C12), pp. 9704–9706. doi:10.1029/JC087iC12p09704.

Young, I.R. (1995). The determination of confidence limits associated with estimates of the spectral peak frequency. *Ocean Engineering*, 22(7), pp. 669–686. doi: 10.1016/0029-8018(95)00002-3.

Zieger, S., Babanin, A.V., Erick Rogers, W., and Young, I.R. (2015). Observation-based source terms in the third-generation wave model WAVEWATCH. *Ocean Modelling*, 96(1), pp. 2–25. doi:10.1016/j.ocemod.2015.07.014.

I

Reprinted, with kind permission, from
Journal of Marine Systems, 171, 43-53
doi:10.1016/j.jmarsys.2016.07.005

Journal of Marine Systems 171 (2017) 43–53

Contents lists available at ScienceDirect

Journal of Marine Systems

journal homepage: www.elsevier.com/locate/jmarsys

Improved estimates of nearshore wave conditions in the Gulf of Finland

Jan-Victor Björkqvist*, Laura Tuomi, Carl Fortelius, Heidi Pettersson, Kimmo Tikka, Kimmo K. Kahma

Finnish Meteorological Institute, P.O. Box 503, FI-00101 Helsinki, Finland

ARTICLE INFO

Article history:
Received 30 March 2016
Received in revised form 24 June 2016
Accepted 11 July 2016
Available online 14 July 2016

Keywords:
Wave modelling
Baltic Sea
Fetch-limited
Wind wave spectrum
Sheltering
Archipelago

ABSTRACT

The heterogeneous coastline of the Gulf of Finland can result in widely varying wave conditions in a small geographical area. It is therefore challenging to obtain comprehensive information about the wave spectrum, which is needed to accurately quantify, e.g. the wave-bottom interactions. In this study, we implemented the wave model WAM to the coastal waters off Helsinki using a high-resolution 0.1 nmi grid and found that the model mostly predicts the wave field well. However, WAM overestimated the wave energy for south-westerly winds blowing over the peninsula sheltering the study area. This spurious behaviour was not caused by inaccuracies in the wind forcing, the boundary wave field or the available bathymetric grids. We present two methods for improving the prediction of the near-shore wave field. The first approach, which is also used to describe the structure of the wave field, is based on e.g. wave growth relations and models the fetch-limited and the longer waves separately. The second method determines a so-called effective wind forcing for the wave model by comparing the observed and modelled non-dimensional wave spectra. Both methods were validated using wave buoy observations and were found to clearly improve the predictions for the significant wave height and wave spectrum at the study site for south-westerly winds. Because some prior information on the wave conditions is required to implement the methods, they are best suited for expanding the usability of any limited measurement dataset available for a study. The method based on the effective wind forcing can also be implemented for operational forecasting or be used to gather statistics from hindcasts.

1. Introduction

Wind-driven surface waves affect a number of coastal processes. They must therefore be accounted for when studying e.g. the transportation of bottom sediments (Nielsen, 1992; Erm et al., 2011; Kaitaranta et al., 2013) or the living conditions of organisms in the benthic zone (Rinne et al., 2014). However, there is typically a lack of wave measurements from the shorelines, leaving environmental studies to rely on wave exposure indexes (Isaeus, 2004) when mapping marine protected areas. Waves are also an important consideration with respect to marine traffic and the planning of coastal constructions. In particular, a location-specific wave run-up is crucial for determining building heights. Previously estimates were based on the fetch (Kahma et al., 2014), but recently Kahma etal. (2016) were able to determine location-specific values for the shoreline of Helsinki as a result of an extensive multiyear measurement campaign commissioned by the City of Helsinki. The wave set-up, i.e. the mean increase in sea level caused by breaking waves, has been modelled by Soomere et al. (2013a), while Alari and Kõuts (2012) modelled both the wave set-up and the wave run-up.

One approach to quantifying e.g. the wave exposure or closure depths is via integrated parameters (e.g. Ekebom et al., 2003; Soomere et al., 2013b). However, approximations that rely on the significant wave height, the peak period and results from linear wave theory implicitly assume that waves have certain universal properties. Although this might be a fair approximation for the open sea, e.g. Pettersson (2004) has shown that the distribution of energy is affected by the shape of the basin and the slanting fetch near the shore. Moreover, complex shorelines can result in multiple intertwined wave systems of a similar magnitude that cannot be accurately described by a standard set of wave parameters, but instead need to be quantified using the wave spectrum.

The mapping of the coastal wave field by observations alone is costly and time consuming. Spectral wave models are an applicable way to obtain wave data both when considering available resources and spatial coverage. The wave model WAM (Komen et al., 1994; WAMDIG, 1988) has been found accurate in a variety of open-sea condition (Bertotti et al., 2014; Galanis et al., 2010), including the Baltic Sea (Tuomi et al., 2011). The physics of the model are suitable to modelling nearshore waves (Monbaliu et al., 2000), and some issues related to archipelagos have been adequately addressed

* Corresponding author.
E-mail address: jan-victor.bjorkqvist@fmi.fi (J. Björkqvist).

http://dx.doi.org/10.1016/j.jmarsys.2016.07.005
0924-7963/

(Tuomi et al., 2014). Nevertheless, WAM's performance has not been extensively validated near complex shorelines. Therefore the wave model results for complex coastal areas cannot be used with such confidence as for the open sea or less complicated geographical coastlines (Björkqvist et al., 2014).

Partially sheltered conditions still pose a challenge for wave models. The effect of islands can be incorporated into the models by attenuating an appropriate amount of energy from the wave field when entering the archipelago (Tolman, 2003; Tuomi et al., 2014). In this paper, we study the sheltering effect a peninsula has on the wave field, in which case the main issue is the interaction and separation of two partially distinct wave systems. While archipelagos are mostly concentrated to the northern part of the Gulf of Finland, areas sheltered by peninsulas are common also along the southern coastlines, e.g. along the coast of Tallinn. Wave information for areas near both the capital cities of Helsinki and Tallinn is in high demand; wave data has been obtained via observations (Erm et al., 2011; Kahma etal., 2016), numerical models (Soomere, 2005; Soomere et al., 2013a; Soomere et al., 2011) and models based on fetch-limited growth relations (Suursaar, 2013).

The paper is organised as follows. In Section 2, we present the study area, the datasets and the modelling tools. Section 3 is dedicated to an evaluation of the wave model results, a more in-depth analysis of the semi-sheltered wave field and the alternative prediction methods developed for such conditions. We then discuss the applicability and limitations of the different modelling approaches and conclude our findings.

2. Materials and methods

2.1. The study area and bathymetric data-sets

The area of interest is the Helsinki coastal area in the northern part of the Gulf of Finland (GoF) (Fig. 1). We constructed two high-resolution 0.1 nmi (~0.185 km) grids using different bathymetrical sources. The first grid was based on information derived mainly from nautical charts, as described by Björkqvist et al. (2014). The second grid used had previously been constructed as a part of the Velmu project run by the Finnish Environment Institute (http://www.ymparisto.fi/en-US/VELMU/). It uses additional depth data from water quality stations and the Baltic Sea Bathymetry Database (Baltic Sea Hydrographic Commission, 2013).

The 1′ latitude, 2′ longitude (~1 nmi) Baltic Sea grid used to solve the basin-scaled bathymetric features was constructed using freely available data from the Leibniz Institute for Baltic Sea Research, Warnemünde (IOW) (Seifert et al., 2001) and ETOPO1 (Amante and Eakins, 2009).

2.2. Measurements datasets

We used wave buoy data from two locations. During the period 27.9–27.10.2012 we deployed a GPS-based Datawell DWR-G4 wave buoy at the edge of the Helsinki archipelago near Harmaja ("The Harmaja wave buoy") where the water depth is 29 m (Fig. 1). The GPS-based Waveriders have been shown to produce a spurious f^{-2} low-frequency trend, which has later been explained as being a result of gaps in the GPS signal. The wave spectra were corrected for these artefacts following Björkqvist et al. (2016). The operational, accelerometer-based Directional Waverider ("The Helsinki wave buoy") is anchored at a depth of 62 m in the central GoF (Fig. 1). The Helsinki wave buoy is operated by FMI and has been deployed permanently during the ice-free period since the year 2000 (and also the years 1982–85, 90–92 and 94). In this study, we used the dataset that coincided with the measurements of the Harmaja wave buoy for the year 2012. The wave buoys provided data every 30 min, with the exception of six gaps in the records for the Helsinki wave buoy, with the longest being 1.5 h.

Wind measurements from the automated coastal weather stations of the Finnish Meteorological Institute (FMI) provided wind data for the study. The Harmaja station is located at the edge of the Helsinki archipelago (60° 6.29′N 24° 58.53′E) on the 0.02 km^2 island of Harmaja, 3 km north-east of the Harmaja wave buoy. The wind is measured at a height of 16.5 m above sea level. Kalbådagrund is located in the centre of the GoF (59° 59.11′N 25° 35.91′E) 20 km east of the Helsinki wave buoy. The wind is measured at 31.8 metres above sea level.

2.3. Wave growth relations

Off-shore winds often result in fetch-limited waves, which are restricted by the distance to the shore in the upwind direction and not by the duration the wind has been blowing. Wave growth formulas have long been used to predict the basic wave parameters under fetch-limited conditions (e.g. Hasselmann et al., 1973; Kahma, 1981; Kahma and Calkoen, 1992) and they have also been utilised for wave hindcasts and making future projections (e.g. Suursaar, 2013; Suursaar et al., 2016). According to the wave growth formula from the composite dataset compiled by Kahma and Calkoen (1992), the dimensionless energy and dimensionless angular peak frequency of a fetch-limited wave field can be estimated based on the following relations:

$$\frac{g^2\varepsilon}{U_{10}^4} = 5.2\cdot 10^{-7}\left(\frac{gX}{U_{10}^2}\right)^{0.9} \tag{1}$$

$$\frac{\omega_p U_{10}}{g} = 13.7\left(\frac{gX}{U_{10}^2}\right)^{-0.27}, \tag{2}$$

where ε is the total variance of the wave field, U_{10} is the wind speed at 10-metre height, X is the fetch, ω_p is the peak angular frequency and g is the acceleration due to gravity.

2.4. The wave model WAM

We used the wave model WAM Cycle 4.5.1 (Komen et al., 1994; WAMDIG, 1988) to model the wave field off Helsinki. WAM solves the spectral action balance equation, which without currents takes the following form:

$$\frac{\partial}{\partial t}\left(\frac{F}{\sigma}\right) + \nabla\cdot\left[\mathbf{c}_g\left(\frac{F}{\sigma}\right)\right] - \nabla_k\cdot\left[\nabla\sigma(k,h)\left(\frac{F}{\sigma}\right)\right] = S_{tot}, \tag{3}$$

where the spatial coordinates in the ∇-operator and the variables of F have been omitted for the sake of brevity. The terms on the left side represent the change in wave energy over time and the propagation of wave energy in space, where F is the wave energy spectrum, σ is the intrinsic frequency, k is the wave number, h is the water depth and $\mathbf{c}_g$ is the group velocity. The right side is the sum of the source terms: wind input, dissipation due to white capping and weakly non-linear wave–wave interactions calculated using the discrete interactions proposed by Hasselmann et al. (1985) (hereafter DIA). The WAM Cycle 4.5.1 also includes bottom friction and depth-induced wave breaking source terms (Battjes and Janssen, 1978; Hasselmann et al., 1973), both as described by Monbaliu et al. (2000).

The model spectra had 36 equally distributed directional bands and 40 frequency bands, ranging from 0.060 Hz to 2.468 Hz. The high-resolution 0.1 nmi coastal grid was nested inside the 1 nmi Baltic Sea grid (Fig. 1). Both model grids were regular grids with a fixed spatial spacing. Both the propagation time step and the source term integration time step were 2 s.

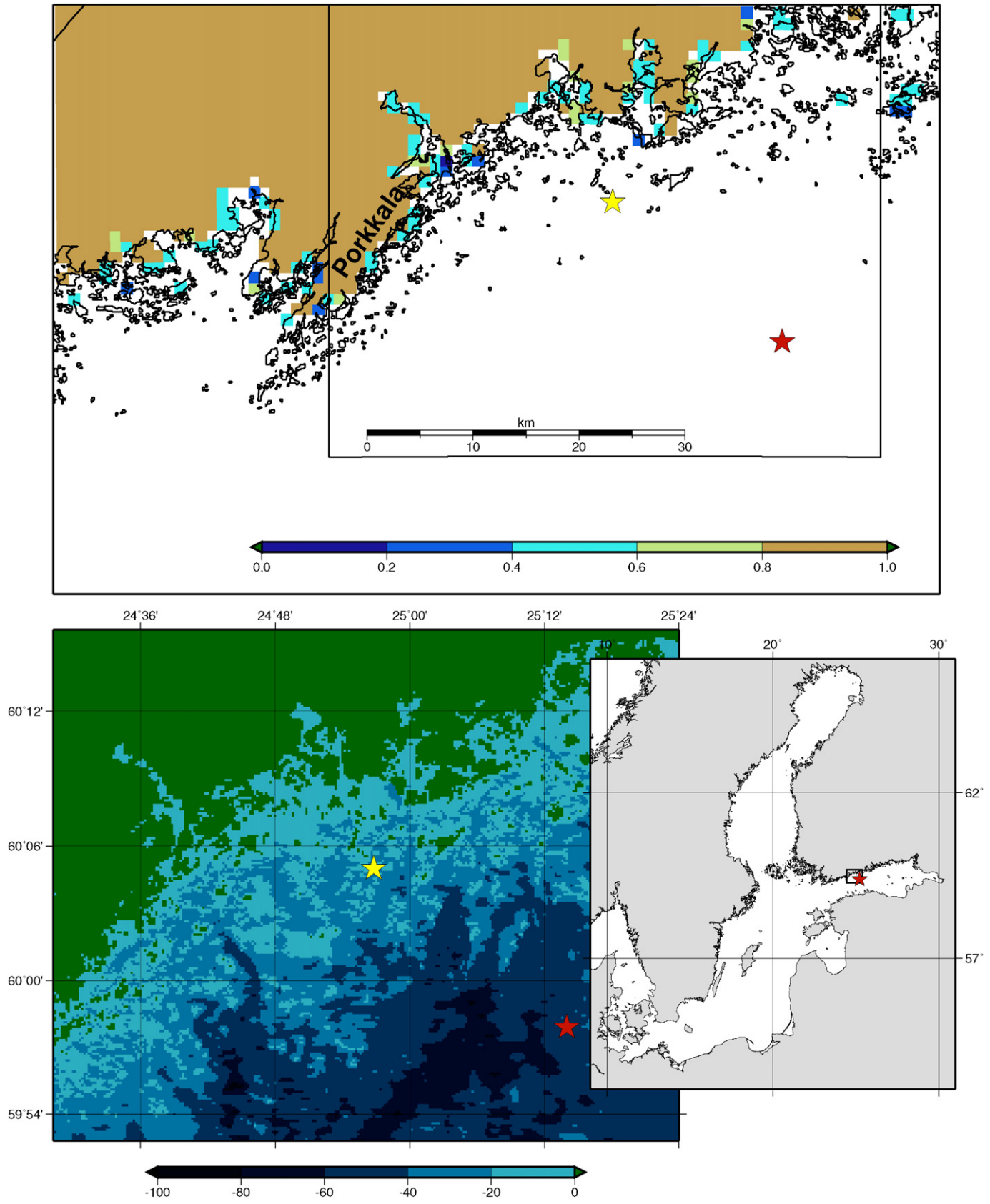

Fig. 1. Top: the fraction of land used at every grid point in HARMONIE (1 = land, 0 = sea). The bottom left shows the bathymetry used in WAM. The stars mark the locations of the Helsinki wave buoy at 59° 57.90′N 25° 14.11′E (red) and the Harmaja wave buoy at 60° 5.02′N 24° 56.78′E (yellow). The nested grid (bottom left) is marked by the black squares in the top and the bottom right.

2.5. Meteorological forcing

We obtained the wind forcing for the wave model from FMI's operational Numerical Weather Prediction (NWP) system, HIRLAM version 7.4 (HIRLAM-B, 2012), post-processed to a height of 10 m above the surface. The model grid, which covers the European regions, had a horizontal resolution of 11 km and a vertical resolution of 65 terrain-following hybrid levels, the lowest level being about 12 m above the sea surface.

Because the wave model's sensitivity to the horizontal resolution of the forcing wind field is a factor to consider (Cavaleri and Bertotti, 2004; Tuomi et al., 2014), we also implemented the HARMONIE NWP model as an alternative high-resolution wind forcing. HARMONIE is a non-hydrostatic, convection-permitting model based on AROME (Seity et al., 2011). For the purpose of this study HARMONIE cycle 38h1 was run with a grid spacing of 1 km on 65 levels in the vertical direction (the same as for HIRLAM) on a domain slightly larger than the GoF.

The ECMWF's Boundary Condition Optional Project provided the boundary conditions for both domains, and we used data from the first 6 h of each run. The model output for HIRLAM and HARMONIE was saved every 3 h and 15 min, respectively.

3. WAM results

3.1. The coastal wave field

For our study area, WAM forced with HIRLAM modelled the general characteristics of the wave field accurately, as seen in Table 1 and Fig. 2. However, a more detailed analysis revealed that the significant wave height at the Harmaja wave buoy was overestimated for south-westerly winds (Table 1), which is one of the prevailing wind directions in the GoF. Wind directions between 210° and 270° accounted for 28% of the cases during the period of the Harmaja wave buoy measurements. An illustrative example is the period of 05–07 October when the measured wind direction was near 240° for the entire period (Fig. 3), but the same behaviour was observed during e.g. 16, 18–19 and 24 October (Fig. 2).

Also the peak period at Harmaja was overestimated by WAM during south-westerly winds, but the bias of the model for the entire dataset is negative because of the volatile nature of the parameter for significant wave heights under 0.5 m (Fig. 2, 09–13 October). The mean direction was modelled with a sufficient level of accuracy for all frequencies (Fig. 4), which is also reflected in the modelled mean direction at the spectral peak (Fig. 2).

The HARMONIE NWP system had a higher spatial and temporal resolution than HIRLAM and was therefore able to capture smaller variations in the wind speed (Fig. 5). Nevertheless, the wave model results from our study site were almost identical when using HARMONIE instead of HIRLAM (Table 1). Hereafter, the analysis will focus only on the WAM results obtained using the HIRLAM forcing.

On 06 October 12:30–17:00 UTC, the wind speed was fairly steady (11.8–13.0 m s^{-1}), while the measured significant wave height at Harmaja was near constant, between 1.16 and 1.25 m. The waves were fetch-limited, which can been seen from the lack of evolution of the observed spectra from Harmaja (Fig. 6). There are several reasons why this period is especially suitable for further inspection: the speed of the south-westerly winds increased steadily from about 7 m s^{-1} until it reached a near constant value, which was then sustained for several hours. In addition, the significant wave height at the beginning of the period was relatively low, indicating an absence of swell.

The wave field modelled by WAM is not consistent with the fetch-limited observations, as the significant wave height continued to rise until the wind speed began to decrease. During the steady wind on 06 October the modelled energy exceeded the observations for almost the entire frequency range (Fig. 4a). WAM expressed similar behaviour during other days with south-westerly winds (Fig. 4b–d).

3.2. The forcing wind field and the boundary wave field

Inaccuracies in the meteorological forcing could explain the discrepancies in magnitude and evolution between the modelled and observed wave energy. However, comparing the modelled wind speed at 10-metre height with measurements from Harmaja shows that both HIRLAM and HARMONIE performed well, with a bias of 0.50 and 0.58 m s^{-1} (model overestimates), and an RMSE of 1.45 and 1.47 m s^{-1} respectively when evaluated for the entire measurement period. Fig. 5 shows the good performance of the NWP systems on 06 October — our period of special interest. The modelled wind speed also matched the observations in the respect that they were almost constant between 12:30 and 17:00 UTC. Both NWP systems calculated the wind direction with good accuracy at Harmaja (Fig. 5).

We observed no overestimation of the wind forcing for south-westerly winds that could explain the spurious model behaviour on 06–07, 16, 18–19 and 24 October. The only major discrepancy for both the NWP systems was an underprediction of the wind speed at Kalbådagrund on 14 October during easterly winds (not shown here). While this was clearly reflected in the significant wave height even at Harmaja (Fig. 2), it is totally unrelated to the problem at hand.

Björkqvist et al. (2014) showed that the choice of land sea mask used for the boundary grid can affect large areas of the wave field modelled with the nested grid. While the authors found no significant impact at the area around Harmaja, it is possible that inaccuracies in the boundary wave field further to the east could have affected the results at our study site. The accuracy of the boundary wave field was therefore evaluated by comparing the significant wave height modelled with the basin scale grid to the measurements from the open-sea Helsinki wave buoy (location shown in Fig. 1).

A general comparison showed that the modelled significant wave height was in good accord with the measurements. The bias of the model was 0.07 m with an RMSE of 0.20 m. Reviewing individual cases of south-westerly winds revealed an overestimation on 28

Table 1
The accuracy of WAM at the Harmaja wave buoy when forced with HIRLAM and HARMONIE winds, and with the effective HIRLAM wind forcing. Results for the whole dataset (left) and those for only south-westerly winds (i.e. 240° ± 30°, right) are shown separately. In addition, the results of the fetch-limited approximation are listed (valid only for south-westerly winds).

	All data				South-westerly winds			
	H_s (m)		T_p (s)		H_s (m)		T_p (s)	
Model	bias	RMSE	bias	RMSE	bias	RMSE	bias	RMSE
WAM (HIRLAM)	0.07	0.22	−0.41	1.76	0.25	0.34	0.45	1.10
WAM (HARMONIE)	0.08	0.23	−0.49	1.90	0.31	0.38	0.52	1.18
WAM (Eff. wind forc.)	0.00	0.13	−0.35	1.80	0.04	0.14	0.64	1.32
Fetch-limited approx.	–	–	–	–	0.03	0.16	–	–

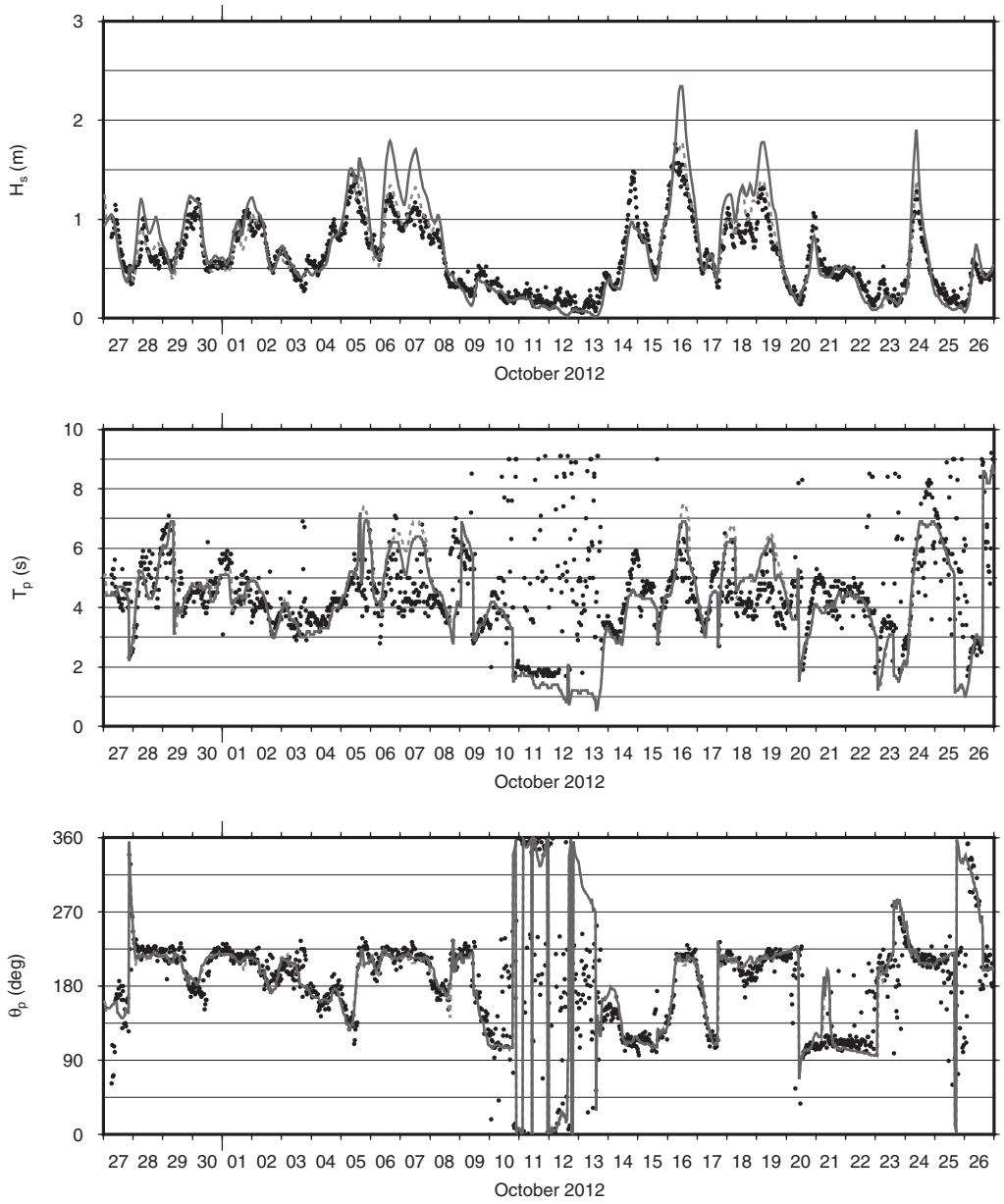

Fig. 2. Times series of the significant wave height, peak period and mean direction at the spectral peak (direction from) at the location of the Harmaja wave buoy. Measured value (black dots), WAM (solid blue) and WAM forced with the effective wind forcing (dashed red).

September and 18–19 October, as well as an underestimation on 29 September and 01 October. However, the significant wave height was modelled accurately at the Helsinki wave buoy during the most prominent south-westerly cases (6–7, 16 and 24 October, Fig. 7). Therefore the reason for the spurious behaviour of WAM must have been caused by some other factor.

3.3. The effect of the bathymetry

The waves propagating from the south-west travel over an area of shallow depth (Fig. 1). The accuracy of the bathymetric data is therefore one factor that might have affected the wave model results at the Harmaja wave buoy. We tested the model's sensitivity to bottom related processes in several ways. First, we used two different depth models to produce bathymetric grids for WAM. The depth models, which differed both in terms of the grid generation method and source data, yielded two realisations of the bathymetry. Second, we changed the free parameters in, or even excluded, the bottom friction and depth-induced wave breaking source terms. The differences uncovered by these sensitivity tests were, at most, in an order of magnitude smaller than the observed error at Harmaja. These factors were therefore excluded as explanations for the observed discrepancies.

4. Methods to supplement the WAM results

4.1. The structure of the wave field

The spurious WAM behaviour seems to take place when modelling two different wave systems: one is limited by the fetch, while the other propagates around the sheltering peninsula. Our aim is not to build a comprehensive alternative model, but to gain

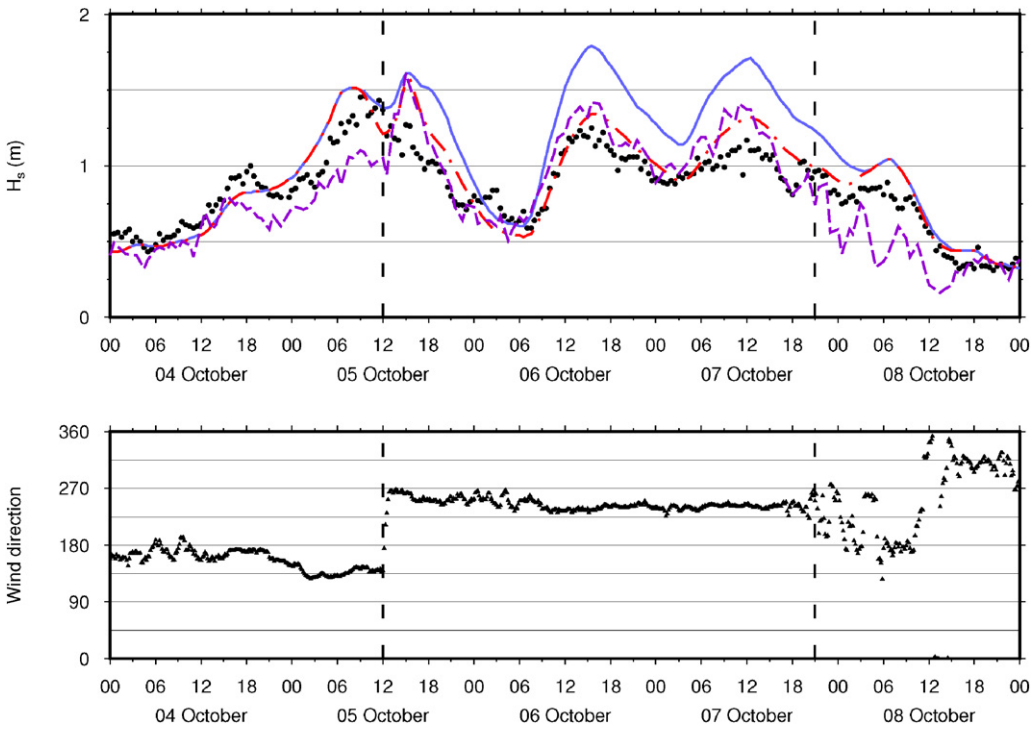

Fig. 3. The significant wave height at the Harmaja wave buoy; wave buoy (black dots), WAM (blue solid), WAM forced with the effective wind forcing (dashed-dotted red). Black triangles on the bottom show the measured wind direction at the Harmaja weather station. The results based on wave growth relation (dashed magenta) are only valid for wind directions near 240° (vertical dashed lines).

insight into the balance and interaction of the two observed wave systems. Nonetheless, as an alternative prediction method for the semi-sheltered conditions we also estimated the wave spectrum in a way that accounted for both the fetch-limited waves and the propagating longer waves, thus expanding the usability of the simple growth formulas. This method is presented in Section 4.2.

In this study, we use the equations of Kahma and Calkoen (1992) (Section 2.3). To get the energy of the wave field from Eq. (1), we needed an estimate of the fetch. For south-westerly winds with a direction of 240° the distance from the Harmaja wave buoy to the islands near the shore is slightly more than 20 km in the upwind direction (Fig. 1). With a wind speed of 13 m s^{-1}, this fetch would produce a peak period of 4 s (Eq. (2)), which is also in line with the observed directional spectra from 06 October (not shown).

Since Eqs. (1)–(2) have been determined for perpendicular fetch only, they are not directly applicable to more complex situations (Bottema and van Vledder, 2008; Kahma and Pettersson, 1994; Pettersson, 2004). In particular, we had to account for the longer waves propagating around the peninsula separately. The ratio of the spectral variance under 0.2 Hz between the Harmaja wave buoy and the Helsinki wave buoy provided an estimate for the wave attenuation. On 06 October 06:00–18:00 the ratio was 0.16. By adding this attenuated variance of the longer waves (ε_L) to the fetch-limited variance from Eq. (1) (ε_F), we obtained an approximation of the total significant wave height at Harmaja, defined as $H_s = 4\sqrt{\varepsilon_L + \varepsilon_F}$. Because this model is based on the fetch it is, of course, valid only for wind directions between 210° and 270°.

The mean value of the ratio $\varepsilon_F/\varepsilon_L$ for 06 October was 1.8 (2.4 for all south-westerly wind cases). This finding indicates that even though the fetch-limited wave system is more dominant, we cannot completely disregard the longer waves. The presence of a significant amount of energy at frequencies lower than the ones generated by the wind blowing over the Porkkala peninsula can also be seen from the observed peak period, which was determined somewhat randomly by either the fetch-limited or the longer waves (see, e.g. 06–07 October in Fig. 2). The relative balance of these two systems seems to be fairly independent of the wind and wave conditions; neither the local observed wind speed nor the significant wave height at Harmaja correlated with the ratio $\varepsilon_F/\varepsilon_L$ ($r^2 < 0.13$). This was to be expected, since the longer waves were generated almost simultaneously with the fetch-limited waves by the wind behind the peninsula, and they can therefore not be considered swell.

The combined variance $\varepsilon_F + \varepsilon_L$ describes the significant wave height at Harmaja well (Fig. 3, Table 1). Because of the complex geographical conditions the determination of the fetch is still a source of error and is also a likely explanation for the slight overestimation. By assuming a constant value of $\varepsilon_F/\varepsilon_L = 2.4$ we get an approximation for the significant wave height at Harmaja that depends solely on ε_F, and thus only on the local wind speed (and the fetch), as determined by Eq. (1). This approximation yields a bias of 0.04 m and an RMSE of 0.20 m, which are almost identical to the values obtained from the method using the combined variance $\varepsilon_F + \varepsilon_L$ (Table 1). These results indicate that the wave field at Harmaja is shaped by the reoccurring balance between the two wave systems. This balance, again, is a result of the geographical conditions (i.e. the sheltering effect of the peninsula). Since the importance of the different wave components is not determined merely by their energy, but also by their wave length, we now need to estimate the wave spectrum.

4.2. Augmented fetch-limited approximation

There is no straightforward way to use the results of the wave growth relations to actually predict the wave spectra, since the widely used spectral shape from the JONSWAP experiment (Hasselmann et al., 1973) is, as such, not applicable to more complex situations. We found an improved agreement if the dimensionless

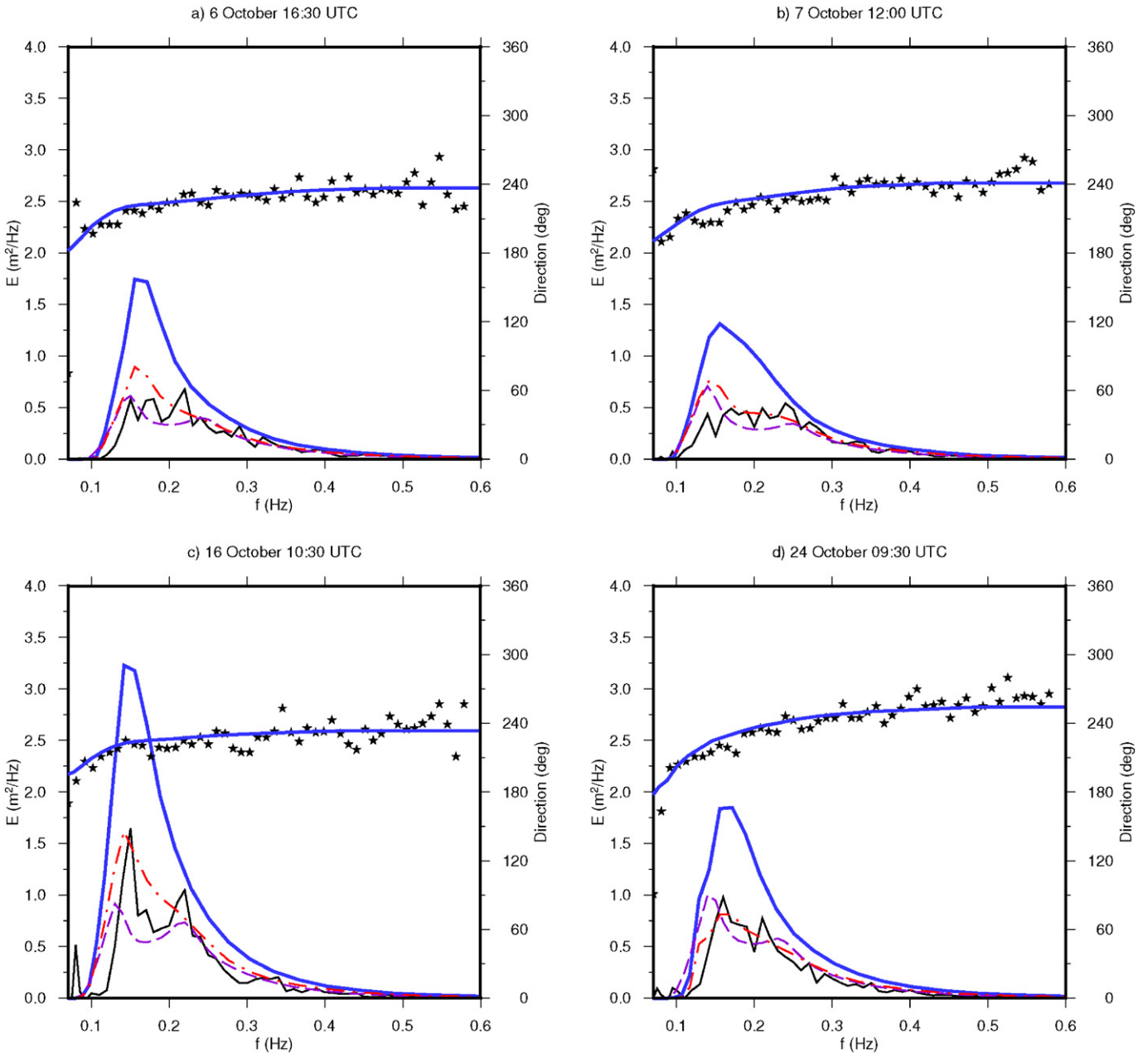

Fig. 4. The wave spectrum at the Harmaja wave buoy during four days of south-westerly winds. Wave buoy (solid black), WAM (thick solid blue), WAM forced with the effective wind forcing (dashed-dotted red) and the augmented fetch-limited approximation (dashed magenta). The mean direction (from) is shown for the wave buoy (black stars) and for WAM (thick solid blue).

peak frequency determined during JONSWAP was discarded in favour of Eq. (2) and the peak enhancement parameter γ was decreased to better match the shape of the wave spectra under slanting and narrow fetch conditions, as found by Pettersson (2004). The parameter γ controls the shape of the spectrum around the peak frequency, with a lower value resulting in a less peaked spectrum. We found a value of 1.5 for the γ-parameter (default $\gamma = 3.3$) to resemble the spectra for inverse wave ages $U/c_p = 1 - 1.5$ of Pettersson (2004). The inverse wave age for the fetch-limited wave system during the steady wind situation on 06 October at Harmaja was around 1.3 (estimated based on Eq. (2)).

We could predict the wave spectrum based on the assumptions of the model for the significant wave height. To approximate the open-sea waves propagating around the peninsula, we used a JONSWAP spectrum ($\gamma = 1.5$) with the same peak period and significant wave height as measured by the Helsinki wave buoy. For practical applications, the estimate for the longer waves can be taken from any other source considered sufficiently reliable, such as wave model results from the open-sea area. The spectrum representing the longer waves was multiplied by a factor of 0.16 to account for the observed wave attenuation. A JONSWAP spectrum ($\gamma = 1.5$) with a peak frequency from Eq. (2) for the observed wind speed at Harmaja represented the fetch-limited spectrum. The final prediction is the superimposition of these two theoretical spectra.

The results from four cases of south-westerly winds are illustrated in Fig. 4. While the double peaked shape of the two superimposed JONSWAP spectra differs from the observations, the general characteristics of the energy distribution are captured well. The analysis done here suggests that there exists a limited interaction between the two described wave systems. While this cannot

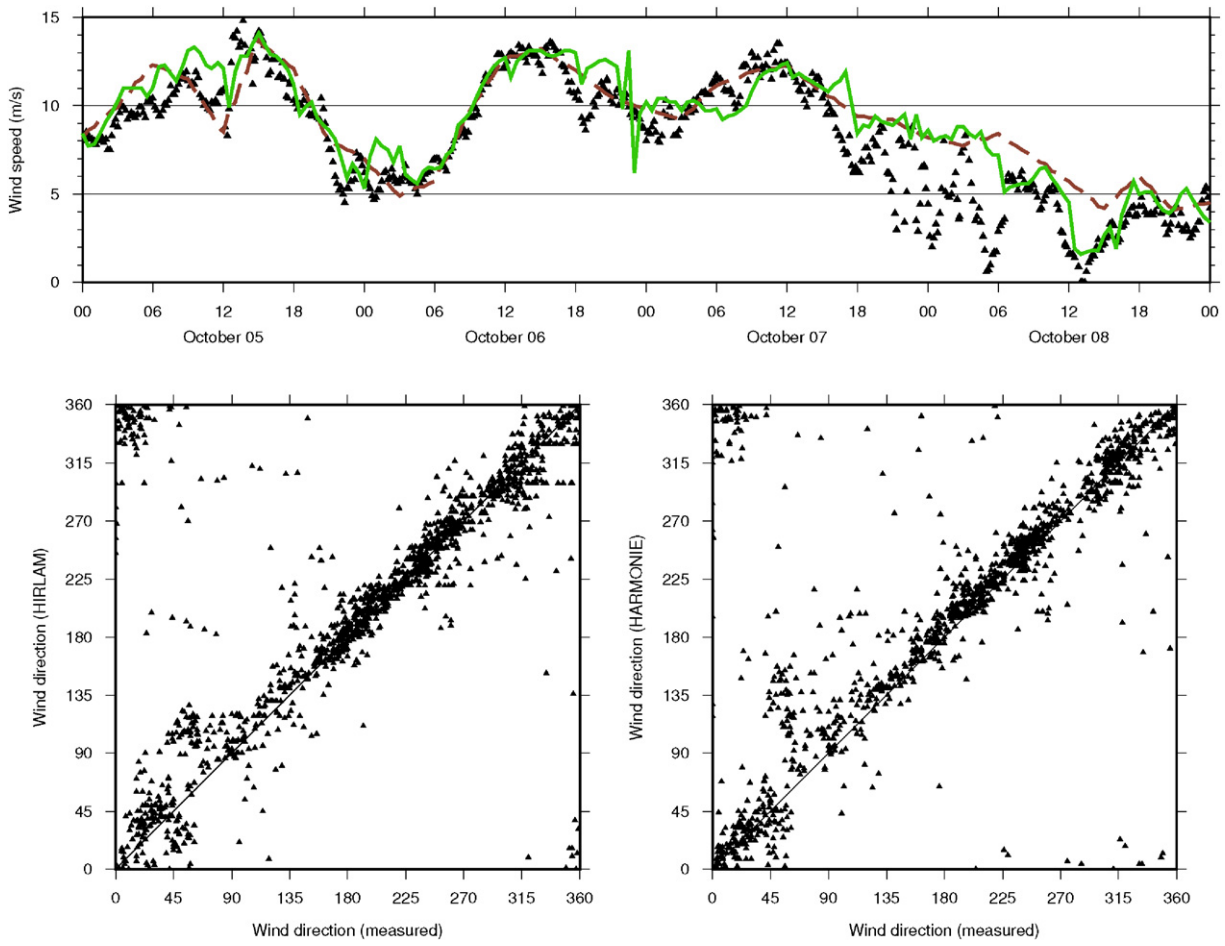

Fig. 5. A comparison of the measured and modelled wind parameters at the Harmaja weather station. On top: wind speed measured (black triangles) and modelled by HIRLAM (dashed brown) and HARMONIE (solid green). On bottom: wind direction modelled by HIRLAM (left) and HARMONIE (right) compared to measurements.

be accounted for by modelling them separately, the distribution of energy is sufficiently accurate for practical applications when quantifying e.g. the wave-bottom interactions.

4.3. Effective wind forcing

Our second approach to obtain more accurate wave data under semi-sheltered conditions involved altering the forcing of the wave model. We have established that the overprediction of the wave energy by WAM was not caused by a too strong wind forcing. Nevertheless, one method to get better results could be to quantify an "effective wind forcing", scaled to reproduce the observed behaviour of the wave field.

The observed dimensionless spectra for the fetch-limited case of 06 October 06:00–16:30 UTC followed a wind speed dependent ω^{-4} power law. The mean value of the dimensionless observed spectra was calculated for this interval, and we note that the value $3.3 \cdot 10^{-3}$ (Fig. 6) is well in line with the value proposed by Kahma (1986). After repeating the same calculations for the modelled spectra, we determined the respective value to be roughly 1.3 times higher. Since the dimensionless spectra are scaled with the wind speed, this means that the energy of the wave field in the WAM results was what would be expected of wind speeds 1.3 times stronger than the ones actually used to force the model.

On the basis of these findings, we ran WAM forced with HIRLAM-winds attenuated by a factor of 1.3. Because there was no need to attenuate winds from directions other than the south-west, we only applied the correction for wind directions between 210° and 270°. The significant wave height was modelled with a clearly better accuracy at Harmaja when using this effective wind forcing (Fig. 3, Table 1). However, even with the attenuated wind speeds, the modelled significant wave height never reached a constant value in line with the fetch-limited observations from 06 October. This further reinforces our finding that the surplus wave energy in WAM is not solely a result of inaccuracies in the wind forcing. The modelled wave spectra match well with the observed ones during all four periods with south-westerly winds (Fig. 4), indicating that the effective wind forcing is useful even in more complex turning wind conditions, such as on 16 October.

Areas further away from the shore were also affected by the attenuation of the wind speed. For example the significant wave height at the Helsinki wave buoy was underestimated with the effective wind forcing for cases with south-westerly winds (bias −0.12 ms^{-1} and RMSE 0.23 m s^{-1}, compared to 0.07 m s^{-1} and 0.24 m s^{-1} using the original HIRLAM winds). For this reason the approach should not be used for exposed open-sea areas.

5. Discussion

When simulating the wave field near shore in a semi-sheltered area, we found that the WAM model performed variably depending on the wind direction. The results were generally good for directions from the open sea, but the wave energy was overestimated for

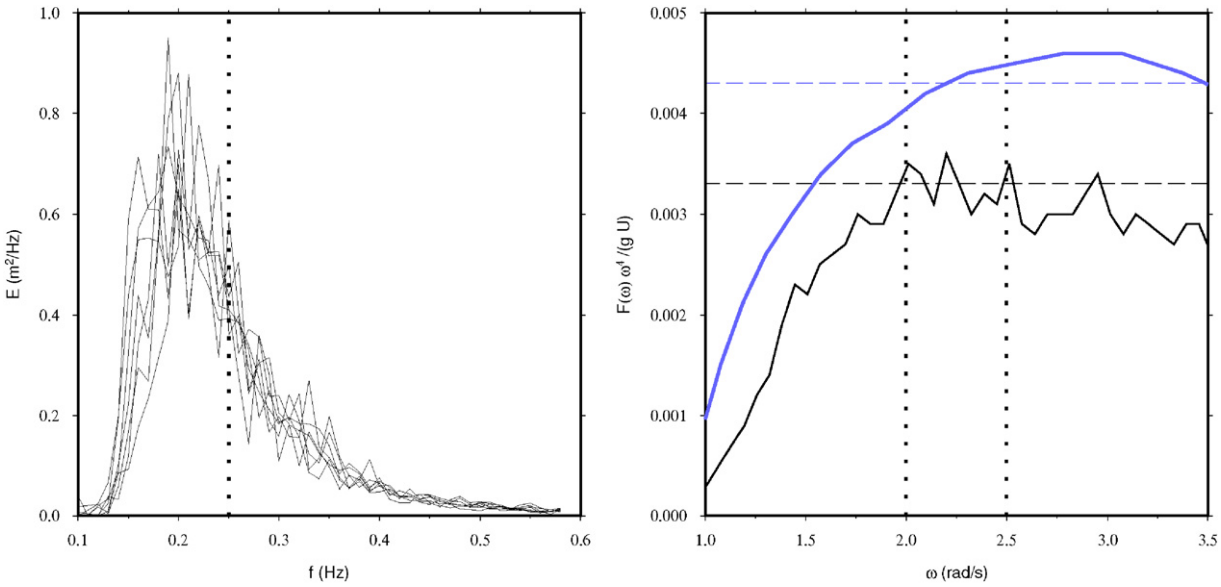

Fig. 6. On the left: the measured wave spectra during steady wind on 06 October 12:00–15:00 UTC. The vertical dotted line marks the approximate peak of the fetch limited wave system. On the right: the measured (black) and modelled (thick blue) dimensionless wave spectra averaged over 06 October 06:00–16:30 UTC. The mean value of the averaged spectra in the frequency interval where the averaged observed spectra follow the ω^{-4} power law (vertical dotted) is shown by the dashed lines.

south-westerly winds blowing over the peninsula of Porkkala. The sheltering effect of islands on swell in archipelagos has mostly been solved by Tuomi et al. (2014), but that same method is not applicable here. The wave field generated by the south-westerly winds in this study was shaped by the sheltering effect of a peninsula and had a few reoccurring characteristic features. It consisted of two separate wave systems that were close in frequency (e.g. 0.15 and 0.25 Hz), close in direction (about 20° apart) and both were under the direct influence of the wind (e.g. U/c_p 1.2 and 1.3, respectively). The wave systems are distinguishable in the observations and the good results

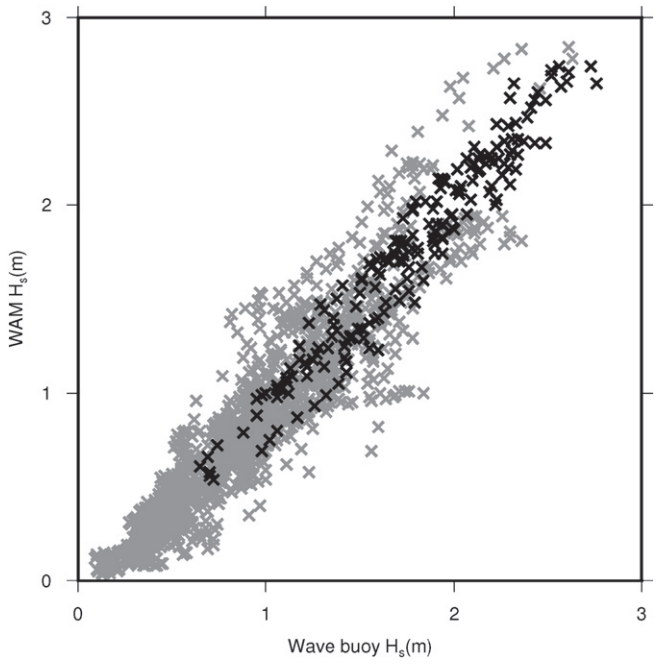

Fig. 7. A scatter plot comparing the significant wave height measured by the open-sea Helsinki wave buoy to the values modelled by WAM. The days 06–07, 16 and 24 October are highlighted by black crosses.

when modelling them separately in Section 4.2 indicate that their interaction is somewhat limited. The wave model, however, was unable to model them as two separate systems, thereby transferring an excessive amount of energy especially to the lower frequencies below 0.20 Hz.

Of the source terms used in the WAM model, the one responsible for the non-linear energy transfer between waves of different frequency and length is the only one that is explicitly known. The exact solution for the interactions (Hasselmann, 1962; van Vledder, 2006) is nevertheless too computationally demanding to be used routinely in wave models, and the discrete interaction (DIA) proposed by Hasselmann et al. (1985) is a widely implemented approximation. The weakly non-linear wave–wave interactions transfer energy both to longer waves (responsible for wave growth) and to shorter waves (where the energy is dissipated through wave breaking). While DIA can capture both of these phenomena, it has been shown to transfer too much energy to lower frequencies in less peaked spectra (van Vledder, 1999), similar to the one observed in this study.

The source term transferring energy from the wind field to the waves has several different parametrisations (Janssen, 1991; Snyder et al., 1981; Tolman and Chalikov, 1996). The parametrisations differ both in terms of the directional spread and the amount of energy input, and none of them has been tested in detail under the complex conditions studied here. The energy input, non-linear energy transfer and energy dissipation through white-capping form an interlinked balance that is not yet fully understood. As a result, wave model predictions are often a sum of the errors in the source terms that cancel each other out to produce a sufficiently accurate outcome (e.g. Ardhuin et al., 2007). We surmise that the spurious model behaviour is caused by either the wind input or shortcomings in the DIA. One possible reason for this behaviour might be that the narrow $\cos^2\theta$ distribution of the wind forcing by Janssen (1991) feeds an excessive amount of energy to the longer waves travelling at a small angle relative to the wind direction, but further research into the deep water source term balance is required to resolve this issue.

Inaccuracies in the forcing wind field can mostly be excluded as a factor for the wave model error, since both NWP systems agreed well with the wind measurements at Harmaja. Moreover, under fetch-limited conditions a simple overestimation of the wind speed by a

certain factor should only lead to an overestimation of the significant wave height by that same factor. Nevertheless, WAM – in direct contrast to the observed fetch-limited measurements – continued the wave growth during a constant wind speed, even when using the effective wind forcing (Fig. 3). This further reinforces that the observed model bias in the significant wave height was not caused by overly strong forcing wind speeds.

The modelling of both the wind speed and the atmospheric boundary layer in archipelagos has not been addressed in a completely satisfactory manner (Keevallik et al., 2010; Tisler et al., 2007; Tuomi et al., 2014). However, the good results using the wave growth relations suggest that the relevant wind conditions can be described reasonably well by the observations made near our study site. While not crucial for the problem at hand, the accurate modelling of the boundary layer might still affect the wave model results closer to the archipelago, as the islands are presently not properly accounted for in the land–sea mask of the NWP systems (Fig. 1).

There is no single solution for how to obtain accurate information about the wave conditions in a semi-sheltered location similar to those in this study. The “effective wind forcing” might be suitable for operational forecasts and for hindcasts in areas where the wave model is expected to perform poorly. We do not recommend using this particular approach in open sea areas far from the calibration point in order avoid possibly underpredicting the wave energy. Unlike the results from the pure wave growth relations, the augmented method presented in this paper produced a reasonable prediction of also the wave spectrum, making it suitable for studying the waves’ impact on, e.g. bottom sediments in some locations of interest. Both of the presented methods require some a priori knowledge about the wave field. While they cannot be used independently, they are useful for expanding on information gathered from short measurement campaigns.

6. Conclusions

In this study, we reviewed the performance of the wave model WAM in simulating the wave field at a location partially sheltered by a peninsula. While the wave model results were generally accurate when compared to a month of wave buoy measurements, the wave energy was systematically overestimated for wind directions falling over the peninsula. For these wind directions, the observed wave field can be described as one fetch-limited wave system and one wave system consisting of longer waves propagating around the peninsula. The observed structure of the semi-sheltered wave field was caused by a certain balance between these two wave systems, which WAM cannot sufficiently reproduce. However, the exact problem in the model physics responsible for the less than ideal WAM results is still not clear. We presented two approaches to obtain a more accurate description of the wave field under these semi-sheltered conditions, and we will now conclude our findings.

- The spurious model results cannot be explained by inaccuracies in the wind forcing, boundary wave field, available bathymetric data or the model source terms related to the bottom processes.
- Wave growth relations combined with an estimate of the longer waves propagating around the peninsula can predict the significant wave height well, and a combination of two JONSWAP spectra gave a sufficiently accurate description of the wave spectra for practical purposes.
- A so-called effective wind forcing, obtained by scaling the observed and modelled dimensionless wave spectra, predicted both the significant wave height and the wave spectra well.
- Both methods can be used at locations where some a priori information about wave conditions is available.
- The effective wind forcing can also be applied to operational forecasting or hindcasts, but it should not be used in exposed areas to avoid possibly underestimating the significant wave height.
- The current WAM model cannot be used “blindly” to provide wave data near complex coasts of the Gulf of Finland, even when the forcing factors are deemed reliable.

While the methods presented here can provide better approximations of the wave field in semi-sheltered conditions, the wave model’s behaviour should be addressed by further research into the deep water source term balance of the model. The energy input from the wind, and especially its directional distribution, should be examined in situations where multiple wind sea systems are present. This should ideally be done using the exact solution to the weakly non-linear wave–wave interactions.

Acknowledgements

We are grateful to Gerbrant van Vledder for his input during our discussions and acknowledge the efforts of Mr. Hannu Jokinen in processing the wave buoy data. We would also like to thank the anonymous reviewers for their constructive comments. This work was partially funded by Arvid och Greta Olins fond (Svenska kulturfonden, 15/0334-1505).

References

Alari, V., Kõuts, T., 2012. Simulating wave–surge interaction in a non-tidal bay during cyclone Gudrun in January 2005. Ocean: Past, Present and Future – 2012 IEEE/OES Baltic International Symposium, BALTIC 2012, Art. No. 6249185.

Amante, C., Eakins, B.W., 2009. Etopo1 1 arc-minute global relief model: procedures, data sources and analysis. NOAA Technical Memorandum NESDIS NGDC-24 March, 19.

Ardhuin, F., Herbers, T.H.C., van Vledder, G., Watts, K.P., Jensen, R., Graber, H.C., 2007. Swell and slanting-fetch effects on wind wave growth. J. Phys. Oceanogr. 37, 908–931.

Baltic Sea Hydrographic Commission, 2013. Baltic sea bathymetry database version 0.9.3. URL http://data.bshc.pro/.

Battjes, J.A., Janssen, J.P.F.M., 1978. Energy loss and set-up due to breaking of random waves. In: Proceedings of the 16th International Conference on Coastal Engineering. American Society of Civil Engineers, New York 569–587.

Bertotti, L., Cavaleri, L., Soret, A., Tolsana-Delgado, R., 2014. Performance of global and regional nested meteorological models. Cont. Shelf Res. 87, 17–27.

Björkqvist, J.-V., Pettersson, H., Laakso, L., Kahma, K.K., Jokinen, H., Kosloff, P., 2016. Removing low-frequency artefacts from Datawell DWR-G4 wave buoy measurements. Geosci. Instrum. Method. Data Syst. 5, 1–9.

Björkqvist, J.-V., Tuomi, L., Pettersson, H., Fortelius, C., Tikka, K., Kahma, K.K., 2014. The effect of boundary field accuracy on high-resolution coastal wave modelling. Proceedings of 6th IEEE/OES Baltic Symposium, 26–29 May 2014, Tallinn.

Bottema, M., van Vledder, G., 2008. Effective fetch and non-linear four-wave interactions during wave growth in slanting fetch conditions. Coast. Eng. 55, 261–275.

Cavaleri, L., Bertotti, L., 2004. Accuracy of the modelled wind and wave fields in enclosed seas. Tellus 56A, 167–175.

Ekebom, J., Laihonen, P., Suominen, T., 2003. A GIS-based step-wise procedure for assessing physical exposure in fragmented archipelagos. Estuar. Coast. Shelf S. 57, 887–898.

Erm, A., Alari, V., Kask, J., 2011. Resuspension of sediment in a semi-sheltered bay due to wind waves and fast ferry wakes. Boreal Environ. Res. 16, 149–163.

Kallos, Galanis, G., Chu, P.C., Kuo, Y.H., 2010. Evaluation of the new ECMWF WAM model. SeaSAR 2010, Proceedings of the Third International Workshop held 25–29 January, 2010 at ESRIN, Frascati, Italy.

Hasselmann, K., 1962. On the non-linear energy transfer in a gravity-wave spectrum: part 1. General theory. J. Fluid Mech. 12, 481–500.

Hasselmann, K., Barnett, T.P., Bouws, E., Carlson, H., Cartwright, D.E., Enke, K., Ewing, J.A., Gienapp, H., Hasselmann, D.E., Kruseman, P., Meerburg, A., Müller, P., Olbers, D.J., Richte, K., Sell, W., Walden, H., 1973. Measurements of wind-wave growth and swell decay during the joint north sea wave project (JONSWAP). Ergnzungsheft zur Deutschen Hydrographischen Zeitschrift Reihe A(8) 12,

Hasselmann, S., Hasselman, K., Allender, J., Barnett, T., 1985. Computation and parameterizations of the nonlinear energy transfer in a gravity-wave spectrum. Part ii: parameterizations of the nonlinear energy transfer for application in wave models. J. Phys. Oceanogr. 15, 1378–1391.

HIRLAM-B, 2012. System documentation. URL http://hirlam.org.
Isaeus, M., 2004. Factors Structuring Fucus Communities at Open and Complex Coastlines in the Baltic Sea. Stockholm University, Faculty of Science, Department of Botany. (Ph.D. thesis)
Janssen, P.A.E.M., 1991. Quasi-linear theory of wind-wave generation applied to wave forecasting. J. Phys. Oceanogr. 21, 1631–1642.
Kahma, K.K., 1981. A study of the growth of the wave spectrum with fetch. J. Phys. Oceanogr. 11, 1504–1515.
Kahma, K.K., 1986. On prediction of the fetch-limited wave spectrum in a steady wind. Finn. Mar. Res. 253, 53–78.
Kahma, K.K., Björkqvist, J.-V., Johansson, M., Jokinen, H., Leijala, U., Särkkä, J., Tikka, K., Tuomi, L., 2016. Turvalliset rakentamiskorkeudet Helsingin rannoilla 2020, 2050 ja 2100. English: Safe Building Elevations on the Shores of Helsinki 2020, 2050 and 2100. Geoteknisen osaston julkaisut., online. 14.2.2016. URL http://www.hel.fi/static/kv/turvalliset-rakentamiskorkeudet.pdf.
Kahma, K.K., Calkoen, C.J., 1992. Reconciling discrepancies in the observed growth of wind-generated waves. J. Phys. Oceanogr. 22, 1389–1405.
Kahma, K.K., Pellikka, H., Leinonen, K., Leijala, U., Johansson, M., 2014. Pitkän aikavälin tulvariskit ja alimmat suositeltavat rakentamiskorkeudet Suomen rannikolla. English: Long-term Flooding Risks and Recommendations for Minimum Building Elevations on the Finnish Coast. Reports 2014:6. Finnish Meteorological Institute, online. 7.3.2016. URL https://helda.helsinki.fi/handle/10138/135226.
Kahma, K.K., Pettersson, H., 1994. Wave growth in narrow fetch geometry. Global Atmos. Ocean Syst. 2, 253–263.
Kaitaranta, J., Niemistö, J., Buhvestova, O., Nurminen, L., 2013. Quantifying sediment resuspension and internal phosphorus loading in shallow near-shore areas in the Gulf of Finland. Boreal Environ. Res. 18, 473–487.
Keevallik, S., Männik, A., Hinnov, J., 2010. Comparison of HIRLAM wind data with measurements at Estonian coastal meteorological stations. Est. J. Earth Sci. 59, 90–99. http://dx.doi.org/10.3176/earth.2010.1.07.
Komen, G.J., Cavaleri, L., Donelan, M., Hasselmann, K., Hasselmaan, S., Janssen, P.A.E.M., 1994. Dynamics and Modelling of Ocean Waves. Cambridge University Press, Cambridge.
Monbaliu, J., Padilla-Hernández, R., Hagreaves, J.C., Albiach, J.C.C., Luo, W., Sclavo, M., Günter, H., 2000. The spectral wave model, WAM, adapted for applications with high spatial resolution. Coast. Eng. 41, 41–62.
Nielsen, P., 1992. Coastal Bottom Boundary Layer and Sediment Transport, Advanced Series on Ocean Engineering — volume 4. World Scientific Publishing, Singapore.
Pettersson, H., 2004. Wave growth in a narrow bay. Finn. Inst. Marine Res. Contrib. 9,
Rinne, H., Kaskela, A., Downie, A., Tolvanen, H., von Numers, M., Mattila, J., 2014. Predicting the occurrence of rocky reefs in a heterogeneous archipelago area with limited data. Estuar. Coast. Shelf Sci. 138, 90–100. URL http://www.sciencedirect.com/science/article/pii/S0272771413005490. http://dx.doi.org/10.1016/j.ecss.2013.12.025.
Seifert, F., Tauber, B., Kayser, B., 2001. A high resolution spherical grid topography of the Baltic sea. 2nd edition. Baltic Sea Science Congress Stockholm 25-29. November Poster 147. pp. 19. http://www.io-warnemuende.de/iowtopo.
Seity, Y., Brousseau, P., Malardel, S., Hello, G., Bénard, P., Bouttier, F., Lac, C., Masson, V., 2011. The AROME-France convective-scale operational model. Mon. Weather Rev. 139, 976–991.
Snyder, R.L., Dobson, F.W., Elliot, J.A., Long, R.B., 1981. Array measurements of atmospheric pressure fluctuations above surface gravity waves. J. Fluid. Mech. 102, 1–59.
Soomere, T., 2005. Wind wave statistics in Tallinn Bay. Boreal Environ. Res. 10, 103–118.
Soomere, T., Pindsoo, K., Bishop, S.R., Käärd, A., Valdmann, A., 2013a. Mapping wave set-up near a complex geometric urban coastline. Nat. Hazards Earth Syst. Sci. 13, 3049–3061.
Soomere, T., Viška, M., Eelsalu, M., 2013b. Spatial variations of wave loads and closure depths along the coast of the eastern Baltic Sea. Est. J. Eng. 19:2, 93–109. http://dx.doi.org/10.3176/eng.2013.2.01.
Soomere, T., Zaitseva-Pärnaste, I., Räämet, A., 2011. Variations in wave conditions in Estonian coastal waters from weekly to decadal scales. Boreal Environ. Res. 16, 175–190.
Suursaar, Ü., 2013. Locally calibrated wave hindcasts in the Estonian coastal sea in 1966–2011. Est. J. Earth Sci. 62, 42–56.
H., T., Suursaar, Ü., Alari, V., Raudsepp, U., Rästas, H., Anderson, A., 2016. Projected changes in wave conditions in the Baltic Sea by the end of 21st century and the corresponding shoreline changes. J. Coastal Res. SI75-203.1, 1012–1016.
Tisler, P., Gregow, E., Niemelä, S., Savijärvi, H., 2007. Wind field prediction in coastal zone: operational mesoscale model evaluation and simulations with increased horizontal resolution. J. Coastal Res. 233, 721–730.
Tolman, H.L., 2003. Treatment of unresolved islands and ice in wind wave models. Ocean Model. 5, 219–231.
Tolman, H.L., Chalikov, D., 1996. Source terms in a third-generation wind wave model. J. Phys. Oceanogr. 26, 2497–2518.
Tuomi, L., Kahma, K.K., Pettersson, H., 2011. Wave hindcast statistics in the seasonally ice-covered Baltic Sea. Boreal Environ. Res. 16(6), 451–472.
Tuomi, L., Pettersson, H., Fortelius, C., Tikka, K., Björkqvist, J.-V., Kahma, K.K., 2014. Wave modelling in archipelagos. Coast. Eng. 83, 205–220.
van Vledder, G., 1999. Source term investigation SWAN. Technical Report A162. Alkyon Hydraulic Consultancy & Research.
van Vledder, G., 2006. The WRT method for the computation of non-linear four-wave interactions in discrete spectral wave models. Coast. Eng. 53, 223–242.
WAMDIG, 1988. The WAM model—a third generation ocean wave prediction model. J. Phys. Oceanogr. 18, 1775–1810.

II

Reprinted, with kind permission, from
Journal of Operational Oceanography
doi:10.1080/1755876X.2019.1633236

JOURNAL OF OPERATIONAL OCEANOGRAPHY
https://doi.org/10.1080/1755876X.2019.1633236

WAM, SWAN and WAVEWATCH III in the Finnish archipelago – the effect of spectral performance on bulk wave parameters

J.-V. Björkqvist [a], O. Vähä-Piikkiö [a], V. Alari [b], A. Kuznetsova [c] and L. Tuomi [a]

[a]Finnish Meteorological Institute, Helsinki, Finland; [b]Department of Marine Systems, Tallinn University of Technology, Tallinn, Estonia; [c]Institute of Applied Physics of the Russian Academy of Sciences, Nizhny Novgorod, Russia

ABSTRACT

WAM, SWAN and WAVEWATCH III® were implemented to the Finnish archipelago with a 0.1 nmi grid. A comparison with coastal wave buoy observations showed that the models agreed on the significant wave height, with biases and root-mean-square-errors (RMSE) differing at most 0.06 m. In a general sense, WAM propagated most long wave energy into the archipelago, while SWAN generated the highest local waves. The performance of WAVEWATCH III was wind direction dependent. The model tendencies caused them to disagree on the peak period near the coast, with differences in mean values being up to 1.4 s. The large scatter (RMSE>2 s) inside the archipelago was mostly explained by the ill-defined nature of the parameter in more complex wave conditions. The mean period had less scatter (RMSE<1.5 s), but changes in the upper integration frequency from 0.6 Hz to 1 Hz affected the bias by roughly 1 s in all models. WAM and WAVEWATCH III underestimated the high-frequency wave energy for certain wind directions, possibly because of a too small friction velocity. A wind forcing taken every 3 h from a 7.4 km operational atmospheric model was found to be sufficient to force the high-resolution wave models.

ARTICLE HISTORY
Received 29 December 2017
Accepted 12 June 2019

KEYWORDS
Wave period; wave model; buoy measurements; coastal; validation

1. Introduction

Forecasting waves in coastal areas is a challenging and topical issue. The first numerical forecasts had coarse spatial resolutions and were mainly suitable for simulating open sea conditions (Komen et al. 1994). The present operational systems and computing facilities have allowed us to increase the spatial resolution of the wave forecast systems, thus rendering reasonably accurate wave predictions in increasingly complex coastal areas.

Currently, three state-of-the art numerical wave models are widely used. They are WAM (WAveModel, Komen et al. 1994), SWAN (Simulating WAves Nearshore, Booij et al. 1999) and WW3 (WAVEWATCH III®, Tolman et al. 2002). The principal similarity of these models is the use of the action balance equation with sources and sinks, but they differ in terms of numerical implementation and the parameterisation of the physical processes. WAM is built around one set of source terms, while SWAN and WW3 has a wide range of different source terms and parameterisations available to the user. WAM and WW3 were originally developed as large scale models, while SWAN was specifically built to simulate waves nearshore. Nevertheless, new source terms and parameterisations to resolve nearshore processes – along with more advanced numerics – have later been added to both WAM and WW3. Today, all three models are capable of simulating waves in coastal areas. Extensive reviews of the current state of wave modelling can be found in the papers of Cavaleri et al. (2007) and Cavaleri et al. (2018), where the latter is concentrated on coastal and inner seas.

The European Centre for Medium-Range Weather Forecasts (ECMWF) provides global wave forecast produced with WAM (Bidlot et al. 2007; Haidem et al. 2018). WW3 have been implemented globally by the National Oceanic and Atmospheric Administration (NOAA) (Chawla et al. 2013). SWAN, again, has been widely implemented to coastal areas. In the Nearshore Wave Prediction System (NWPS) of the National Centers for Environmental Prediction (NCEP), the coastal SWAN forecasts receive their boundary conditions from larger scale WW3 simulations (van der Westhuysen et al. 2013, 2014). For the Portuguese coast Guedes Soares et al. (2011) implemented a coastal forecast system where SWAN is nested in the WAM model. Perrie et al. (2017) have also implemented other wave models in a comparative study between three models in the Northwest Atlantic, where they concluded that the parameterisations of the physics explained more of the

CONTACT J.-V. Björkqvist jan-victor.bjorkqvist@fmi.fi Finnish Meteorological Institute, P.O. Box 503, FI-00101 Helsinki, Finland

differences between the models compared to the numerical implementation.

All three models have also been implemented to semi-enclosed basins. Mentaschi et al. (2015) evaluated the performance of WW3 in the Mediterranean Sea, WAM has been validated both in the Baltic Sea (e.g. Tuomi et al. 2011) and in the Mediterranean (e.g. Cavaleri and Bertotti 2004), while SWAN has been used both in the Baltic Sea (Björkqvist et al. 2018) and in the Black Sea (Akpınar et al. 2012). Regional models covering only parts of a larger basin, including coastal applications, have also been established (Bertotti and Cavaleri 2009; Pallares et al. 2014). The local studies have been used both to map wave energy resources (Akpınar et al. 2012; Ayat 2013; Lavidas and Venugopal 2017) and to evaluate suitable implementations for operational products (Dykes et al. 2009; Atan et al. 2017; Pallares et al. 2017). Presently, operational forecasts for complex areas with numerous islands are given to e.g. the Aegan Sea by the University of Athens using the WAM model with a 6 km resolution.

The Baltic Sea is a semi-enclosed basin with a complex coastal geometry (Figure 1). The Copernicus Baltic Monitoring and Forecasting Centre (BAL MFC) is providing wave forecasts for the Baltic Sea with a 1 nmi (1.85 km) horizontal resolution (Tuomi et al. 2018). This forecast is produced by FMI, but several countries around the Baltic Sea also provide national forecasts. The Finnish Meteorological Institute (FMI), the Danish Meteorological Institute (DMI) and the German Weather Service (DWD, Behrens and Günther 2009) use the WAM model, while the Swedish Meteorological and Hydrological Institute (SMHI) uses SWAN. The resolution used in the basin scale models is typically 1–3 nmi, which is sufficient to represent the wave conditions in open sea areas. A higher resolution is nevertheless needed in order to satisfactory resolve complex nearshore areas.

The smallest islands and islets in the Finnish archipelago are of the order of tens of metres, but their sheer collective magnitude still have a determining role in shaping the wave field near the coast. These islands can be properly accounted for only with a high-resolution regular grid or an unstructured grid, possibly complemented with sub-grid parameterisations. One method to increase the accuracy of the modelled wave field in archipelago areas is to use obstructions grids to account for islands that are unresolved by the land sea mask. These kind of obstruction grids were first implemented in WAM by Hardy et al. (2001) to account for the wave attenuation of shallow coral reefs (Hardy and Young 1996). Tolman (2003) used sub-grid obstructions to account for unresolved islands and ice on an oceanic scale, and today they can be used with all of the three aforementioned models (WAM, SWAN and WW3); WW3 even includes a package for their automatic generation (Chawla and Tolman 2008). In the Baltic Sea (Tuomi et al. 2014) found them to be highly useful on a smaller scale in the Finnish Archipelago Sea.

A decisive step was taken when a high-resolution (0.5 nmi) wave forecast covering the highly complex Archipelago Sea was launched by FMI in 2014 (Tuomi and Björkqvist 2014). A similar system was applied to the Helsinki coastal area in April 2017. Although these systems provide better forecasts for the complex coastal areas, they still have issues regarding the overestimation of the significant wave height in some locations and for certain wind conditions. These challenges need to be solved before the results for the nearshore areas can reach the same accuracy as has been shown for the open sea. Previous studies in the Helsinki archipelago have found that the discrepancies between the modelled and measured wave parameters cannot be explained simply by external forcing factors (Björkqvist et al. 2017a). Thus, additional research into the performance of the models is warranted.

High-quality data sets are needed to study the performance of wave models and their parameterisations. Special challenges are imposed by the heterogeneous wave conditions of coastal archipelagos, which ideally require data from numerous sites to properly validate the model. In the Helsinki coastal area a data set have been collected during the years 2012–2016, which consists of wave buoy measurements at numerous locations within the Helsinki archipelago (see Figure 1). Most of the data were collected within a commissioned project by the City of Helsinki (Kahma et al. 2016), but the data set also includes measurements from two location made for research purposes, along with observations from two operational wave buoys.

In this paper, we use wave buoy measurements from nine locations to study the performance and differences between WAM, SWAN and WW3 in the highly complex Helsinki coastal archipelago in the Gulf of Finland (GoF), Baltic Sea. All wave models are implemented with an identical 0.1 nmi (185 m) grid and forced with two different wind forcings. Special attention is given to the comparison against the longest observations from an operational wave buoy moored in the middle of the archipelago. The challenges associated with defining a robust and representative measure of the wave period for complex archipelago wave fields is also raised. We end this paper by discussing our findings, and giving recommendations for model implementations and future research.

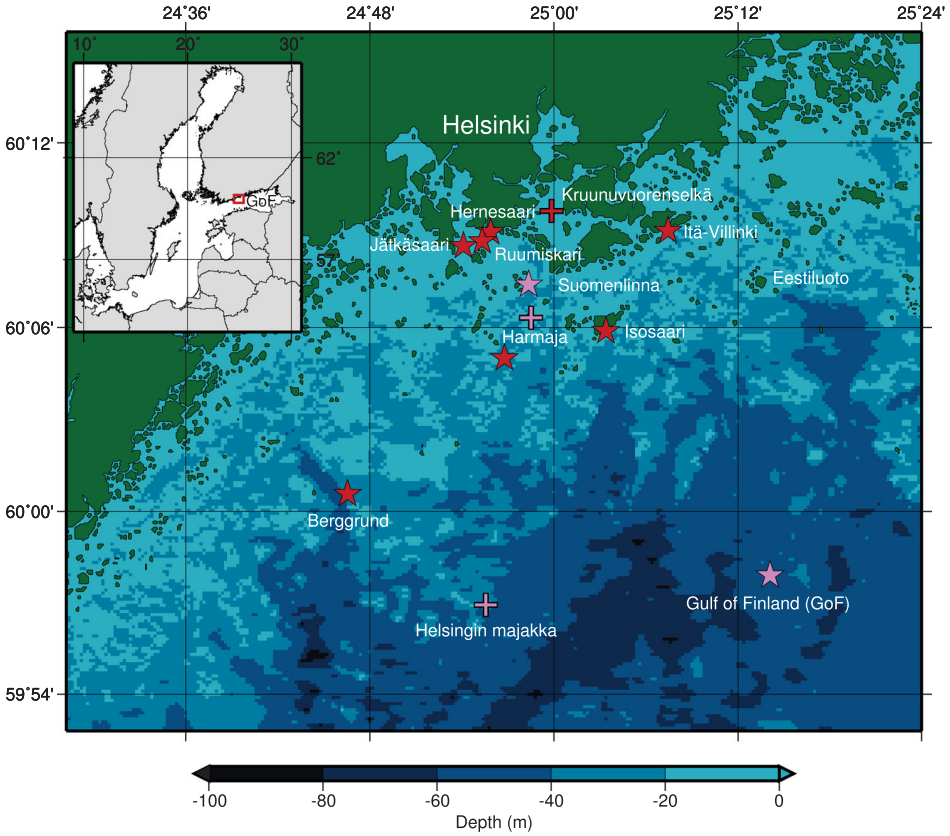

Figure 1. The study area and the measurement sites. Wave buoys are marked with stars and wind stations with a plus (+). Operational and research stations are shown in magenta and red respectively. The eastern island of Eestiluoto is also shown on the map.

2. Wave model set-up and atmospheric forcing

2.1. Wave model description

In this paper three models are used: WAM (WAMDIG 1988; Komen et al. 1994; Monbaliu et al. 2000), SWAN (Booij et al. 1999) and WAVEWATCH III (WW3, Tolman et al. 2002; WW3DG 2016). All are third-generation spectral wave models, which impose no a priori restrictions on the shape of the wave spectrum. They simulate the wave field energy by solving the action balance equation:

$$\frac{\partial N}{\partial t}+\frac{\partial c_x N}{\partial x}+\frac{\partial c_y N}{\partial y}+\frac{\partial c_\sigma N}{\partial \sigma}+\frac{\partial c_\theta N}{\partial \theta}=\frac{S_{\mathrm{tot}}}{\sigma}, \qquad (1)$$

where $N(x, y, \sigma, \theta)$ is the wave action density, c is the propagation velocity of the wave energy, x,y are the cartesian coordinates, σ is the intrinsic frequency and θ is the propagation direction. The left side of the equation describes the propagation of energy in spatial and spectral space, while S_{tot} is the total sum of the sources and sinks of different physical processes that have been parameterised in the model.

The difference between the models are in the parameterisations of the physical processes and the numerical solutions of the action density equations. For regular grids, WAM and WW3 use explicit propagation schemes subject to the CFL-criteria, while SWAN uses an iterative approximation to a fully implicit scheme. An overview of the chosen physics parameterisations and settings can be found in Table 1. The different spectral bins of the models introduce a slight uncertainty in the spectral comparison, but it is expected to not affect the conclusions of this paper.

The models were implemented to the Helsinki coastal archipelago using a high-resolution 0.1 nmi (185 m) structured bathymetrical grid. The grid is mainly based on information from nautical charts (Björkqvist et al. 2014, 2017a) and covers the area 24° 28'–25° 24' E, 59° 52'–60° 16' N. Unstructured grids are not available in WAM, and even though they are available in SWAN (Zijlema 2010) and WW3 (e.g. Roland and Ardhuin 2014), using fundamentally different descriptions of the archipelago would not have allowed for a fair comparison between the models. All three models were therefore implemented with an identical structured grid. The land-sea mask of the bathymetrical grid is fine enough to

Table 1. Settings and physical parameterisations used in the wave models.

	WAM	SWAN	WW3
Model version	Cycle 4.5.4	41.10AB	v5.16
Advection time step	2 s	10 min, 5 iterations	5 s
Intra-spectral time step[a]	N/A	N/A	2 s
Source term integration time step	10 min	10 min	10 min
Global times step[a]	N/A	N/A	30 s
Propagation scheme	First order upwind	Fully implicit four sweep	Third order upwind
Wind input	Janssen (1991)	Komen et al. (1984), Wu (1982)	Ardhuin et al. (2010)
Dissipation	Komen et al. (1994), $\delta = 0.6$	Komen et al. (1994)[b], $\delta = 1$	Ardhuin et al. (2010)
Bottom friction	Hasselmann et al. (1973)	Hasselmann et al. (1973)	SHOWEX (Ardhuin et al. 2003)
Wave breaking	Battjes and Janssen (1978)	Battjes and Janssen (1978)	Battjes and Janssen (1978)
Non-linear four wave interactions	DIA (Hasselmann et al. 1985)	DIA (Hasselmann et al. 1985)	DIA (Hasselmann et al. 1985)
Non-linear triad interactions	–	LTA (Eldeberky 1996)	-
Spectrum	0.0418–1.0672 Hz	0.05–1 Hz	0.05–1.2774 Hz
Number of frequencies	35	35	35
Number of directions	36	36	36
Other	-	land set to 500 m (not described with exception values)	-

[a]This cannot be explicitly set by the user in WAM and SWAN.
[b]This is the current default setting in SWAN, although it is called Komen et al. (1984) in the SWAN Technical Manual.

capture even small islands, and it has been used to compile sub-grid obstruction for coarser model grids (Tuomi et al. 2014). Separate sub-grid obstructions were therefore not considered necessary in this study, although they are natively available in WW3, SWAN and WAM (since cycle 4.6). Obstructions grids have also been implemented in the FMI version of WAM cycle 4.5.4.

The boundary conditions for the 0.1 nmi grids were extracted from Baltic Sea wide 1 nmi (1.85 km) simulations with the same wave model and wind forcing as used for the coastal grids – i.e. each of the three wave models were nested within basin scale versions of themselves. The bathymetry used in the coarse grid models is based on Seifert et al. (2001) and the Baltic Sea Bathymetric Database (BSBD 2013).

Using the existing setups of 1 nmi and 0.1 nmi resolution implementation at FMI, WAM was run for the all the months in 2012–2016 when nearshore measurements were available. The new SWAN and WW3 implementations were run to cover measurements for the years 2012 and 2016. These two years are the most relevant considering the evaluation of the three models because of the long time series available in 2016 (Suomenlinna), and the good spatial coverage of 2012 (Harmaja, Jätkäsaari and Hernesaari). Together, these observations from 2012 and 2016 form a cross section extending through the archipelago.

2.2. Atmospheric forcing

The wave models were forced with winds from the numerical weather prediction (NWP) systems HIRLAM and HARMONIE (HIRLAM 2017). FMI-HIRLAM has a spatial resolution of 7.4 km and the wind speed at 10 metre height was provided to the wave models every hour (every 3 hours in 2016). FMI-HARMONIE was used for 2016 to evaluate the effect of an high-resolution atmospheric forcing. HARMONIE is a relatively new NWP system and has been used as forcing for FMI's operational wave forecasts since April 2017. HARMONIE has a spatial resolution of 2.5 km and data was provided every hour. The wind speeds were interpolated to a 10 minute temporal resolution within all models.

The domain for both NWP-systems covered an area larger than the entire Baltic Sea. HIRLAM has been validated near the Finnish coastline by Tisler et al. (2007), Tuomi et al. (2014) and Björkqvist et al. (2017a). The last two studies also validated the HARMONIE model.

3. Available data

3.1. Wind observations

Wind observations from the operational weather stations at Harmaja, Helsingin majakka and Kalbådagrund were used to validate the wind forcing. The measurement heights were 17.5 m, 31.3 m and 31.8 m respectively. For 2016 measurements from the research station at Kruunuvuorenselkä (height 12.5 m) were also available (Figure 1). Kalbådagrund is located slightly east of the high-resolution grid at 59° 59.11' N, 25° 35.9' E and is thus not visible in the figure. All observations were 10 minute averages.

The wind observations were adjusted following the recommended procedures of WMO (2014) to establish the potential wind speed over the sea at 10 metre height. This was done by calculating the effective roughness length and using a reference roughness length of $z_0 = 0.0007$ m. For the operational stations the effective roughness length was determined using the standard deviation for the wind speed and direction. For the

Kruunuvuorenselkä research station the effective roughness length was determined using the wind gusts (Verkaik 2000).

3.2. Wave observations

Wave measurements from 2012–2016 were used in this study. Between 2012 and 2015 short measurements were carried out, mostly within a commissioned project by the City of Helsinki (Kahma et al. 2016). A permanent wave buoy was anchored in the Helsinki archipelago in 2016, providing a continuous time series of about seven months. Data from FMI's operational wave buoy in the Gulf of Finland (GoF) were also used. The locations of the wave buoys are visible in Figure 1 and the measurement times and mooring depths are listed in Table 2.

The wave buoy measurements were made with Datawell Directional Waveriders. The operational buoys are accelerometer based, model Mk-III, buoys. The shorter measurements were conducted with GPS-based G4 buoys, which have been corrected for low-frequency artefacts following Björkqvist et al. (2016). The wave buoys had an sampling frequency of 1.28 Hz and used 26 minute time series to calculate the wave spectrum, which was then used to calculate the wave parameters.

3.3. Wave parameters and statistics

Most wave parameters are calculated using the spectral moments

$$m_n = \int f^n S(f)\,\mathrm{d}f, \tag{2}$$

where $S(f)$ is the power density spectrum. The significant wave height H_s is calculated through

$$H_s = H_{m_0} = 4\sqrt{m_0}. \tag{3}$$

The mean period is defined as

$$T_m = T_{m_{-10}} = \frac{m_{-1}}{m_0}, \tag{4}$$

while the peak period is given by

$$T_p = (\arg\max_f S(f))^{-1}. \tag{5}$$

In this paper both the modelled and measured values of the peak period were determined using a parabolic fit in order to reduce the effect of the discrete frequency bins.

The mean period, T_m, was determined from both the modelled and measured wave spectra by an integration up to 0.6 Hz, which is the upper frequency of the wave buoy.

Basic statistical parameters were used to assess the model performance. The modelled and observed values are denoted M_i and O_i, while $\overline{M}$ and $\overline{O}$ are their mean values. The bias and the root-mean-square-error (RMSE) were calculated as

$$\text{bias} = \overline{M} - \overline{O}, \tag{6}$$

$$\text{RMSE} = \sqrt{\frac{1}{N}\sum_{i=1}^{N}(M_i - O_i)^2}. \tag{7}$$

In this paper a positive bias therefore means that the model overestimates the parameter.

Table 2. Bias, RMS-error, scatter index (SI) and correlation coefficient (ρ) of the wave models calculated at the nearshore wave buoys. Locations where all three models are validated are shown in bold. Results are with the HIRLAM forcing.

	H_s (m)				T_p (s)				T_m (s)				
	Bias	RMSE	SI	ρ	Bias	RMSE	SI	ρ	Bias	RMSE	SI	ρ	Time (days)
Location (depth)								WAM					
Berggrund (27 m)	0.10	0.20	0.31	0.95	−0.11	1.67	0.36	0.36	−0.06	0.70	0.18	0.63	July 2015 (12)
Harmaja (29 m)	0.11	0.26	0.33	0.93	−0.13	1.79	0.37	0.37	−0.05	0.70	0.17	0.65	Sept.–Oct. 2012 (31)
Isosaari (7 m)	0.03	0.15	0.34	0.95	−0.47	2.42	0.51	0.18	−0.11	0.93	0.25	0.60	Aug.–Sept. 2014 (39)
Itä-Villinki (9 m)	−0.01	0.07	0.19	0.95	−0.31	2.14	0.44	0.21	0.00	0.86	0.23	0.64	Sept.–Oct. 2013 (39)
Suomenlinna (22 m)	−0.01	0.08	0.19	0.95	−0.44	2.11	0.49	0.24	0.04	0.74	0.21	0.57	Apr.–Nov. 2016 (216)
Ruumiskari (12 m)	−0.01	0.05	0.18	0.95	0.38	2.11	0.50	0.44	0.84	1.35	0.31	0.69	Nov.–Dec. 2014 (29)
Hernesaari (13 m)	0.03	0.07	0.26	0.93	1.03	2.03	0.44	0.30	0.70	1.16	0.27	0.63	Aug.–Oct. 2012 (32)
Jätkasaari (13 m)	0.05	0.07	0.20	0.96	0.17	3.78	0.92	0.08	0.74	1.26	0.31	0.65	Oct.–Nov. 2012 (31)
								SWAN					
Harmaja (29 m)	0.16	0.27	0.32	0.93	−0.15	1.67	0.35	0.38	−0.12	0.75	0.18	0.56	Sept.–Oct. 2012 (31)
Suomenlinna (22 m)	0.02	0.09	0.22	0.94	0.77	2.09	0.46	0.16	−0.32	0.79	0.21	0.47	Apr.–Nov. 2016 (216)
Hernesaari (13 m)	0.07	0.10	0.30	0.93	−0.35	2.09	0.52	0.09	0.24	1.04	0.30	0.64	Aug.–Oct. 2012 (32)
Jätkäsaari (13 m)	0.09	0.13	0.40	0.96	−0.49	2.35	0.56	0.14	0.21	1.01	0.29	0.59	Oct.–Nov. 2012 (31)
								WW3					
Harmaja (29 m)	0.11	0.25	0.32	0.92	−0.05	1.76	0.37	0.36	0.09	0.69	0.17	0.61	Sept.–Oct. 2012 (31)
Suomenlinna (22 m)	−0.01	0.08	0.20	0.95	−0.53	2.15	0.50	0.16	−0.09	0.80	0.23	0.45	Apr.–Nov. 2016 (216)
Hernesaari (13 m)	0.01	0.08	0.33	0.93	0.89	2.06	0.47	0.33	0.62	1.16	0.28	0.67	Aug.–Oct. 2012 (32)
Jätkasaari (13 m)	0.03	0.07	0.30	0.96	0.15	2.59	0.63	0.15	0.82	1.41	0.34	0.54	Oct.–Nov. 2012 (31)

We also calculated normalised statistical parameters. The scatter index (SI) is defined as

$$\mathrm{SI} = \sqrt{\frac{\sum_{i=1}^{N}\left[\left(M_i - \overline{M}\right) - \left(O_i - \overline{O}\right)\right]^2}{\sum_{i=1}^{N} O_i^2}}, \tag{8}$$

and the correlation coefficient as

$$\rho = \frac{1}{N}\frac{\sum_{i=1}^{N}\left(M_i - \overline{M}\right)\left(O_i - \overline{O}\right)}{\sigma(M)\sigma(O)}, \tag{9}$$

where $\sigma(M)$ and $\sigma(O)$ are the standard deviations of the modelled and observed values.

4. Wave model validation

4.1. A spatial overview

The 1 nmi boundary wave field was compared with observations from the GoF wave buoy and the results from the 0.1 nmi nested runs. The significant wave height was modelled well at the centre of the GoF with the coarser 1 nmi implementations (Table 3). The 1 nmi results were practically identical to the 0.1 nmi resolution implementation. The difference in bias of less than 0.04 m are at the limit what the wave buoys can reasonably be expected to resolve (Campos et al. 2018). The use of the HARMONIE wind forcing resulted in a somewhat higher significant wave height compared to runs with HIRLAM (difference up to 0.06 m, Table 3). The bias for the peak period was negative even with HARMONIE, with the exception of the 0.1 nmi implementation of WAM.

The positive bias in significant wave height cannot be explained by the wind forcing, which compared well to the observations (Table 4). There was no significant difference in the bias at Kalbådagrund and Helsingin majakka between HIRLAM and HARMONIE, although HARMONIE had higher RMS-errors at all locations. Closer to the shoreline the bias of HIRLAM and HARMONIE started to differ, and at Harmaja HIRLAM performed better. HARMONIE has previously been found to produce stronger winds compared to HIRLAM despite of its higher resolution, meaning that this was an expected result in line with previous findings (Tuomi et al. 2014; Björkqvist et al. 2017a). However, in contrast to the results from Harmaja, the previously unavailable observations from Kruunuvuorenselkä revealed that HARMONIE had a clearly smaller bias than HIRLAM at this station located deep in the inner archipelago.

The performance of the wave models closer to the shore varied by geographical location, as shown in Table 2. Björkqvist et al. (2017a) found WAM to overestimate the wave height significantly at Harmaja with both HIRLAM and HARMONIE wind forcings for south-westerly winds. The same behaviour was reproduced in this study by all three models, even though they were all equipped with different physical parameterisations and propagation schemes (Table 1). A similar bias was also

Table 3. Bias, RMS-error, scatter index (SI) and correlation coefficient (ρ) at the GoF wave buoy with HIRLAM and HARMONIE wind forcing for 2016. Results from both the 0.1 nmi nested runs and the 1 nmi Baltic Sea scale runs are shown.

	HIRLAM				HARMONIE			
H_s (m)	Bias	RMSE	SI	ρ	Bias	RMSE	SI	ρ
WAM	0.05	0.20	0.20	0.96	0.09	0.23	0.23	0.96
WAM (1 nmi)	0.04	0.19	0.19	0.97	0.07	0.22	0.21	0.96
SWAN	0.09	0.20	0.18	0.96	0.13	0.23	0.19	0.96
SWAN (1 nmi)	0.06	0.20	0.15	0.97	0.12	0.22	0.19	0.97
WW3	0.02	0.17	0.17	0.96	0.06	0.19	0.18	0.96
WW3 (1 nmi)	0.02	0.16	0.17	0.97	0.05	0.18	0.18	0.96
T_p (s)	Bias	RMSE	SI	ρ	Bias	RMSE	SI	ρ
WAM	−0.26	1.34	0.27	0.62	0.17	1.38	0.28	0.58
WAM (1 nmi)	−0.31	1.34	0.27	0.61	−0.22	1.33	0.26	0.63
SWAN	−0.19	1.29	0.26	0.61	−0.09	1.29	0.26	0.62
SWAN (1 nmi)	−0.10	1.01	0.20	0.79	−0.15	1.28	0.26	0.61
WW3	−0.22	1.31	0.26	0.62	−0.02	1.28	0.26	0.63
WW3 (1 nmi)	−0.19	1.28	0.26	0.62	−0.08	1.27	0.26	0.63

Table 4. Wind validation (U_{10}) for year 2016 (May – November)

	HIRLAM				HARMONIE			
	Bias (ms^{-1})	RMSE (ms^{-1})	SI	ρ	Bias (ms^{-1})	RMSE (ms^{-1})	SI	ρ
Kalbådagrund	0.29	1.46	0.19	0.91	0.29	1.57	0.20	0.90
Helsingin majakka	0.37	1.47	0.19	0.91	0.38	1.56	0.21	0.90
Harmaja	0.69	1.50	0.21	0.90	0.89	1.76	0.24	0.89
Kruunuvuorenselkä	0.14	1.29	0.19	0.90	0.00	1.49	0.22	0.87

identified at Berggrund, 13 km south-west of the Harmaja wave buoy. The overestimated significant wave height for this specific wind sector was large enough to have a measurable impact on the bias at these locations (Table 2). The chosen physics of WW3 (ST4) has an improved treatment of swell. However, even the longer wave components propagating around the Porkkala peninsula (not shown on the map) were wind waves. The ST2 physics package (Tolman and Chalikov 1996) in WW3 is unlikely to solve this issue, since Rogers et al. (2012) suggested that the ST2 might be less suitable for small-scale applications compared to ST4. A tuning of the source term parameters (e.g. $\beta_{\max}$ in the wind input, or C_{ds} and δ in the dissipation) might increase the accuracy of the modelled spectrum. Nevertheless, this can have a possible negative effect on other exposed locations (Isosaari and Itä-Villinki) that did not suffer from this same overestimation of the significant wave height.

Surprisingly, the error at Harmaja didn't propagate further in to the archipelago to Suomenlinna, where the model bias' ranged from −0.01 to 0.02 m. Deep inside the archipelago at Jätkasaari, Hernesaari and Ruumiskari all models had a somewhat higher bias compared to Suomenlinna, but the significant wave height was nevertheless modelled fairly well (Figure 2, Table 2).

4.2. Validation at Suomenlinna

Since most data were available at Suomenlinna, it was possible to perform a more in-depth validation of the different models here. The model performance at Harmaja is known to depend on the wind direction (Björkqvist et al. 2017a), and the bias of the significant wave height was therefore plotted against the wind direction from the Harmaja weather station (Figure 3 a)). The wave models reproduced the significant wave height well for the most common wind direction around 225 degrees; the bias of all models was close to zero, being slightly negative in WAM and positive in SWAN.

There was a shift to a more negative bias at wind directions of 180 degrees, which was most notable in WW3. The bias for the easterly wind directions (less than 120 degrees) turned towards positive. Northerly winds cannot produce high waves and the wave model performance for these cases are therefore not equally important. Overall, SWAN simulated somewhat higher values compared to WAM and WW3, possibly because of the more advanced physics used to calculate the wind input of Janssen (1991) (WAM) and the ST4 physics package (WW3). The use of a HARMONIE forcing resulted in higher significant wave height when used instead of HIRLAM. Nevertheless, the discrepancies were small.

The difference between the modelled and the observed wave energy as a function of the frequency is shown in Figure 3(b)). The values were calculated using events in the 90th percentile of the observed significant wave height, and all wave spectra were normalised by the maximum value of the observed wave spectra prior to calculating the difference. It's evident that the wave models disagreed on the energy distribution even though the significant wave height at Suomenlinna was modelled well. WAM (and to some degree WW3) underestimated the energy at the higher frequencies. SWAN had a zero bias for frequencies over 0.4 Hz, while overestimating the energy in the frequency range of 0.25–0.35 Hz. WAM and WW3, again, had a negative bias in this frequency range. All three models had a positive bias for the longest waves, with WAM propagating most long wave energy through the outer archipelago to the Suomenlinna wave buoy.

Finally, one easterly and one westerly case was chosen for closer inspection. The wave spectra were averaged over five hours and reviewed in more detail. The two selected situations (in 23 and 28 October 2016) both had a relatively steady wind of 13 ms^{-1} and therefore provided a good overview of the typical wave conditions for easterly and westerly winds. The identical wind speeds and the low significant wave height prior to the events allowed for an unbiased comparison of the difference in model performance between the cases.

For the westerly case the wave spectra had a unimodal shape (Figure 4(a)). A 13 ms^{-1} wind speed and the 4 km fetch to the closest islands south-west of the wave buoy would result in a peak frequency of 0.45 Hz (according to Kahma and Calkoen (1992)). This means that the bulk of the wave energy was propagated beyond these islands from the GoF. The positive bias was most pronounced for frequencies under 0.20 Hz, which were also the most strongly refracted waves. This was not surprising considering the overestimation in long wave energy that have been identified at the Harmaja wave buoy under 5 km from this location. However, all models underestimated the energy at and above the observed spectral peak.

A positive bias in SWAN for waves around 0.3 Hz was visible in the easterly case (Figure 4(b)). The frequency of 0.3 Hz is the peak of the waves that can be generated from Eestiluoto (see Figure 1) 13 km east of the Suomenlinna wave buoy with a wind speed of 13 ms^{-1}. WAM modelled these waves better, while WW3 fell in between. Previously in our analysis WAM and WW3 (with the newer deep water physics) have had similar tendencies. This was, however, not the case for the longer waves ($\sim$ 0.15 Hz) refracted from the GoF into the archipelago. These waves – coming from a 120 degree direction (roughly 20 degree offset to the wind direction) – were

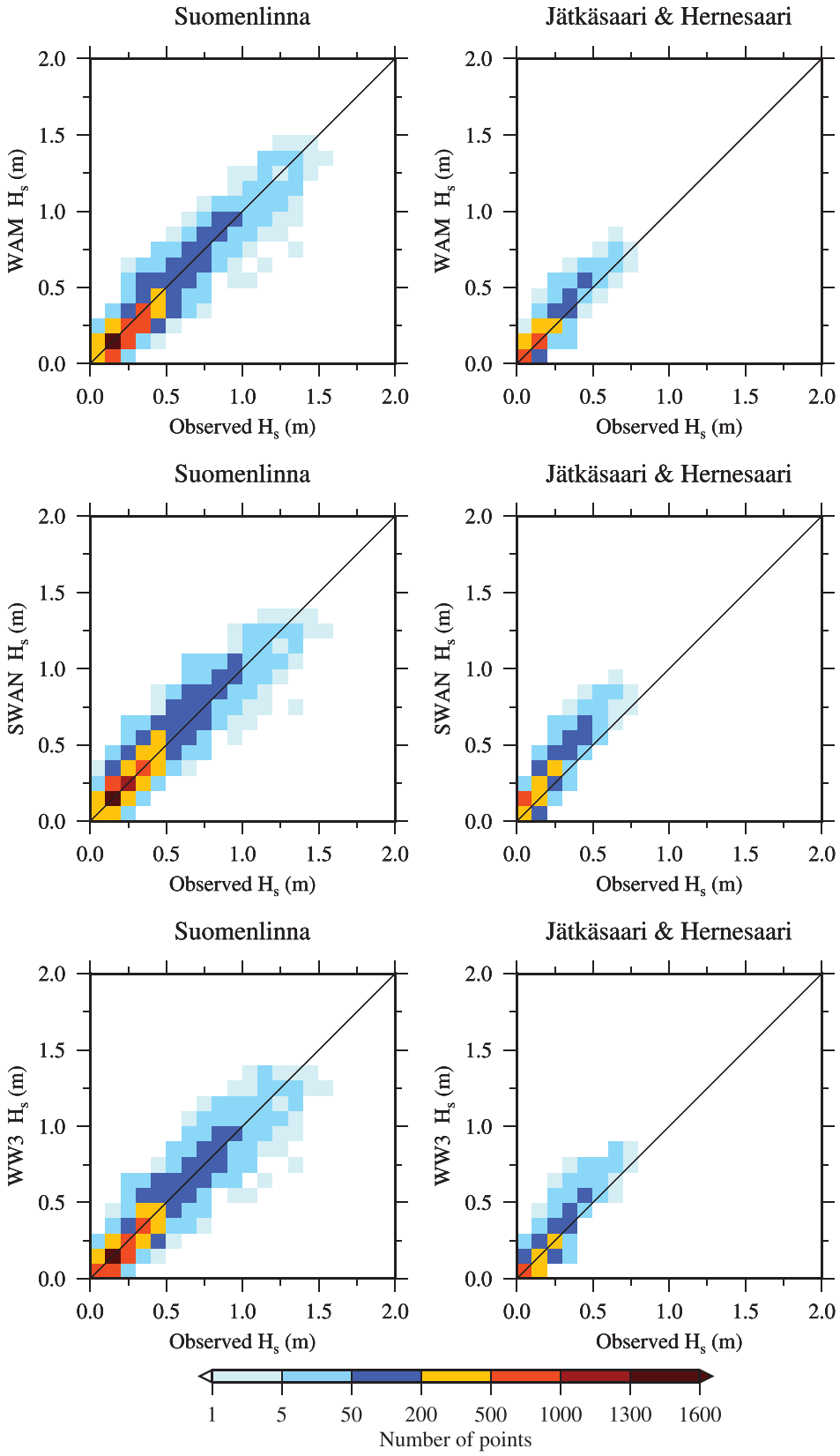

Figure 2. The observed significant wave height compared against values modelled by WAM, SWAN and WW3 when using the HIRLAM forcing. Jätkäsaari and Hernesaari are combined because of their geographical proximity.

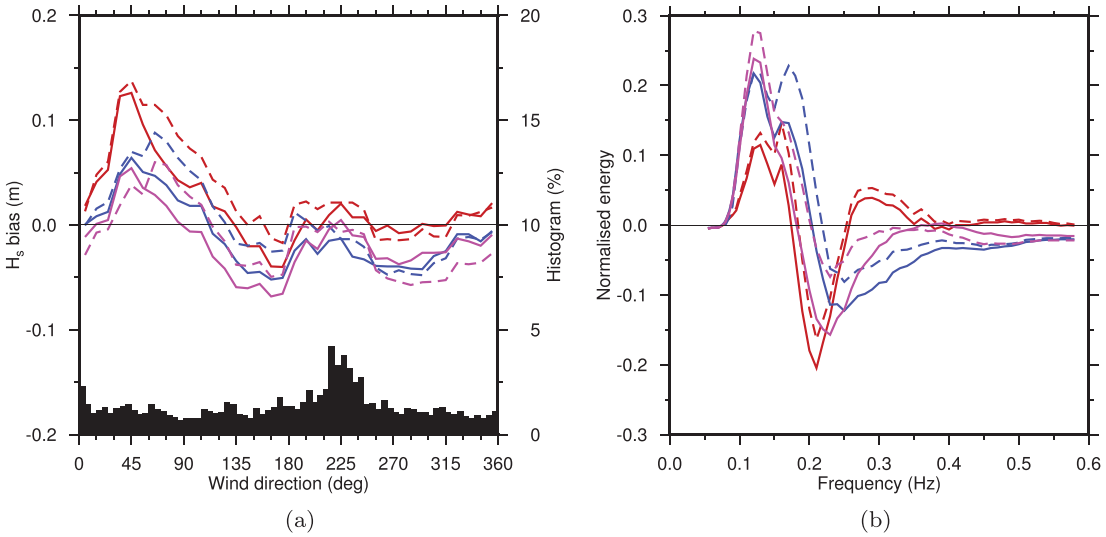

Figure 3. The bias in significant wave height at the Suomenlinna wave buoy for WAM (blue), SWAN (red) and WW3 (magenta). Results when using HIRLAM as the wind forcing is shown with solid lines, while HARMONIE results are in dashed. (a) Model bias as a function of the wind direction. (b) Model bias as a function of frequency calculated from the 90th percentile (based on the observed H_s).

overestimated by WAM, but represented correctly by SWAN and WW3. The positive bias in WAM might simply have been caused by an overestimation of the longer waves in the GoF (Figure 5), but interestingly the same discrepancy was not seen for westerly waves. The role of the numerics in the propagation scheme cannot be completely ruled out, even though differences caused by the numerics have been found to be secondary to the choise of physics (Perrie et al. 2017)

While SWAN modelled the highest frequencies over 0.35 Hz correctly, WAM and WW3 showed a clear negative bias during the westerly wind case. During the westerly case all models had an identical friction velocity (not shown), but for the *easterly* winds the friction velocity in both WW3 and WAM was higher than in SWAN (9 % and 24 % respectively). This suggests that the Janssen (1991) and ST4 wind input needed a higher friction velocity to produce the same high-frequency energy levels that were achieved by the older Komen et al. (1984) used in SWAN (or that the more advanced source terms underestimated the friction velocity in the westerly case). This indicates that the use of the older physics package in SWAN can still have the advantage of being more robust in the high-frequency part of the spectrum in complex archipelago conditions.

4.3. The wave period

The wave period is not as straightforward to define as the significant wave height, and several alternative definitions exist. In this paper the peak period (T_p) and the mean period (T_m) are used (see Equations (5) and (4)).

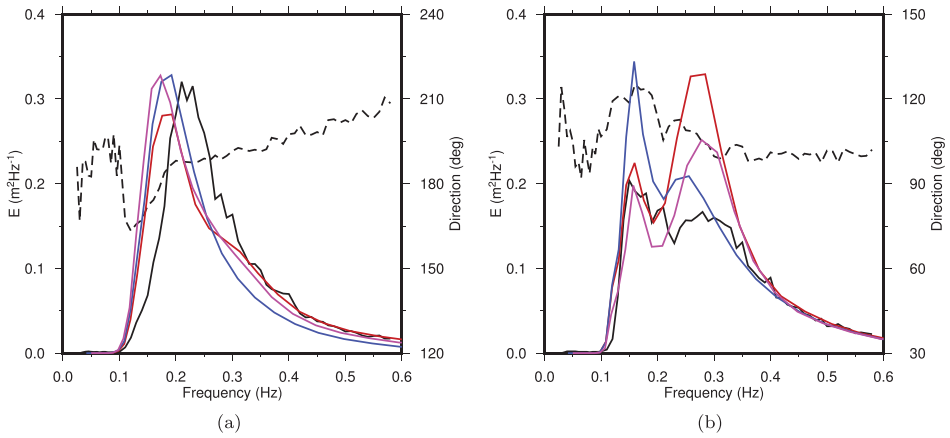

Figure 4. The wave spectra averaged over five hours at the Suomenlinna wave buoy. The observations (black), WAM (blue), SWAN (red) and WW3 (magenta). The observed direction is showed with the dashed line. (a) Westerly wind case (b) Easterly wind case

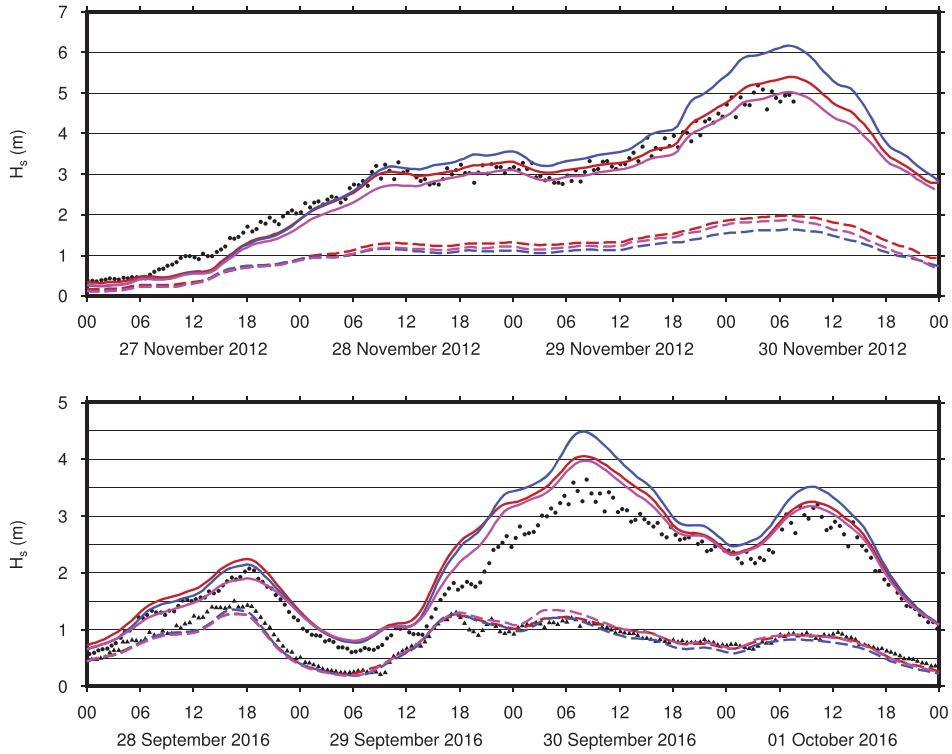

Figure 5. The significant wave height at the wave buoys during the maximum wave height for both easterly (top) and westerly (bottom) waves. WAM (blue), SWAN (red) and WW3 (magenta) are shown for the GoF wave buoy in solid, and Suomenlinna wave buoy in dashed. Black dots and triangles are wave buoy observations.

At the GoF wave buoy the peak period was somewhat underestimated, but the overall performance was good, with all configurations having RMS-errors under 1.5 s (Table 3). For the coastal locations the statistics were highly variable (Table 2). The peak period compared best to the measurements for the least sheltered locations (Harmaja and Berggrund), with a RMSE under 2 s for all the models, but even for these locations the SI over 0.30 was higher than at the GoF wave buoy. In the outer archipelago (Isosaari, Itä-Villinki and Suomenlinna) the negative bias was slightly stronger and the SI also rose to over 0.40.

For the most sheltered locations (Ruumiskari, Hernesaari and Jätkäsaari) the bias became positive in WAM and WW3, while it remained negative for SWAN. This was because of the stronger positive bias for the low-frequency energy in the first two models (Figure 3(b)), while the true peak period was sometimes determined by an almost equally strong higher frequency peak (Björkqvist et al. 2017b). This issue was present already at Suomenlinna, but was reflected even more strongly in the less well-defined situations in the very sheltered conditions. The instability of the parameter, especially for low winds, was also reflected in low correlations between the modelled and observed values (as low as 0.08 for Jätkäsaari). SWAN's tendency to overestimate the energy of the waves generated by the local fetch resulted in a negative bias for the peak period inside the archipelago. From the point of determining the peak period, the models emphasised opposite parts of the complex wave conditions in the archipelago in a too deterministic fashion, which caused both a bias and an increased scatter compared to the observations.

The scatter was reduced when the mean period was used instead of the peak period, which was an expected consequence when using an integrated parameter. The RMSE and SI were below 1.5 s and 0.35 for the nearshore points in all models, while being a maximum of 0.93 s and 0.25 elsewhere (Table 2). The mean period was more robust also in the sense that the models' results were more consistent, with even SWAN showing a positive bias at the nearshore points (Hernesaari and Jätkäsaari). The largest differences were at Suomenlinna where SWAN had a stronger negative bias compared to the two other models, even though all three models agreed very well on the significant wave height. The correlations for the mean period ($\rho = 0.54$–0.67) were higher than for the peak period ($\rho < 0.45$), but still lower than the $\rho > 0.9$ found for the significant wave height.

As noted by e.g. Akpınar et al. (2012), a fair comparison for the mean period can only be made if the upper integration limit is constant. The mean period were

therefore calculated from the model spectra by integrating only to the highest frequency of the wave buoy (0.6 Hz). The effect of the integration limit was particularly important near the shore, where an increasing percentage of the energy was concentrated to the higher frequencies. If the model spectra were integrated to 1 Hz, the bias changed 0.2–0.3 s at Harmaja, 0.5–0.7 s at Suomenlinna and 1.0–1.2 s at Jätkäsaari (modelled values decreased).

4.4. Comparing coastal wave fields

Extreme wave conditions are often a safety concern. However, because of the limited coverage of measurements, the community often have to rely on information from models to gain insight into conditions during e.g. an exceptional storm. The possible discrepancies between the information given by the different models are therefore of considerable interest, which is why the most severe easterly and westerly wave events from the observations at the GoF wave buoy were identified. The results in this section were obtained using the HIRLAM forcing.

During an easterly case in 30 November 2012 the GoF wave buoy measured a significant wave height of 5.2 m for the second time in its measurement history. At the location of the Suomenlinna wave buoy WW3 simulated higher significant wave heights than WAM, but slightly smaller than SWAN (Figure 5, top dashed). Figure 6 reveals that the differences in how the models simulated the wave field around the Suomenlinna wave buoy were reflected in the wave field all the way to the shore.

The differences were not caused by the wave field at the GoF wave buoy, since WAM simulated higher waves there compared to both SWAN and WW3 (Figure 5, top solid). This difference between the models was also readily seen in the wave field just east and south-west of Isosaari. The differences at the Suomenlinna buoy can be explained by the higher wave growth in SWAN north of Isosaari, which was already identified for another easterly wind event in Figure 4(b). Conversely, the higher long wave energy in WAM that was identified earlier in Figure 4(b) might be partially explained by a stronger incident wave field reaching the archipelago.

During a westerly wind case in 30 September 2016 the GoF wave buoy measured a 3.6 m significant wave height, which is in the 99.5th percentile (Tuomi et al. 2011). WAM, again, produced a higher significant wave height at the GoF wave buoy compared to the other two models (Figure 5, bottom solid). This was also reflected in a slightly higher significant wave height entering the outer edge of the archipelago (Figure 6), but the difference was not as large as for the easterly case, especially compared to WW3.

The significant wave height at the Suomenlinna wave buoy were practically identical between WAM and SWAN, while WW3 simulated slightly higher waves during the beginning of 30 September (Figure 5, bottom dashed). The differences between the models were also visible east of Suomenlinna, and the differences were also – to a degree – propagated to the area north of the wave buoy (Figure 6, left column). However, all in all, the three models compared very well with the observations, as seen in Figure 5 (bottom dashed).

The high significant wave heights simulated by WAM in these two chosen cases suggests that the deep water source terms of cycle 4.5.4 could require a re-tuning to more accurately simulate the highest wave heights at the GoF wave buoy. The tendency to overestimate was smaller for both the ST4 source terms in WW3 and the older Komen et al. (1984) source terms in SWAN. Nevertheless, a more extensive study in the simulating of the highest percentile wave heights is required to draw any definitive conclusions.

5. Discussion

The characterising feature of coastal archipelagos is their irregular nature, which sets great challenges for the validation of any kind of model. In addition to the uncertainties in the actual wave model, the performance of the atmospheric forcing in areas with scattered islands is still not fully understood, and have been a topic of discussion in the past (Tisler et al. 2007; Tuomi et al. 2014; Björkqvist et al. 2017a). However, the comparison to the research wind station at Kruunuvuorenselkä indicated that the atmospheric forcing was fairly accurate even deep inside the archipelago (Table 4). The wave models were also not very sensitive to the temporal or spatial resolution of the wind forcing in a larger part of the domain. Thus, operational products should provide an adequate wind forcing for wave models in a scattered archipelago, even if their spatial resolution is an order of magnitudes coarser than that of the wave model and the wind field is updated only every third hour.

While it is unlikely that inaccuracies in the wind forcing would have been the main cause for any systematic errors in the simulated wave field, more subtle issues connected to e.g. the wind direction or the duration of exceedance have not been studied. Studies made by e.g. de Rooy and Kok (2004) have shown that the use of downscaling methods can improve the accuracy of simulated winds. Nevertheless, as the spatial resolution of HARMONIE is quite high, and it accounts for sub-grid scale terrain differences, the added benefits of using such downscaling methods on the data of this study are not expected to be significant.

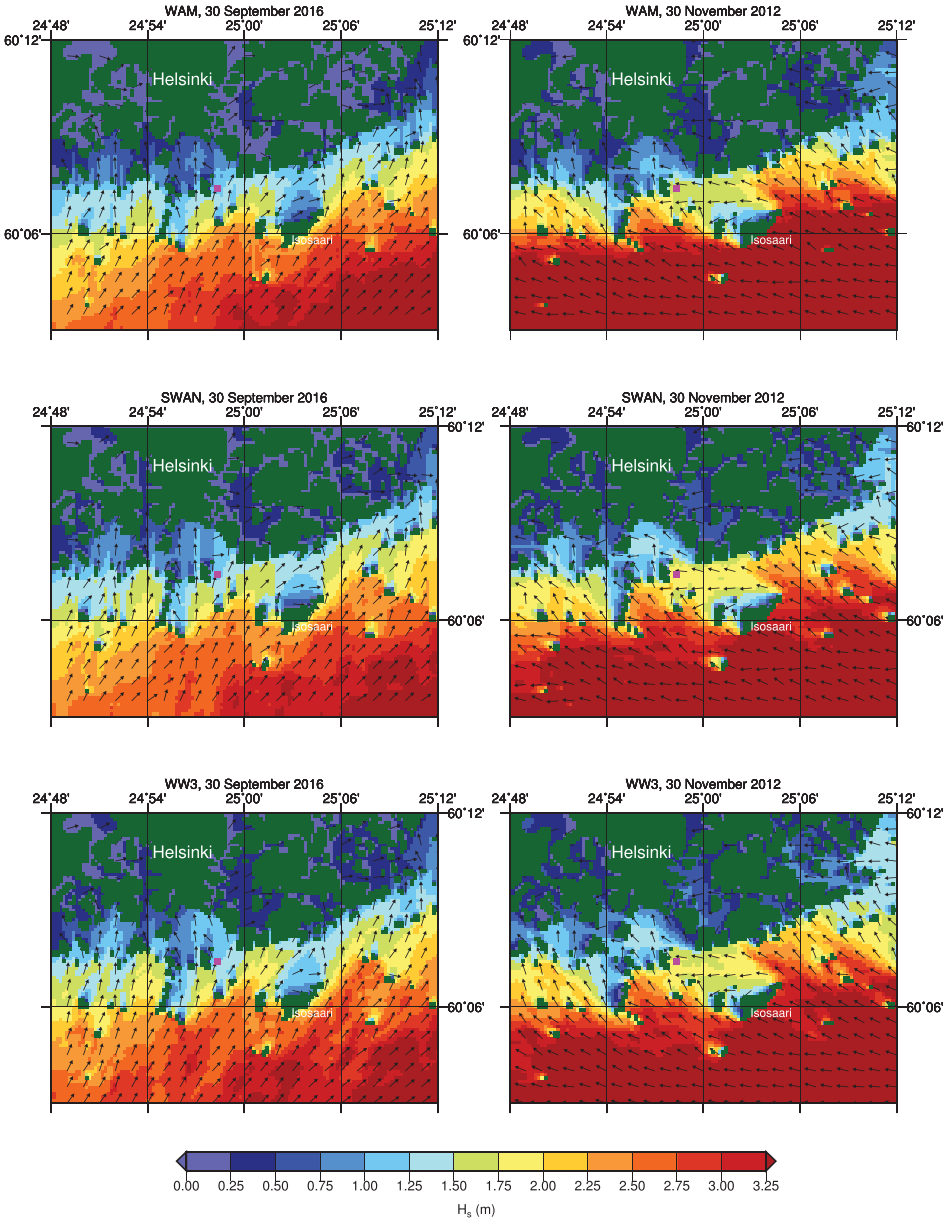

Figure 6. Nearshore wave fields from the different models during the maximum wave height for both westerly (left) and easterly (right) waves. The Suomenlinna wave buoy is marked with a magenta square.

The difference in performance between Harmaja and Suomenlinna highlight the great variability in model performance on the scale of 25–30 model grid points (5 km in this study). All wave models exhibited a large positive bias in the significant wave height at the Harmaja wave buoy just outside the archipelago. However, this bias was only propagated in a weak manner to Suomenlinna, located 5 km closer to the shore.

At Suomenlinna the results indicated that WAM and WW3 (with our chosen set-ups) required a higher friction velocity to reproduce the observed high-frequency energy compared to SWAN. For the easterly winds WAM had a friction velocity 1.2 times higher than SWAN, but all models agreed with the observed wave spectrum for the spectral tail (Figure 4 b)). For the westerly winds WAM had the same friction velocity as SWAN and at the same time underestimated the energy at the spectral tail, as did WW3 (Figure 4(a)). The friction velocity in WAM and WW3 depend on the wave induced stress (Ardhuin et al. 2010; Janssen 1991), while it is determined simply using a bulk drag law in SWAN (Komen et al. 1984; Wu 1982). Ultimately, the overall performance of each model is largely determined by the choice of physical source terms, and our results reflect the settings visible in Table 1. An improved performance for each of the models can be expected if the

source terms are tuned using the data in this study instead of the standard values.

The poor validation statistics for the peak period (large scatter and bias, see Table 2) can partly be explained by the nature of the parameter. The wave field inside the archipelago typically has several peaks of similar magnitude and the peak period is therefore often determined in an almost random fashion. This behaviour is something that is well beyond what can be reasonably expected to be simulated by the wave models. We also want to stress that these peaks are not sporadic swell, since all components generally have phase speeds lower than the wind. They are a product of the several varying fetches and the attenuation caused by the islands.

The modelled mean period compared well with measurements as long as a consistent upper integration frequency was used. It should nevertheless be noted that for typical archipelago wave fields there can exist a significant amount of wave energy for waves longer than the mean period, even if swell is completely absent (see Figure 4(b)). Therefore, the mean period doesn't necessarily describe the properties of the wave field in the way one might expect, even though it has the obvious benefit of being more stable compared to the peak period. Near the shore the observed values of the mean period are also biased by the limited upper frequency of the wave buoy, especially for lower wind speeds. It is therefore not obvious how to determine the 'true' mean period. These considerations present practical challenges when a representative measure of the wave period have to be provided to end users, especially when wave observations and model results are presented side by side. However, the issues in reconciling observed and modelled wave period parameters cannot be solved purely by model development, but reflect the inherent difficulties in finding a good descriptor for 'the wave period' in the complex and heterogeneous wave conditions of the archipelago.

While from a physical perspective a lot of questions are still left unanswered, the overall differences in the models' capabilities in simulating the nearshore wave field were found to be small. The choice of model can therefore largely be made based on practical operational considerations, such as the compatibility with existing infrastructure and running time.

6. Conclusions

We implemented three wave models (WAM, SWAN and WAVEWATCH III®) in the Finnish coastal archipelago. The models were validated against wave measurements from nine wave buoys. The two different wind forcings (HIRLAM and HARMONIE) were compared to wind observations from four measurement sites. A 7.4 km spatial resolution and 3 h temporal resolution in the wind forcing was found to be sufficient to force the high-resolution 0.1 nmi wave model implementations. The use of HARMONIE resulted in slightly higher waves, which was in line with previous findings (Tuomi et al. 2014; Björkqvist et al. 2017a). However, at the Kruunuvuorenselkä station deepest inside the archipelago the bias in the wind speed was smaller for the 2.5 km HARMONIE compared to the 7.4 km HIRLAM (Table 4).

All models produced similar results for the significant wave height at all the measurement locations. SWAN tended to simulate higher locally generated waves for the short fetches inside the archipelago compared to WAM. The same is true for WW3 (ST4, default settings), although to a slightly lesser degree. Conversely, WAM typically propagated more long wave energy into the archipelago compared to SWAN. For the low frequencies WW3 roughly agreed with WAM for the westerly winds and with SWAN for the easterly winds.

The above tendencies were reflected strongly in the determining of the peak period close to the shore, leading to a negative bias in SWAN and a positive bias in the other two models. The SI for all models were quite large, which reflected the somewhat ill-defined nature of the peak period in the complex nearshore archipelago conditions. The mean period gave a more robust description of the wave period, which lead to a smaller scatter when the model results were compared with observations. However, the results near the shore were very sensitive to the the chosen upper frequency for the integration. An integration to 1 Hz instead of 0.6 Hz (the upper frequency of the wave buoy) affected the bias by roughly 1 s.

In the middle of the archipelago, at Suomenlinna, both WAM and WW3 underestimated the high-frequency wave energy for certain wind directions. This is surmised to have been caused by a too low friction velocity, since SWAN that used a simple bulk drag law of Wu (1982) to determine the friction velocity did not exhibit this behaviour. In general, almost every aspect of the model performances were determined by the properties of the shoreline and islands, and were therefore wind direction dependent.

All three models (with the set-ups chosen in this paper) were found to be equally suitable to provide wave predictions in archipelagos, although the possibility of significant biases in semi-sheltered conditions just outside the archipelago should be considered (see also, Björkqvist et al. 2017a).

The existence of discrepancies in duration in the wind forcing and their possible impact on the nearshore wave

conditions should still be explored. Further research into the friction velocity used in the model, and the general performance of the wind input source term function, is recommended to resolve discrepancies between the models for the high-frequency wave energy during certain wind and wave conditions. A natural starting point for this work is a tuning of the source term packages to improve the performance relative to the measurement presented in this paper. The Suomenlinna wave measurements are ongoing, meaning that they present a possibility to validate the modified source terms against independent data collected from later years.

Acknowledgments

We are grateful to Mr Ari Aaltonen and Mr Mikael Frisk for performing the height adjustments to the wind observations. We also gratefully acknowledge the City of Helsinki for releasing the wave data gathered within the paid commissioned works, and the Weather Service of the Estonian Environment Agency for allocating computing time on their High Performance Computing cluster. The time and effort taken by the anonymous reviewers to critique our manuscript are also greatly appreciated.

Disclosure statement

No potential conflict of interest was reported by the authors.

Funding

This work was partly funded by the Finnish State Nuclear Waste Management Fund through SAFIR2018, the Finnish Nuclear Power Plant Safety Research Programme 2015–2018; CMEMS COPERNICUS under Grant WAVE2NEMO; and Arvid of Greta Olins fond (Svenska Kulturfonden) under Grant 17/103386. We would like to thank RFBR (17-05-41117, 18-35-00602) and Russian Science Foundation (15-17-20009) for the test numerical experiments. This study has utilised research infrastructure facilities provided by FIN-MARI (Finnish Marine Research Infrastructure network).

ORCID

J.-V. Björkqvist http://orcid.org/0000-0001-8981-2758
A. Kuznetsova http://orcid.org/0000-0001-6458-2597
L. Tuomi http://orcid.org/0000-0003-2471-6815

References

Akpınar A, van Vledder GPh, Kömurku MI, Özger M. 2012. Evaluation of the numerical wave model (SWAN) for wave simulation in the Black Sea. Cont Shelf Res. 50–51: 80–99.

Ardhuin F, O'Reilly WC, Herbers THC, Jessen PF. 2003. Swell transformation across the continental shelf. Part I: Attenuation and directional broadening. J Phys Oceanogr. 33(9):1921–1939.

Ardhuin F, Rogers E, Babanin AV, Filipot J-F, Magne R, Roland A, van der Westhuysen A, Queffeulou P, Lefevre J-M, Aouf L, et al. 2010. Semiempirical dissipation source functions for ocean waves. Part I: definition, calibration, and validation. J Phys Oceanogr. 40(9):1917–1941.

Atan R, Nash S, Goggins J. 2017. Development of a nested local scale wave model for a 1/4 scale wave energy test site using SWAN. J Oper Oceanogr. 10(1):59–78.

Ayat B. 2013. Wave power atlas of Eastern Mediterranean and Aegean Seas. Energy. 54:251–262.

Battjes JA, Janssen JPFM. 1978. Energy loss and set-up due to breaking of random waves. Proceedings of 16th International Conference on Coastal Engineering; August 27–September 3, 1978, Hamburg. p. 569–587.

Behrens A, Günther H. 2009. Operational wave prediction of extreme storms in northern europe. Nat Hazards. 49 (2):387–399.

Bertotti L, Cavaleri L. 2009. Wind and wave predictions in the Adriatic Sea. J Marine Syst. 78:227–234.

Bidlot J-R, Janssen P, Abdalla S. 2007. A revised formulation of ocean wave dissipation and its model impact, January.

Björkqvist J-V, Lukas I, Alari V, van Vledder GPh, Hulst S, Pettersson H, Behrens A, Männik A. 2018. Comparing a 41-year model hindcast with decades of wave measurements from the Baltic Sea. Ocean Eng. 152:57–71.

Björkqvist J-V, Pettersson H, Laakso L, Kahma KK, Jokinen H, Kosloff P. 2016. Removing low-frequency artefacts from Datawell DWR-G4 wave buoy measurements. Geosci Instrum Method Data Syst. 5:1–9.

Björkqvist J-V, Tuomi L, Fortelius C, Pettersson H, Tikka K, Kahma KK. 2017a. Improved estimates of nearshore wave conditions in the Gulf of Finland. J Marine Syst.. 171:43–53.

Björkqvist J-V, Tuomi L, Pettersson H, Fortelius C, Tikka K, Kahma KK. 2014. The effect of boundary field accuracy on high-resolution coastal wave modelling. Proceedings of 6th IEEE/OES Baltic Symposium, 26–29 May 2014, Tallinn.

Björkqvist J-V, Vähäaho I, Kahma KK. 2017b. Spectral field measurements of wave reflection at a steep shore with wave damping chambers. WIT Trans The Built Environ. 170:185–191.

Booij N, Ris RC, Holthuijsen LH. 1999. A third-generation wave model for coastal regions: 1. Model description and validation. J Geophy Res Oceans. 104(C4):7649–7666.

BSBD. 2013. Baltic sea hydrographic commission. Baltic Sea Bathymetry Database version 0.9.3, Downloaded from http://data.bshc.pro/ on 2015-10-27.

Campos RM, Alves J-HGM, Penny SG, Krasnopolsky V. 2018. Assessments of surface winds and waves from the NCEP ensemble forecast system. Weather Forecast. 33(6):1533–1546.

Cavaleri L, Abdalla S, Benetazzo A, Bertotti L, Bidlot JR, Breivik Ø, Carniel S, Jensen RE, Portilla-Yandun J, Rogers WE, et al. 2018. Wave modelling in coastal and inner seas. Prog. Oceanogr.. 167(March):164–233.

Cavaleri L, Alves JHGM, Ardhuin F, Babanin A, Banner M, Belibassakis K, Benoit M, Donelan M, Groeneweg J, Herbers THC, et al. 2007. Wave modelling - The state of the art. Prog. Oceanogr.. 75(4):603–674.

Cavaleri L, Bertotti L. 2004. Accuracy of the modelled wind and wave fields in enclosed seas. Tellus. 56A:167–175.

Chawla A, Tolman HL. 2008. Obstruction grids for spectral wave models. Ocean Model. 22(1):12–25.
Chawla A, Tolman HL, Gerald V, Spindler D, Spindler T, Alves JHGM, Cao D, Hanson JL, Devaliere E-M. 2013. A multigrid wave forecasting model: a new paradigm in operational wave forecasting. Weather Forecast. 28(4):1057–1078.
de Rooy WC, Kok K. 2004. A combined physical–statistical approach for the downscaling of model wind speed. Weather Forecast. 19:485–495.
Dykes JD, Wang DW, Book JW. 2009. An evaluation of a high-resolution operational wave forecasting system in the Adriatic Sea. J Mar Syst. 78:255–271.
Eldeberky Y. 1996. Nonlinear transformation of wave spectra in the nearshorezone, PhD thesis, Delft University of Technology, Department of Civil Engineering, The Netherlands..
Guedes Soares C, Rusu L, Bernardino M, Pilar P. 2011. An operational wave forecasting system for the Portuguese continental coastal area. J Oper Oceanogr. 4(2):17–27.
Haiden T, Janousek M, Bidlot J, Buizza R, Ferranti L, Prates F, Vitart F. 2018. Evaluation of ECMWF forecasts, including the 2018 upgrade, October.
Hardy TA, Mason LB, McConochie JD. 2001. A wave model for the Great Barrier Reef. Ocean Eng. 28(1):45–70.
Hardy TA, Young IR. 1996. Field study of wave attenuation on an offshore coral reef. J. Geophys. Res. 101(C6): 14311–14326.
Hasselmann K, Barnett TP, Bouws E, Carlson H, Cartwright DE, Enke K, Ewing JA, Gienapp H, Hasselmann DE, Kruseman P, et al. 1973. Measurements of wind-wave growth and swell decay during the Joint North Sea Wave Project (JONSWAP). Ergnzungsheft zur Deutschen Hydrographischen Zeitschrift Reihe A(8), 12.
Hasselmann S, Hasselmann K, Allender J, Barnett TP. 1985. Computation and parameterizations of the nonlinear energy transfer in a gravity-wave spectrum. Part II: parameterizations of the nonlinear energy transfer for application in wave models. J Phys Oceanogr. 15:1378–1391.
HIRLAM-B. System documentation. 2017. http://hirlam.org.
Janssen PAEM. 1991. Quasi-linear theory of wind-wave generation applied to wave forecasting. J Phys Oceanogr. 21:1631–1642.
Kahma KK, Björkqvist JV, Johansson M, Jokinen H, Leijala U, Särkkä J, Tikka K, Tuomi L. 2016. Turvalliset rakentamiskorkeudet Helsingin rannoilla 2020, 2050 ja 2100. Technical Report 96, City of Helsinki, Real Estate Department, Geotechnical Division. http://www.hel.fi/static/kv/turvalliset-rakentamiskorkeudet.pdf. Online. 14.2.2016.
Kahma KK, Calkoen CJ. 1992. Reconciling discrepancies in the observed growth of wind-generated waves. J Phys Oceanogr. 22:1389–1405.
Komen GJ, Cavaleri L, Donelan M, Hasselmann K, Hasselmaan S, Janssen PAEM. 1994. Dynamics and modelling of ocean waves. Cambridge: Cambridge University Press.
Komen GJ, Hasselmann S, Hasselmann K. 1984. On the existence of a fully developed wind-sea spectrum. J Phys Oceanogr. 14(8):1271–1285.
Lavidas G, Venugopal V. 2017. A 35 year high-resolution wave atlas for nearshore energy production and economics at the Aegean Sea. Renewable Energy. 103:401–417.
Mentaschi L, Besio G, Cassola F, Mazzino A. 2015. Performance evaluation of WAVEWATCH III in the Mediterranean sea. Ocean Model. 90(Supplement C):82–94.
Monbaliu J, Padilla-Hernández R, Hagreaves JC, Carretero-Albiach JC, Luo W, Sclavo M, Günter H. 2000. The spectral wave model, WAM, adapted for applications with high spatial resolution. Coast Eng. 41:41–62.
Pallares E, Lopez J, Espino M, Sánchez-Arcilla A. 2017. Comparison between nested grids and unstructured grids for a high-resolution wave forecasting system in the western Mediterranean sea. J Oper Oceanogr. 10(1):45–58.
Pallares E, Sánchez-Arcilla A, Espino M. 2014. Wave energy balance in wave models (SWAN) for semi-enclosed domains–application to the Catalan coast. Cont Shelf Res. 87:41–53.
Perrie W, Toulany B, Roland A, Dutour-Sikiric M, Chen C, Beardsley RC, Qi J, Hu Y, Casey M, Shen H. 2017. Modeling North Atlantic nor'easters with modern wave forecast models. J Geophys Res: Oceans. 123(1):533–557.
Rogers WE, Dykes JD, Wang DW, Carroll SN, Watson K. 2012. Validation Test Report for WAVEWATCH III. Technical report, Naval Research Laboratory. Memorandum Report 7320-12-9425.
Roland A, Ardhuin F. 2014. On the developments of spectral wave models: Numerics and parameterizations for the coastal ocean. Ocean Dyn. 64(6):833–846.
Seifert F, Tauber B, Kayser B. 2001. A high resolution spherical grid topography of the Baltic Sea – 2nd ed. Baltic Sea Science Congress Stockholm 25–29. November 2001, Poster 147, www.io-warnemuende.de/iowtopo.
Tisler P, Gregow E, Niemelä S, Savijärvi H. 2007. Wind field prediction in coastal zone: operational mesoscale model evaluation and simulations with increased horizontal resolution. J Coastal Res. 233:721–730.
Tolman HL. 2003. Treatment of unresolved islands and ice in wind wave models. Ocean Model. 5(3):219–231.
Tolman HL, Balasubramaniyan B, Burroughs LD, Chalikov DV, Chao YY, Chen HS, Gerald VM. 2002. Development and implementation of wind-generated ocean surface wave models at NCEP. Weather Forecast. 17(2):311–333.
Tolman HL, Chalikov D. 1996. Source terms in a third-generation wind wave model. J Phys Oceanogr. 26:2497–2518.
Tuomi L, Björkqvist J-V. 2014. Wave forecasting in coastal archipelagos. Proceedings of 6th IEEE/OES Baltic Symposium, 26–29 May 2014, Tallinn.
Tuomi L, Kahma KK, Pettersson H. 2011. Wave hindcast statistics in the seasonally ice-covered Baltic Sea. Boreal Environ Res. 16(6):451–472.
Tuomi L, Pettersson H, Fortelius C, Tikka K, Björkqvist J-V, Kahma KK. 2014. Wave modelling in archipelagos. Coast Eng. 83:205–220.
Tuomi L, Vähä-Piikkiö O, Siili T, Alari V. 2018. CMEMS Baltic Monitoring and Forecasting Centre: High-resolution wave forecasts in the seasonally ice-covered Baltic Sea. Proceedings of the eight EuroGOOS conference, 3–5 October 2017, Bergen, Norway, eds E. Buch, V.Fernàndez, D. Eparkhina, P. Gorringe, and G. Nolan, EuroGOOS. Brussels, Belgium.
van der Westhuysen AJ, Padilla R, Santos P, Gibbs A, Gaer D, Nicolini T, Tajed S, Devaliere E-M, Tolman HL. 2013. Development and validation of the wave prediction system. 93rd AMS Annual Meeting, Austin, TX, January 5–10.

van der Westhuysen AJ, Taylor A, Padilla-Hernández R, Gibbs A, Santos P, Gaer D, Cobb III H, Lewitsky J, Rhome J. 2014. Enhancements to NWPS to provide coastal and overland hurricane wave guidance. 94th AMS Annual Meeting, Atlanta, GA, February 2–6. p. 1–8.

Verkaik JW. 2000. Evaluation of two gustiness models for exposure correction calculations. J Appl Meteorol. 39 (9):1613–1626.

WAMDIG. 1988. The WAM model – A third generation ocean wave prediction model. J Phys Oceanogr, 18:1775–1810.

The WAVEWATCH III® Development Group (WW3DG). 2016. User manual and system documentation of WAVEWATCH III® version 5.16. Technical report, NOAA/NWS/NCEP/MMAB, College Park, MD. 326 pp. + Appendices.

WMO. 2014. Guide to Meteorological Instruments and Methods of Observation. ISBN 978-92-63-10008-5. http://www.wmo.int/pages/prog/www/IMOP/CIMO-Guide.html. Accessed 2018 May 5.

Wu J. 1982. Wind-stress coefficients over sea surface from breeze to hurricane. J Geophys Res. 87(C12):9704–9706.

Zijlema M. 2010. Computation of wind-wave spectra in coastal waters with SWAN on unstructured grids. Coast Eng. 57 (3):267–277.

III

Reprinted, with kind permission, from
Ocean Science, 15, 1469-1487
doi:10.5194/os-15-1469-2019

Ocean Sci., 15, 1469–1487, 2019
https://doi.org/10.5194/os-15-1469-2019

Ocean Science Open Access EGU

The wave spectrum in archipelagos

Jan-Victor Björkqvist, Heidi Pettersson, and Kimmo K. Kahma

Finnish Meteorological Institute, P.O. Box 503, 00101, Helsinki, Finland

Correspondence: Jan-Victor Björkqvist (jan-victor.bjorkqvist@fmi.fi)

Received: 28 May 2019 – Discussion started: 19 June 2019
Revised: 12 September 2019 – Accepted: 9 October 2019 – Published: 13 November 2019

Abstract. Sea surface waves are important for marine safety and coastal engineering, but mapping the wave properties at complex shorelines, such as coastal archipelagos, is challenging. The wave spectrum, $E(f)$, contains a majority of the information about the wave field, and its properties have been studied for decades. Nevertheless, any systematic research into the wave spectrum in archipelagos has not been made. In this paper we present wave buoy measurements from 14 locations in the Finnish archipelago. The shape of the wave spectrum showed a systematic transition from a single-peaked spectrum to a spectrum with a wide frequency range having almost constant energy. The exact shape also depended on the wind direction, since the fetch, island, and bottom conditions are not isotropic. The deviation from the traditional spectral form is strong enough to have a measurable effect on the definitions of the significant wave height. The relation between the two definitions in the middle of the archipelago was $H_{1/3} = 0.881 H_s$, but the ratio varied with the spectral width (H_s was defined using the variance). At this same location the average value of the single highest wave, H_{max}/H_s, was only 1.58. A wider archipelago spectrum was also associated with lower confidence limits for the significant wave height compared to the open sea (6 % vs. 9 %). The challenges caused by the instability of the peak frequency for an archipelago spectrum are presented, and the mean frequency, weighted with $E(f)^4$, is proposed as a compromise between stability and bias with respect to the peak frequency. The possibility of using the frequency and width parameters of this study as a starting point for a new analytical parameterisation of an archipelago type spectrum is discussed.

1 Introduction

Since the 1950s the wave spectrum has been the central way to define the properties of random sea-surface wind waves (Pierson and Marks, 1952). Although the exact power law describing the high-frequency part of the spectrum is still an open question (e.g. Phillips, 1958; Toba, 1973; Kitaigorodskii, 1983; Kahma, 1981; Banner, 1990; Lenain and Melville, 2017), the central determining feature has been the location of the spectral maximum, which then consequently determines the total wave energy (Hasselmann et al., 1973; Donelan et al., 1985). From a practical perspective of derived wave parameters the spectral features translate into the peak frequency, f_p, and the significant wave height, H_s. The evolution of these two parameters, as a function of the fetch and the wind speed, has been extensively studied by laboratory and field experiments (e.g. Pierson and Moskowitz, 1964; Toba, 1972; Hasselmann et al., 1973; Kahma, 1981; Donelan et al., 1985; Kahma and Calkoen, 1992).

In the coastal region, waves are important for coastal engineering, erosion, small-vessel safety, and biological processes. Coastal waves deviate from deep-water open-sea waves, but their exact properties depend on the shoreline structure. On sloping beaches the limitation by the water depth is a major factor shaping the wave properties through bottom friction, depth-induced wave breaking, and shallow-water non-linear wave interactions (SPM, 1984; Eldeberky, 1996). Coastal coral reefs shape the wave spectrum away from the deep-water form (Hardy and Young, 1996); the same thing can be said for tidal inlets where the waves are also affected by strong currents (van der Westhuysen et al., 2012).

One of the most complex nearshore conditions can be found in coastal archipelagos where islands, the irregular shoreline, the slanting fetch, and the decreasing depth affect

the attenuation and local growth of the waves. Collections of large islands, in the scale of kilometres, can be found in, for example, the Gulf of Mexico, outside of Louisiana, or between Vancouver and Seattle (the San Juan Islands). In Europe an example is the Aegean Sea, which separates parts of Turkey and Greece from the Mediterranean Sea. Denser archipelagos, where the island sizes are of the order of hundreds of metres, are even more complex. An archipelago made up of a large number of small islands has a strong effect on the wave field by attenuating the waves and diffracting the remaining wave energy behind them. At the same time groups of islands practically define new fetches for local wave systems to grow from, thus giving birth to unique wave conditions. Examples of such archipelagos are the Thousand Islands at the US–Canadian border or the coastline of Maine. In Europe dense coastal archipelagos can be found especially in the Baltic Sea, with examples being the Stockholm archipelago and the Archipelago Sea. Also the coastline near the Finnish capital, Helsinki, has a characteristic archipelago with heavy commercial and recreational marine traffic.

Although coastal archipelagos are usual – almost typical – in the Baltic Sea, there is a limited amount of data available on their effect on waves. Kahma (1979) presented measurements of wave spectra in the archipelago that showed an almost complete absence of the traditional spectral peak. Single measurements like these have proven the shape of the wave spectrum to differ significantly from both open-sea observations and theoretical spectral models. Nevertheless, there exists no broader methodological study into the different spectral shapes and the transition between the two extremes, not least because of the limited amount of available observational data. Efforts to simulate the wave field in the archipelagos have been made (Soukissian et al., 2004; Mazarakis et al., 2012; Tuomi et al., 2014; Anderson et al., 2015; Björkqvist et al., 2019a), but, while fairly successful, they are still not a substitute for measurements.

The shape of the wave spectrum is of pure theoretical interest. Still, it also has direct and indirect consequences for practical applications, such as for estimating the expected height of single waves. An atypical spectral shape also affects the applicability and reliability of engineering formulas using integrated wave parameters and alters the sampling variability in standard wave buoy measurements. The spectral shape can be atypical at any location because of swell or decaying and turning winds. Nonetheless, in the archipelago an atypical spectral shape forms even under steady wave conditions, thus giving the wave field inside the archipelago its prevailing properties. These properties need to be identified and quantified in order to fundamentally understand waves in archipelagos.

This paper aims to fill the knowledge gap regarding the properties of the wave field inside dense coastal archipelagos. The study relied on spatially extensive wave buoy measurements; all data were collected in the Helsinki archipelago, which is located in the Gulf of Finland, the Baltic Sea. The data and methods are introduced in Sect. 2, while Sect. 3 presents and quantifies the transformation of the mean spectral shape in the archipelago. Section 4 is dedicated to studying what implications the results have for the determination of derived wave parameters, such as the significant wave height, the maximum height of a single wave, and the peak frequency. One candidate for a characteristic frequency, suitable for a wide range of wave conditions, is proposed. We end the paper by discussing and concluding our findings.

2 Materials and methods

2.1 Wave measurements

We conducted wave measurements at 14 locations off Helsinki in the Gulf of Finland (GoF). An overview of the sites can be found in Fig. 1 and Table 1. All observations were made with Datawell Directional Waverider buoys. Some of the data originate from smaller 40 cm GPS-based DWR-G4 buoys (henceforth G4), which use the Doppler shift of the GPS signal to measure the surface elevation. Measurements from larger (70–90 cm) accelerometer-based Mk-III and DWR4/ACM buoys (henceforth Mk-III and DWR4) were available from two operational wave buoys: one is located in the centre of the GoF (Fig. 1), while the other is deployed in the middle of the archipelago outside of the island Suomenlinna (T2, Fig. 2).

The nearshore measurements with the G4 buoys – conducted as part of a commissioned work by the city of Helsinki – were made for about a month at each location between 2012 and 2014 (Table 1). The exceptions are the Berggrund (O1) and Harmaja (O2) sites, where measurements were made for research purposes in 2015 and 2012. The shortest deployment time was 11 d (at Länsikari, T1) and the longest 39 d (at Isosaari, O2). Except for the July campaign at O1, the measurements were made between August and November to capture the harshest wave conditions before the areas froze. While observations at 12 out of the 14 locations were made with the smaller G4 buoys, most of the data originate from the long time series of the operational Mk-III and DWR4 wave buoys at GoF and Suomenlinna (T2). Data from the Suomenlinna (T2) wave buoy were available from 2016–2018. Operational wave measurements from the GoF have been conducted for every year in this study (2012–2018), but the results are based only on the years 2016–2018 to coincide with the Suomenlinna (T2) data.

Both the G4 and the Mk-III use a sampling frequency of 1.28 Hz and calculate the spectrum up to 0.58 Hz. A DWR4 buoy was used at the GoF site in 2018 and part of the year 2016. The DWR4 has a sampling frequency of 2.56 Hz and the 90 cm version calculates the spectrum up to 1 Hz. Nevertheless, only data up to 0.58 Hz were used to keep all results comparable, since the change in upper frequency would

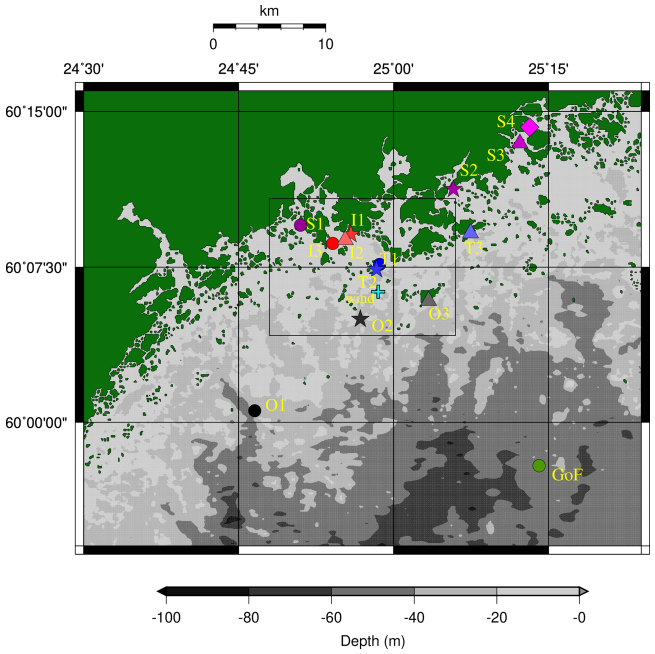

Figure 1. The bathymetry and the measurement locations. GoF (green) is the open-sea wave buoy. The stations are divided into groups: outer archipelago (O1–O3), transition zone (T1–T3), inner archipelago (I1–I3), and sheltered archipelago (S1–S4). The plus (+) marks the Harmaja weather station. The Kalbådagrund weather station is outside of the map. The black box marks the area of Fig. 2.

affect the calculations of higher spectral moments. No parametric tail was added to the observed spectra.

For the G4 buoys, the low-frequency artefacts, which have later been identified to be caused by the filter response to a missing GPS signal, were corrected following Björkqvist et al. (2016). Since the authors found that the correction can affect the high-frequency part of the spectrum, the corrected spectrum was only used for frequencies below $0.8\,f_\mathrm{m}$, where f_m is the mean frequency (see Eq. 4). For frequencies above $1.2\,f_\mathrm{m}$ Hz, the original spectrum was used, while a linear combination was used for intermediate frequencies to avoid discontinuities.

2.2 Wind measurements

We used wind measurements from two of the Finnish Meteorological Institute's operational automatic weather stations. Harmaja (measuring height 17.5 m) is located less than 10 km from the Helsinki shoreline, about 2 km from the Suomenlinna wave buoy (T2, Fig. 2). The Kalbådagrund station (measuring height 31.8 m) is located in the middle of the Gulf of Finland, about 20 km east of the operational GoF wave buoy. Both stations have been active during the entire period of the study, but there are long gaps in the Kalbådagrund data in August and September 2018.

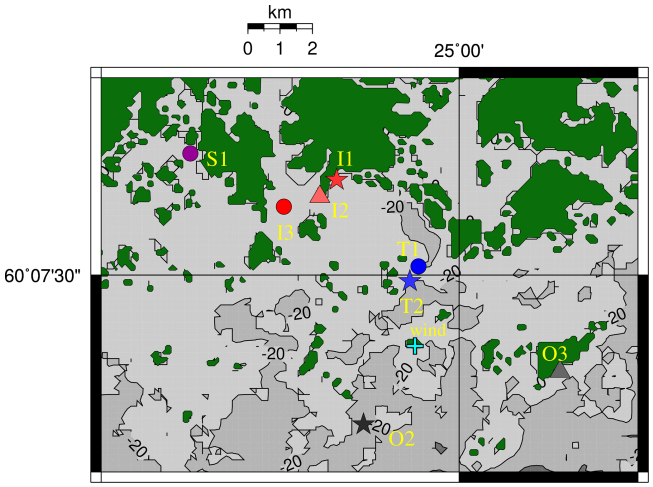

Figure 2. A more detailed map of the measurement locations close to the Helsinki shoreline. This area is marked with a black box in Fig. 1. See the caption of Fig. 1 for the explanation of the symbols.

The weather stations provided the wind speed and direction averaged over 10 min. We calculated the 30 min averages from these data to coincide with the time series used to compute a single wave spectrum. The mean wind speed at Harmaja and Kalbådagrund for the years 2016–2018 were 6.1 and 7.8 $\mathrm{m\,s^{-1}}$. The 80th percentiles were 8.7 and 11.0 $\mathrm{m\,s^{-1}}$, respectively. The corresponding values calculated from the data coinciding with the wave measurements at each location are given in Table 1.

2.3 Wave parameters and definitions

2.3.1 Spectral wave parameters

The wave buoys calculated the wave spectrum $E(f)$ ($\mathrm{m^2\,Hz^{-1}}$), where f (Hz) is the frequency. The nth order moment of the wave spectrum is

$$m_n = \int f^n E(f)\,\mathrm{d}f. \tag{1}$$

All integrals were evaluated up to 0.58 Hz without adding a parametric tail. Using these moments we defined most of the relevant wave parameters. The significant wave height H_{m_0} was defined as

$$H_{m_0} = 4\sqrt{m_0}. \tag{2}$$

A spectral version of the zero down-crossing period was defined as

$$T_{m02} = \sqrt{\frac{m_0}{m_2}}, \tag{3}$$

Table 1. The measurement time and depth at the different sites (see Fig. 1 for an overview). The mean and 80th and 20th percentiles are shown for the significant wave height (H_{m_0}), the peak frequency (f_p), the mean frequency (f_m), and the 30 min wind speed (U). The most probable value of the mean direction at the spectral peak (θ_p) is also shown. All available spectra between 2016 and 2018 (and the coinciding wind data) were used to compile these statistics.

			Mean	P_{80}	Mean	P_{20}	Mean	P_{20}	Most probable	Mean	P_{80}
Name (code)	Days	Depth	H_{m_0} (m)		f_p (Hz)		f_m (Hz)		θ_p (deg)	U (m s^{-1})	
Gulf of Finland (GoF)	790	62 m	0.80	1.22	0.23	0.16	0.29	0.23	245–255	7.7	10.9
Outer archipelago											
Harmaja (O1)	30	29 m	0.61	0.92	0.24	0.18	0.29	0.25	215–225	6.2	8.9
Isosaari (O2)	38	7 m	0.34	0.51	0.27	0.19	0.31	0.26	205–215	4.2	6.2
Berggrund (O3)	11	27 m	0.45	0.59	0.25	0.18	0.30	0.26	215–225	4.4	6.0
Transition zone											
Länsikari (T1)	10	10 m	0.49	0.65	0.24	0.20	0.30	0.27	185–195	7.3	9.9
Suomenlinna (T2)	662	22 m	0.33	0.50	0.29	0.19	0.34	0.29	195–205	6.1	8.7
Itä-Villinki (T3)	31	9 m	0.28	0.49	0.24	0.18	0.31	0.27	135–145	6.5	8.7
Inner archipelago											
Hernesaari (I1)	31	13 m	0.20	0.29	0.28	0.22	0.33	0.30	155–165	7.1	9.1
Ruumiskari (I2)	28	12 m	0.24	0.40	0.30	0.19	0.35	0.31	145–155	8.3	12.0
Jätkäsaari (I3)	30	13 m	0.17	0.27	0.30	0.22	0.35	0.31	165–175	6.2	9.3
Sheltered archipelago											
Koivusaari (S1)	27	5 m	0.05	0.08	0.42	0.32	0.41	0.38	175–185	4.4	6.6
Ramsinniemi (S2)	31	9 m	0.05	0.08	0.45	0.33	0.42	0.38	115–125	6.5	8.7
Vuosaaren satama (S3)	14	8 m	0.02	0.04	0.48	0.39	0.43	0.41	155–165	4.3	6.2
Talosaari (S4)	33	7 m	0.02	0.03	0.49	0.44	0.45	0.41	195–205	4.6	7.0

while the mean frequency was given by

$$f_\mathrm{m} = \frac{m_1}{m_0}. \tag{4}$$

We defined the peak frequency as

$$f_\mathrm{p} = \arg\max_f E(f), \tag{5}$$

i.e. the frequency where the wave spectrum has its maximum value. Because of the discrete frequency intervals and statistical variations in the spectrum, several methods for calculating the peak frequency have been proposed. In this paper we calculated f_p using a parabolic fit. We, however, also applied an integrated definition (Young, 1995):

$$f_\mathrm{p}^q = \frac{\int f E(f)^q \,\mathrm{d}f}{\int E(f)^q \,\mathrm{d}f}, \tag{6}$$

where q in a positive integer. Note that for $q = 1$, Eq. (6) equals the mean period f_m given by Eq. (4).

2.3.2 Wave parameters from time series

We also determined wave parameters directly from the 30 min vertical displacement time series, $\eta(t)$.

The significant wave height, H_s, was defined as

$$H_\mathrm{s} = 4\sigma(\eta), \tag{7}$$

where σ is the standard deviation. This definition is identical to Eq. (2) with the exception of the statistical variability introduced by the window tapering of the time series before calculating the spectrum.

The traditional definition of the significant wave height is the mean height of the highest one-third of the individual waves in the time series. To distinguish it from the significant wave height calculated using the variance, we will denote this parameter $H_{1/3}$. The individual waves were determined between two zero down-crossings, sorted in descending order, and the mean was calculated as

$$H_{1/3} = \frac{1}{N/3}\sum_{i=1}^{N/3} H_i, \tag{8}$$

where H_i is the height of a single wave and N is their total number.

The zero down-crossing period, T_z, was calculated as

$$T_\mathrm{z} = \frac{T}{N}, \tag{9}$$

where T is the length of the time series $\eta(t)$.

Assuming that $\eta(t)$ is Gaussian, $T_z = T_{m_{02}}$; assuming that H_i values are Rayleigh distributed, $H_s = H_{m_0} = H_{1/3}$.

2.3.3 Spectral width parameters

Several parameters to quantify the spectral width have been proposed. The width parameter ε (Cartwright and Longuet-Higgins, 1956) depends on the fourth moment, m_4, and is therefore sensitive to noise in the higher frequencies.

Longuet-Higgins (1975) defined a spectral width parameter, ν, as

$$\nu = \sqrt{\frac{m_0 m_2}{m_1^2} - 1}, \tag{10}$$

which, to a certain degree, suffers from similar issues as ε. Two other width (narrowness) parameters were used in this study. The first was the κ^2 parameter of Battjes and van Vledder (1984):

$$\kappa^2 = \frac{1}{{m_0}^2}\left(\left[\int_0^\infty E(f)\cos\left(\frac{2\pi f}{f_{m_{02}}}\right)\mathrm{d}f\right]^2 + \left[\int_0^\infty E(f)\sin\left(\frac{2\pi f}{f_{m_{02}}}\right)\mathrm{d}f\right]^2\right), \tag{11}$$

where $f_{m_{02}} = T_{m_{02}}^{-1} = \sqrt{m_2/m_0}$. This parameter was used as the main way to quantify the width of different spectral shapes. The other parameter was the Goda peakedness parameter (Goda, 1970), defined as

$$Q_p = \frac{2}{m_0^2}\int f E(f)^2 \mathrm{d}f. \tag{12}$$

The Goda peakedness parameter was needed in the definition of the Benjamin–Feir index (BFI; Janssen, 2003), which is essentially the wave steepness divided by the spectral width. We used the BFI to quantify its possible connection with single waves that are high compared to the significant wave height, i.e. so called "rogue waves", where $H/H_s > 2$. The formulation given by Serio et al. (2005) is

$$\mathrm{BFI} = \sqrt{m_0} k_p Q_p \sqrt{2\pi}\alpha_0 \sqrt{\frac{|\beta_{\mathrm{BFI}}|}{\alpha_{\mathrm{BFI}}}}, \tag{13}$$

where the peak wavenumber, k_p, is estimated from f_p using linear wave theory. The coefficients $\alpha_0, \alpha_{\mathrm{BFI}}$, and β_{BFI} depend on the dimensionless depth, $k_p h$. Their exact expressions are given by, for example, Serio et al. (2005).

2.4 Choosing wave spectra and spectral scaling

Data were available from more locations than the 14 presented in this paper (Kahma et al., 2016). We, however, excluded some stations based on the following: (i) very small maximum wave heights, meaning that the wave buoy was often unable to measure the entire spectrum; (ii) the location was not even remotely exposed to open-sea waves (a determining factor for the archipelago type spectrum); or (iii) the location was too exposed to external disturbances, such as wave reflection or ship wakes.

As a loose definition of well defined wave conditions we used the 80th percentile of the significant wave height as a cut-off for each location. The 80th percentiles for the 13 coastal locations were determined using all available data. For the GoF, only data from the years 2016–2018 were used to keep the measurement period comparable with the Suomenlinna (T2) observations. In addition we used a cut-off of $U \geq 5\,\mathrm{m\,s^{-1}}$, where U is the 30 min average wind speed. For the GoF wave buoy, we used the Kalbådagrund data, while Harmaja wind data were used for all other locations. For the nearshore locations, only onshore winds were considered ($70° \leq U_d \leq 250°$), while no restrictions on the wind direction was set for the GoF. Henceforth, we will call this data set the P80 data set.

The choice of the 80th percentile was a compromise between (i) removing the smallest wave heights, e.g. $H_s < 0.5$ at Suomenlinna (T2), since they are bound to be noisy, and (ii) not excluding too much data from the limited data sets available from the short measurements. Using a different cut-off for the significant wave height (60–90th percentiles) resulted in very similar results. We also tried setting restrictions with respect to the steadiness of the wind direction and the wind speed, but imposing these additional restrictions resulted in very similar results and identical conclusions. To avoid adding unnecessary complexity, these additional constraints were dropped. Also, some of the highest wave heights at the GoF buoy were measured during a time when no wind data were available (August–September 2018). Cases with missing wind data were therefore included if they fulfilled the conditions set for the significant wave height.

Because the short waves are generated by the shortest fetch, they are least affected by the varying spectral shape inside the archipelago. The chosen spectra were therefore normalised using the values at the high frequencies ($f > 0.4\,\mathrm{Hz}$). The scaled spectra were calculated as

$$\widetilde{E}(f) = \frac{E(f) f_0^4}{\beta}, \tag{14}$$

where

$$\beta = \langle E(f) f^4 \rangle_{f > f_1}, \tag{15}$$

f_0 is any fixed frequency, and the brackets signify a mean value over frequencies $f > f_1$. We chose $f_0 = f_1 = 0.4\,\mathrm{Hz}$

for simplicity, but the two frequencies need not be the same. The exact value of f_1 is unimportant as long as the spectrum follows some kind of power law for higher frequencies. If an f^{-4} power law exists, the frequency f_1 can even change between spectra and still provide a consistent normalisation. Nevertheless, since we had no reliable way of determining the starting point of the power laws in the spectra, we chose a frequency that was sufficiently high for the strong wind conditions that are represented in the P80 data set.

The frequencies were then normalised with respect to the mean frequency and the spectra, $\widetilde{E}$, were interpolated to a common set of dimensionless frequencies, $\widetilde{f} = f/f_{\mathrm{m}}$. This resulted in the final scaled spectra $\widetilde{E}(\widetilde{f})$. The mean frequency was chosen instead of the peak frequency because it is more stable. Using this same data set Björkqvist et al. (2019a) found that the peak frequency can be highly noisy in the archipelago, and this parameter is therefore unusable to scale the spectra. The choice of a good characteristic frequency for archipelago conditions will be studied in Sect. 4.5.

2.5 Determining groups

The 13 measurement stations in the archipelago were divided into four groups based on a visual estimation of the geographical conditions. The attenuation coefficients for the significant wave height compared to the GoF wave buoy were used as a crude check to ensure that the visual determination of the amount of sheltering was reasonable. The attenuation coefficients, K, were determined by a linear fit using the effective variance method (Orear, 1982). The different groups, visible in Fig. 1, can be described as follows.

Outer archipelago (O1–O3). The locations are not inside the archipelago, but the effect of the finite depth and/or the limited fetch caused by the irregular shoreline might be visible in the wave spectrum. Although the O2 station (Harmaja) seems to be very exposed, Björkqvist et al. (2017a) have shown that the wave field here is already restricted by the peninsula of Porkkalanniemi for south-westerly winds. The attenuation coefficients for the significant wave height were $K = 0.6$–0.7.

Transition zone (T1–T3). The sheltering of the islands plays a significant role in shaping the wave field, but the longer waves propagating from the GoF are still somewhat dominant. The attenuation coefficients for the significant wave height were all $K = 0.4$.

Inner archipelago (I1–I3). There is a clearly defined local fetch, but there is still a significant contribution from longer propagating waves. The attenuation coefficients for the significant wave height were $K = 0.2$.

Sheltered archipelago (S1–S4). These locations should be dominated by the locally generated waves. Residuals of longer waves can, however, still be present. The attenuation coefficients for the significant wave height were very small (all $K < 0.10$).

The common denominator throughout the archipelago is that the waves travel slower than the wind. Thus, the longer waves propagating from the open sea are not swell. In this paper we will show that the sheltering effect of the archipelago is a continuum and several reasonable classifications could therefore be made. The main purpose of the classification was to make the results more presentable.

3 The archipelago spectrum

3.1 Transition from peaked to flat spectra

The main result of this section is that the wave spectrum transitioned from a, more traditional, single-peaked spectrum to a flat spectrum inside the archipelago. The transition was continuous, as readily seen in Fig. 3. In the outer archipelago (black) the mean spectrum had a very similar shape to the open-sea conditions observed at the GoF wave buoy (green). Namely, it had a single peak even if it lacked the overshooting of an even more peaked fetch-limited spectrum.

When moving closer towards the coast the spectral shape started to flatten out in the transition zone (blue). Länsikari (T1) and Suomenlinna (T2) are located very close to each other (Fig. 2), and the similar spectral shapes give confidence to the fact that we captured the shape of the mean spectrum even with the shorter measurement time series. Although the mean spectral profiles in the transition zone were still peaked, the rear face of the spectrum was starting to collapse. In contrast to the outer archipelago, the mean spectra in the transition zone decayed slower than $\widetilde{f}^{-4}$ just above the spectral peak. Especially T3 was showing a clear collapse towards a flat spectral shape.

In the inner archipelago (red) the spectral shape had collapsed around the peak and exhibited a constant energy in a broad frequency interval ($0.6 f_{\mathrm{m}} \leq f \leq 1.1 f_{\mathrm{m}}$). Even if the peak frequency could be reliably determined – which is challenging because of the statistical variability – it is obvious that it would not characterise the spectrum in a similar fashion as the spectral peak in, for example, the outer archipelago. There were, however, small low-frequency peaks, most notably at Jätkäsaari (I3). Relying on the directional spectrum from this same site presented by Björkqvist et al. (2017b), we concluded that these peaks were caused by refracted narrowband waves. These kinds of peaks are therefore expected to be specific to the bathymetrical conditions of the area.

In the sheltered archipelago (magenta) even these attenuated low-frequency peaks were no longer visible. The mean spectrum at Koivusaari (S1) was still flat (in a similar fashion to sites I1–I3), but for the other sheltered locations the spectra almost transitioned back to a single-peaked shape – the local fetch was starting to dominate over the very attenuated longer waves. The tail of the spectrum was not determined

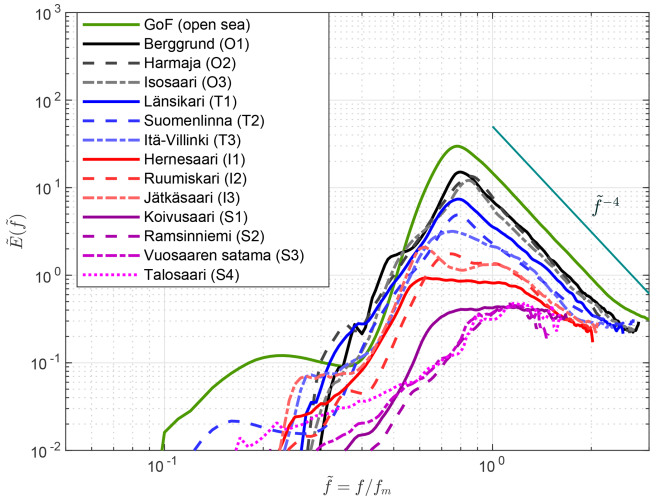

Figure 3. The mean wave spectra divided into the open sea and four archipelago areas: outer archipelago (O1–O3), transition zone (T1–T3), inner archipelago (I1–I3), and sheltered archipelago (S1–S4). An overview of the locations can be found in Fig. 1.

reliably, since these short waves were often not captured by the wave buoy.

3.2 Quantifying the spectral width

We quantified the change in width (or more exactly, narrowness) of the spectrum using the κ^2 narrowness parameter (Eq. 11) of Battjes and van Vledder (1984). The mean width of the wave spectrum changed when moving into the archipelago, with κ^2 being 0.03–0.07 in the inner archipelago (signalling a wide spectrum), while being 0.18–0.19 in the outer archipelago (Table 2). The values in the outer archipelago were close to the one at the open-sea location in the GoF. As an example, we also calculated the κ^2 parameter for the single storm spectrum of the measured maximum 5.2 m significant wave height during the easterly Antti storm in 2012. The value of $\kappa^2 = 0.33$ was higher than the average value at the GoF, but this storm spectrum is affected by the narrow fetch geometry of the GoF, which leads to a less peaked spectrum (Pettersson, 2004). Higher values (up to $\kappa^2 = 0.46$) were found at the GoF.

The spectral width in the transition zone was in between those of the outer and inner archipelago ($0.08 \leq \kappa^2 \leq 0.15$). The almost identical width of T1 and T2, and the wider shape of T3, was in good agreement with what was determined visually from Fig. 3. The κ^2 values for the sheltered archipelago sites (S1–S4) were variable, which was a consequence of the wave buoys' issues with resolving the entire spectrum. The results from sites S1–S4 can therefore not be considered entirely reliable.

Quantifying the spectral width is no trivial matter, but the good agreement between the κ^2 parameter and the obvious visual changes suggests that the parameter is applicable over a wide range of conditions.

3.3 Directional dependence

Although the mean spectral profiles were shown to change when moving through the archipelago towards the shore, the spectral shape also varied with the wind direction because of the anisotropic fetch conditions. We used the wind direction because the instability of the spectral peak at Suomenlinna (T2) made it hard to define the dominant wave direction. The wave direction at the GoF buoy, again, collapses to be aligned with the gulf, thus causing a misalignment of up to 50° between the direction of the wind and the dominant waves (Pettersson et al., 2010). Nevertheless, the local fetch at Suomenlinna (T2) would still vary significantly within this large wind sector. Suomenlinna (T2) is the only location in the archipelago with enough data to partition it further with respect to the wind direction. This section will therefore be based on data from Suomenlinna (T2) only.

The most peaked spectra at Suomenlinna (T2) were generated by southerly winds (Fig. 4), since only small islands block the wave propagation in this direction (Fig. 1). For easterly winds, the spectral shape was flat, resembling the profiles of the inner archipelago (I1–I3, Fig. 3). Such a variation was identified already by Björkqvist et al. (2019a) when studying wave model performance against the Suomenlinna (T2) wave data, but our results showed a systematic behaviour. Importantly, the eastern wind directions showed a very flat mean spectrum even though the average shape over all wind directions was peaked. This discrepancy is explained by easterly winds not being dominant ($45° \leq U_d \leq 135°$ 10 % of the times). Nevertheless, strong easterly winds are possible in the GoF; the maximum significant wave height of 5.2 m at the GoF wave buoy has been measured twice, both during south-westerly winds (in 2001; Tuomi et al., 2011) and easterly winds (in 2012; Pettersson et al., 2013).

4 Implications

This section presents some implications of the results of Sect. 3. The quantification of the spectral narrowness, κ^2, revealed that the measurements from the sheltered archipelago (S1–S4) did not capture all the properties of the wave field reliably enough. The issue was connected to low wave heights that were not captured entirely by the 40 cm wave buoys, as seen in Fig. 3. The shorter measurements from the slightly more exposed transition zone, and inner and outer archipelago, showed consistent results, and they were deemed reliable.

When appropriate, the results make use of all available data. Nonetheless, especially Sect. 4.2–4.4 will rely only on the long time series from Suomenlinna in the transition zone

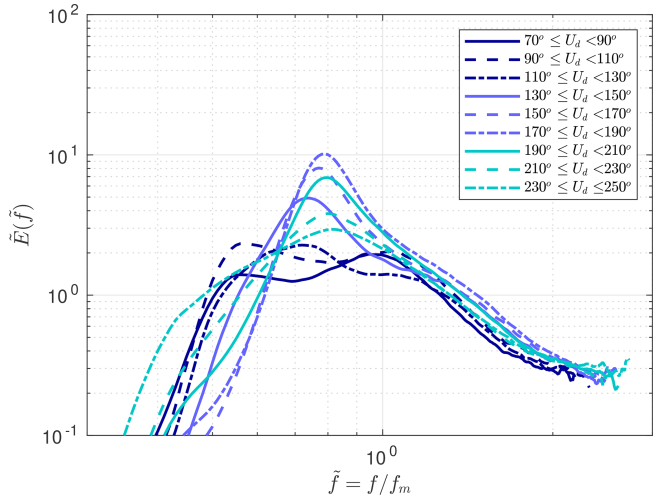

Figure 4. The mean wave spectra at Suomenlinna (T2) as a function of the wind direction.

(T2) and the GoF. Such an analysis was possible because these data captured a variety of spectral shapes depending on the amount of sheltering for different wind directions (Fig. 4). The advantages of using data from only T2 were that (i) the analysis was based on a long time series coinciding with open-sea wave measurements from the GoF, (ii) the water depth was constant for all spectral shapes, and (iii) the spectral tail was captured equally well for all different spectral shapes, because they were all measured at the same location with an identical device.

4.1 Confidence limits of significant wave height

The confidence limits of observed wave spectra follow a χ^2_k distribution, where k is the degrees of freedom determined by the number of averaged elementary bins. The confidence limits of the spectrum propagate to its integral, which is also the total variance of the wave field, m_0. By Eq. (2) the confidence limits of the observed significant wave height follow from those of m_0.

The final degrees of freedom (d.o.f.) of the integral of a measured spectrum depend on the shape of the spectrum in the following way (Donelan and Pierson, 1983):

$$\text{d.o.f.}(m_0) = \frac{k\left[\sum_{i=1}^{N} E(f)\right]^2}{\sum_{i=1}^{N}\left[E(f)\right]^2}. \tag{16}$$

It immediately follows that $\text{d.o.f.}(m_0) = kN$ for a white noise spectrum ($E(f) \equiv$ const.), while $\text{d.o.f.}(m_0) = k$ for an infinitely peaked spectrum ($E(f) = \delta(f - f_\text{p})$). Thus, a broader spectrum will have more d.o.f., leading to smaller confidence limits for the significant wave height.

In Sect. 3.2 we quantified the spectral width using the κ^2 parameter. The change in spectral width should also be seen in the d.o.f. calculated at the different locations. This was, indeed, the case: the d.o.f. in the inner archipelago were roughly 500–600, while the corresponding values in the outer archipelago were around 300 (Table 2). The transition zone, again, had values falling in between the inner and outer archipelago, with the d.o.f at site T3 being closest to the inner archipelago. In the open-sea location (GoF) the d.o.f. values of the variance were lower than anywhere in the archipelago, and the low d.o.f. of the single GoF storm spectrum went hand in hand with the large κ^2 value.

The increase in the d.o.f. in the archipelago had a direct implication for the confidence limits of the significant wave height: the confidence limits at the GoF wave buoy were 50 % larger than at the inner archipelago points (Table 2). The confidence limits of the single storm spectrum was twice that of the average value in the inner archipelago (12 % vs. 6 %).

Because the spectral shape depended strongly on the wind direction at Suomenlinna (T2), the confidence limits for easterly winds were close to those of the inner archipelago, while south-westerly – and especially southerly – winds resulted in confidence limits in line with the open sea (Fig. 5a). By comparing the d.o.f. to the κ^2 parameter it is obvious that they were both quantifying a similar property of the spectrum (Fig. 5b). The correlation between these two parameters was $r = -0.94$, and also the Goda peakedness parameter (Eq. 12) was correlated ($r = -0.86$) with the d.o.f. of the spectrum (Fig. 5c).

The correlation between the d.o.f. and the spectral width parameter ν by Longuet-Higgins (1975) was only $r = 0.2$ (Fig. 5d), and the correlation was equally low for the spectral width parameter ε proposed by Cartwright and Longuet-Higgins (1956) (not shown).

4.2 The significant wave height: $H_{1/3}$ vs. H_s

The significant wave height is the most central and widely used wave parameter. Still, it can be defined in a couple of different ways. The connection between the definition using the mean height of the highest one-third of the single waves and the definition based on the variance of the vertical displacement was made based on the assumption of a narrowband spectrum, deep water, and that the height of single waves are Rayleigh distributed with the parameter $\sqrt{4m_0}$. These conditions lead to a proportionality constant of 4 in the equality,

$$H_{1/3} = 4\sqrt{m_0} = 4\sigma(\eta). \tag{17}$$

Studies have shown, however, that the assumption of a Rayleigh distribution (with a parameter $\sqrt{4m_0}$) for the height of individual waves predicts higher values of $H_{1/3}/H_\text{s}$ compared to observations (Forristall, 1978; Longuet-Higgins, 1980; Casas-Prat and Holthuijsen, 2010). The discrepancy has been solved, for example, by assuming a Weibull distri-

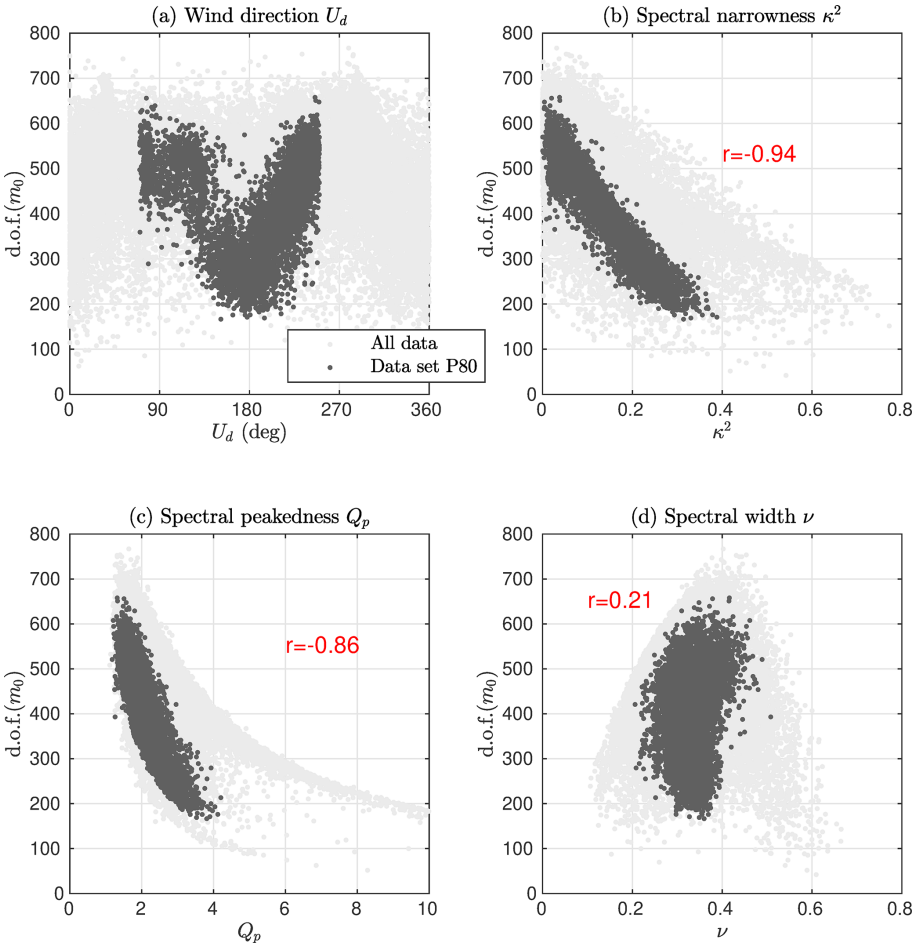

Figure 5. The degrees of freedom of the Suomenlinna (T2) wave variance as a function of the wind direction **(a)** and the different spectral width and narrowness parameters **(b–d)**.

bution (Forristall, 1978) or by simply scaling the Rayleigh parameter as $\alpha\sqrt{4m_0}$ (Longuet-Higgins, 1980). The use of a scaled Rayleigh distribution modifies Eq. (17) to

$$H_{1/3} = 4\alpha\sqrt{m_0}. \tag{18}$$

Longuet-Higgins (1980) determined α as a function of the spectral width:

$$\alpha = \sqrt{1 - \left(\frac{\pi^2}{8} - \frac{1}{2}\right)\nu^2}, \tag{19}$$

where ν is the spectral width parameter of Longuet-Higgins (1975) (Eq. 10). Since the original derivation of Eq. (17) assumed a narrowband spectrum with symmetrical Gaussian water level displacements, we expected that the two definitions for the significant wave height would vary even more in the archipelago than previously observed for open-sea conditions.

We determined the fit between $H_{1/3}$ (Eq. 8) and H_s (Eq. 7) that was calculated from the vertical displacement time series. The fit to the Suomenlinna (T2) P80 data set was $H_{1/3} = 0.881 H_s$ (Fig. 6a), which is a stronger deviation from Eq. (17) than found by previous studies (Table 3). The coefficient depended on the wind direction in a similar fashion as the spectral shape shown in Fig. 4; the more peaked spectral shapes of the southerly winds resulted in a proportionality constant of 0.90, while the corresponding value for the flat easterly spectra was around 0.86 (Fig. 6c).

Vandever et al. (2008) found that $H_{1/3}/H_s$ depended on the spectral width and determined a best fit of $H_{m_0}/H_{1/3} = 0.996 + 0.181\nu$ from Doppler wave gauge data. We note that calculating the ratio α from Eq. (19) using ν, as proposed by Longuet-Higgins (1980), increased the disagreement with our data for both Suomenlinna (T2) and GoF (Table 3). The value determined empirically by Longuet-Higgins (1980) using the data of Forristall (1978) (0.925) was, however, in very close agreement with 0.927 determined from our GoF data. The issue might have been caused by the reliable determi-

Table 2. Mean values of the spectral narrowness parameter (κ^2) and the number of degrees of freedom for the variance of the wave field. The mean values are calculated only from the data set P80. In the confidence limits, $\hat{H}_{m_0}$ denotes a sample from a wave field with a significant wave height of H_{m_0}.

Name (code)	$<\kappa^2>$	<d.o.f.(m_0)>	95 % confidence limits
Single storm spectrum (GoF)	0.33	132	$0.88 < \hat{H}_{m_0}/H_{m_0} < 1.12$
Gulf of Finland (GoF)	0.22	234	$0.91 < \hat{H}_{m_0}/H_{m_0} < 1.09$
Outer archipelago			
Harmaja (O1)	0.19	316	$0.92 < \hat{H}_{m_0}/H_{m_0} < 1.08$
Isosaari (O2)	0.19	323	$0.92 < \hat{H}_{m_0}/H_{m_0} < 1.08$
Berggrund (O3)	0.18	309	$0.92 < \hat{H}_{m_0}/H_{m_0} < 1.08$
Transition zone			
Länsikari (T1)	0.15	370	$0.93 < \hat{H}_{m_0}/H_{m_0} < 1.07$
Suomenlinna (T2)	0.14	410	$0.93 < \hat{H}_{m_0}/H_{m_0} < 1.07$
Itä-Villinki (T3)	0.08	454	$0.93 < \hat{H}_{m_0}/H_{m_0} < 1.06$
Inner archipelago			
Hernesaari (I1)	0.07	485	$0.94 < \hat{H}_{m_0}/H_{m_0} < 1.06$
Ruumiskari (I2)	0.05	524	$0.94 < \hat{H}_{m_0}/H_{m_0} < 1.06$
Jätkäsaari (I3)	0.03	577	$0.94 < \hat{H}_{m_0}/H_{m_0} < 1.06$
Sheltered archipelago			
Koivusaari (S1)	0.13	496	$0.94 < \hat{H}_{m_0}/H_{m_0} < 1.06$
Ramsinniemi (S2)	0.35	367	$0.93 < \hat{H}_{m_0}/H_{m_0} < 1.07$
Vuosaaren satama (S3)	0.27	394	$0.93 < \hat{H}_{m_0}/H_{m_0} < 1.07$
Talosaari (S4)	0.27	347	$0.93 < \hat{H}_{m_0}/H_{m_0} < 1.07$

nation of ν; the mean value of $\nu = 0.36$ (GoF) is lower than $\nu = 0.41$–0.83 reported by Vandever et al. (2008), although their data had swell present. We instead determined a linear fit using the narrowness parameter κ^2 and our Suomenlinna (T2) data, which resulted in $H_{1/3}/H_s = 0.85 + 0.15\kappa^2$ (Fig. 7a). For an infinitely narrow spectrum ($\nu = 0$, $\kappa^2 = 1$), both fits result in approximately unity, which is in accordance with the narrowband assumption used to derive Eq. (17).

Even for the southerly waves at Suomenlinna (T2) $H_{1/3}/H_s$ was no higher than 0.90. It is therefore possible that the finite water depth (22 m at Suomenlinna) affected the results to a certain degree. The ratio $H_{1/3}/H_s$, however, showed a *negative* correlation ($r = -0.52$) with the dimensionless depth, $k_p h$, meaning that the largest deviations from deep-water values are found for the cases where the water is deepest (relative to the waves). This is the opposite of what we would expect if the deviation from Eq. (17) was indeed caused by the finite depth effects. The apparent correlation was created by more sheltering simultaneously leading to both shorter waves (i.e. higher $k_p h$) and a wider wave spectrum. The wider spectrum can then explain the discrepancy through the κ^2 parameter as outlined above. We concluded that the deviation from Eq. (17) was mainly caused by the spectral shape, not the finite depth at the measurement site.

4.3 Single wave statistics: H_{max}/H_s

The highest expected single wave is often of considerable interest, and usually this single wave is given relative to the significant wave height. The estimate is made based on the assumption that the height of the single waves are either Rayleigh or Weibull distributed. The estimated highest single wave thus depends on the assumed distribution and the number of waves encountered during the measurement period (N).

We determined the highest single wave from the vertical displacement time series of the P80 data sets. For the GoF, the connection between the single wave height and the significant wave height was determined to be $H_{max} = 1.61 H_s$ using a linear fit. The coefficient 1.61 was lower than assuming the Rayleigh distribution of Longuet-Higgins (1952), but it was in good agreement with the prediction of Forristall (1978) and Casas-Prat and Holthuijsen (2010) (Table 3). The maximum crest height at the GoF were well predicted by Casas-Prat and Holthuijsen (2010), but the wave troughs (η_{min}) agreed better with Longuet-Higgins (1980).

The linear regression to the Suomenlinna (T2) data was $H_{max} = 1.58 H_s$ (Fig. 8a). The ratio was lower compared to the GoF even though we would expect the higher N

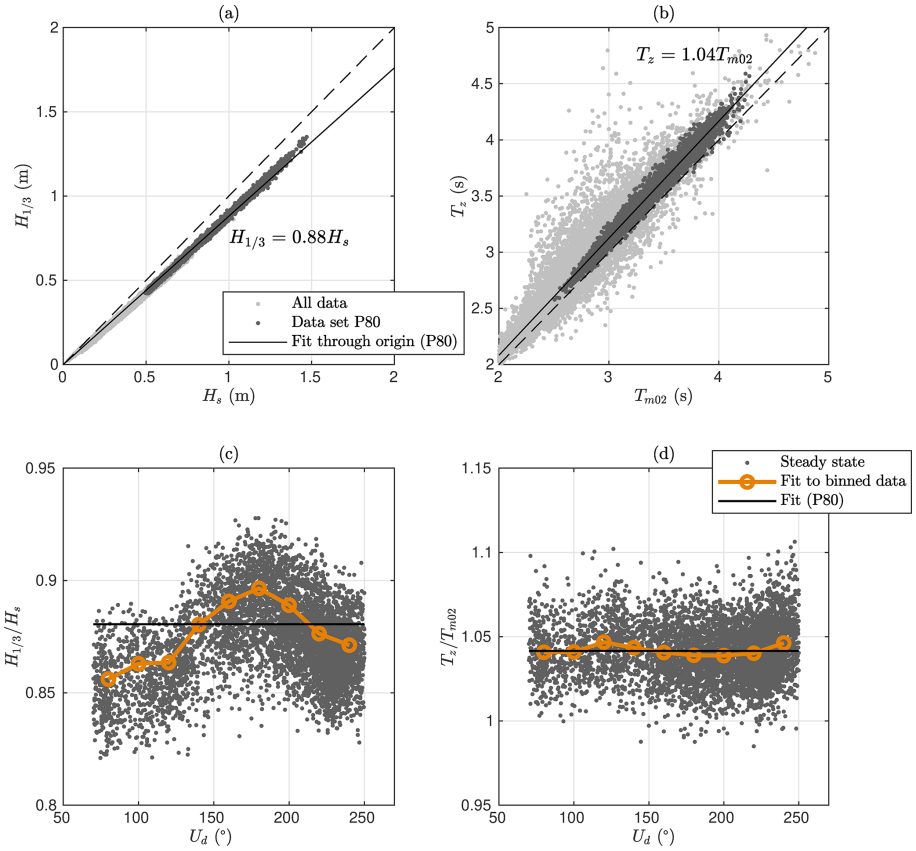

Figure 6. Comparison of $H_{1/3}$ and T_z with respect to H_s and T_{m02} at Suomenlinna (T2). In panels **(c)** and **(d)** the ratios are given as a function of the wind direction.

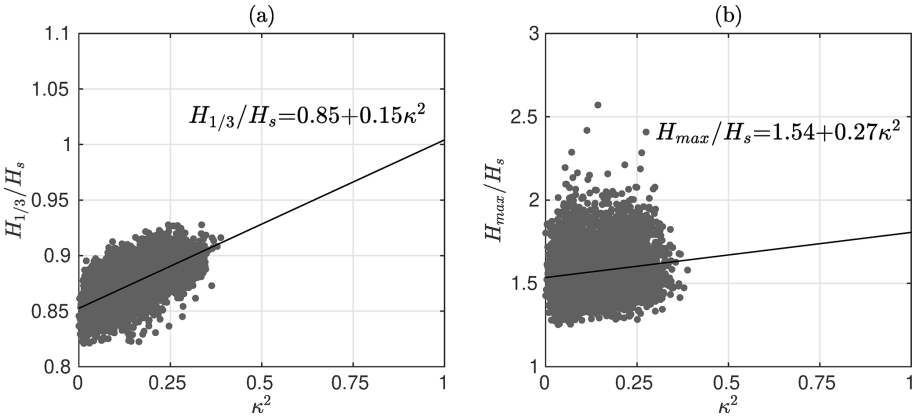

Figure 7. $H_{1/3}$ **(a)** and $H_{\max}$ **(b)** at Suomenlinna (T2) relative to the significant wave height. The ratios are plotted against the spectral narrowness κ^2. For an infinitely narrow spectrum ($\kappa^2 = 1$), the linear regressions ($H_{1/3}/H_s = 1.00$ and $H_{\max}/H_s = 1.81$) are in good agreement with the theoretical predictions that Longuet-Higgins (1952) derived for a narrowband spectrum (Table 3).

at Suomenlinna (caused by shorter waves) to result in a higher single wave $H_{\max}/H_s$. The disagreement with previous studies was also more pronounced (Table 3). We determined a linear fit with the spectral narrowness to be $H_{\max}/H_s = 1.54 + 0.27\kappa^2$ (Fig. 7b). This regression results in $H_{\max}/H_s = 1.81$ for a theoretical infinitely peaked spectrum ($\kappa^2 = 1$), which is in good agreement with the theoretical derivations of Longuet-Higgins (1952) that assumed a narrowband spectrum (Table 3). Nevertheless, the very low correlation between the variables ($r = 0.15$) limits the confidence in this specific result. Vandever et al. (2008) found no connection between $H_{\max}/H_{1/3}$ and ν. The correlation be-

Table 3. The different wave height and crest height parameters at the Gulf of Finland (GoF) and Suomenlinna (T2). The values have been determined using a linear fit through the origin of the P80 data set. The ratio $H_{1/3}/H_s$ was taken as reported in the literature. The single wave statistics for the distributions given in the literature have been determined using the individual number of waves for each wave record and the mean value of the spectral width parameter ν (when given).

	$H_{1/3}/H_s$	H_{max}/H_s	η_{max}/H_s	η_{min}/H_s
Gulf of Finland (GoF)				
Measured (this study)	0.927	1.61	0.93	−0.85
Longuet-Higgins (1952) [a]	1	1.80	0.90	−0.90
Forristall (1978) [b]	0.942	1.64	–	–
Longuet-Higgins (1980) [c]	0.925	1.67	0.84	−0.84
Longuet-Higgins (1980)[c] ($\nu = 0.361$)	0.951	1.72	0.86	−0.86
Casas-Prat and Holthuijsen (2010) [d]	0.957	1.63	0.93	−0.90
Suomenlinna (T2)				
Measured (this study)	0.881	1.58	0.92	−0.83
Longuet-Higgins (1952) [a]	1	1.84	0.92	−0.92
Forristall (1978) [b]	0.942	1.68	–	–
Longuet-Higgins (1980) [c]	0.925	1.71	0.85	−0.85
Longuet-Higgins (1980)[c] ($\nu = 0.335$)	0.958	1.77	0.88	−0.88
Casas-Prat and Holthuijsen (2010) [d]	0.957	1.67	0.95	−0.92

[a] Assuming a narrowband spectrum in deep water, Gaussian water level elevations with respect to the still water level, and a Rayleigh distribution for the heights of single waves. [b] Empirical Weibull fit to storm data. [c] Empirical Rayleigh fit to the storm data of Forristall (1978). [d] Empirical Rayleigh fit based on 15 years of measurements from four wave buoys.

tween $H_{max}/H_{1/3}$ and κ^2 was zero also in our data, most probably because of the self-scaling nature of $H_{max}/H_{1/3}$.

The maximum crest height, η_{max}/H_s, at Suomenlinna (T2) was only slightly lower than at the GoF (Table 3). If symmetry would be assumed, the maximum crest heights would be in perfect agreement with the estimates from the Rayleigh distribution of Longuet-Higgins (1952), which was also found by Casas-Prat and Holthuijsen (2010). The troughs were slightly shallower in our data compared to, for example, Casas-Prat and Holthuijsen (2010), but they were well described by the scaled Rayleigh distribution of Longuet-Higgins (1980). There was no correlation between η_{max}/H_s (or η_{min}/H_s) and the spectral narrowness κ^2 ($r = 0.0$).

None of the aforementioned dimensionless wave or crest heights had any correlation with the dimensionless depth, $k_p h$ ($r = 0.0$). Together these results suggests that the main factor controlling the magnitude of the highest single waves was the spectral shape. Thus, the differences from previous results were mainly caused by the violation of the assumption of a narrowband spectrum, not the assumption of deep water. The exceptions were the crest and trough heights, which exhibited no connection to the spectral width.

The maximum single wave measured at Suomenlinna (T2) was H_{max}=2.92 m ($H_{max}/H_s = 2.41$), having a crest height of $\eta_{max} = 1.54$ m. This wave was measured during south-easterly winds ($U_d = 152°$). It is evident from Fig. 7b that a ratio over 2 was not a rare occurrence, since it happened 45 times during the 3-year deployment period of the buoy. Still, the criterion of (roughly) $H_{max}/H_s > 2$ is often taken as a definition for "rogue waves" (e.g. Onorato et al., 2002). Also Casas-Prat and Holthuijsen (2010) found thousands of single waves exceeding twice the significant wave height. The generation of rogue waves has been proposed to be controlled by modulation instability (Janssen, 2003), which is quantified using the Benjamin–Feir index (Eq. 13). Nevertheless, the correlation between BFI and H_{max}/H_s (or η_{max}/H_s) was only 0.1 for the Suomenlinna (T2) P80 data set (not shown). The lack of descriptive power of the BFI is expected, because the modulation instability is strongest for narrowband spectra – the exact opposite of the conditions that we have observed in the archipelago.

4.4 The zero-crossing period, T_z

As for the significant wave height, the zero-crossing period, T_z, is one of the oldest wave parameters. Based on theoretical arguments about the Gaussian distribution of the water level displacement, it can be calculated from the spectral moments as $T_{m_{02}}$ (Eq. 3). Since this connection is based on theoretical assumptions, it might not be valid for atypical spectral shapes, such as the ones found in the archipelago.

We compared these two definitions of the zero-crossing period using a linear fit to the P80 data sets. For the GoF data, the two definitions agreed well, with a linear fit giving a proportionality coefficient of 1.02. For the Suomenlinna (T2) data, the linear fit was $T_z = 1.04 T_{m_{02}}$ (Fig. 6c), meaning that the traditional definition of the zero-crossing period was

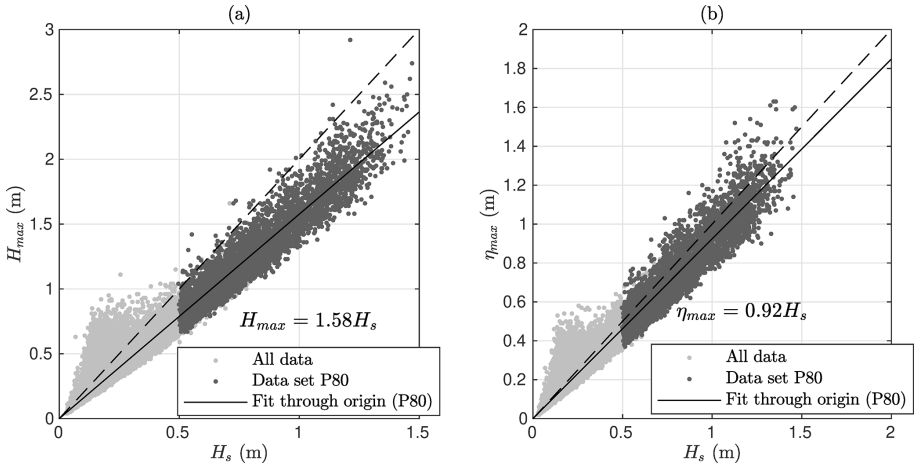

Figure 8. The wave height of the single highest wave ($H_{\max}$, **a**) and the maximum crest height ($\eta_{\max}$, **b**) relative to the significant wave height, H_{S}, at Suomenlinna (T2).

quite robust and coincided well with the one calculated from the spectral moments over a wide range of spectral shapes. In the Suomenlinna (T2) data the ratio $T_{\mathrm{z}}/T_{m_{02}}$ was only weakly correlated with the κ^2 narrowness parameter ($r = -0.18$). A linear fit ($T_{\mathrm{z}}/T_{m_{02}} = 1.05 - 0.04\kappa^2$) still gave almost unity for a theoretical narrowband spectrum ($\kappa^2 = 1$).

The ratio $T_{\mathrm{z}}/T_{m_{02}}$ at Suomenlinna (T2) was also correlated with the dimensionless depth $k_{\mathrm{p}}h$ ($r = -0.16$). The explanation for this, possibly spurious, correlation might be the same as for the significant wave height, namely that more sheltering results in both a wider spectrum and a deeper dimensionless depth. Nonetheless, the sign of the correlation was what would be expected if the variations were really explained by the variations in dimensionless depth. The reason for the slight 4 % bias at Suomenlinna (T2) was therefore left undetermined.

4.5 Finding a characteristic frequency, f_{c}

Often the full spectrum is not available, and the characteristics of the wave field are described using a limited set of integrated parameters. If directionality is ignored, the choice is usually a measure for the height and a measure for the length, or equally well the frequency. A unimodal spectrum, for example, is quite well described by the significant wave height and the peak frequency. Nevertheless, the flat spectral shape in the archipelago leads to a low stability of the peak frequency. The mean frequency, again, is stable but biased compared to the peak frequency for the more unimodal spectra in the outer archipelago.

Young (1995) proposed a definition for the peak frequency, f_{p}^q, that is based on a weighted mean integral of the spectrum (Eq. 6). This expression has a free parameter, q, that needs to be determined. We set out to study if any exponent of q could produce a characteristic frequency (henceforth, f_{c}) that would be more stable than simply taking the argument maximum of the spectrum but still would not be as biased as f_{m} compared to the peak frequency. The challenge in choosing a value for q is that minimising the scatter suggests low values for q (with q=1 resulting in f_{m}), while minimising the bias compared to f_{p} requires a high value for q. To determine a best estimate, we defined an error function:

$$\mathrm{Er}(q) = \left[\langle f_{\mathrm{p}} - f_{\mathrm{p}}^q \rangle^2 + \left(\sigma(f_{\mathrm{p}}^q) \right)^2 \right]^{\frac{1}{2}}, \tag{20}$$

where $\langle \cdot \rangle$ denotes the mean and σ is the standard deviation. In other words, it is the norm of the bias and the standard deviation of f_{p}^q.

We determined this error function for each location separately using the P80 data set. The minimum was achieved between $q = 3$ and $q = 5$, with the exception of the sheltered archipelago sites ($q = 2$–3). These values are in line with $q = 4$ of Young (1995) but lower than $q = 8$ of Sobey and Young (1986), which the authors recommended for an alternative definition of the peak frequency.

In addition to a best estimate of $q = 4$ we compared the peak frequency to f_{p}^q using the values $q = 1$ and $q = 10$. As a metric quantifying how different candidates for f_{c} characterise the spectrum, we determined the relative amount of energy that is carried by waves below the characteristic frequency, i.e.

$$E_0(f_{\mathrm{c}}) = \frac{1}{m_0} \left(\int_0^{f_{\mathrm{c}}} E(f)\, \mathrm{d}f \right). \tag{21}$$

In the GoF data roughly 65 % of the energy was below the mean frequency regardless to the wind direction ($E_0(f_{\mathrm{m}}) \approx 0.65$, Fig. 9c). For the peak frequency, the respective value was 29 %, but it varied with the wind direction, being as high

as 40 % for southerly winds. The southerly wind sector produces waves that are unaffected by the narrow fetch geometry of the gulf. They should therefore most closely resemble classic fetch-limited spectra, although they might still be affected by swell propagating along the gulf, especially from the Baltic Proper in the west. With a choice of $q = 4$ the integrated parameter f_p^q agreed well with the peak frequency for southerly winds in the GoF data set (Fig. 9c). For other wind directions, where the narrow fetch effects came into play, $f_p^{q=4}$ resulted in slightly higher frequency estimates compared to f_p (Fig. 9c). Since the most dominant wind directions are along the axis of the Gulf, it is clear that $f_p^{q=4}$ does not produce an unbiased estimate in a general sense. A choice of $q = 10$ introduced practically no bias, and it can therefore be used as an alternative definition for the peak frequency (Table , Fig. 9c).

For Suomenlinna (T2), $f_p^{q=4}$ also showed a good general agreement with the peak frequency, and the mean value of $E_0(f_p^{q=4})$ was almost identical (35 % vs. 34 %) to the one determined for the GoF (Fig. 9b and d). The energy below the mean frequency was, on average, only 60 %, but this value depended strongly on the wind direction. For the southerly winds – where the spectral shape was most peaked – $E_0(f_m)$ agreed with the GoF data. For the wider spectra of the other wind directions, the two sites disagreed; especially for eastern winds the amount of energy below the mean frequency was only slightly above 50 %, which would be the value for a theoretical white noise spectrum. Also $E_0(f_p^q)$ varied with the wind direction for both $q = 4$ and $q = 10$. Even though a similar variation was seen also in the GoF, the easterly wind directions at Suomenlinna (T2) produced wave spectra where, on average, only 20 % of the energy was below the peak frequency – a situation that was not possible at the GoF.

Choosing $q = 4$ resulted in $E_0(f_c)$ being roughly between 30 % and 40 % at both in the open sea (GoF) and in the archipelago (Suomenlinna, T2). While the integrated definition using $q = 4$ was not identical to the peak frequency, it had the advantage of describing a similar characteristic feature in both locations. Namely, in a mean sense, 30 %–40 % of the wave energy was contained by waves with a frequency lower than f_c. A consistency in this respect might be important for constructing an accurate analytical parameterisation of the archipelago spectrum. Using $q = 10$ is attractive as its bias with respect to the peak frequency was small at all locations (Table). On the other hand, the scatter (as measured by the standard deviation) was only reduced slightly compared to the peak frequency.

5 Discussion

5.1 Direct implications

The spectral shape affected the relation between the different definitions of the significant wave height ($H_{1/3}$ vs. H_s). The ratio $H_{1/3}/H_s$ varied, in a mean sense, as a function of the spectral narrowness κ^2 (Fig. 7a). Regardless of the scatter, this connection suggested a decreased height of the highest single waves compared to the total variance for a wider spectrum. The highest single wave H_{max}/H_s was, indeed, statistically lower at Suomenlinna (T2) compared to the open sea (Table 3). A connection to κ^2 was also found (Fig. 7b), although with a very weak correlation ($r = 0.15$). The low correlation between the highest single wave and the spectral width might partly be explained by the higher number of waves associated with a wider spectrum: a wide spectrum would suggest a low maximum wave, while the accompanying increase in the number of single waves in the time series (N) has an opposite effect. If the average values at Suomenlinna (T2) are viewed as a function of the wind direction (as d.o.f.(m_0) in Fig. 6a), the relevant parameters had a variation of $494 \leq N \leq 577$ and $1.54 \leq H_{max}/H_s \leq 1.60$ (not shown). Assuming a single Rayleigh distribution, the variation in N would cause a difference of 1.1 % in estimates for H_{max}/H_s, which is a similar order of magnitude to the observed variation in the average value of H_{max}/H_s (3.9 %).

The reduction of the single highest wave in a wider spectrum has been explained by the de-correlation of the following crests and troughs: a deep trough is less likely to be followed by a high wave crest, even if the maximum and minimum water levels are not affected (e.g. Tayfun, 1983). This is also supported by our data, since we found no connection between the crest (or trough) heights and the spectral width. Goda (1970) found that in computer-simulated data the height of the single waves followed a Rayleigh distribution regardless of the spectral width (as quantified by ε of Cartwright and Longuet-Higgins, 1956). Nevertheless, based on a very extensive data set, Casas-Prat and Holthuijsen (2010) pointed out that the use of other distributions can have an advantage over the Rayleigh distribution for large numbers of N. Further research is needed to resolve the open questions regarding the affect of spectral width on the distribution of the height of single waves.

The d.o.f. of the wave variance (m_0) closely reflected the spectral width, and they seemed to correlate well with the narrowness parameter κ^2 (Fig. 5). Wider (flatter) spectra had more degrees of freedom, which lead to smaller confidence limits for the measured significant wave height (Table 2). It follows that when evaluating a wave model in archipelago conditions, a constant performance will lead to a smaller scatter index (or normalised root-mean-square error) inside the archipelago compared to the open sea. The peak frequency, again, is a very noisy parameter for the flat spectral shape found in the archipelago. This noise is connected to the

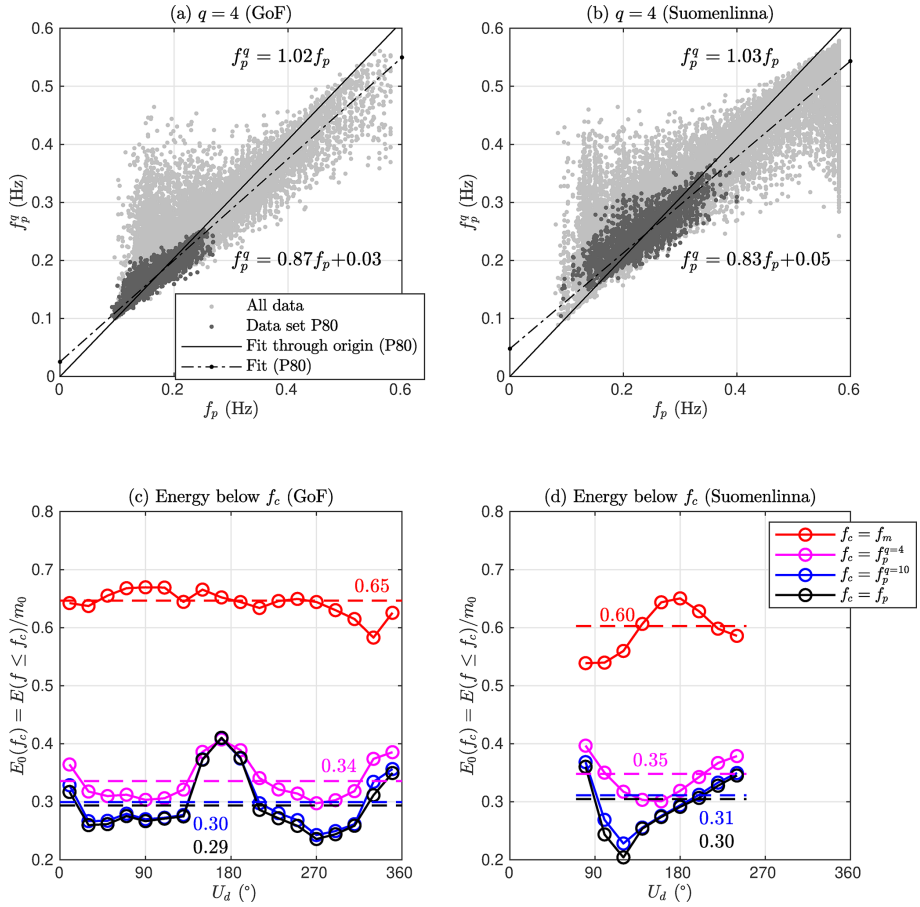

Figure 9. The characteristic wave frequency $f_c = f_p^q$ compared to f_p for different values of q at the open sea (GoF, left column) and in the middle of the archipelago (Suomenlinna (T2), right column). Note that f_m is identical to $f_p^{q=1}$.

sampling variability of a spectrum that has a wide frequency range with an almost constant variance density – the peak frequency is determined by the variability of the peaks in this region. A theoretical perfect model would therefore show an increased accuracy for the significant wave height when moving through the archipelago, while conversely showing a decrease in the accuracy in the peak frequency. We do, however, want to point out that the latter effect is much stronger.

5.2 Parameterising the spectrum

Section 4.5 was dedicated to finding a good characteristic frequency for the varying wave conditions encountered in the archipelago. Equation (6) with $q = 4$ was proposed as a balanced choice between the mean frequency's stability and the peak frequency's skill in identifying the energy-dominated part of the spectrum. Nonetheless, simply redefining the peak frequency in traditional spectral parameterisation (such as JONSWAP; Hasselmann et al., 1973) does not make archipelago wave spectra comparable with traditional unimodal open-sea spectra. Especially engineering approaches that are a function of (H_s, f_p) or (H_s, f_m) will not be reasonable for any choice of a characteristic frequency.

The overall results of this study showed that general archipelago conditions need to be quantified using at least three parameters. If the total energy is known, a frequency will give – in some sense – the location where the energy of the wave spectrum is concentrated. The spectral width, again, quantifies how narrowly the energy is distributed around this frequency. Traditionally the variation in spectral width has been relatively small, but in an archipelago setting it is dominant. Clearly, advancing our knowledge of waves in archipelagos hinges on the development of an analytical parameterisation for the archipelago type spectrum. Both f_c and κ^2 have shown desirable properties in regards to stability and descriptive power. The triplet (H_s, f_c, κ^2) can therefore serve as a starting point for further studies, and the analytical expression can then consequently be used to derive practical formulas for wave bottom interaction. Even before a parameterisation of the archipelago wave spectrum has been established, wave model studies (and other comparative analyses)

Table 4. The mean values and the scatter (standard deviation) of the characteristic wave frequency $f_c := f_p^q$ for three different values of q (see Eq. 6) compared to that of the peak frequency, f_p. Note that $f_p^q = f_m$ for $q = 1$.

	All data						Data set P80					
	$\langle f_c \rangle / \langle f_p \rangle$			$\sigma(f_c)/\sigma(f_p)$			$\langle f_c \rangle / \langle f_p \rangle$			$\sigma(f_c)/\sigma(f_p)$		
Name (code)	$q = 10$	$q = 4$	$q = 1$	$q = 10$	$q = 4$	$q = 1$	$q = 10$	$q = 4$	$q = 1$	$q = 10$	$q = 4$	$q = 1$
Gulf of Finland (GoF)	1.01	1.04	1.23	0.96	0.92	0.73	1.00	1.02	1.26	0.95	0.87	0.79
Outer archipelago												
Harmaja (O1)	1.00	1.02	1.19	0.94	0.85	0.52	1.00	1.01	1.18	0.82	0.68	0.54
Isosaari (O2)	1.00	1.03	1.18	0.94	0.88	0.60	1.00	1.02	1.21	0.94	0.90	0.85
Berggrund (O3)	1.01	1.04	1.19	0.95	0.86	0.58	1.01	1.03	1.25	0.90	0.87	0.91
Transition zone												
Itä-Villinki (T3)	1.01	1.05	1.27	0.94	0.88	0.57	1.02	1.09	1.33	0.87	0.76	0.57
Länsikari (T1)	1.00	1.03	1.23	0.92	0.84	0.57	1.00	1.03	1.28	0.87	0.79	0.78
Suomenlinna (T2)	1.01	1.04	1.16	0.93	0.83	0.45	1.01	1.04	1.26	0.90	0.85	0.72
Inner archipelago												
Jätkäsaari (I3)	1.01	1.05	1.16	0.90	0.77	0.38	1.01	1.09	1.24	0.80	0.59	0.27
Hernesaari (I1)	1.01	1.05	1.18	0.90	0.79	0.48	1.01	1.05	1.21	0.85	0.73	0.44
Ruumiskari (I2)	1.01	1.04	1.15	0.90	0.75	0.36	1.04	1.15	1.48	0.93	0.81	0.35
Sheltered archipelago												
Koivusaari (S1)	1.00	1.00	0.97	0.89	0.73	0.35	1.00	1.00	0.97	0.83	0.58	0.27
Ramsinniemi (S2)	1.00	0.99	0.94	0.92	0.75	0.36	0.99	0.98	0.89	0.85	0.71	0.38
Vuosaaren satama (S3)	1.00	0.98	0.91	0.84	0.64	0.32	0.99	0.98	0.91	0.85	0.68	0.29
Talosaari (S4)	1.00	0.99	0.90	0.88	0.68	0.35	0.99	0.98	0.87	0.91	0.77	0.38

can benefit by expanding the validation to cover the aforementioned triplet.

5.3 Limitations of the data set

This study was done using the most extensive wave data set that is available from dense archipelago areas. Still, since the material was not primarily collected for fundamental research purposes, it has a few limitations. The first limitation is the sheltered archipelago locations (S1–S4), where the standard 40 cm wave buoy was unable to capture the entire spectrum because of the very low wave conditions. Visually, the spectra from the sheltered archipelago are qualitatively consistent with the rest of the data (Fig. 3). The missing spectral tail, however, rendered quantitative metrics – such as the degrees of freedom or the κ^2 narrowness parameter – unreliable (Table 2). The challenges caused by low wave heights inside the archipelago were mitigated by appropriately analysing the long time series at Suomenlinna (T2), since these data contained almost the full range of the different spectral shapes. Instead of actual geographical sites, we could then use the wind direction as a proxy for different amounts of sheltering (Fig. 4).

The second limitation is the short duration of the measurements in 12 of the 14 locations (Table 1). Since the measurements were mostly made during the autumn, they are comparable to each other, and also representative of the harsher wave conditions of the area. While short, the data show a consistent transition of the spectral shape throughout the archipelago (Fig. 3). Also, the shortest time series (T1) is in close proximity to the longest time series (T2), and the results from the two locations agree well, both visually (Fig. 3) and quantitatively (Table 2). All in all, the quality of the available data was sufficient to reach the objectives of the study and to support our conclusions.

6 Conclusions

An extensive field measurement campaign consisting of wave buoy measurements from 14 locations was performed in the Helsinki archipelago during 2012–2018. Multi-year time series were available from two operational wave buoys in the middle of the Gulf of Finland (GoF) and in the middle of the archipelago (Suomenlinna, T2). Measurements from the other sites in the archipelago lasted for about a month. These measurements were used to study the shape of the wave spectrum in the archipelago and the consequences that the variations in the spectrum have for derived wave parameters.

The mean spectral shape in the middle of the GoF was unimodal with a distinct peak. No peak was identifiable close to the shoreline, where the spectrum was best described by a wide energy-carrying range with almost constant variance density. At Suomenlinna (T2), located in between these two extremes, the spectral shape varied strongly with the wind direction because of the anisotropic fetch conditions. For south-westerly, and especially southerly, winds, the spectral shape was peaked. For easterly winds, the spectral shape was wide, being close to that of the sites near the shore. The wide spectral shape in the archipelago was not created by swell, since even the longer waves travelled slower than the wind. Rather, the spectra reflected complex wind sea conditions where waves grow from different fetches and are attenuated by the islands.

The mean shape of the spectra was well quantified by the spectral narrowness parameter (κ^2) of Battjes and van Vledder (1984), but a scatter still persisted. The width parameter ν of Longuet-Higgins (1975) had no predictive value, possibly because of the challenges imposed by measuring the short waves in the archipelago with wave buoys. The spectral width was also connected to the degrees of freedom of the wave variance (m_0), with a wider spectrum having more degrees of freedom. As a direct consequence, the confidence limits for the measured significant wave height are lower inside the archipelago compared to the open sea (Table 2).

The spectral shape affected the ratio $H_{1/3}/H_\mathrm{s}$, with a wider spectrum resulting in a lower ratio (H_s was defined using the variance). The ratio between the two definitions of significant wave height was determined to be $H_{1/3} = 0.881 H_\mathrm{s}$ at Suomenlinna (T2), but the ratio varied as a function of the spectral narrowness κ^2 (Fig. 7a). The effect of the spectral shape on the ratio $T_\mathrm{z}/T_{m02} = 1.04$ was weak.

The highest single wave $H_\mathrm{max}/H_\mathrm{s}$ was, on average, 1.58 at Suomenlinna (T2), which is lower both compared to the open-sea measurements at GoF (1.61) and to estimates using the literature (1.67–1.84, Table 3). Our results suggest that the deviation in $H_\mathrm{max}/H_\mathrm{s}$ from previous studies is mainly caused by a wider spectral shape (Fig. 7b), not by the finite water depth. Nevertheless, the weak correlation found in the data can offer no solid conclusions, and the issue warrants further research.

The traditional peak frequency, f_p, was practically undefinable in the archipelago. As a compromise between scatter and bias with respect to f_p, the integrated frequency weighted by $E(f)^4$ was proposed as a characteristic frequency, f_c. This definition was applicable over a wide range of wave conditions, and it functioned as a non-biased estimate for f_p in a wide fetch geometry. Nevertheless, a proper parameterisation of the archipelago wave field cannot be obtained using only two parameters (e.g. H_s and f_c), but the triplet (H_s, f_c, κ^2) seems like a promising candidate for developing an analytical form of a wave spectrum that covers also archipelago conditions.

Data availability. The data are available through the following DOI: https://doi.org/10.5281/zenodo.3482304 (Björkqvist et al., 2019b).

Author contributions. JVB initiated the study based on previous conceptualisations of KK and HP. KK and JVB took part in designing the field measurements. JVB produced the methodology and performed the analysis. JVB did the visualisation. JVB wrote the article with contributions from HP and KK. HP supervised the study.

Competing interests. The authors declare that they have no conflict of interest.

Acknowledgements. We want to acknowledge the work done by the technical staff at FMI, namely Tuomo Roine, Heini Jalli, and Riikka Hietala. The efforts of Hannu Jokinen in processing the raw wave buoy data are also gratefully acknowledged. Most of the wave buoy observations in this study have been collected through work commissioned by the city of Helsinki. The data is used in this paper with their kind permission. We thank the anonymous reviewers for their constructive critique and comments. They helped us improve our article.

Financial support. This research has been supported by the University of Helsinki and the Svenska Kulturfonden (grant no. 17/103386).

Review statement. This paper was edited by Judith Wolf and reviewed by two anonymous referees.

References

Anderson, J. D., Wu, C. H., and Schwab, D. J.: Wave climatology in the Apostle Islands, Lake Superior, J. Geophys. Res.-Oceans, 120, 4869–4890, https://doi.org/10.1002/2014JC010278, 2015.

Banner, M. L.: Equilibrium Spectra of Wind Waves, J. Phys. Oceanogr., 20, 966–984, https://doi.org/10.1175/1520-0485(1990)020<0966:ESOWW>2.0.CO;2, 1990.

Battjes, J. A. and van Vledder, G. P.: Verification of Kimura's Theory for Wave Group Statistics, in: Proc. 19th Int. Conf. Coastal Engineering, 642–648, ASCE, New York, https://doi.org/10.1061/9780872624382.044, 1984.

Björkqvist, J.-V., Pettersson, H., Laakso, L., Kahma, K. K., Jokinen, H., and Kosloff, P.: Removing low-frequency artefacts from Datawell DWR-G4 wave buoy measurements, Geosci. Instrum. Method. Data Syst., 5, 17–25, https://doi.org/10.5194/gi-5-17-2016, 2016.

Björkqvist, J.-V., Tuomi, L., Fortelius, C., Pettersson, H., Tikka, K., and Kahma, K. K.: Improved estimates of nearshore wave conditions in the Gulf of Finland, J. Mar. Syst., 171, 43–53, https://doi.org/10.1016/j.jmarsys.2016.07.005, 2017a.

Björkqvist, J.-V., Vähäaho, I., and Kahma, K. K.: Spectral field measurements of wave reflection at a steep shore with wave damping chambers, in: WIT Transactions on the Built Environment, 170, 185–191, https://doi.org/10.2495/CC170181, 2017b.

Björkqvist, J.-V., Vähä-Piikkiö, O., Alari, V., Kuznetsova, A., and Tuomi, L.: WAM, SWAN and WAVEWATCH III in the Finnish archipelago – the effect of spectral performance on bulk wave parameters, J. Oper. Oceanogr., 1–16, https://doi.org/10.1080/1755876X.2019.1633236, 2019a.

Björkqvist, J.-V., Pettersson, H., and Kahma, K.: Wave and wind data from the Helsinki archipelago and Gulf of Finland (Version Version1) [Data set], Zenodo, https://doi.org/10.5281/zenodo.3482304, 2019b.

Cartwright, D. and Longuet-Higgins, M. S.: The Statistical Distribution of the Maxima of a Random Function, P. R. Soc. London, 237, 212–232, 1956.

Casas-Prat, M. and Holthuijsen, L. H.: Short-term statistics of waves observed in deep water, J. Geophys. Res.-Oceans, 115, 1–20, https://doi.org/10.1029/2009JC005742, 2010.

Donelan, M. A. and Pierson, W. J.: The Sampling Variability of Estimates of Spectra of Wind-Generated Gravity Waves, J. Geophys. Res., 88, 4381–4392, https://doi.org/10.1029/JC088iC07p04381, 1983.

Donelan, M. A., Hamilton, J., and Hui, W. H.: Directional Spectra of Wind-Generated Waves, Philos. T. Roy. Soc. A, 315, 509–562, https://doi.org/10.1098/rsta.1985.0054, 1985.

Eldeberky, Y.: Nonlinear transformation of wave spectra in the nearshore, PhD thesis, Delft University of Technology, 1996.

Forristall, G. Z.: On the statistical distribution of wave heights in a storm, J. Geophys. Res., 83, 2353, https://doi.org/10.1029/JC083iC05p02353, 1978.

Goda, Y.: Numerical experiments on wave statistics with spectral simulation, Report of the Port and Harbour Research Institute, Ministry of Transport, Nagase, Yokosuka, Japan, 9, 3–57, 1970.

Hardy, T. A. and Young, I. R.: Field study of wave attenuation on an offshore coral reef, J. Geophys. Res., 101, 14311–14326, https://doi.org/10.1029/96JC00202, 1996.

Hasselmann, K., Barnett, T. P., Bouws, E., Carlson, H., Cartwright, D. E., Enke, K., Ewing, J. A., Gienapp, H., Hasselmann, D. E., Kruseman, P., Meerburg, A., Muller, P., Olbers, D. J., Richter, K., Sell, W., and Walden, H.: Measurements of Wind-Wave Growth and Swell Decay during the Joint North Sea Wave Project (JONSWAP), Ergnzungsheft zur Deutschen Hydrographischen Zeitschrift Reihe, A(8), p. 95, 2710264, 1973.

Janssen, P. A. E. M.: Nonlinear Four-Wave Interactions and Freak Waves, J. Phys. Oceanogr., 33, 863–884, https://doi.org/10.1175/1520-0485(2003)33<863:NFIAFW>2.0.CO;2, 2003.

Kahma, K. K.: On a two-peak structure in steady-state fetch-limited wave spectra, Licentiate thesis in Geophysics, University of Helsinki, p. 75, 1979.

Kahma, K. K.: A Study of the Growth of the Wave Spectrum with Fetch, J. Phys. Oceanogr., 11, 1503–1515, https://doi.org/10.1175/1520-0485(1981)011<1503:ASOTGO>2.0.CO;2, 1981.

Kahma, K. K. and Calkoen, C. J.: Reconciling Discrepancies in the Observed Growth of Wind-generated Waves, J. Phys. Oceanogr., 22, 1389–1405, https://doi.org/10.1175/1520-0485(1992)022<1389:RDITOG>2.0.CO;2, 1992.

Kahma, K. K., Björkqvist, J.-V., Johansson, M. M., Jokinen, H., Leijala, U., Särkkä, J., Tikka, K., and Tuomi, L.: Turvalliset rakentamiskorkeudet Helsingin rannoilla 2020, 2050 ja 2100, Tech. rep., 96, City of Helsinki, Real Estate Department, Geotechnical Division, available at: http://www.hel.fi/static/kv/turvalliset-rakentamiskorkeudet.pdf (last access: 11 November 2019), 2016.

Kitaigorodskii, S. A.: On the Theory of the Equilibrium Range in the Spectrum of Wind-Generated Gravity Waves, J. Phys. Oceanogr., 13, 816–827, https://doi.org/10.1175/1520-0485(1983)013<0816:OTTOTE>2.0.CO;2, 1983.

Lenain, L. and Melville, W. K.: Measurements of the directional spectrum across the equilibrium-saturation ranges of wind-generated surface waves, J. Phys. Oceanogr., 47, 2123–2138, https://doi.org/10.1175/JPO-D-17-0017.1, 2017.

Longuet-Higgins, M. S.: On the Statistical Distribution of the Heights of Sea Waves, J. Mar. Res., 11, 245–266, 1952.

Longuet-Higgins, M. S.: On the Join Distribution of the Periods and Amplitudes of Sea Waves, J. Geophys. Res., 80, 2688–2694, https://doi.org/10.1029/JC080i018p02688, 1975.

Longuet-Higgins, M. S.: On the distribution of the heights of sea waves: Some effects of nonlinearity and finite band width, J. Geophys. Res., 85, 1519, https://doi.org/10.1029/JC085iC03p01519, 1980.

Mazarakis, N., Kotroni, V., Lagouvardos, K., and Bertotti, L.: High-resolution wave model validation over the Greek maritime areas, Nat. Hazards Earth Syst. Sci., 12, 3433–3440, https://doi.org/10.5194/nhess-12-3433-2012, 2012.

Onorato, M., Osborne, A. R., and Serio, M.: Extreme wave events in directional, random oceanic sea states, Phys. Fluids, 14, 3–6, https://doi.org/10.1063/1.1453466, 2002.

Orear, J.: Least squares when both variables have uncertainties, American J. Phys., 50, 912–916, https://doi.org/10.1119/1.12972, 1982.

Pettersson, H.: Wave growth in a narrow bay, PhD thesis, University of Helsinki, 2004.

Pettersson, H., Kahma, K. K., and Tuomi, L.: Wave Directions in a Narrow Bay, J. Phys. Oceanogr., 40, 155–169, https://doi.org/10.1175/2009JPO4220.1, 2010.

Pettersson, H., Lindow, H., and Brüning, T.: Wave climate in the Baltic Sea 2012, Tech. rep., available at: http://www.helcom.fi/Documents/Balticseatrends/Environmentfactsheets/Wave_climate_in_the_Baltic_Sea_2012_BSEFS2013.pdf (last access: 11 November 2019), 2013.

Phillips, O. M.: The equilibrium range in the spectrum of wind-generated waves, J. Fluid Mech., 4, 426–434, https://doi.org/10.1017/S0022112058000550, 1958.

Pierson, W. J. and Marks, W.: The power spectrum analysis of ocean-wave records, EOS T. Am. Geophys. Un., 33, 834–844, https://doi.org/10.1029/TR033i006p00834, 1952.

Pierson, W. J. and Moskowitz, L.: A proposed spectral form for fully developed wind seas based on the similarity theory of S. A. Kitaigorodskii, J. Geophys. Res., 69, 5181–5190, https://doi.org/10.1029/JZ069i024p05181, 1964.

Serio, M., Onorato, M., Osborne, A. R., and Janssen, P. A. E. M.: On the computation of the Benjamin-Feir Index, Nuovo Cimento C, 28, 893–903, https://doi.org/10.1393/ncc/i2005-10134-1, 2005.

Sobey, R. J. and Young, I. R.: Hurricane Wind Waves–A Discrete Spectral Model, in: Journal of Waterway, Port,

Coastal and Ocean Engineering, 112, 370–389, ASCE, https://doi.org/10.1061/(ASCE)0733-950X(1986)112:3(370), 1986.

Soukissian, T. H., Prospathopoulos, A. M., and Diamanti, C.: Wind and Wave Data Analysis for the Aegean Sea – Preliminary Results, J. Atmos. Ocean Sci., 8, 163–189, https://doi.org/10.1080/1023673029000003525, 2004.

SPM: Shore Protection Manual, Vol. I, Dept. of the Army, Waterways Experiment Station, Corps of Engineers, Coastal Engineering Research Center,, available at: http://www.biodiversitylibrary.org/item/102420 (last access: 11 November 2019), 1984.

Tayfun, M. A.: Effects of spectrum band width on the distribution of wave heights and periods, Ocean Eng., 10, 107–118, https://doi.org/10.1016/0029-8018(83)90017-3, 1983.

Toba, Y.: Local balance in the air-sea boundary processes – I. on the growth process of wind waves, J. Oceanogr. Soc. Jpn., 28, 109–120, https://doi.org/10.1007/BF02109772, 1972.

Toba, Y.: Local balance in the air-sea boundary processes – III. On the Spectrum of Wind Waves, J. Oceanogr. Soc. Jpn., 29, 209–220, https://doi.org/10.1007/BF02108528, 1973.

Tuomi, L., Kahma, K. K., and Pettersson, H.: Wave hindcast statistics in the seasonally ice-covered Baltic Sea, Boreal Environ. Res., 16, 451–472, 2011.

Tuomi, L., Pettersson, H., Fortelius, C., Tikka, K., Björkqvist, J.-V., and Kahma, K. K.: Wave modelling in archipelagos, Coast. Eng., 83, 205–220, https://doi.org/10.1016/j.coastaleng.2013.10.011, 2014.

van der Westhuysen, A. J., van Dongeren, A. R., Groeneweg, J., van Vledder, G. P., Peters, H., Gautier, C., and van Nieuwkoop, J. C.: Improvements in spectral wave modeling in tidal inlet seas, J. Geophys. Res.-Oceans, 117, 1–23, https://doi.org/10.1029/2011JC007837, 2012.

Vandever, J. P., Siegel, E. M., Brubaker, J. M., and Friedrichs, C. T.: Influence of Spectral Width on Wave Height Parameter Estimates in Coastal Environments, J. Waterw. Port Coast., 134, 187–194, https://doi.org/10.1061/(ASCE)0733-950X(2008)134:3(187), 2008.

Young, I. R.: The determination of confidence limits associated with estimates of the spectral peak frequency, Ocean Eng., 22, 669–686, https://doi.org/10.1016/0029-8018(95)00002-3, 1995.

Reprinted, with kind permission, from
Journal of Geophysical Research: Oceans, 124, 3097-6119
doi:10.1029/2018JC014904

IV

JGR Oceans

RESEARCH ARTICLE
10.1029/2018JC014904

A New Inverse Phase Speed Spectrum of Nonlinear Gravity Wind Waves

Jan-Victor Björkqvist[1], Heidi Pettersson[1], William M. Drennan[2], and Kimmo K. Kahma[1]

[1]Finnish Meteorological Institute, Helsinki, Finland, [2]Rosenstiel School of Marine and Atmospheric Science, University of Miami, Miami, FL, USA

Key Points:
- A spectrum representing wind waves as a function of their inverse phase speed is defined and examined using wave staff observations
- The new spectrum is consistent with the wavenumber spectrum for the shortest waves
- The inconsistencies observed in the frequency spectra are deduced to mainly be a result of wave nonlinearities

Correspondence to:
J.-V. Björkqvist,
jan-victor.bjorkqvist@fmi.fi

Citation:
Björkqvist, J.-V., Pettersson, H., Drennan, W. M., & Kahma, K. K. (2019). A new inverse phase speed spectrum of nonlinear gravity wind waves. *Journal of Geophysical Research: Oceans*, *124*. https://doi.org/10.1029/2018JC014904

Received 23 DEC 2018
Accepted 3 AUG 2019
Accepted article online 7 AUG 2019

Abstract The rear face of the wave spectrum is described by an equilibrium and a saturation subrange. Although accurate information about these ranges are highly relevant for wave modeling and many practical applications, there have been inconsistencies between results originating from temporal and spatial measurements. These discrepancies have been explained by the Doppler shift and the harmonics of nonlinear waves. We present high-frequency wave measurements from the Baltic Sea gathered with R/V *Aranda* using a wave staff array, which provided directional frequency-wavenumber data. In addition to the traditional wavenumber and frequency spectra, $F(k)$ and $S(\omega)$, we also define a new spectrum that is a function of the inverse phase speed. We denote this spectrum $Q(\nu)$, where $\nu = k\omega^{-1}$. The properties of this Q-spectrum were studied using data from four different sites. A strongly forced fetch-limited case showed an equilibrium-to-saturation transition in the Q-spectrum, with less variations in the equilibrium constants compared to the frequency spectra. The transition to a saturation regime happened around $U\nu = 3$ in all spectra where an equilibrium range was identified. Most duration-limited spectra had no equilibrium range in the inverse phase speed domain. The absence of an equilibrium range was consistent with the wavenumber domain, but the frequency spectra still showed an apparent equilibrium subrange extending to $\omega U/g$=5. The consistency of the saturation ranges between the Q-spectrum and the wavenumber spectrum indicate a weak Doppler shift effect. We deduced that the main factor distorting the frequency spectra was wave nonlinearities.

Plain Language Summary Surface waves are studied by partitioning them according to their length expressed in wave periods (seconds) or wavelengths (meters). Both approaches should give a similar descriptions of the waves, but in practice they produce inconsistent results. This limits our fundamental knowledge of waves and complicates practical applications. Measuring the wave period and the wavelength simultaneously is difficult, and there are not a lot of good data to study this problem. We measured the waves in the Baltic Sea from the ship R/V *Aranda* by recording the water level elevations using several thin submerged wires. From these observations we could describe the waves using both wave periods and wavelengths. The central part of our work was presenting the waves in a new way: We combined the wavelength and period measurements and partitioned the waves according to the speed which with they travel. The new partitioning shed light on the physical processes responsible for the discrepancies between the two traditional ways of representing the waves. This new approach might turn out to be useful, since many properties of the waves—such as the energy transfer from the wind—are controlled by their speed relative to the wind.

1. Introduction

Finding the proper description of wind generated surface waves is important for wave modeling, remote sensing, and air-sea interaction studies. Surface waves have traditionally been described by the variance density spectrum, either in the frequency or in the wavenumber domain. While real ocean waves are known to be nonlinear, the Fourier transform used to determine the wave spectrum still breaks down the data into linear components. One physical nonlinear wave in, for example, the frequency spectrum is thus described by its linear harmonics, which are indistinguishable from shorter free-traveling waves with the same frequency, but different phase speed.

Observed wave spectra, in particular, the frequency spectrum, contain significant contributions from nonlinear components that do not follow the linear dispersion (Donelan et al., 1985; Hara & Karachintsev, 2003;

Janssen, 2009; Leckler et al., 2015). In a study relying on Hamiltonian theory, Janssen (2009) determined the second-order correction to linear waves both in the wavenumber and frequency domain by including additional nonlinear terms that had not been accounted for in the previous studies of Barrick and Weber (1977) and Komen (1980). The author concluded that the second-order nonlinear effects were marginal in the wavenumber spectrum but distorted the higher part of the frequency spectrum. The results received experimental verification by Leckler et al. (2015).

What a nonlinear wave and its harmonics have in common is that they all travel with the same phase velocity—an obvious consequence of them collectively being one physical wave. This motivated us to define a new wave spectrum that is a function of the inverse phase velocity. For the approach to be fruitful, one needs to discard the assumptions relying on linear theory. In other words, we need to determine the frequency-wavenumber spectrum using spatiotemporal wave measurements. Such data can be extracted from, for example, marine radars (e.g., Lund et al., 2016) or stereo video footage (e.g., Leckler et al., 2015), and the latter technique has in later years led to studies of the directional frequency-wavenumber spectrum (Leckler et al., 2015; Peureux et al., 2018). Spatial and temporal wave data can also be acquired simultaneously using a large amount of wave staffs (Donelan et al., 1985). As shown by Donelan et al. (1996, 2015), even a smaller array is sufficient if the time series are processed using a tool suitable for nonstationary analysis, such as the Wavelet Directional Method (WDM; Donelan et al., 1996).

Regardless of the spectral domain, different regions of the wave spectrum above the spectral peak have long been described using two subranges: one wind-speed-dependent ω^{-4} range, and one wind-speed-independent ω^{-5} range (ω is the wave frequency). Different theories for the mechanisms causing the apparent power laws in the respective subranges have been proposed (Banner, 1990; Kitaigorodskii, 1983; Phillips, 1958, 1985; Toba, 1973), but this fundamental question is not yet solved. Nevertheless, the existence of both subranges—and some kind of transition between them—has been established in several studies (e.g., Forristall, 1981; Kahma, 1981; Kahma & Calkoen, 1992; Lenain & Melville, 2017; Tamura et al., 2014). The names for these regions (the equilibrium/saturation range) have historically been used interchangeably to refer to either one (or both) of the subranges. We will henceforth call the wind-dependent ω^{-4} region the *equilibrium range*. The ω^{-5} region governing the shorter waves is referred to as the *saturation range*.

Theory predicts that there should be a connection between the subranges in the wavenumber and frequency domain, but field measurements have revealed inconsistencies where a transition to the saturation subrange is identifiable only in the wavenumber domain (Lenain & Melville, 2017). Interpreting frequency measurements are especially challenging since, compared to wavenumber measurements, they are more strongly affected by wave nonlinearities (Janssen, 2009). Moreover, they are also affected by the Doppler shift; the shorter waves are modulated by ambient currents, the wind induced drift, and the orbital motions of the longer waves (Banner, 1990; Guimarães, 2018; Kitaigorodskii et al., 1975; Leckler et al., 2015). We note that while the higher-order harmonics won't be separated from the dominant wave in the new inverse phase speed spectrum, it will also be modulated by currents.

In this study we aim to compare all three spectral representations of the wave field and have structured the paper as follows. In section 2 we describe the analysis methods and introduce the different spectra, while section 3 presents the experimental setup and available data. Section 4 starts by studying the saturation range in the wavenumber domain; any deviations from this constant in the new inverse phase speed measurements are expected to be caused mainly by the Doppler shift. The section continues with a presentation of the observed frequency spectra. Finally, we calculate the new inverse phase speed spectrum. The results are compared to the frequency spectra in an attempt to study the effect of wave non-linearities in the frequency measurements. We end by discussing and concluding our findings.

2. Analysis Methods

2.1. The Fourier Frequency Spectrum

We define dimensionless quantities for the frequency spectrum:

$$\tilde{\omega} = \omega U/g \tag{1}$$

$$\tilde{S}(\omega) = S(\omega)\omega^5/g^2 \tag{2}$$

$$\tilde{S}(\omega)\tilde{\omega}^{-1} = S(\omega)\omega^4/(Ug), \tag{3}$$

where $\omega = 2\pi f$ is the angular frequency, $S(\omega)$ is the omnidirectional frequency spectrum, and U is the wind speed. We will call $\tilde{S}(\omega)$ the frequency saturation spectrum and $\tilde{S}(\omega)\tilde{\omega}^{-1}$ the frequency equilibrium spectrum. The equilibrium spectrum is expected to be valid for certain subranges above the spectral peak, while the saturation spectrum is expected to describe the spectral region above the equilibrium range. These subranges are often displayed using their respective proportionality constants α and α_u:

$$S(\omega) \sim \alpha g^2 \omega^{-5} \tag{4}$$

$$S(\omega) \sim \alpha_u U g \omega^{-4}, \tag{5}$$

where the wind speed (U) can be given as, for example, the mean 10-m wind speed (U_{10}), or the friction velocity (u_*).

2.2. The WDM

The WDM (Donelan et al., 1996) is a tool for nonstationary wave analysis. The WDM gives information about the wave energy as a function of time and frequency (actually scale). If data from at least three different wave staffs are available, the phase lags between the staffs also determine the wavenumber, k, and the direction, θ, of the waves.

We determined the directional frequency spectrum $\mathcal{S}(\omega, \theta)$ (m^2/Hz/rad) by binning the variance in each time and frequency bin with respect to the direction.

2.2.1. Wavenumber Spectrum

By binning the variance with respect to the wavenumber and the direction, we obtained the directional wavenumber spectrum $\Psi(\mathbf{k}) = \Psi(k, \theta)$ (m^4/rad).

The omnidirectional wavenumber spectrum, $F(k)$ (m^3), is determined as

$$F(k) = \int_{-\pi}^{\pi} \Psi(k, \theta) k \, \mathrm{d}\theta. \tag{6}$$

The frequency–wavenumber spectrum $\mathbb{F}(\mathbf{k}, \omega) = \mathbb{F}(k, \omega, \theta)$ (m^4/Hz) and its omnidirectional form $\int_{-\pi}^{\pi} \mathbb{F}(k, \omega, \theta) k \, \mathrm{d}\theta$ (m^3/Hz) were determined by a similar binning technique.

We define dimensionless quantities for the wavenumber spectrum:

$$\tilde{k} = kU^2/g \tag{7}$$

$$B(k) = F(k)k^3, \tag{8}$$

where $B(k)$ is the wavenumber saturation spectrum. As with the frequency spectrum, both the saturation and the equilibrium ranges can be presented using proportionality constants

$$F(k) \sim \frac{\alpha}{2} k^{-3} \tag{9}$$

$$F(k) \sim \frac{\alpha_u}{2} U g^{-0.5} k^{-2.5}, \tag{10}$$

where α and α_u are the constants of the frequency spectrum introduced above (see, e.g., Kitaigorodskii, 1983).

2.2.2. Wave Spectrum as a Function of the Inverse Phase Speed

It is possible to assign each wave component a phase speed if both the wavenumber and the frequency are measured. This is the case when using, for example, the WDM, which can resolve waves with the same frequency, but different wavenumbers. Nevertheless, we will replace the phase speed with the inverse phase speed, $\nu = c^{-1}$, to regain an orientation familiar from traditional wave spectra.

We normalize this new directional spectrum in a similar fashion to the wavenumber domain such that

$$Q(\nu) = \int_{-\pi}^{\pi} \mathcal{Q}(\nu, \theta) \nu \, \mathrm{d}\theta \tag{11}$$

$$\boldsymbol{\nu} = \frac{\mathbf{k}}{\omega} \tag{12}$$

Table 1
Wind and Wave Conditions for the Different Sites

Run ID	Depth (m)	Length (h)	Date	H_s (m)	U_{10} (m/s)	U/c_p (-)
15031	68	6.0	08 July 2015	0.61–0.71	1.7–7.0	0.16–0.99
15033	25	3.5	09 July 2015	0.28–0.35	6.1–9.6	1.51–2.88
15034	122	5.5	10 July 2015	0.32–0.43	1.5–6.3	0.29–1.93
15035	122	6.0	10 July 2015	0.47–1.49	6.2–8.8	0.82–1.88
15040	235	4.0	13 July 2015	0.55–0.76	0.0–2.3	0.00–0.33
15042	159	1.5	13 July 2015	0.27–0.32	1.6–2.1	0.26–0.34
15043	121	1.0	13 July 2015	0.26–0.29	0.6–0.7	0.11–0.13
15044	35	5.0	14 July 2015	0.21–0.29	1.7–3.3	0.30–0.61

Note. The length in hours refers to the length of the measurement time series.

$$\nu = |\boldsymbol{\nu}|, \tag{13}$$

where ν is the inverse phase velocity and ν is its modulus, $Q(\nu, \theta)$ ($m^4/(s^2 rad)$) is the directional spectrum, and $Q(\nu)$ (m^3/s) is the omnidirectional spectrum. We will henceforth call the omnidirectional version of this new spectrum the inverse phase speed spectrum or the Q-spectrum.

To our knowledge this kind of spectrum has not previously been formally defined and examined. To provide the reader with some intuition we note that for linear waves in deep water $\nu = c^{-1} = \omega g^{-1}$. This also means that the inverse phase speed spectrum adds no new information unless frequency-wavenumber measurements provide the true phase speed of the waves.

The omnidirectional Q-spectrum has dimensionless forms corresponding to ν^{-4} and ν^{-5} power laws, which are analogous to the regimes in the frequency spectrum; the former is a wind speed-dependent equilibrium range, while the latter is a saturation range scaling only with the gravitational acceleration. Since the normalization of the directional Q-spectrum is similar as for the wavenumber spectrum, one directional slice might be expected to follow a ν^{-6} power law (cf. a k^{-4} slice in the wavenumber domain). The directional properties of the Q-spectrum will, however, not be the focus of this paper.

As with the frequency and wavenumber spectra, we can define dimensionless quantities

$$\tilde{\nu} = \nu U \tag{14}$$

$$\tilde{Q}(\nu) = Q(\nu)\nu^5 g^2 \tag{15}$$

$$\tilde{Q}(\nu)\tilde{\nu}^{-1} = Q(\nu)\nu^4 g^2 / U, \tag{16}$$

where $\tilde{\nu}$ is merely U/c. The two spectra resemble the saturation and equilibrium spectra of the frequency domain in a natural way with the same proportionality constants α and α_u:

$$Q(\nu) \sim \alpha g^{-2}\nu^{-5} \tag{17}$$

$$Q(\nu) \sim \alpha_u U g^{-2}\nu^{-4}. \tag{18}$$

3. Data

3.1. Experimental Setup

The data were collected in the Baltic Sea during R/V *Aranda*'s research expedition in July 2015. The Baltic Sea is a semienclosed basin with a mean depth of about 50 m. The longest fetches, of around 700 km, are found in the Baltic Proper. The shorelines are complex and often have dense archipelagos—especially the Finnish coastline in the north. Table 1 and Figure 1 provides an overview of the eight measurement runs that form the data set for this study. Each run is denoted with an index from 15031 to 15044.

R/V *Aranda* was aligned with the wind in the beginning of each measurement. If the discrepancy between the wind direction and ship direction grew too large (greater than ~20°), the ship direction was slowly

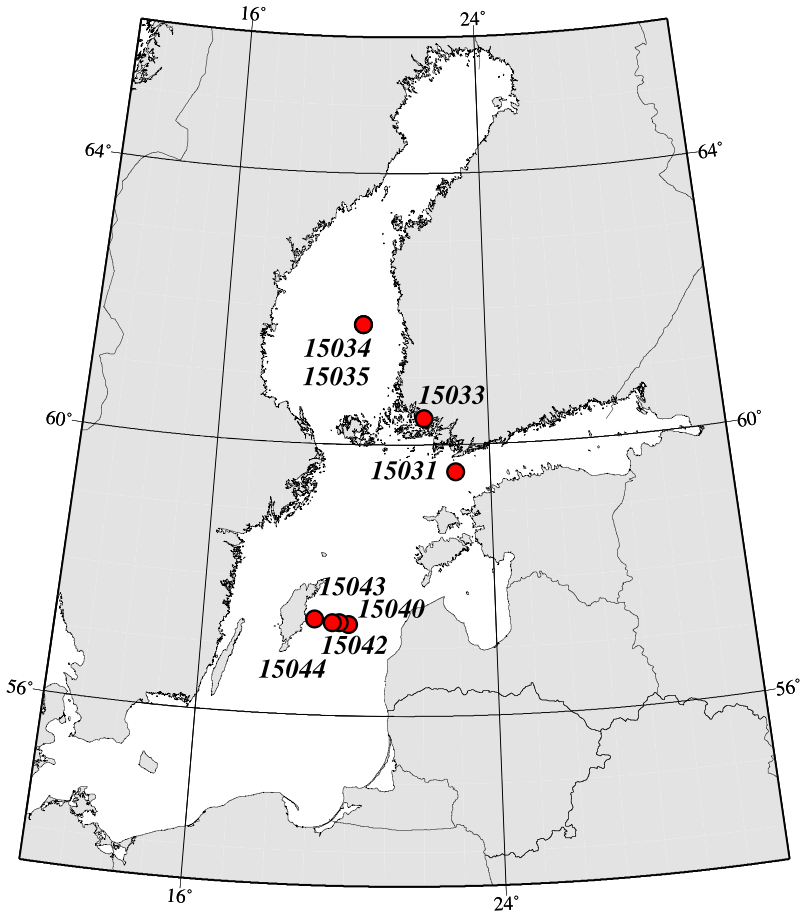

Figure 1. Measurement locations for the 2015 R/V *Aranda* summer expedition.

realigned with the wind. During Runs 15040 and 15044 the ship was aligned with the swell, since the wind was very weak (0–2 m/s) with a varying direction.

The full ship motion (6 degrees of freedom) was registered by an MRU6 (Motion Reference Unit). Following Drennan et al. (1994), a full correction for the movement of the ship was applied to both the wind and the wave measurements.

3.2. Wave Measurements

We conducted wave measurements with a wave staff array submerged in front of the bow of a stationary R/V *Aranda* (Figure 2). The array had five wave staffs fixed 25 cm apart in the shape of a plus sign. For Run 15042 the wave staffs were 15 cm apart and the middle staff was removed. A 24-bit QuantumX AD converter equipped with a Bessel antialiasing filter sampled the data at 200 Hz.

The voltage logged by the capacitive wave staffs were transformed to water level elevations by multiplying with a calibration coefficient. Some of the wave staffs were calibrated statically, while the rest were calibrated dynamically by matching the variance to a statically calibrated wave staff.

We calculated the omnidirectional frequency wave spectra from 30-min surface level elevation data of a single wave staff. The time series were tapered by a Blackman-Harris window, and the final wave spectra were calculated by averaging elementary bins of the raw fast Fourier transform spectra. The final spectra had a frequency resolution of $\Delta\omega = 0.1\pi$ rad/s up to $\omega = 2\pi$, and a resolution of $\Delta\omega = 0.2\pi$ rad/s above that.

An example of wave spectra is given in Figure 3a. The wave staff array registered data near Finnish Meteorological Institute's Bothnian Sea wave buoy (Runs 15034 and 15035), and the wave buoy near the island Gotland in the Baltic Proper (Run 15044; Figure 1). Both buoys were accelerometer-based Datawell

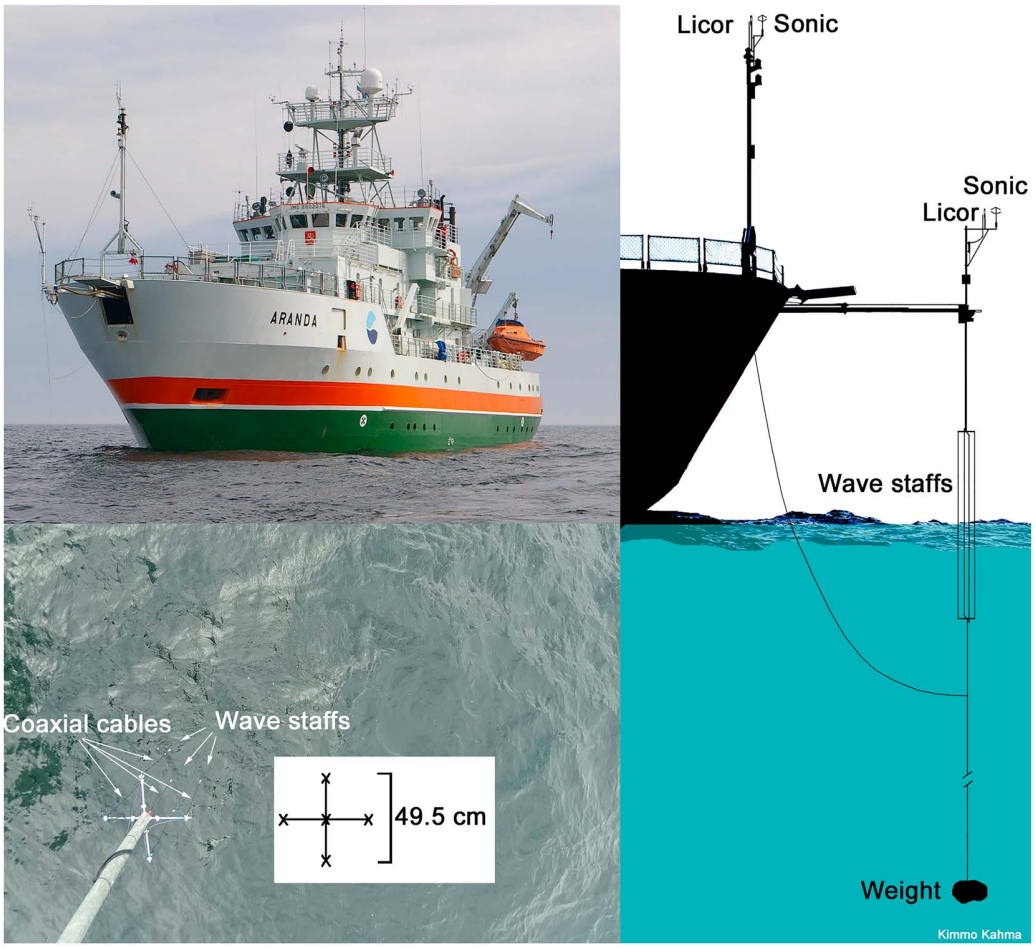

Figure 2. A slightly older version of the experimental setup on R/V *Aranda* (top left). The wave staff array used in this study (bottom left). A schematic picture over the current experimental setup (right).

Directional Waveriders (Mk-III). The wave spectra calculated from the wave staff data were found to be in good accord with the wave buoy spectra (Figure 3).

The peak frequency was calculated by a parabolic fit from a spectra where only 31 elementary bins had been averaged to increase the frequency resolution near the spectral peak. The significant wave height $H_s = H_{m_0}$ was calculated using an upper integration limit of 20π rad/s (10 Hz).

3.2.1. Wave Data From the Array

We used the WDM to analyze the simultaneous data from all five wave staffs in the array. The implementation relied on the code by Donelan et al. (1996, 2015), with minor modifications.

Prior to the application of the WDM we applied a Gaussian filter (25-ms standard deviation and 405-ms window length) and downsampled the time series to 25 Hz in order to avoid interpreting high-frequency noise as true water level differences. To minimize spatial aliasing, we also did not use wave staff pairs with a distance greater than 25 cm. The four remaining 25-cm pairs (see Figure 2) gave four estimates of the wavenumber and direction at each time and frequency, which we consequently averaged.

We used four voices in addition to the base Morlet wavelets, resulting in 15 logarithmically spaced angular frequencies (scales) between 0.25π and 6.35π rad/s. In practice, we determined the final spectra by binning the variance as a function of the other desired variables (wavenumber k, inverse phase speed ν, and/or direction θ). The directional spectra where binned with a resolution $\Delta\theta = 10°$. The wavenumbers and inverse phase speeds were binned with resolutions of $\Delta k = 1/12$ rad/m $\Delta\nu = 1/50$ s/m. We only used wavenumbers less than 9 rad/m in the binning of the inverse phase speed spectrum because of the high noise close to the Nyquist wavenumber.

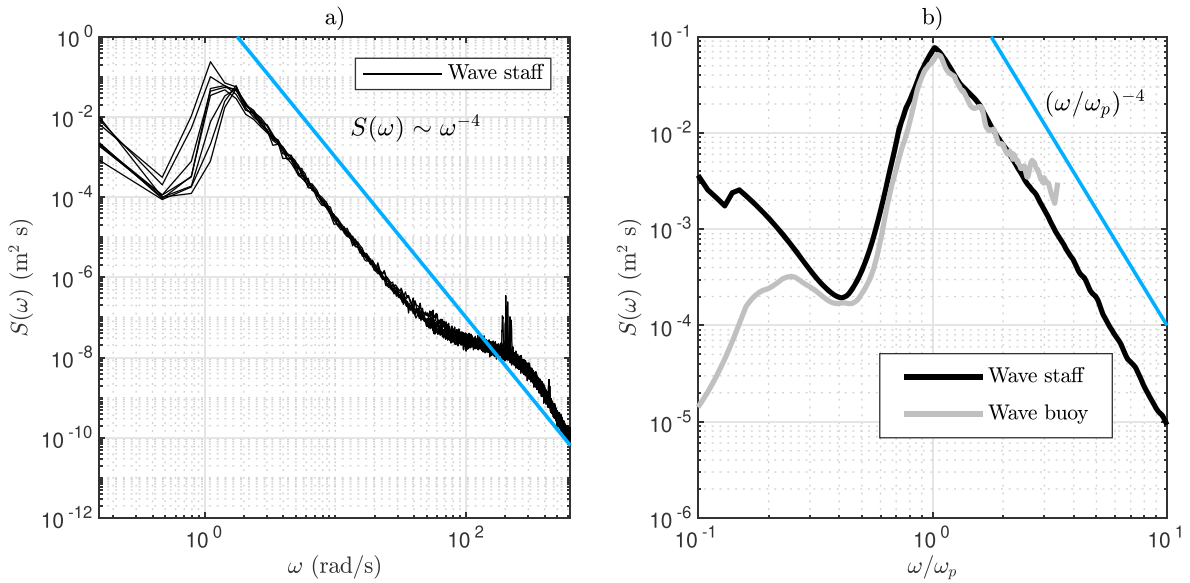

Figure 3. (a) The evolution of the wave spectrum at location 15035 over 4 hr (2015-07-10T14:39 to 2015-07-10T18:09). (b) The average spectrum calculated from the wave staff (black) and a wave buoy located 3.5 km upwind (gray). The blue line shows an ω^{-4} power law.

3.3. Wind Measurements

Sonic anemometers (Metek USA-1) installed at 10.1 and 16.2 m above sea level provided eddy-covariance measurements. The lower device was mounted on a horizontal boom projecting from the bow of the ship, while the other anemometer was installed at the top of a mast near the edge of the bow. Two CO_2/H_2O gas analyzers—an open path LI-COR (*LI-7500*) and an enclosed path LI-COR (*LI-7200*)—were installed at both heights and provided humidity fluxes. All six devices were sampled at 10 Hz. An overview of the experimental setup is shown in Figure 2.

In this paper we used the measurements from the height of 10.1 m. Numerical flow modeling, wind tunnel measurements with a scaled ship model, and field comparisons have all consistently shown the wind speed measurements at this height to be 6% too low when the bow was within ±20° into the wind direction. This bias was corrected in the mean wind speed, which we calculated as 30-min averages.

The friction velocity u_* was determined from the time series assuming that the stress and wind vectors are aligned:

$$u_* = \left(-\overline{u'w'}\right)^{\frac{1}{2}}, \tag{19}$$

where $\overline{u'w'}$ is the momentum flux in the along wind direction. Comparison measurements have indicated that the flow distortion effects on turbulence are within error limits, which is why we used the friction velocity as is, following Dupuis et al. (2003)

3.4. Weather Conditions

The data set of this study consists of observations made from R/V *Aranda* in the Baltic Sea. The wind conditions varied between 0 and 10 m/s, and the significant wave height ranged from 0.2 to 1.5 m. A numerical overview is available in Table 1, and the measurement locations can be found in Figure 1. We will now briefly introduce the different runs.

15031 (*Gulf of Finland*): A 0.2-Hz swell propagated from 240° to the entrance of the Gulf of Finland. A southerly wind rose during the first hours, with the wind speed finally staying between 5 and 7 m/s for 5 hr. The wind gradually turned toward the southeast, where the fetch was around 60 km. The significant wave height stayed between 0.6 and 0.7 m, while the inverse wave age, U/c_p, fluctuated around 0.8 because of the swell.

15033 (*Archipelago Sea*):The wind speed was initially 9–10 m/s, but slowly decayed to 6 m/s while maintaining a direction around 200°. The fetch to the nearest island was about 2 km, but

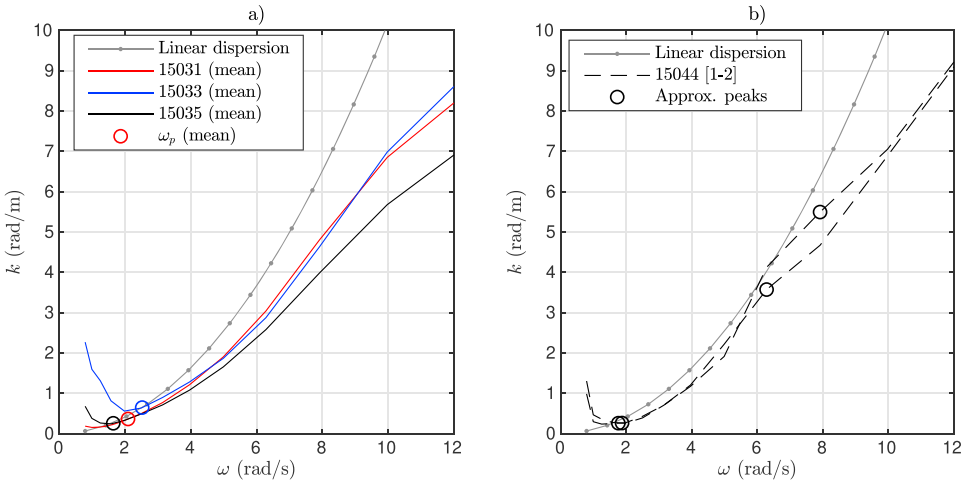

Figure 4. The measured dispersion relation. The solid lines (a) shows the mean values (U/c_p>0.8) of the dispersion curves calculated for three different runs, and the circles denote the mean of the peak frequencies. The dashed lines (b) show the dispersion curves determined from a two 30-min time series where the spectrum is double peaked. The black circles are the spectral peaks approximated from the Wavelet Directional Method spectrum. The gray dotted line is the theoretical linear dispersion curve.

a narrow passage in the southern direction had a fetch around 14 km. The waves were strongly forced (U/c_p=1.5–2.9).

15034 (*Bothnian Sea*): During the first 3 hr the wind speed was less than 3 m/s and the waves were swell ($U/c_p \sim 0.3$). By the time the inverse wave age exceeded 0.8 the wind had turned from the east to the north. The northerly wind kept rising, ending up at 6 m/s.

15035 (*Bothnian Sea*): 15035 was from the same location as the previous run, and directly followed it. A northerly duration-limited wave system developed. The wind speed was 7–8 m/s the first 3 hr; the significant wave height grew from 0.5 to 0.9 m. After a 1-hr dip to 6 m/s, the wind speed continued at 8–9 m/s for two more hours, finally growing the significant wave height to 1.5 m and the peak frequency to 0.2 Hz. The inverse wave age was between 0.8 and 1.9.

15040 (*Baltic Proper*): With no wind for the first two and a half hours, R/V *Aranda* was aligned with a 0.2-Hz northerly swell. For the last hours a 2-m/s northerly wind generated a 1.5-Hz wind sea.

15042 (*Baltic Proper*): This station was located 15 km west of 15040. The main part of the wave field was a 0.3 m northerly swell at 0.2–0.3 Hz, resulting in an inverse wave age of 0.3. The speed of the northerly wind was 2 m/s.

15043 (*Baltic Proper*): This 1-hr measurement was made 12 km west of 14042. The same northerly swell still dominated; the wind speed was below 1 m/s.

15044 (*Gotland*): The wind speed from the east and north-east was 2–3 m/s. The dominant wave system was a 0.2 m swell at 0.2–0.3 Hz coming from north-north-east. The wind sea evolved from 1.5 Hz to around 0.6 Hz over the course of 6 hr; the total significant wave height rose to 0.3 m. The inverse wave age was constantly below 0.8 because of the swell, but the wind sea was actively forced the entire time.

4. Results

4.1. The Dispersion Relationship and Directional Properties

In Figure 4a we show the measured mean dispersion relation for three stations that have the highest wind speeds and most well-defined conditions. The duration-limited case (15035) differ more from the linear relation compared to the fetch-limited cases (15031 and 15033). A comparison between runs 15031 and 15033 also show that the deviation from the linear dispersion is not tied to a certain multiple of the peak

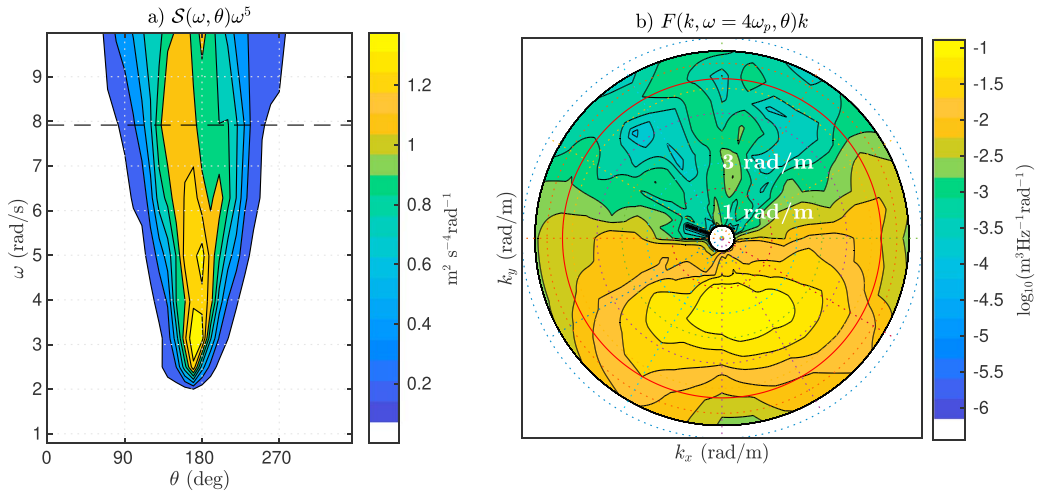

Figure 5. The directional frequency spectrum multiplied by ω^5 (a) and a frequency slice $\mathbb{F}(k,\omega{=}4\omega_p,\theta)k$ (b) as seen by the Wavelet Directional Method (spectrum 15035 [1]). The black dashed line marks $\omega{=}4\omega_p$. The red line marks the linear dispersion shell.

frequency, since their mean dispersion curves overlap for higher frequencies even though their mean peak frequency differ. The variance with respect to the peak can also readily be seen from run 15031, where the mean value of the peak frequency is closer to that of run 15035, but the mean dispersion curve for the higher frequencies is close to that of 15033. Figure 4b illustrates the dispersion relation determined from individual spectra that have a peak frequency of 2 rad/s and a wind sea peaks at around 6–8 rad/s (U_{10} =2–3 m/s). The dispersion curves at both peaks are very close to the linear dispersion relation. The instability of the higher peak is mainly because of the limited frequency resolution in the WDM spectrum.

A deviation from the linear dispersion relation has been found by several authors (e.g., Donelan et al., 1985, 2015; Hara & Karachintsev, 2003; Wang & Hwang, 2004) and the nonlinearities have been explained to be caused by bound harmonics. If the full direction frequency-wavenumber spectrum is available, these harmonics should be visible by examining all the wavenumbers at a certain frequency. This was done explicitly by Leckler et al. (2015) and Peureux et al. (2018). The energy of wave components having different wavenumbers (but the same frequency) are also distinguishable in our measurements, although both the measurement technique and our analyzing method are different (Figure 5b).

4.2. Wavenumber Saturation Spectrum

We grouped the saturation spectra, $B(k)$ (equation (8)), according to the wind speed, and each spectrum in Figure 6a thus represents one group average. The individual spectra are shown in Figure 6b. Most averaged spectra have a $B(k) \propto k^{0.5}$ equilibrium slope before saturating at the higher wavenumbers. In the equilibrium regime the wave energy increases with the wind speed, but the saturation collapse the spectra to a value of $B(k)$=5–6·10^{-3}. For wind speeds under 3 m/s the saturation range is not captured in the measurements because of limitations in the wave staff spacing. The $k^{0.5}$ slope is still visible, with the exception of the 0- to 1-m/s group. Nevertheless, the scatter in the lower wind speed bins is large (Figure 6b).

An averaging effect is also seen for the wind speed bin 4–5 m/s, where an equilibrium range is present for two individual spectra, but absent in the average. These spectra belong to run 15034, where the wind turns, thus resulting in a swell not aligned with the wind.

The data consist of measurements from different geographical conditions (see Figure 1). We therefore decided to treat the three main sites with the highest wind speeds (15031, 15033, and 15035) separately, while using the dimensionless wavenumber $\tilde{k} = kU^2/g$ to compare spectra from different wind conditions. Because of the measurement noise caused by the limitations in the wave staff spacing, wavenumbers greater than 4 rad/m were discarded, along with data below the spectral peak k_p.

Spectra in both 15031 and 15033 transition from the equilibrium to the saturation regime at about $\tilde{k}$ = 10, with saturation values near 6·10^{-3} (Figures 7a and 7b). For 15035 the equilibrium regime is visible at

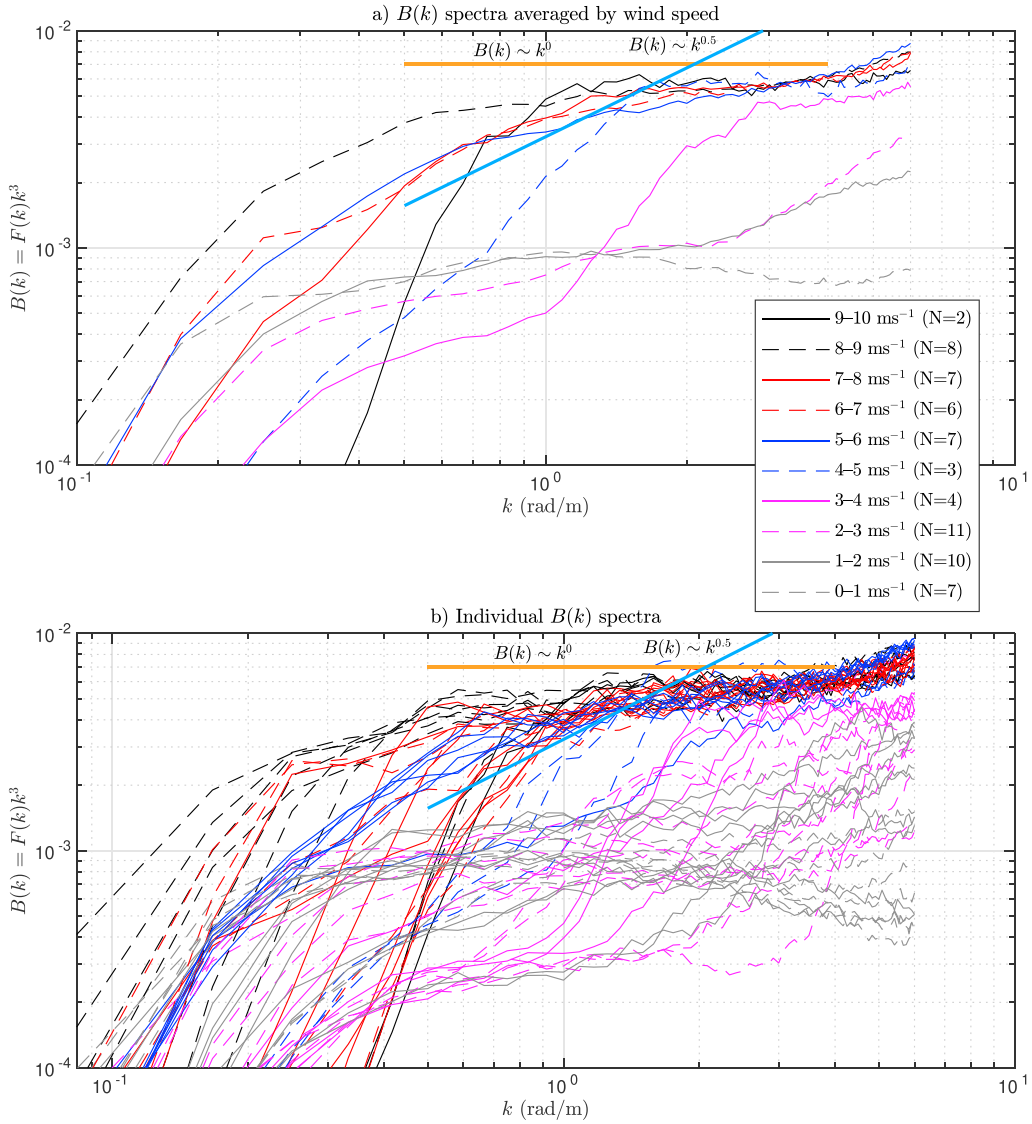

Figure 6. Saturation spectra $B(k) = F(k)k^3$ for different ranges of the wind speed (a). The individual spectra are shown in panel (b).

$2 < \tilde{k} < 4$, but the transition is less clear. The dimensionless wavenumber collapses the spectra also in the equilibrium regime, a feature especially visible for run 15035.

The spectra calculated using the combined data from all three aforementioned runs collapse well, although the limited amount of data causes some instability in the mean spectra (Figure 8a). After the equilibrium-to-saturation transition at around $\tilde{k} = 10$ this composite data set saturates to $B(k)$=5.8·10^{-3}, which means that the Phillips' constant would have a value of $\alpha = 1.2 \cdot 10^{-2}$.

The dimensionless wavenumber can also be defined using the friction velocity, that is, as $k^* = ku_*^2/g$. Scaling with the friction velocity also produces a coherent group of spectra saturating at higher values of k^* (Figure 8b). It is challenging to determine an exact point of transition between the regimes, but it falls in the range of k^*=0.01–0.02. This transition point is in line with the findings of Lenain and Melville (2017), whose results show an equilibrium range extending to $k^* \approx 0.01$.

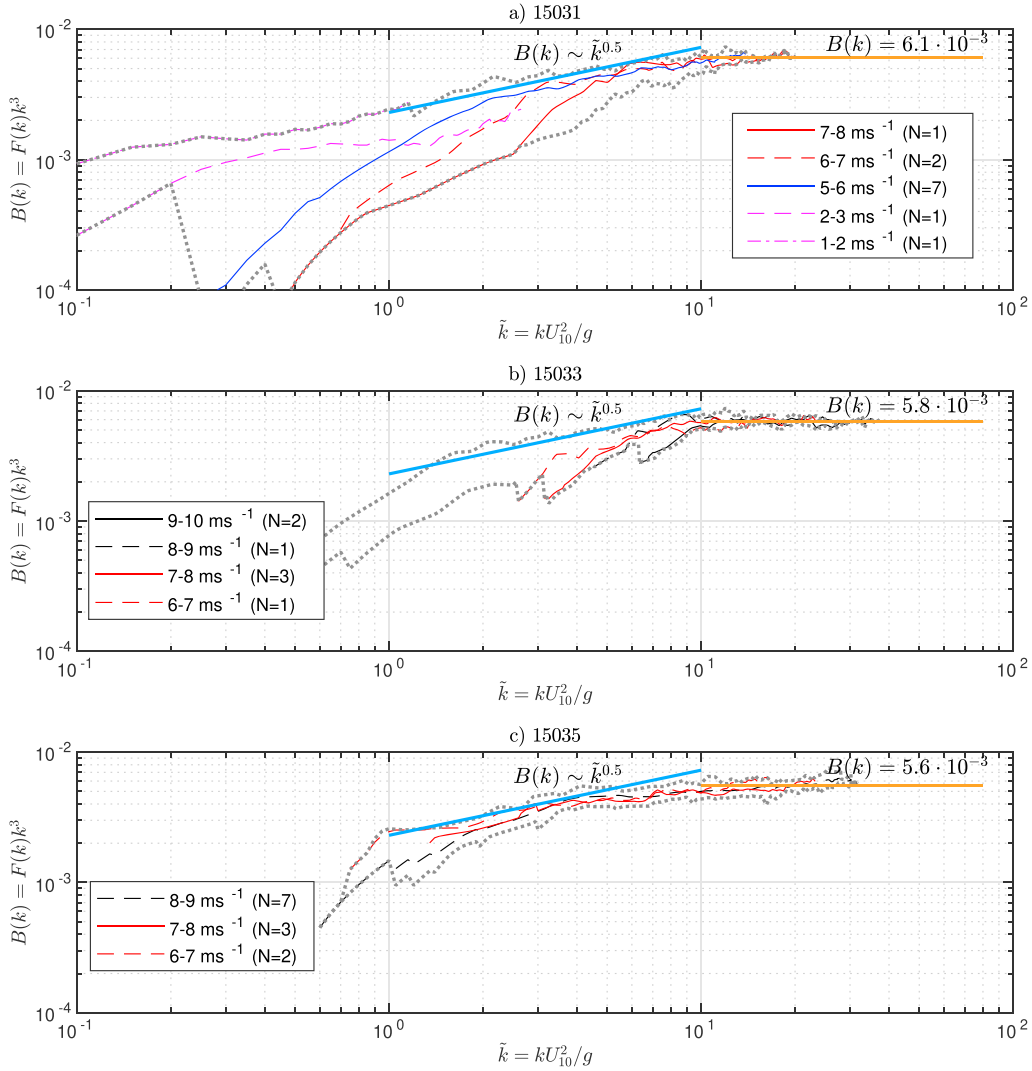

Figure 7. Saturation spectra $B(k)=k^3F(k)$ as the function of the dimensionless wavenumber at three different sites (a–c). The gray dotted lines mark the maximum and minimum values of individual spectra. Only wavenumbers $k_p \leq k \leq 4$ rad/m are included in the average.

4.3. Frequency Equilibrium Spectrum

We grouped the equilibrium spectra $S(\omega)\omega^4/(Ug)$ according to the wind speed. Situations with an inverse wave age under 0.8 were excluded, as were frequencies below the spectral peak. Data from each group formed a mean spectrum representative for that wind speed range, which we plotted as a function of two nondimensional angular frequencies, $\tilde{\omega} = \omega U/g$ and ω/ω_p (Figure 9).

As a function of $\tilde{\omega}$ the spectra show two ω^{-4} power law regions (Figure 9a). The equilibrium range extend from roughly $\tilde{\omega}$=1–2 to $\tilde{\omega}$=4–5, and its equilibrium level is in line with $\alpha_u = 4.5 \cdot 10^{-3}$ (found by Kahma, 1981). The only outlier is the highest wind speed class (9–10 m/s, solid black). A connection to the strength of the forcing (as proposed by Donelan et al., 1985) can be seen when the spectra are binned with respect to the inverse wave age instead of the absolute wind speed (Figure 9c). An increased forcing lowers the equilibrium level and increases the transition frequency. As the second ω^{-4} range will not be considered in this paper, we simply note in passing that it ranges from approximately $\tilde{\omega} = 10$ to at least $\tilde{\omega} = 20$; this is well beyond what we can resolve in the wavenumber domain.

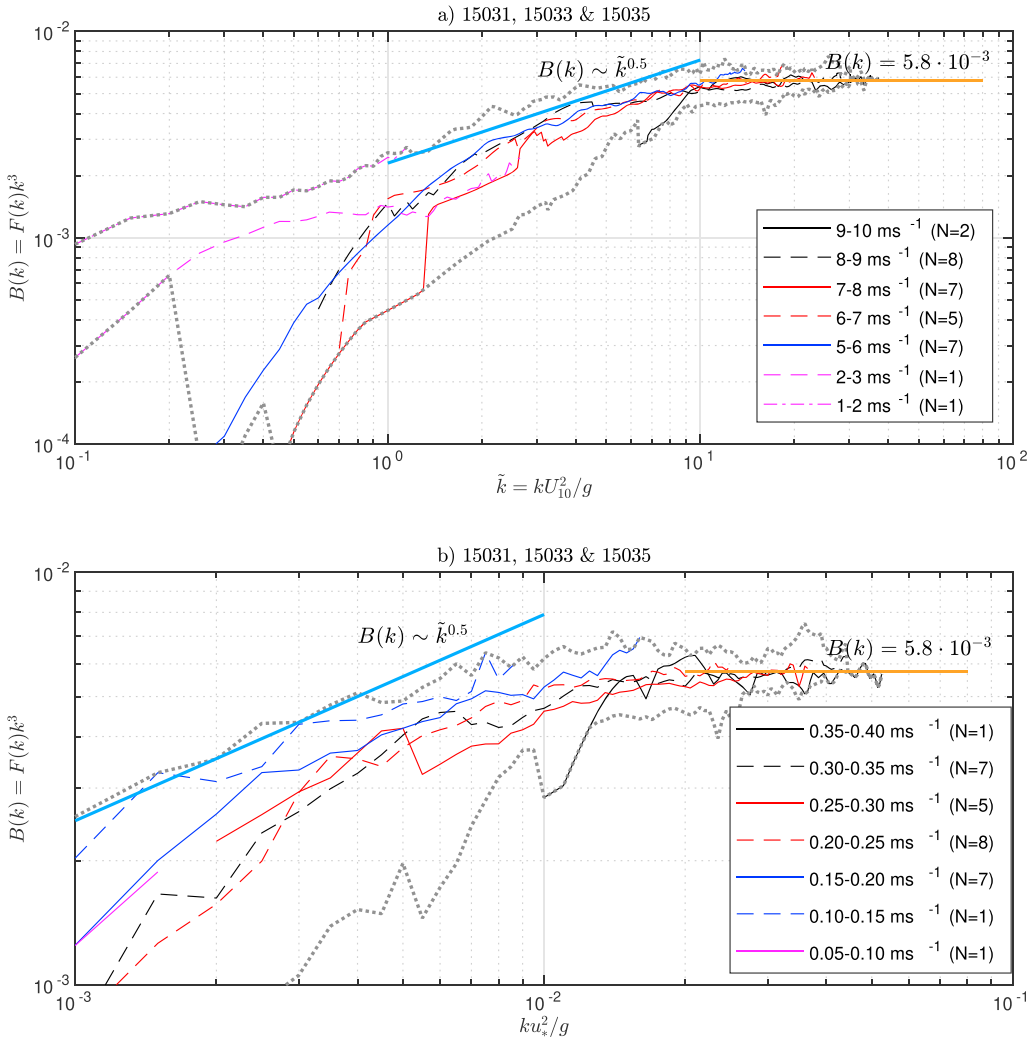

Figure 8. Saturation spectra $B(k)=k^3F(k)$ from sites 15031, 15033, and 15035 as the function of the dimensionless wavenumbers (a) kU_{10}^2/g and (b) ku_*^2/g. The gray dotted lines mark the maximum and minimum values of individual spectra. Only wavenumbers $k_p \leq k \leq 4$ rad/m are included in the average.

Although the transition point between the different regimes cannot be determined unequivocally, most of the spectra show a shift around $\tilde{\omega}$ =4–5, which is consistent with $\tilde{\omega} = 5$ determined by Kahma and Calkoen (1992). The two ω^{-4} ranges are connected by a transition slightly slower than ω^{-5}. Banner (1990) attributed the deviation from the ω^{-5} form of Phillips (1958) to the Doppler shift, but later studies have determined that this effect is relatively small (Guimarães, 2018; Leckler et al., 2015; Peureux et al., 2018), and the presence of nonlinear harmonics have been offered as the explanation (e.g., Hisaki & Tokuda, 1995; Janssen, 2009).

The picture is less clear when the frequencies are scaled with respect to ω_p (Figure 9b). For the highest wind speeds ($U > 7$ m/s) it is possible to interpret the spectra to have an equilibrium range ending at $3\omega_p$. Still, for the wind speeds 4–6 m/s the equilibrium range seems to extend to 5–6ω_p. When binned with respect to the inverse wave age (Figure 9d), a somewhat consistent transition is visible around 3–4ω_p, which is in line with Banner (1990).

In summary, while different parts of our results do not directly contradict previous findings of Kahma (1981), Donelan et al. (1985), and Banner (1990), none of the four representations in Figure 9 can provide a comprehensive description of the frequency spectra. Our data seem to be best explained by the assumptions in panel (c), namely, that there exist a fixed saturation level ($\alpha \approx 2.5 \cdot 10^{-2}$) and that the equilibrium level depends on the strength of the forcing.

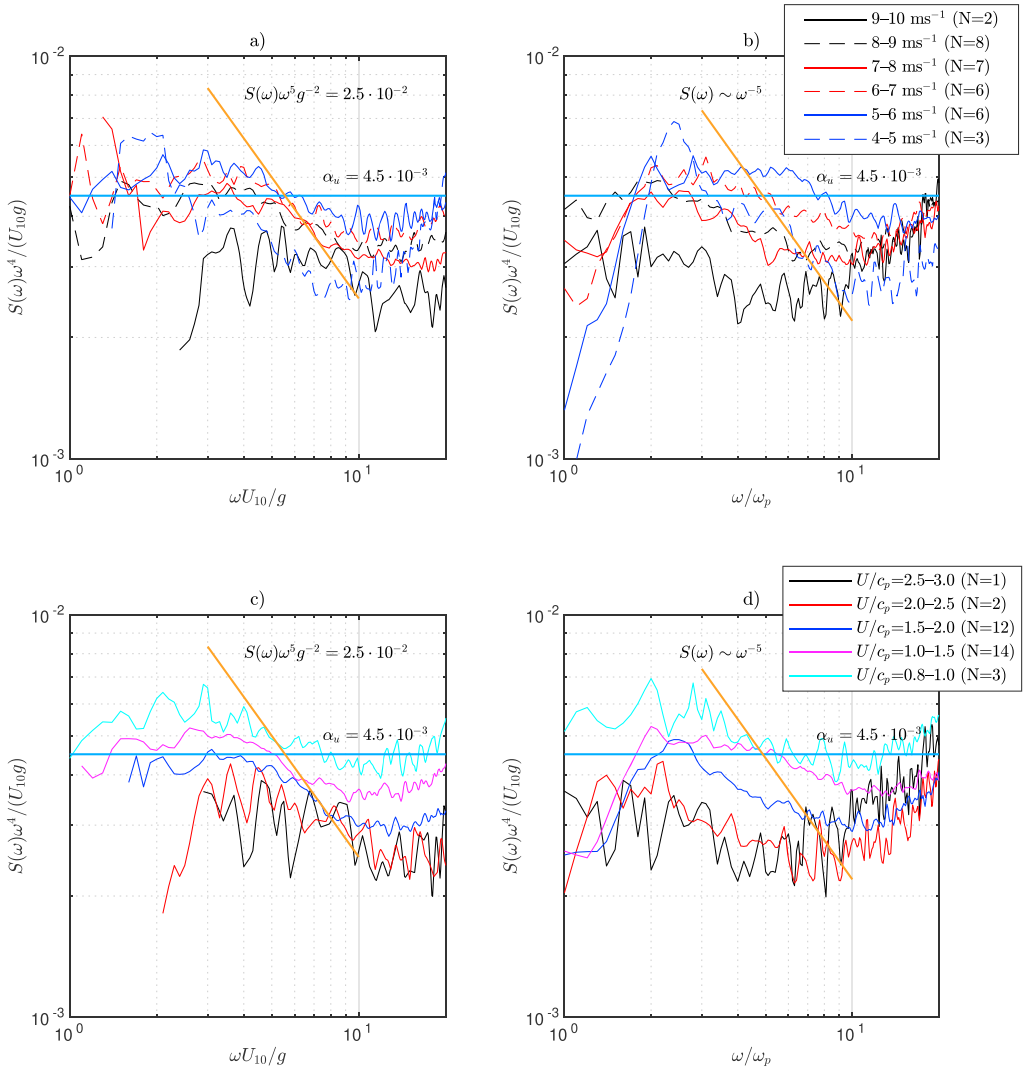

Figure 9. Equilibrium spectra $S(\omega)\omega^4/(U_{10}g)$ classified according to the wind speed (a, b) and the wave age (c, d) as a function of the dimensionless angular frequencies $\omega U/g$ (a, c) and ω/ω_p (b, d). In both plots only cases where $U/c_p > 0.8$ are accepted and frequencies $\omega < \omega_p$ are discarded from the spectral averages.

4.4. Inverse-Speed Spectrum $Q(\nu)$

In deep water the dimensionless frequency, $\omega U/g$, and the dimensionless wavenumber, kU^2/g, are often interpreted as the inverse wave age, U/c, or as $(U/c)^2$, respectively. Such an interpretation, however, assumes that every wave component obeys the linear dispersion relation. Because of wave nonlinearities, this is a poor assumption especially in the rear face of the frequency spectrum. Although not easily defined using traditional frequency measurements, the relation between the phase speed of the wave component and the wind speed is still a central quantity. To examine this aspect without being bound by the assumptions of linear theory, we defined a spectrum using the measured phase speed of the wave components.

Example spectra of a strongly forced, fetch-limited case is presented in Figure 10. The omnidirectional inverse phase speed spectrum (a) shows a transition from the ν^{-4} equilibrium subrange to the ν^{-5} saturation subrange at about $\nu = 0.4$ s/m. The omnidirectional wavenumber spectrum (b) shows k^3 the saturation range already identified in Figure 7b, but the existence of a $k^{2.5}$ region is less clear. The inverse phase speed spectra estimated from $S(\omega)$ and $F(k)$ using linear theory shows that the Q-spectrum is not merely a rescaling of the traditional spectra (a). Unsurprisingly, the disagreement is largest for the short waves in spectrum estimated from the frequency measurements. Although directional properties are not discussed in more

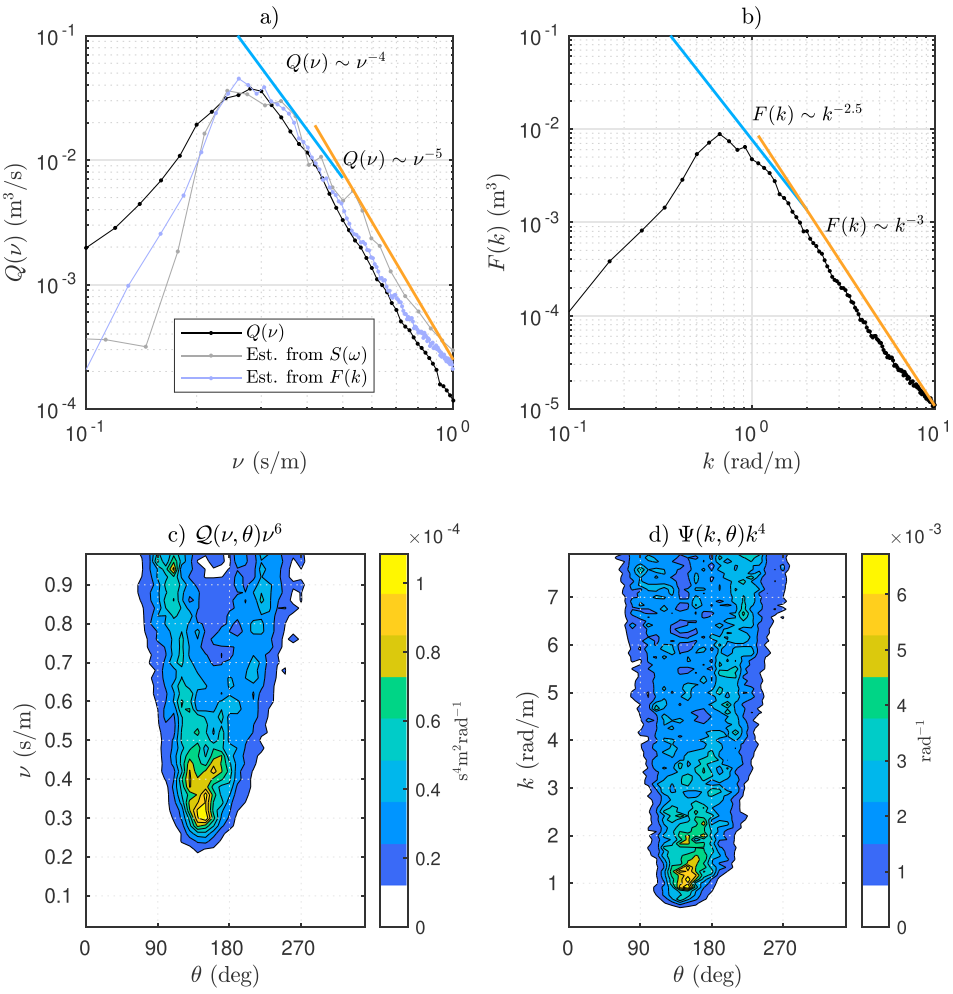

Figure 10. The third spectra in Run 15033. (a, c) The omnidirectional and directional inverse phase speed spectra. (b, d) The corresponding wavenumber spectra. Panel (a) also shows the Q-spectra estimated from $S(\omega)$ and $F(k)$ using linear wave theory.

detail in this paper, we still present an example of the directional inverse phase speed spectrum (c) next to the normal directional wavenumber spectrum (d). The spectrum shows a similar bimodal characteristic that has previously been found for wavenumber spectra (e.g., Hwang et al., 2000).

We will now present data from four runs gathered under various conditions.

4.4.1. Run 15033: Strongly Forced Fetch Limited

The noise of the higher wavenumber (Figure 11b) is also visible in the Q-spectrum (a). The general shape of the Q-spectrum resembles that of the frequency spectrum because of the similar equilibrium normalization, but the possible second power law transition—which takes place at $\tilde{\omega} = 10$ in the frequency spectrum—is masked by noise in the Q-spectrum.

The Q-spectrum differs from the frequency spectrum especially in two aspects. First, in the Q-spectrum the power law in the assumed saturation range follows a ν^{-5} form closely, while the ω^{-5} part in the frequency spectrum is distorted. The saturation level in the Q-spectrum is also close to twice that of the wavenumber domain, as is expected from theory; in the frequency spectrum this is not the case. (The individual frequency spectra are compatible with the saturation value of $\alpha \approx 2.5 \cdot 10^{-3}$ that was deduced from the averaged spectra in Figure 9.) Second, the equilibrium values of the different Q-spectra collapse around $3 \cdot 10^{-3}$, while the frequency equilibrium values have a larger spread (roughly 3–4.5$\cdot 10^{-3}$). As a consequence, the equilibrium-to-saturation transition point also varies more in the frequency spectrum compared to the Q-spectrum.

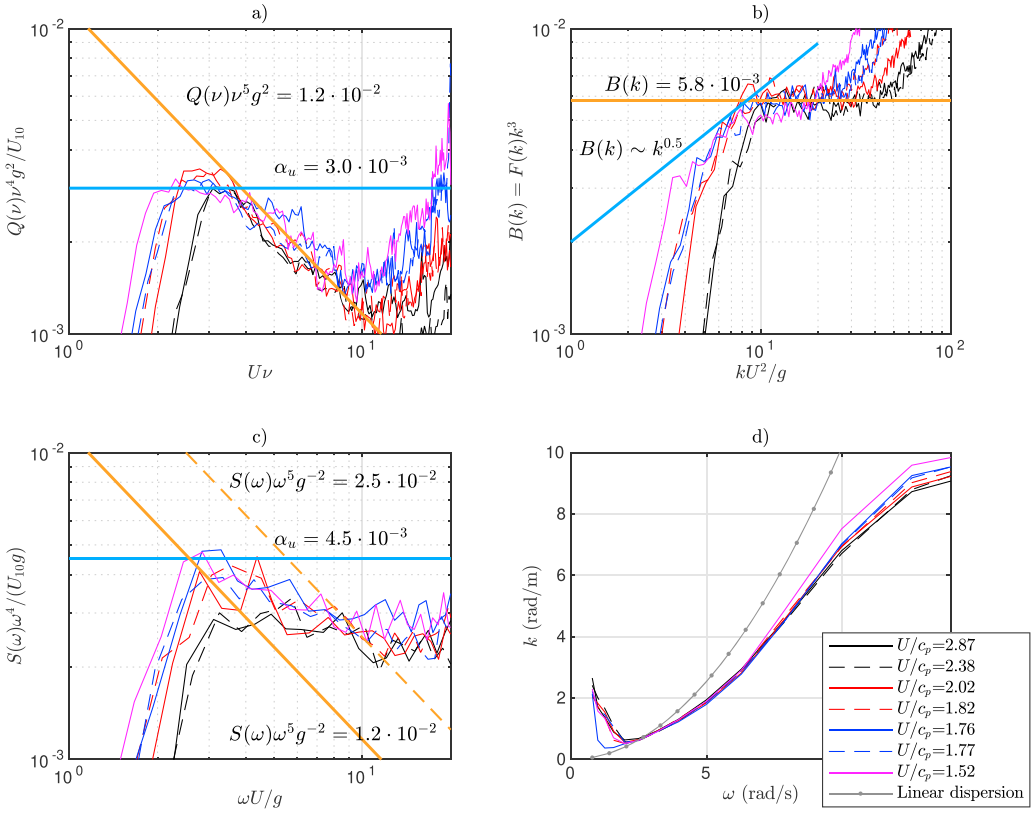

Figure 11. The wave spectra from Run 15033. The equilibrium spectra are shown for the inverse phase speed and frequency (a) and the frequency spectra (c), while the saturation spectrum are showed for the wavenumber (b). The mean dispersion relation for all the spectra are shown in panel (d).

The inconsistencies in the frequency spectra seem to depend on the strength of the forcing. The first two spectra—solid and dashed black—are most strongly forced with U/c_p over 2. These spectra have the lowest equilibrium levels (around $3{\cdot}10^{-3}$). They also seem to transition to the saturation range at a higher dimensionless frequency, around $\tilde{\omega} = 8$; the transition for the last spectra, with $U/c_p = 1.4$, happens around $\tilde{\omega} = 4$. A similar strong pattern in the transition point is absent in the Q-spectra, although some variation exists.

In Figure 9 the frequency spectra—averaged according to wind speed bins—showed a power law decaying slower than ω^{-5}. Still, the individual spectra in Figure 11c seem to follow an ω^{-5} power law more closely than the spectral average. The deviation from the ω^{-5} is partially explained as an artifact of the averaging process caused by the variations in equilibrium levels and transition points when the frequency spectra was determined as a function of the dimensionless frequency, $\tilde{\omega}$. Nevertheless, even for individual spectra the ν^{-5} regime is more clear than to the corresponding ω^{-5} region—the averaging artifact is therefore only a partial explanation.

The mean dispersion curves in Figure 11d differ between the different spectra in such a way that a stronger forcing is connected to a greater deviation from the theoretical linear dispersion curve. A stronger U/c_p forcing produces steeper waves, thus increasing the amount of energy recorded at higher-frequency harmonics. The leakage to higher frequencies also partially overlap with the saturation range, thus distorting the ω^{-5} power law in the frequency domain, as determined by Janssen (2009).

4.4.2. Run 15031: Swell and Turning Winds

For the first two spectra the wind sea peaks are visible above the lower frequency, 240°, southwestern swell. After the wind turned to the southeast the individual spectra were very flat and the wind sea cannot clearly be separated from the swell in the omnidirectional spectra (Figure 12d).

The first two spectra that were measured before the wind had turned had power law transitions at about $U\nu = 3$ in the inverse phase speed spectra, and a similar transition can be identified in the wavenumber

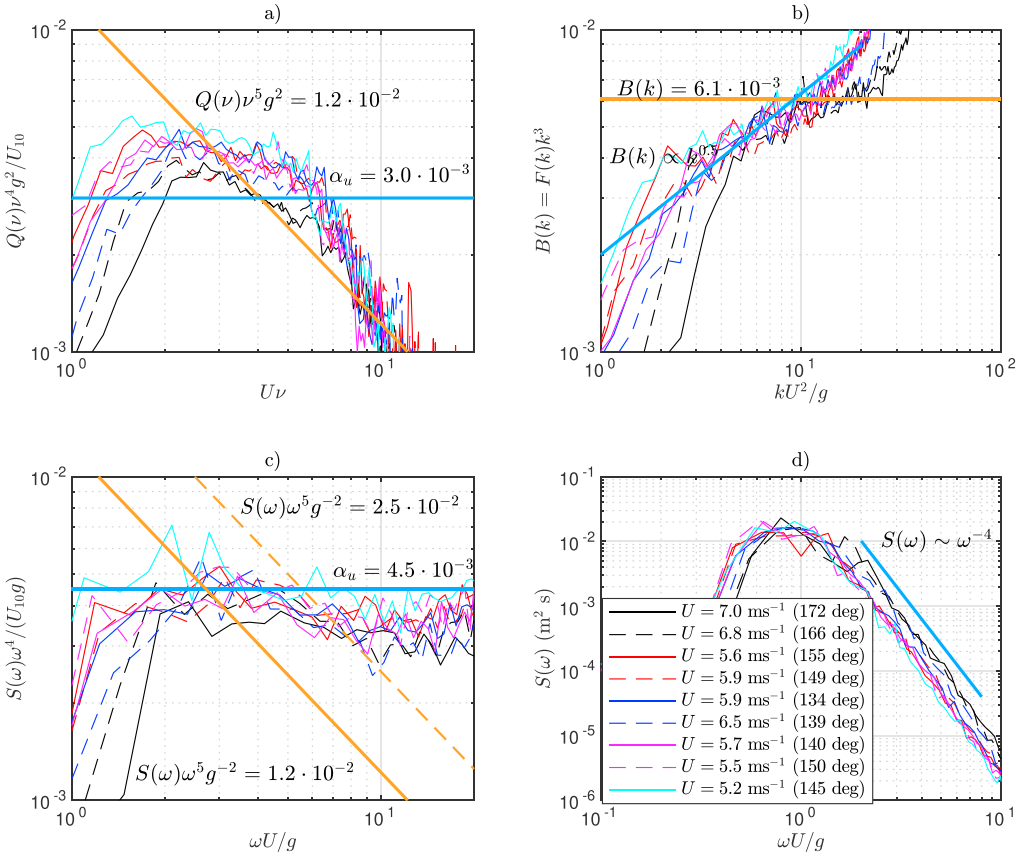

Figure 12. The wave spectra from Run 15031 ($U/c_p > 0.8$). The equilibrium spectra are shown for the inverse phase speed and frequency (a) and the frequency spectra (c), while the saturation spectra are showed for the wavenumber (b). The normal frequency spectra are shown in panel (d).

domain. In the frequency domain a transition exist at around $\tilde{\omega} = 5$, but it is relatively weak (although consistent with the saturation level determined value from the entire data set). After the wind has turned, the wind sea was fetch limited. The fetch-limited Q-spectra could easily be interpreted to have a long ν^{-4} range, but they can also be viewed as having a transition at roughly $U\nu$=3, the spectra after the transition point just decays slower than ν^{-5}. The slower decay is also visible in the frequency domain (c).

The slow decay and higher equilibrium levels in the Q-spectra (compared to Run 15033) would then be explained by the background swell. The slower decay of the tail could also, in theory, be caused by an opposing ambient current (see Appendix B). This is not supported by the data, because an opposing current would simultaneously cause the frequency spectra to decay more *rapidly* than ω^{-5} in the saturation range.

4.4.3. Run 15035: Duration Limited

There is no direct connection between a duration-limited and fetch-limited wave field, since in a duration-limited case all wave components are governed by their own "fetch." Looking at the individual wavenumber saturation spectra (Figure 13b), they can be interpreted to have an equilibrium-to-saturation transition at $\tilde{k} \approx 4$. After a lower saturation level of about $4.5 \cdot 10^{-3}$ the spectra decays slower.

This interpretation of a "saturation-to-equilibrium" transition is supported by the inverse phase speed spectra (d). The second transitions also explains the difficulties to interpret the mean spectra in Figure 7c and the contradiction between the higher saturation value determined from the averaged spectra.

Figure 13a shows the equilibrium Q-spectra, which have a very short ν^{-4} range (if any) that transitions into a ν^{-5} range. The saturation level determined from the Q-spectra are slightly below the value determined from the wavenumber spectra (Figure 13d), which is possibly caused by currents. The assumed saturation range is followed by a long ν^{-4} tail in a similar fashion what is seen in the frequency domain (Figure 13c).

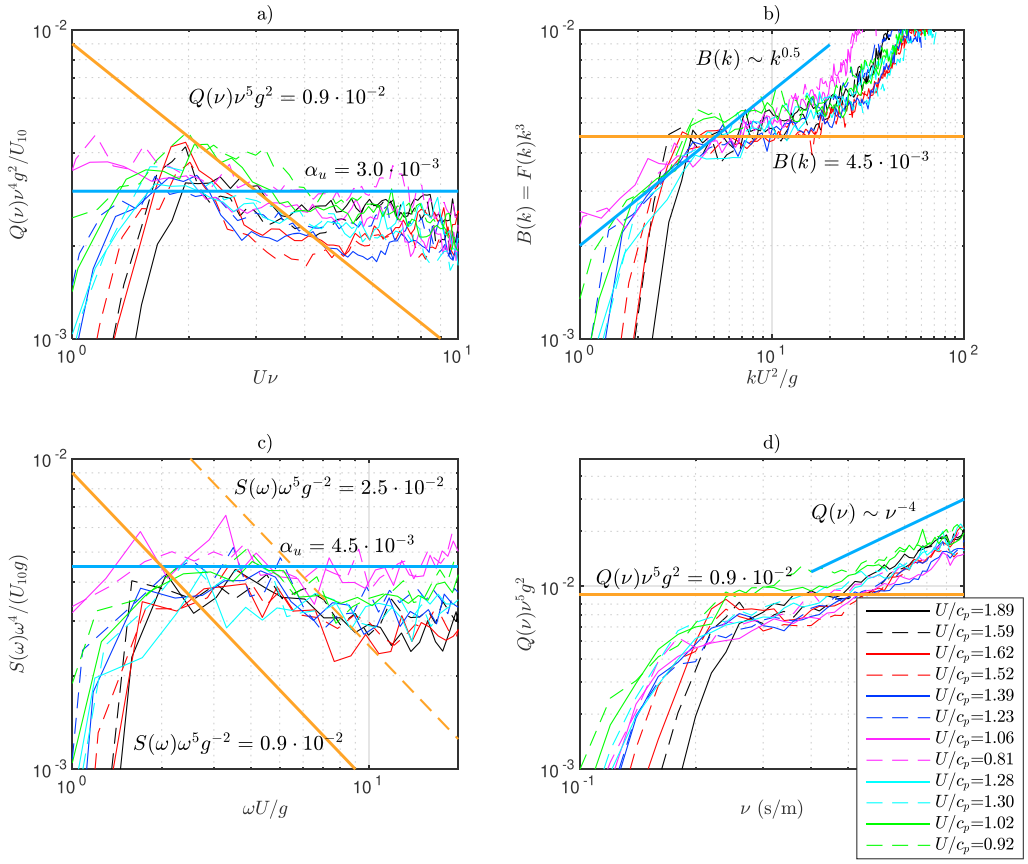

Figure 13. The wave spectra from the duration-limited Run 15035. The equilibrium spectra are shown for the inverse phase speed (a) and the frequency spectra (c). The saturation spectra are showed for the wavenumber (b) and the inverse phase speed domain (d).

The frequency spectra have an identifiable ω^{-4} range extending to approximately $\tilde{\omega}$=5, and a somewhat unclear transition to an ω^{-5} range. The ω^{-4} transition at $\tilde{\omega}$=10 is not a product of measurement noise, since the frequency measurements are made with a single wave staff. Similar ν^{-4} and $k^{-2.5}$ subranges (from $U\nu$ =3–4 and $\tilde{k} \approx 10$) are also visible in the inverse phase speed and wavenumber domain. The end of the ranges are still probably tainted by high wavenumber noise, and the possible connection between these higher subranges is therefore left undetermined.

4.4.4. Run 15044: Weak Winds With Aligned Swell

Run 15044 had very weak winds ($U = 3$ m/s) growing waves on top of a dominant swell with the same direction. An ω^{-4} range is visible in the frequency domain despite both the wavenumber and the inverse phase speed spectra show only a saturation range (Figure 14) with saturation coefficients resembling the lower value determined from the duration-limited Run 15035.

The frequency spectra follow a typical ω^{-4} shape with a power law transition at roughly $\tilde{\omega} = 5$ despite this feature being absent in the other two spectral domains. The wave nonlinearities seem to have an ability to create this type frequency spectra in a wide variety of conditions. The apparent equilibrium level in the frequency spectrum is higher than previous values from the literature, which might be caused by the background swell.

5. Discussion

Determining the phase speed of waves is not trivial, since it varies over time periods clearly shorter than what is typically used to calculate wave spectra (e.g., Fedele, 2014; Melville, 1983). Using a long time series to determine one phase speed for a wave component is therefore clearly inadequate. If full spatiotemporal data

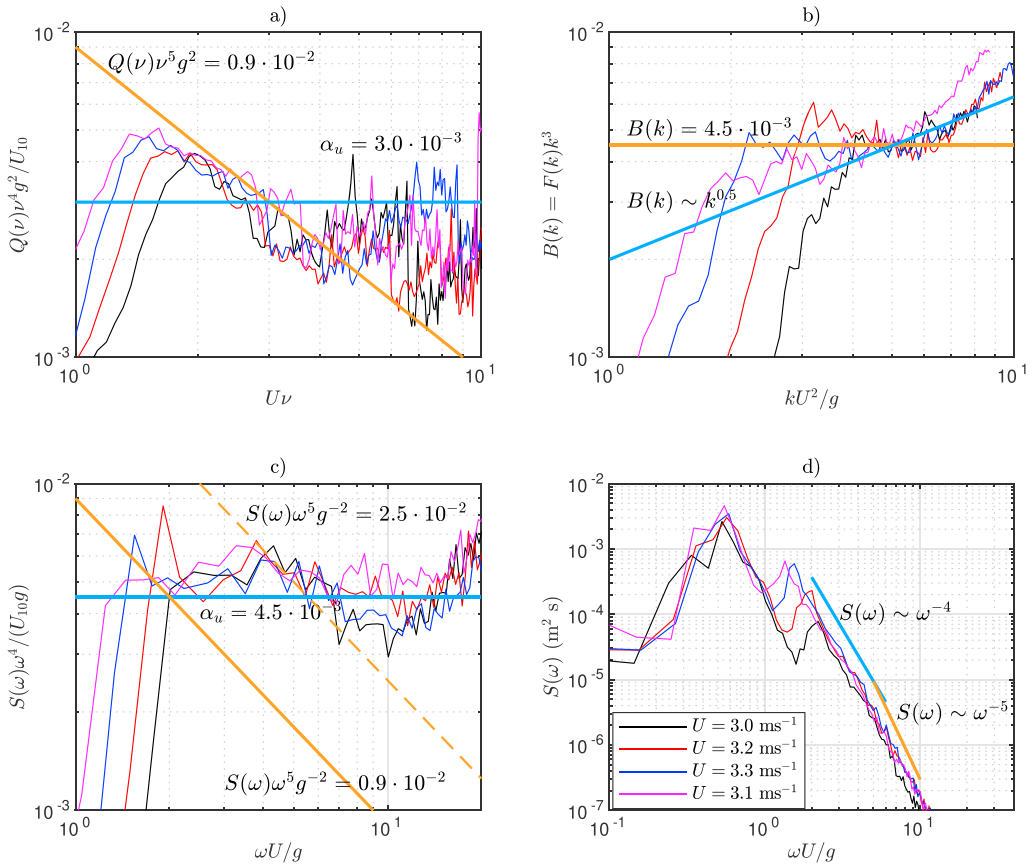

Figure 14. The wave spectra from Run 15044 with a wind speed of at least 3 m/s. The equilibrium spectra are shown for the inverse phase speed and frequency (a) and the frequency spectra (c), while the saturation spectra is showed for the wavenumber domain (b). The normal frequency spectra are shown in panel (d).

are available, a 3-D Fourier transform can be applied. In the case of wave staff measurements, some kind of nonstationary analysis must be used, as in Melville (1983). In this paper we adopted the WDM, following Donelan et al. (1996). The main challenge is determining the wavenumber as a function of frequency and time, $k(\omega, t)$, since the (inverse) phase speed is then straightforwardly given as $k(\omega, t)/\omega$. The suitability of the WDM to calculate inverse phase speed spectra therefore relies on the ability to determine wavenumber spectra.

While the WDM can resolve similar frequency waves with different wave numbers, it will also—if two waves transit the array simultaneously—average two waves to one, thus assigning it a wavenumber in between and biasing the wavenumber estimate low. As noted by Donelan et al. (2015), such an artifact produces a too narrow directional distribution, but it will also cause lower saturation levels in the high wavenumber tail. This behavior seems like a plausible explanation to why the saturation levels determined using the WDM obtained in this paper ($\approx$5–6 $\cdot 10^{-3}$) and by Tamura et al. (2014; $\approx$4–5 $\cdot\ 10^{-3}$) are slightly lower than those of Lenain & Melville (2017; $\approx 7 \cdot 10^{-3}$), Romero & Melville (2010; $\approx 8 \cdot 10^{-3}$), and Leckler et al. (2015; $\approx 10 \cdot 10^{-3}$). Nevertheless, some scatter is naturally expected because of the variations in wave and wind conditions, and with this in mind our results agree well with previous research.

Assuming a universal saturation range, the transition frequency is determined by the equilibrium constant α_u. The constant α_u in the formulation by Kahma (1981) then necessarily leads to a fixed dimensionless transition frequency $\tilde{\omega}_g = \omega_g U/g = \alpha/\alpha_u$, where α is Phillips' saturation range constant (see Appendix A). Donelan et al. (1985) noted that even though the constant α_u of Kahma (1981) explained the data well in the range they were determined, it could not be comfortably extrapolated to account for the new data in their study. The authors therefore proposed that α_u of the equilibrium range is not universal but depends

on the strength of the forcing, U/c_p. Also, the varying transition frequencies of Kahma and Calkoen (1992) can be seen to suggest a nonconstant value for α_u in the frequency spectrum. Our frequency data were best explained by a constant saturation range combined with an equilibrium range that depended on the inverse wave age.

The equilibrium-range properties of the frequency spectra in our strongly forced fetch-limited case depended on the strength of the forcing, while the inverse phase speed spectra showed smaller variations (Figure 11). The leading explanation for the differences cannot be the Doppler shift (as proposed by Kitaigorodskii et al., 1975, and Banner, 1990), since it would also distort the saturation subrange of the Q-spectra, thus leading to an inconsistency with the wavenumber spectra (see Appendix B). We conclude that the decrease in the frequency equilibrium level—and increase in the transition frequency—is mostly an artifact of steeper waves generated by a stronger forcing; hence, it is questionable to which extent this dependence on the forcing can be seen as a fundamental property of the wave field. The wave nonlinearities can also seemingly create an ω^{-4} range without any counterpart in the wavenumber of inverse phase speed domain (Figure 14).

Our observations offer more direct experimental evidence that wave nonlinearities, not the Doppler shift, is the leading cause in the distortion of the high-frequency part of the spectrum. The good agreement between the saturation ranges of the wavenumber and inverse phase speed spectrum also gives experimental confirmation for the theoretical results of Janssen (2009) that the contributions of the wave nonlinearities are small in the wavenumber domain. We also note, that an inverse phase speed spectrum decaying as ν^{-5} (Figures 11 and 14) would suggest that the first-order spectrum (i.e., the spectrum without higher-order nonlinear effects) decays at an even faster rate, as discussed by Leckler et al. (2015).

A second transition from an ω^{-5} to an ω^{-4} power law in the frequency measurements is observed consistently, but such short waves are not be resolved with complete confidence in the spatial domain. Thus, no comparative analysis could be made. We still note that this transition takes place in the gravity wave regime and is therefore separate from the ω^{-5} to ω^{-4} transition reported by Mitsuyasu (1977) at frequencies affected by capillary effects. These two transitions together create frequency spectra that have an apparent continuous ω^{-4} power law, but with a slightly lower equilibrium level for the highest frequencies. Such a spectrum is visible also in Lenain & Melville (2017, their Figure 7), where this shift happens around $f = 0.6$ Hz (roughly $\omega U/g = 4$). If the spectrum ends before the second transition takes place, one might interpret the spectrum to simply have a transition to an ω^{-5} regime (e.g., Fig 14d).

The wavenumber data in this study also scaled well with the friction velocity, u_*, as was also found by Lenain and Melville (2017). The friction velocity is therefore still a valid candidate to represent the wind conditions, but the physical interpretation of the quantity $u_*\nu$ is not as immediately attractive or straightforward as $U\nu$. One obvious usage of the inverse phase speed spectrum would be in quantifying the momentum flux from the wind to the waves, since the central quantity U/c is directly captured for each wave component without the need for any additional current measurements or corrections. If quality current measurements are available, the difference between the wavenumber spectrum and the Q-spectrum could also be used to study the effect of the Doppler shift over different scales, since it can be accounted for in the Q-spectrum without any additional assumptions about wave dispersion (see Appendix B). On the other hand, the wavenumber spectrum is the proper tool to quantify, for example, wave dissipation, which depends on intrinsic properties, such as the wave steepness.

The directional distribution for higher-frequency/wavenumber waves becomes more complicated, and its exact shape is still not known (Donelan et al., 1985, 2015; Hwang et al., 2000; Hwang & Wang, 2001; Leckler et al., 2015; Peureux et al., 2018; Young et al., 1995). Expectedly, signs of a deviation from a standard unimodal distribution is also found in our data (Figure 5 and 10). Integrating over all directions and calculating the dimensionless phase speed $U\nu$ from the modulus $\nu = |\nu|$ might therefore not be optimal, but we nevertheless chose this approach to allow for a fair comparison to, for example, the omnidirectional wavenumber spectrum. Donelan et al. (1985) scaled his spectra using the wind component in the direction of the spectral peak, but from the point of view of the Q-spectrum the relevant wind speed have to be calculated in the direction of each wave component separately. Nevertheless, such detailed information of the directional

inverse phase speed distribution might be beyond what can be extracted from wave staff measurements using the WDM.

6. Conclusions

High-frequency wave data from R/V *Aranda* were presented and the spectra compared well to measurements from a nearby wave buoy. We used the WDM to extract both the frequency and the wavenumber of wave components from data recorded by five wave staffs.

The main contribution of this paper is the introduction of a new wave spectrum, $Q(\nu)$ (m^3/s), where $\nu = c^{-1} = k\omega^{-1}$ is the inverse phase speed. Determining this spectrum is only meaningful from explicit frequency-wavenumber data that eliminate the need for any assumptions concerning the wave dispersion. Using the linear dispersion relation to determine $\nu = \omega g^{-1}$ would only lead to a trivial rescaling of the frequency spectrum. The Q-spectrum has the following saturation range and equilibrium range:

$$Q(\nu) \sim \alpha g^{-2}\nu^{-5} \tag{20}$$

$$Q(\nu) \sim \alpha_u U g^{-2}\nu^{-4}, \tag{21}$$

where α (Phillips, 1958) and α_u (Kahma, 1981) are the same constants that are normally used to describe the subranges of the frequency spectrum.

We studied the properties of this spectrum for different locations and wave conditions in the Baltic Sea. When it could be determined, the saturation value for the Q-spectrum was roughly $1 \cdot 10^{-2}$. This was close to twice the saturation value calculated from the wavenumber spectra, which is expected from theory. The saturation range in the frequency spectra was less pronounced, decayed slower than ω^{-5}, and had a higher saturation value or about $\alpha = 2.5 \cdot 10^{-2}$, thus being inconsistent with the other spectral domains. We determined that the effect of the Doppler shift in our results was small, since it would have otherwise broken the observed similarity of the saturation ranges in the Q-spectra and the wavenumber spectra. With this uncertainty removed, we deduced that the main explanation for the variations and inconsistencies in the frequency spectra were caused by the presence of nonlinear harmonic components, which is in line with recent studies (Guimarães, 2018; Leckler et al., 2015).

During a strongly forced ($U/c_p = 2$–3) fetch-limited case the equilibrium levels, α_u, in the frequency spectrum varied with the strength of the forcing; such a variation was practically absent in the Q-spectra (Figure 11). The saturation range in the inverse phase speed and frequency domain decayed slower than ν^{-5}, and ω^{-5}, respectively, when a swell propagating with an 90–100° angle with respect to a fetch-limited wind sea (Figure 12). When it could be determined, the equilibrium-to-saturation transition took place slightly above $U\nu = 3$.

In duration-limited cases, with and without swell, the Q-spectra were mostly characterized by a ν^{-5} rear face, while the frequency spectra showed an equilibrium range and a transition at roughly $\tilde{\omega} = 5$ (Figure 13 and 14). Nonetheless, the duration-limited spectra with higher winds still did not show clear subranges and transitions in the wavenumber and inverse phase speed domains.

The wavenumber spectrum is fundamentally correct if the intrinsic nature of the waves, such as the wave steepness, is the main interest. The new inverse phase speed spectrum can offer a more straightforward representation of the waves if the central parameter is the apparent speed of the waves, with the most obvious example being the study of the momentum transfer between the wind and the waves. In such cases $U\nu = U/c$ is given directly by the Q-spectrum without separate current measurements and theoretical assumptions regarding the Doppler shift or velocity bunching.

Appendix A: Connection Between Equilibrium Levels and Transition Frequency

The saturation range of the spectrum of Phillips (1958)—valid above some yet undetermined frequency ω_g—is of the form

$$S(\omega) = \alpha g^2 \omega^{-5}, \tag{A1}$$

where α is a constant.

The equilibrium spectrum of Kahma (1981)—valid on the rear face of the spectrum prior to the Phillips' range—is of the form

$$S(\omega) = \alpha_u U g \omega^{-4}, \tag{A2}$$

where $\alpha_u = 4.5 \cdot 10^{-3}$ is a constant. Donelan et al. (1985) presented the equilibrium range of the spectrum in a form derived from the spectrum by Phillips (1958) by exchanging a frequency for the peak frequency:

$$S(\omega) = \alpha_D g^2 \omega_p^{-1} \omega^{-4}. \tag{A3}$$

In this expression α_D is not a constant but was given as a function of the wave age as

$$\alpha_D = \alpha_u \left(U/c_p\right)^p, \tag{A4}$$

where α_u is a constant and p is a real number. Donelan et al. (1985) proposed $\alpha_u = 6 \cdot 10^{-3}$ and $p = 0.55$. With a choice of $\alpha_u = 4.5 \cdot 10^{-3}$ and $p = 1$ the formulation is equivalent to that of Kahma (1981), since

$$S(\omega) = \left(\alpha_u U/c_p\right) g^2 \omega_p^{-1} \omega^{-4} = \left(\alpha_u U \omega_p g^{-1}\right) g^2 \omega_p^{-1} \omega^{-4} = \alpha_u U g \omega^{-4}. \tag{A5}$$

If we want to introduce the wave age dependent α_u in the spectrum by Kahma (1981), we get

$$S(\omega) = \alpha_u \left(U/c_p\right)^{p-1} U g \omega^{-4}, \tag{A6}$$

where p is the same exponent as used by Donelan et al. (1985).

The transition frequency, ω_g, is defined as the point when the equilibrium range meets the saturation range:

$$\alpha_u \left(U/c_p\right)^{p-1} U g \omega_g^{-4} = \alpha g^2 \omega_g^{-5} \tag{A7}$$

$$\frac{\omega_g U}{g} = \frac{\alpha}{\alpha_u} \left(\frac{U}{c_p}\right)^{1-p}. \tag{A8}$$

It is easy to see that for the expression of Kahma, (1981; $p = 1$), where the equilibrium range depends linearly on the wind speed, the dimensionless transition frequency, $\tilde{\omega}_g$, is constant. For a choice of $p = 0$ the direct wind speed dependence vanishes, and we get

$$\frac{\omega_g U}{g} = \frac{\alpha}{\alpha_u} \left(\frac{U}{c_p}\right)^1 \tag{A9}$$

$$\frac{\omega_g U}{g} = \frac{\alpha}{\alpha_u} \left(\frac{U \omega_p}{g}\right) \tag{A10}$$

$$\frac{\omega_g}{\omega_p} = \frac{\alpha}{\alpha_u}. \tag{A11}$$

In other words, the transition frequency is always a constant multiple of the peak. The equilibrium range is then not a function of the wind speed, but depends only on the peak frequency (which in turn has a dependence on the wind speed). Expressed in terms of the spectrum of Donelan et al. (1985), the case $p = 0$ would mean that the constant α_D is a constant independent of the forcing—a direct analogue to the original Phillips' spectrum.

Appendix B: Doppler Shift of the $Q(\nu)$ Spectrum With an Ambient Current

The intrinsic frequency of a wave is Doppler shifted if a mean current is present. The apparent frequency will then be given by

$$\omega = \sigma + k U_c \cos(\varphi), \tag{B1}$$

where ω and σ are the apparent and intrinsic frequencies, U_c is the current speed, and φ is the angle between the wave and current directions. In the frequency domain the effect of the current on the saturation spectrum has been estimated by assuming that the wavenumbers follow the linear dispersion relation (Kitaigorodskii et al., 1975). If $\varphi > 0$ (a following current) the saturation spectrum will decay slower than ω^{-5} and exhibit higher spectral values (Banner, 1990; Kitaigorodskii et al., 1975).

Since the inverse phase speed spectrum in this paper is calculated from the measured wavenumber and frequency of the wave components, no assumptions about k have to be made. We can therefore simply multiply equation (B1) with k^{-1}:

$$\frac{\omega}{k} = \frac{\sigma}{k} + U_c \cos(\varphi) \tag{B2}$$

$$c = c_\sigma + U_c \cos(\varphi). \tag{B3}$$

The relationship between the intrinsic inverse phase speed, $\nu_\sigma = c_\sigma^{-1}$, and the apparent inverse phase speed, $\nu = c^{-1}$, is now determined by

$$\nu = \frac{1}{(\nu_\sigma)^{-1} + U_c \cos(\varphi)}. \tag{B4}$$

The Jacobian of the transformation will be

$$J = \frac{\partial \nu_\sigma}{\partial \nu} = \frac{1}{\left(1 - U_c \cos(\varphi)\nu\right)^2}. \tag{B5}$$

Under a following current ($\varphi > 0$) the apparent frequency will increase ($\omega > \sigma$). Since the wavenumber is fixed (instead of being estimated from the frequency), the apparent phase speed will also increase ($c > c_\sigma$). This, again, is equivalent with a decrease in the apparent inverse phase speed ($\nu < \nu_\sigma$). As a result, the spectral levels will decrease, thus leading to a lower saturation constant α.

Such a lowering of the saturation constant is seen in Figure 11a, where the saturation values around $\alpha = Q(\nu)g^2\nu^5 = 1 \cdot 10^{-1}$ are slightly lower than what is estimated from the pure wavenumber measurements using liner theory ($\alpha = 1.2 \cdot 10^{-2}$). The factor 1.2 difference roughly corresponds to a current speed of $U_c \cos(\varphi) = 0.1$ m/s (1–2% of the wind speed in Run 15033). The Doppler shift of an ambient current will also affect the power law of the saturation spectrum making it decay slightly faster than ν^{-5}. Nevertheless, this effect is small for such low current speeds.

The Jacobian in equation (B5) becomes infinite in the case of an opposing current with a speed equal to the phase speed of the wave component. While no current measurements are available for this study, the slowest waves captured by the experimental setup are roughly 0.8 m/s. They are therefore faster than even the strong, 0.4 m/s, currents that have been measured in narrow fairways in the Archipelago Sea (Kanarik et al., 2018). Typical current speeds in the Baltic Sea are around 0.1–0.3 m/s. Still, in the case of stronger currents and/or observational techniques capable of resolving slower waves, the singularity issue of the Jacobian can become relevant.

Acknowledgments
This work has been funded by Arvid och Greta Olins Fond (Svenska kulturfonden, 17/103386), Finska Vetenskaps-Societeten, and Magnus Ehrnrooths stiftelse. The research has also received funding from BONUS, the joint Baltic Sea research and development program (Art 185) through Grant 03F0773A (BONUS INTEGRAL). We would like to thank the captain and crew of R/V *Aranda* for their flexibility and expertise shown during the expeditions. This study has utilized research infrastructure facilities provided by FINMARI (Finnish Marine Research Infrastructure network). The data are available through its DOI (https://doi.org/10.5281/zenodo.2516432). We want to extend our thanks to the anonymous reviewers. Their constructive comments and suggestions allowed us to improve and strengthen this manuscript.

References

Banner, M. L. (1990). Equilibrium spectra of wind waves. *Journal of Physical Oceanography*, *20*(7), 966–984. https://doi.org/10.1175/1520-0485(1990)020<0966:ESOWW>2.0.CO;2

Barrick, D. E., & Weber, B. L. (1977). On the nonlinear theory for gravity waves on the ocean's surface. Part II: Interpretation and applications. *Journal of Physical Oceanography*, *7*, 11–21. https://doi.org/10.1175/1520-0485(1977)007<0011:otntfg>2.0.co;2

Donelan, M. A., Babanin, A. V., Sanina, E., & Chalikov, D. V. (2015). A comparison of methods for estimating directional spectra of surface waves. *Journal of Geophysical Research: Oceans*, *120*, 5040–5053. https://doi.org/10.1002/2015JC010808

Donelan, M. A., Drennan, W. M., & Magnusson, A. K. (1996). Nonstationary analysis of the directional properties of propagating waves. *Journal of Physical Oceanography*, *26*(9), 1901–1914. https://doi.org/10.1175/1520-0485(1996)026<1901:NAOTDP>2.0.CO;2

Donelan, M. A., Hamilton, J., & Hui, W. H. (1985). Directional spectra of wind-generated waves. *Philosophical Transactions of the Royal Society A: Mathematical, Physical and Engineering Sciences*, *315*(1534), 509–562. https://doi.org/10.1098/rsta.1985.0054

Drennan, W. M., Donelan, M. A., Madsen, N., Katsaros, K. B., Terray, E. A., & Flagg, C. N. (1994). Directional wave spectra from a swath ship at sea. *Journal of Atmospheric and Oceanic Technology*, *11*(4), 1109–1116. https://doi.org/10.1175/1520-0426(1994)011<1109:DWSFAS>2.0.CO;2

Dupuis, H., Guerin, C., Hauser, D., Weill, A., Nacass, P., Drennan, W. M., et al. (2003). Impact of flow distortion corrections on turbulent fluxes estimated by the inertial dissipation method during the FETCH experiment on R/V L'Atalante. *Journal of Geophysical Research*, *108*(C3), 8064. https://doi.org/10.1029/2001JC001075

Fedele, F. (2014). Geometric phases of water waves. *EPL (Europhysics Letters)*, *107*(6), 224–230. https://doi.org/10.1209/0295-5075/107/69001

Forristall, G. Z. (1981). Measurements of a saturated range in ocean wave spectra. *Journal of Geophysical Research*, *86*(C9), 8075–8084. https://doi.org/10.1029/JC086iC09p08075

Guimarães, P. V. (2018). Sea surface and energy dissipation (Ph.D. thesis), Loire Bretagne University.

Hara, T., & Karachintsev, A. V. (2003). Observation of nonlinear effects in ocean surface wave frequency spectra. *Journal of Physical Oceanography*, *33*(2), 422–430. https://doi.org/10.1175/1520-0485(2003)033<0422:OONEIO>2.0.CO;2

Hisaki, Y., & Tokuda, M. (1995). Detection of nonlinear waves and their contribution to ocean wave spectra. Part II: Observation. *Journal of Oceanography*, *51*(4), 407–419. https://doi.org/10.1007/BF02286388

Hwang, P., & Wang, D. W. (2001). Directional distributions and mean square slopes in the equilibrium and saturation ranges of the wave spectrum. *Journal of Physical Oceanography*, *31*(5), 1346–1360. https://doi.org/10.1175/1520-0485(2001)031<1346:DDAMSS>2.0.CO;2

Hwang, P., Wang, D. W., Walsh, E. J., Krabill, W. B., & Swift, R. N. (2000). Airborne measurements of the wavenumber spectra of ocean surface waves. Part II: Directional distribution. *Journal of Physical Oceanography*, *30*(11), 2753–2767. https://doi.org/10.1175/1520-0485(2001)031<2753:AMOTWS>2.0.CO;2

Janssen, P. (2009). On some consequences of the canonical transformation in the Hamiltonian theory of water waves. *Journal of Fluid Mechanics*, *637*, 1–44. https://doi.org/10.1017/S0022112009008131

Kahma, K. K. (1981). A study of the growth of the wave spectrum with fetch. *Journal of Physical Oceanography*, *11*(11), 1503–1515.

Kahma, K. K., & Calkoen, C. J. (1992). Reconciling discrepancies in the observed growth of wind-generated waves. *Journal of Physical Oceanography*, *22*(12), 1389–1405. https://doi.org/10.1175/1520-0485(1992)022<1389:RDITOG>2.0.CO;2

Kanarik, H., Tuomi, L., Alenius, P., Lensu, M., Miettunen, E., & Hietala, R. (2018). Evaluating strong currents at a fairway in the Finnish Archipelago Sea. *Journal of Marine Science and Engineering*, *6*(122), 1–20. https://doi.org/10.3390/jmse6040122

Kitaigorodskii, S. A. (1983). On the theory of the equilibrium range in the spectrum of wind-generated gravity waves. *Journal of Physical Oceanography*, *13*(5), 816–827. https://doi.org/10.1175/1520-0485(1983)013<0816:OTTOTE>2.0.CO;2

Kitaigorodskii, S. A., Krasitskii, V. P., & Zaslavskii, M. M. (1975). On Phillips' theory of equilibrium range in the spectra of wind-generated gravity waves. *Journal of Physical Oceanography*, *5*(3), 410–420. https://doi.org/10.1175/1520-0485(1975)005<0410:OPTOER>2.0.CO;2

Komen, G. J. (1980). Nonliner contribution to the frequency spectrum of wind-generated water waves. *Journal of Physical Oceanography*, *10*, 779–790.

Leckler, F., Ardhuin, F., Peureux, C., Benetazzo, A., Bergamasco, F., & Dulov, V. (2015). Analysis and interpretation of frequency-wavenumber spectra of young wind waves. *Journal of Physical Oceanography*, *45*(10), 2484–2496. https://doi.org/10.1175/JPO-D-14-0237.1

Lenain, L., & Melville, W. K. (2017). Measurements of the directional spectrum across the equilibrium-saturation ranges of wind-generated surface waves. *Journal of Physical Oceanography*, *47*, 17–0017. https://doi.org/10.1175/JPO-D-17-0017.1

Lund, B., Collins III, C. O., Tamura, H., & Graber, H. C. (2016). Multi-directional wave spectra from marine X-band radar. *Ocean Dynamics*, *66*(8), 973–988. https://doi.org/10.1007/s10236-016-0961-z

Melville, W. K. (1983). Wave modulation and breakdown. *Journal of Fluid Mechanics*, *128*, 489–506. https://doi.org/10.1017/S0022112083000579

Mitsuyasu, H. (1977). Measurement of the high-frequency spectrum of ocean surface waves. *Journal of Physical Oceanography*, *7*(6), 882–891. https://doi.org/10.1175/1520-0485(1977)007<0882:MOTHFS>2.0.CO;2

Peureux, C., Benetazzo, A., & Ardhuin, F. (2018). Note on the directional properties of meter-scale gravity waves. *Ocean Science*, *14*, 41–52. https://doi.org/10.5194/os-14-41-2018

Phillips, O. M. (1958). The equilibrium range in the spectrum of wind-generated waves. *Journal of Fluid Mechanics*, *4*(4), 426–434. https://doi.org/10.1017/S0022112058000550

Phillips, O. M. (1985). Spectral and statistical properties of the equilibrium range in wind-generated gravity waves. *Journal of Fluid Mechanics*, *156*, 505–531. https://doi.org/10.1017/S0022112085002221

Romero, L., & Melville, W. K. (2010). Airborne observations of fetch-limited waves in the Gulf of Tehuantepec. *Journal of Physical Oceanography*, *40*(3), 441–465. https://doi.org/10.1175/2009JPO4127.1

Tamura, H., Drennan, W. M., Sahlée, E., & Graber, H. C. (2014). Spectral form and source term balance of short gravity wind waves. *Journal of Geophysical Research: Oceans*, *119*, 7406–7419. https://doi.org/10.1002/2014JC009869

Toba, Y. (1973). Local balance in the air-sea boundary processes—III. On the spectrum of wind waves. *Journal of the Oceanographical Society of Japan*, *29*, 209–220. https://doi.org/10.1007/BF02108528

Wang, D. W., & Hwang, P. (2004). The dispersion relation of short wind waves from space–time wave measurements. *Journal of Atmospheric and Oceanic Technology*, *21*(12), 1936–1945. https://doi.org/10.1175/JTECH-1669.1

Young, I. R., Verhagen, L. A., & Banner, M. L. (1995). A note on the bimodal directional spreading of fetch-limited wind waves. *Journal of Geophysical Research*, *100*(C1), 773–778. https://doi.org/10.1029/94JC02218

ILMATIETEEN LAITOS
METEOROLOGISKA INSTITUTET
FINNISH METEOROLOGICAL INSTITUTE

FINNISH METEOROLOGICAL INSTITUTE
Erik Palménin aukio 1
P.O. Box 503
FI-00560 HELSINKI
tel. +358 29 539 1000
WWW.FMI.FI

FINNISH METEOROLOGICAL INSTITUTE
CONTRIBUTIONS No. 159
ISSN 0782-6117
ISBN 978-952-336-092-1 (paperback)
ISBN 978-952-336-093-8 (pdf)
https://doi.org/10.35614/isbn.9789523360938
Helsinki, 2020

Edita Prima Oy